



HAL
open science

Multifunctional iron vanadate thin films for spintronics

Antonio Peña Corredor

► **To cite this version:**

Antonio Peña Corredor. Multifunctional iron vanadate thin films for spintronics. Material chemistry. Université de Strasbourg, 2023. English. NNT : 2023STRAE017 . tel-04434709

HAL Id: tel-04434709

<https://theses.hal.science/tel-04434709>

Submitted on 2 Feb 2024

HAL is a multi-disciplinary open access archive for the deposit and dissemination of scientific research documents, whether they are published or not. The documents may come from teaching and research institutions in France or abroad, or from public or private research centers.

L'archive ouverte pluridisciplinaire **HAL**, est destinée au dépôt et à la diffusion de documents scientifiques de niveau recherche, publiés ou non, émanant des établissements d'enseignement et de recherche français ou étrangers, des laboratoires publics ou privés.

ÉCOLE DOCTORALE Physique et Physique - Chimie
Institut de Physique et Chimie des Matériaux de Strasbourg

THÈSE présentée par :
Antonio PEÑA CORREDOR

soutenue le : **20 octobre 2023**

pour obtenir le grade de : **Docteur de l'Université de Strasbourg**

Discipline/S spécialité : **Sciences des Matériaux**

**Multifunctional iron vanadate
thin films for spintronics**

THÈSE dirigée par :

LEFEVRE Christophe

Directeur de recherche, CNRS – Université de Strasbourg

RAPPORTEURS :

JOLY Yves

Directeur de recherche, CNRS – Institut Néel

SÁNCHEZ BARRERA Florencio

Research scientist, ICMAB - CSIC

AUTRES MEMBRES DU JURY :

CASANOVA FERNÁNDEZ Fèlix

Professeur, Ikerbasque - Nanogune

COLIS Silviu

Professeur, Université de Strasbourg

GUILLOUX-VIRY Maryline

Professeure, Université de Rennes

VIART Nathalie

Professeure, Université de Strasbourg

– This page intentionally left blank –

Palos con gusto saben a almendras.

María José Corredor Lara

– This page intentionally left blank –

Thesis outline

List of abbreviations	1
General introduction	3
Chapter I. FeV₂O₄ in the spinel vanadate family	7
1. Spinel vanadates	8
1.1. Spinel vanadates in the vanadate family.....	8
1.2. Spinel vanadates and Mott insulators	13
2. FeV₂O₄: spinel iron vanadate	15
2.1. Structural transitions and orbital ordering	15
2.2. Magnetic orderings.....	16
2.3. Ferroelectric orderings	18
2.4. FeV ₂ O ₄ thin films	21
Chapter II. FeV₂O₄: from the bulk form to the thin film	25
1. Synthesis methods	26
1.1. Bulk target elaboration	26
1.2. Pulsed laser deposition (PLD).....	29
2. Characterisation techniques	34
2.1. Scanning electron microscopy	34
2.2. X-ray characterisation.....	35
2.3. RHEED	43
2.4. Atomic Force Microscopy	45
2.5. Magnetometry measurements.....	46
2.6. Transport measurements	48
3. Results on bulk FeV₂O₄	50
3.1. Granulometry	50
3.2. Scanning electron microscopy	51
3.3. Powder XRD	52
3.4. Temperature-dependant magnetism and specific heat	56
3.5. Hysteresis curves.....	57
3.6. High-temperature measurements.....	58
3.7. AC susceptibility measurements	60
4. Results on FeV₂O₄ thin films	62
4.1. Optimisation of FeV ₂ O ₄ thin-film deposition.....	62
4.2. X-ray reflectivity results	64
4.3. Scanning electron microscopy	66
4.4. RHEED pattern analysis.....	67

4.5.	AFM results	68
4.6.	The structural characterisation of thin films.....	69
4.7.	Magnetic properties of FeV ₂ O ₄ thin films.....	77
4.8.	Transport properties of thin films.....	84
Chapter III. Advanced structural characterisation of FeV₂O₄ films by resonant diffraction		87
1.	Fundamentals of resonant diffraction	89
1.1.	From the classical diffraction problem to the atomic scattering factor	89
1.2.	Anomalous diffraction.....	91
1.3.	Resonant Elastic X-ray Scattering	93
1.4.	Fitting of REXS spectra	94
2.	<i>insex</i>: reflection choice framework for REXS experiments	98
2.1.	Motivation and general description	98
2.2.	Program composition and module interactions	100
2.3.	Output showcase	102
3.	DANES on FeV₂O₄ films: cationic distribution	104
4.	EDAFS on FVO films: oxygen positions.....	108
4.1.	Theoretical validation.....	109
4.2.	Experimental results	111
4.3.	Oxygen positions as a function of temperature.....	115
5.	Neural networks for the refinement of REXS spectra.....	120
5.1.	Artificial neural networks and REXS spectra.....	120
5.2.	Model training and choice of best ANN architecture.....	122
5.3.	ANNs for the cationic distribution in the Fe-V-O system.....	123
5.4.	ANNs for the oxygen positions in FVO thin films	126
Chapter IV. Pt/FeV₂O₄ heterostructures for spintronics.....		129
1.	Introduction.....	130
1.1.	Spin-driven control of magnetic states	130
1.2.	Spin transport and magnetoresistance.....	132
1.3.	Magnetotransport studies	135
1.4.	FeV ₂ O ₄ as ferrimagnetic insulator for spintronics.....	136
1.5.	Quantification of the spin-orbit torque	137
2.	Elaboration of Pt/FeV₂O₄ heterostructures	140
2.1.	Elaboration procedure	140
2.2.	Hall-bar patterning	140
2.3.	Heterostructure characterisation	141
2.4.	Magnetometry measurements on the heterostructures	143
3.	Magnetotransport studies of Pt/FVO/STO heterostructures	146

3.1.	Longitudinal studies.....	146
3.2.	Transverse studies.....	152
4.	Summary and future perspectives	160
Chapter V.	Spinel thin films beyond iron vanadate	161
1.	Introduction: the Fe-V-O system	162
2.	Bulk VFO: synthesis and characterisation	164
3.	VFO thin films	166
3.1.	Thin film obtention and characterisation.....	166
3.2.	Cationic distribution in the thin film.....	169
3.3.	Magnetic and transport properties of VFO films.....	171
	General conclusions and future perspectives	175
	Annexes	179
1.	Figures about the research interest on vanadates.....	179
2.	Derivation of the two anomalous terms for the atomic scattering factor.....	180
3.	Additional information on artificial neural networks.....	181
3.1.	CV prediction deviations. XANES 115.....	181
3.2.	Artificial neural network architectures.....	182
3.3.	MSE model comparison – 333 XANES.....	183
3.4.	CV-train prediction deviations. XANES 333.....	184
3.5.	CV prediction deviations. EXAFS 115.....	185
3.6.	CV prediction deviations. EXAFS 115.....	186
3.7.	MSE evaluation for model comparison – EXAFS 115.....	187
3.8.	MSE evaluation for model comparison – EXAFS 333.....	188
4.	Whole-range diffractogram of Fe ₂ VO ₄ //MgO thin films.....	189
	Résumé de thèse en français	191
1.	Introduction.....	191
2.	FeV ₂ O ₄ : du massif aux couches minces.....	195
3.	Étude structurale avancée par diffraction résonante.....	202
4.	Hétérostructures de Pt/FeV ₂ O ₄ pour la spintronique.....	206
5.	Les couches minces de spinelles oxides au-delà de FeV ₂ O ₄	210
	References	213
	Acknowledgements	229

– This page intentionally left blank –

List of abbreviations

AC: alternative current.	ISHE: inverse spin Hall effect.
AFM: atomic force microscopy.	JT: Jahn-Teller.
AHE: anomalous Hall effect.	LAO: LaAlO ₃ , lanthanum aluminate.
AMR: anisotropy magnetoresistance.	LTO: low-temperature orthorhombic.
ANE: anomalous Nerst effect.	LTT: low-temperature tetragonal.
ANN: artificial neural network.	MAO: LaAlO ₃ , magnesium aluminate.
CIMS: current-induced magnetisation switching.	MFM: magnetic force microscopy.
CV: cross-validation.	ML: machine learning.
DANES: diffraction anomalous near-edge structure.	MPE: magnetic proximity effect.
DFT: differential function theory.	MR: magnetoresistance.
DL: damping-like.	MRAM: magnetic random-access memories.
EDAFS: extended diffraction absorption fine structure.	ND: neutron diffraction.
EDS: energy dispersive spectroscopy.	OHE: ordinary Hall effect.
ES: experimental spectrum.	OO: orbital order.
EXAFS: extended x-ray absorption fine structure.	OOP: out-of-plane.
FC: field cooling.	PED: precession electronic diffraction.
FL: field-like.	PES: pseudo-experimental spectrum.
FM: ferromagnet.	PHE: planar Hall effect.
FMR: ferromagnetic resonance.	PLD: pulsed laser deposition.
FVO: FeV ₂ O ₄ , iron vanadate.	PMA: perpendicular magnetic anisotropy.
FWHM: full width half maximum.	PPMS: physical property measurement station.
GADDS: general area detector diffraction system.	REXS: resonant elastic x-ray scattering.
GMR: giant magnetoresistance.	RHEED: reflection high-energy electron diffraction.
HM: heavy metal.	RIXS: resonant inelastic x-ray scattering.
HTO: high-temperature orthorhombic.	RLP: reciprocal lattice point.
HTT: high-temperature tetragonal.	RSM: reciprocal space mapping.
IP: in-plane.	SEM: scanning electron microscopy.
	SHE: spin Hall effect.
	SMR: spin magnetoresistance.
	SOC: spin-orbit coupling.

List of abbreviations

SOT: spin-orbit torque.

SQUID: superconducting quantum interferometer device.

STEM: scanning transmission electron microscopy.

STO: SrTiO₃, strontium titanate.

STT: spin-transfer torque.

TA: thermal activation.

TGA: thermogravimetric analysis.

TS: theoretical spectrum.

VFO: Fe₂VO₄, vanadium ferrite.

VRH: variable-range hopping.

VSM: vibrating-sample vibratometer.

XANES: x-ray absorption near-edge structure.

XAS: x-ray absorption spectroscopy.

XMCD: x-ray magnetic circular dichroism .

XRD: x-ray diffraction.

XRR: x-ray reflectivity.

YIG: yttrium iron garnet.

YK: Yafet-Kittel.

ZFC: zero-field cooling.

General introduction

Multifunctional materials stand at the forefront of modern Material Sciences research. Multifunctionality comes with the ability to exhibit specific desirable properties across various domains, displaying electronic, magnetic and optical features, among others [1]. By harnessing these combined attributes, multifunctional materials pave the way for breakthroughs in performance metrics that were once deemed unattainable, offering new paradigms in both design and applications.

Delving deeper into the realm of multifunctional materials, multiferroics emerge as a particularly intriguing subset. These materials possess more than one primary ferroic ordering and, very frequently, they are correlated. This coexistence of orders enables a rich interplay between their distinct properties, leading to novel functionalities and potential applications. One example of multiferroism comes in the form of magnetoelectric materials, showcasing the simultaneous presence of both magnetic and electric orderings [2]. The unique property of these materials is their ability to induce a magnetic response when subjected to an electric field and vice versa. This magnetoelectric coupling offers a pathway to control and manipulate one order parameter using the other, which can be exploited for innovative device applications, such as sensors [3], actuators [4], and transducers [5].

In the context of multiferroic materials, thin film materials have garnered significant attention for the design of practical devices. The advances in thin-film growth techniques have provided a controlled way of synthesising high quality single-phase thin films and have allowed the properties of existing materials to be tailored by strain engineering [6]. Besides, the thin film geometry sometimes induces properties which are absent in the bulk material [7], [8] and enables the exploitation of the different ferroic orderings in the form of nanoscaled devices.

The focus of this PhD work has been the study of a multifunctional and multiferroic material: the spinel iron vanadate FeV_2O_4 (FVO) in its thin film form. Iron vanadate outstands due to its interconnected degrees of freedom: magnetic, ferroelectric and orbital; as well as manifesting a plethora of structural transitions with temperature. Research on iron vanadate has been fruitful in its bulk form but, at the commencement of this PhD, there was limited literature on iron vanadate thin films. Consequently, the primary aim of this thesis was to bridge the knowledge gap concerning iron vanadate thin films.

This thesis provides an overview of the research that I have conducted during my three-year PhD journey. It has not been conceived as an exhaustive compendium of all the research actions, and it is worth noting that several subprojects have been deliberately set aside. Nonetheless, this document highlights my contributions to the understanding of iron vanadate and the broader field of Material Sciences.

The initial objective of this doctoral research was to optimise the deposition of high-quality thin films of iron vanadate and to study their structure and physical properties. The results achieved prompted a branching out from this initial objective towards ancillary projects. The progression of this doctoral work, with its most significant points, is summarised in **Figure 0.1**. As can be observed in this diagram, the commencement of this research had a strong solid chemistry component, which gradually shifted towards materials science and, ultimately, to the fields of spintronics and crystallography.

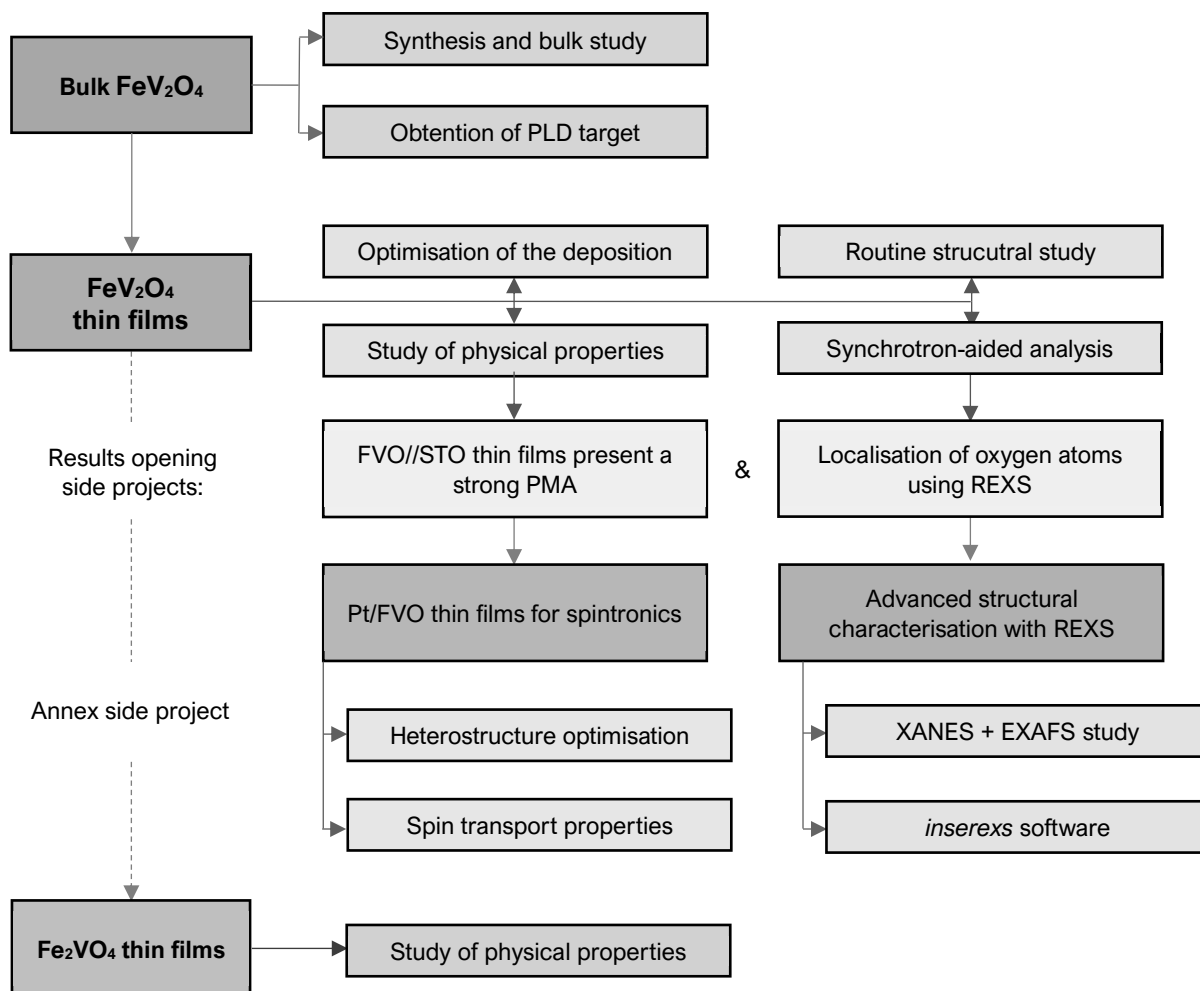


Figure 0.1. Diagram of the thesis progression with main projects highlighted in bold and dark colour, sub-parts of the projects in light colours, and outcomes leading to ancillary projects in pale yellow.

The thesis is composed of five main chapters which will be hereby presented, followed by a general conclusion and the future work perspectives. This is followed by the supplementary annexures. In accordance with university requirements, an extended summary in French language is provided at the close of the document. The bibliographic references and an acknowledgement section concludes this document.

The thesis commences with “**Chapter I.** FeV_2O_4 in the spinel vanadate family”. This initial chapter provides a comprehensive introduction to iron vanadate, beginning with an overview of the broader vanadate family and then focusing on the spinel vanadates subgroup. The unique properties of FVO, influenced by complex physical phenomena, are highlighted, especially in its thin film form. Serving as a foundation, the chapter establishes the theoretical context for the in-depth discussions in subsequent chapters.

The second chapter of this thesis, “**Chapter II.** FeV_2O_4 : from the bulk form to the thin film”, details the process of creating iron vanadate thin films, from the synthesis of ceramic targets to the final deposition. The chapter offers insights on the synthesis methods for bulk ceramics, the Pulsed Laser Deposition of thin films and the characterisation techniques for both bulk and thin film samples. Finally, it presents results of the structural analysis and the study of the physical properties for iron vanadate in both powder and thin film forms. Serving as both a methodological guide and a presentation of specific results, the chapter ensures the accurate crystal phase of iron FeV_2O_4 , setting the groundwork for subsequent in-depth analyses.

The third chapter of this thesis receives the name “**Chapter III.** Advanced structural characterisation of FeV_2O_4 films by resonant diffraction”. This chapter accentuates the importance of understanding the crystallographic structure of materials, specifically focusing on iron vanadate thin films. It highlights the challenges of conventional methods in studying thin films and introduces resonant (or anomalous) diffraction as a promising alternative. The chapter extensively discusses resonant elastic x-ray scattering (REXS) diffraction and its potential the crystal structure of thin films. REXS experiments are used to study the cation distribution in FeV_2O_4 thin films and, for the first time, it is also employed to locate the oxygen atoms in oxide thin films. For that purpose, a proof-of-concept is conducted through confrontation with experiments on a bulk sample, where traditional approaches validate the REXS methodology on the thin films. Additionally, the chapter presents a newly developed computer program for resonant diffraction, *insexs*, and explores the application of artificial neural networks in refining REXS spectra. Overall, it offers innovative methodologies and tools for the structural resolution of FeV_2O_4 thin films and other oxide thin films in the future.

The fourth chapter of the thesis, “**Chapter IV.** Pt/ FeV_2O_4 heterostructures for spintronics” chases the technological applicability of iron vanadate-based thin films, specifically in the form of Pt/ FeV_2O_4 heterostructures, for use in spintronics. The chapter begins with an introduction to the field of spintronics, focusing on the control of magnetic states through spin-driven effects. It then delves into the impact of these effects on the magnetotransport properties of materials and discusses the quantification of spin-orbit torques for reversing magnetisation. The chapter presents an in-depth study of the fabrication and spin transport properties of Pt/ FeV_2O_4 devices. The main finding is that spin-driven effects dominate the magnetoresistance signal, reaching a maximum value of 0.12% at low temperatures. This performance is comparable to optimised oxide-based systems. The results indicate

that iron vanadate is a promising candidate for future multifunctional spintronic devices, although further research is needed to confirm these findings and address existing limitations.

The fifth and final chapter of the thesis receives the name “**Chapter V. Spinel thin films beyond iron vanadate**”. This chapter objective is to overcome the applicability issues of iron vanadate by focusing on vanadium ferrite (Fe_2VO_4), a spinel oxide showcasing room-temperature magnetism. The chapter presents the first successful deposition of Fe_2VO_4 in the form of epitaxial thin films. The high-quality Fe_2VO_4 films are magnetic at room-temperature, and the cation distribution in the spinel structure is studied by means of resonant diffraction experiments. The preliminary results show indicate that the iron addition compromises the structure’s multifunctional features, but they open new avenues for future research.

Chapter I. FeV_2O_4 in the spinel vanadate family

This opening chapter smoothly delves into iron vanadate, FeV_2O_4 (FVO), the material that forms the core of this PhD thesis. For that purpose, we will embark on a brief journey through the broader vanadate family, spotlighting its flourishing significance in recent research. Our exploration will then narrow down to the subgroup of spinel vanadates (AV_2O_4). The metallic cation (A) highly differentiates the different members of this material subfamily, and their particularities will be presented in detail. Furthermore, we will explore the ways in which the transport properties of spinel vanadates can be fine-tuned by adjusting the inter-vanadium distance.

Then, we will present how iron vanadate outstands among spinel vanadates, mostly due to the interplay of complex physical phenomena such as the Jahn-Teller and Spin-orbit-coupling effects. This makes FVO showcase a plethora of structural transitions intertwined with magnetic, orbital, and ferroelectric orderings. As we progress, iron vanadate in its thin film form will be introduced. We will discuss the inherent appeal of depositing this multifunctional material in the thin film form and, finally, the current state of research on FVO thin films will be elaborately presented.

Conclusively, this chapter serves as the foundational bedrock for the subsequent sections of this thesis. By establishing the theoretical underpinnings of iron vanadate and its related materials, we set the stage for a deeper and more nuanced exploration in the chapters to follow.

1. Spinel vanadates

1.1. Spinel vanadates in the vanadate family

Vanadate oxides are a family of inorganic compounds that contain an oxyanion (V_xO^{2-y}) of vanadium and oxygen. Vanadium is a relatively abundant element [9] and can exist in several oxidation states, including +2, +3, +4, and +5, forming vanadates in all of them. The extensive vanadate class is full of compounds of interest for various technological applications in a wide range of different domains. With a steady research interest in the 20th century, the number of publications on the vanadate family (with the “vanadate” keyword) has significantly increased in the last ten years, as illustrated in **Figure I.1a**. A thematical and geographical distributions of articles regarding vanadates can be seen in **Figure A.1** and **Figure A.2** of this thesis’ annexes. The trend observed for the whole vanadate family is also observed for spinel vanadates (**Figure I.1b**), the vanadate subgroup we will focus on; and for iron vanadate (**Figure I.1c**), the main compound that this PhD work revolves around.

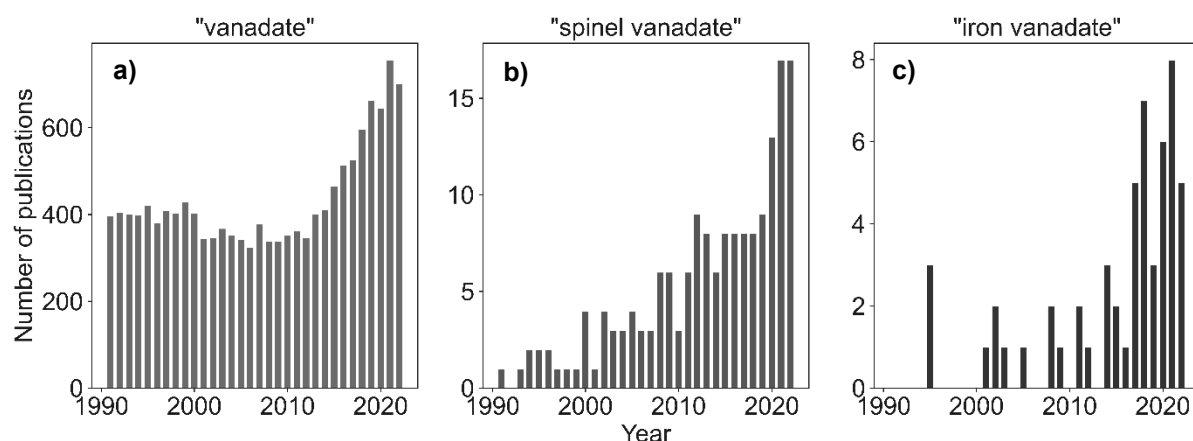


Figure I.1. Number of publications per year found in the <https://www.webofknowledge.com/> database for different search keywords: (a) “vanadate”, (b) “spinel vanadate” and (c) “iron vanadate”. Despite not being an exhaustive search, it clearly shows an increasing trend for the three selected keywords.

As previously said, vanadium’s wide range of oxidation states is the reason behind the great compound diversity in the vanadate family. With a +2 oxidation state, vanadium monoxide (VO) plays a significant role in the industrial process of selective catalytic oxidation of hydrocarbons [10]. The trivalent (+3) vanadium sesquioxide (VO₃) has been used as a gas detector and atmospheric pollutant detector [11]. On the other hand, with a +4-oxidation state, vanadium dioxide (VO₂), has promise for commercial applications that utilise its metal-to-semiconductor phase transition, such as optical switching or data storage [12]. With the same oxidation state, sodium metavanadate (Na₃VO₃) can be used in diabetes treatments thanks to its insulin-mimetic properties [13], and such medical functionalities are also shared by +5 sodium vanadate (Na₃VO₅) [14]. Finally, among the pentavalent vanadate oxides, vanadium pentoxide (V₂O₅) has been studied as a promising cathode material for high-performance rechargeable

batteries [15] and bismuth vanadate (BiVO_4) has gained considerable attention as a photoelectrode for solar water splitting and presents promising prospects for sustainable energy production [16].

Our focus will be directed towards the AV_2O_4 subfamily of vanadates, also known as “spinel vanadates”. These compounds are characterised by their cubic crystal structure, which consists of a spinel-type arrangement ($Fd\bar{3}m$, 227) of oxygen atoms located at the 32e positions (x, x, x). This O-packaging structure defines two different cationic sites in the spinel structure. Firstly, octahedral sites (O_h), placed at the 16d special position ($\frac{1}{2}, \frac{1}{2}, \frac{1}{2}$) and occupied by V atoms in spinel vanadates. The author acknowledges that using “-3 m” would be a more accurate representation of the octahedral crystal sites, but “ O_h ” will be employed to adhere to the existing literature convention. Secondly, tetrahedral sites (T_d), located at the 8a position ($\frac{1}{8}, \frac{1}{8}, \frac{1}{8}$) and filled with another metallic cation (A) – setting n. 2. The V atoms form a pyrochlore sublattice of corner-sharing V-tetrahedra. Such special arrangement of V-atoms causes a strong 3d orbital overlapping and significant exchange interactions between the different atoms of the sublattice [17]. The spinel structure and the pyrochlore sublattice have been schematised in **Figure I.2**.

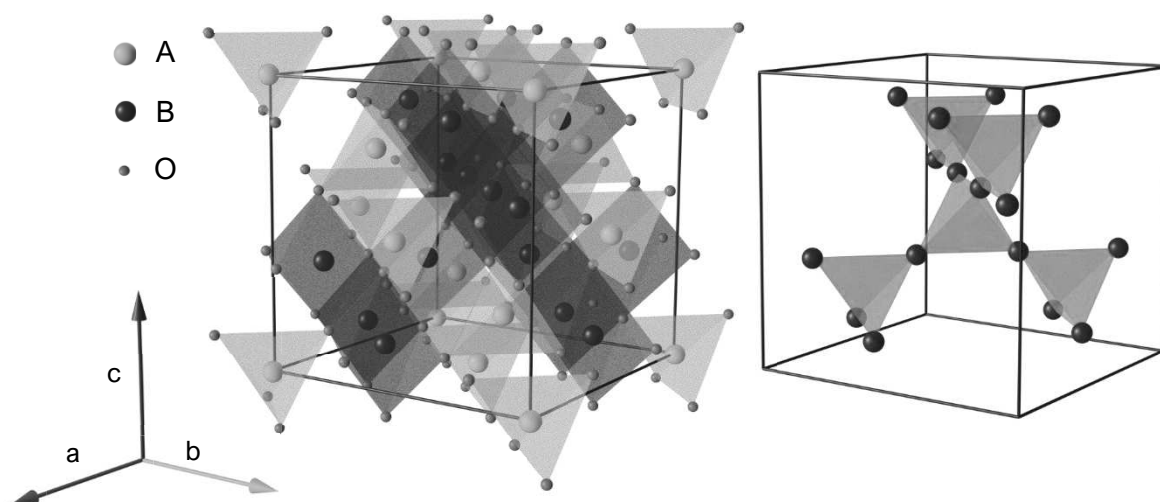


Figure I.2. Left: spinel structure (AB_2O_4) with A (T_d) in orange and B (O_h) in blue. Setting choice number 1: A at 0, 0, 0. All octahedra and tetrahedra which include atoms in the unit cell have been depicted. A unit cell contains four formula units of AB_2O_4 . Right: V-V pyrochlore lattice of corner-sharing tetrahedra between atoms in O_h sites.

The tetrahedra network of localised spins is governed by strong geometrical frustration and can result in exotic ground states such as spin liquid [18] and spin ices [19]. However, it is the cation at the tetrahedral crystal environment that differentiates the different members of the spinel vanadate family. This metallic cation can have either even or odd oxidation states.

In cases where the oxidation state is an odd number, V atoms have a mixed oxidation state, leading to partially occupied t_{2g} . This electronic configuration results in a natural charge order [20], [21]. Examples of such compounds include Al^{III}V₂O₄ (V^{+2.5}: $t_{2g}^{2.5}$) and LiV₂O₄ (V^{+3.5}: $t_{2g}^{1.5}$), the latter also known for presenting a heavy-fermion behaviour. In this material, electrons present a greater effective mass than a free electron, resulting in enhanced interactions and unique magnetic properties [17], [22], such as a high-field metamagnetic transition [23] and a transition from a state of localised magnetic moments to a heavy Fermi liquid [24]. Among these compounds, the spinel vanadate Ga^{III}V₂O₄ has been recently synthesised. It presents a structural arrangement of orbital molecules which resembles the structure of VO₂, and exhibits a high-temperature charge-ordering transition ($T_{CO} = 415$ K) [25].

When the oxidation state of the cation is +2, V cations assume a trivalent state (V³⁺). V³⁺ possesses a $3d^2$ electronic configuration which have the same energy under a spherical electronic environment. However, when surrounded by ligands in an octahedral configuration, the orbitals with high electronic densities along the ligands' directions (d_{z^2} and $d_{x^2-y^2}$) experience an increase in their energies, while the other d orbitals (d_{xz} , d_{yz} and d_{xy}) are stabilised by the effects of the crystal field energy. The d degeneracy is therefore broken into two orbital states: e_g and t_{2g} . This phenomenon has been illustrated in **Figure I.3**, and explains why transition metals are prone to coordinate with anionic ligands and experience stabilisation of their energies.

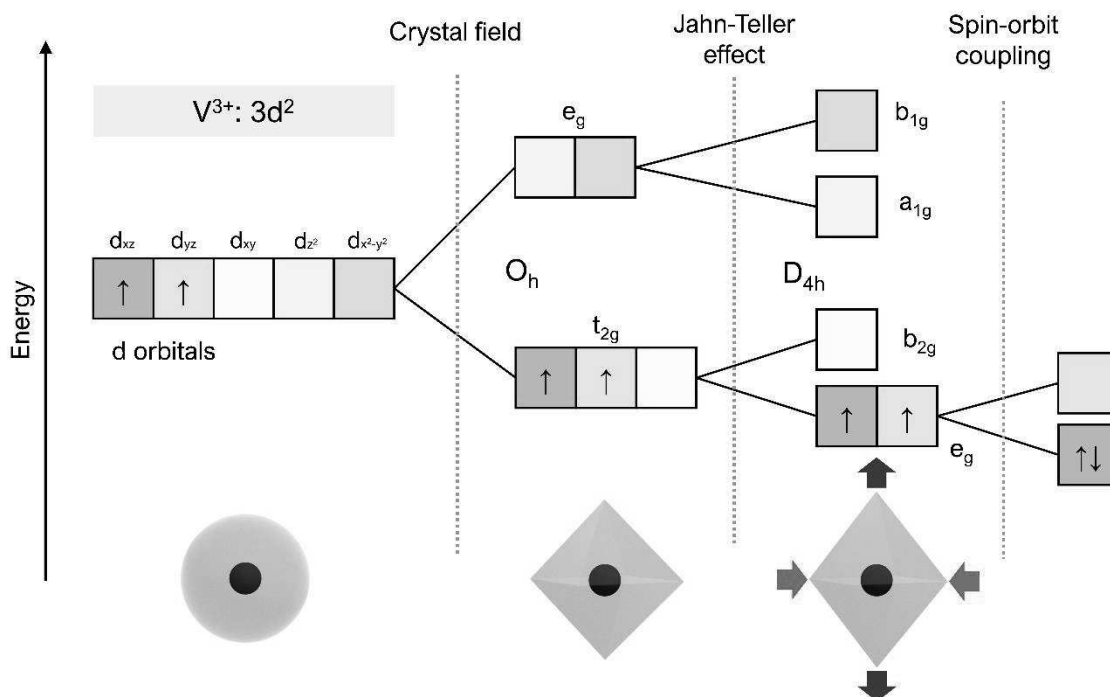


Figure I.3. Schematic representation of the energy stabilisation of V³⁺ in an octahedral electronic density, with the different splittings that can break the 3d degeneracy: i) crystal field splitting, ii) Jahn-Teller effect and iii) Spin-orbit coupling. Figures in the bottom correspond to electronic environments felt by the cation. Spin-orbit-coupling effects have been magnified for the sake of the visualisation.

The crystal field energy splitting caused the V³⁺ 3d orbitals to transition from a five-fold orbital degeneracy into a three-fold one. However, an elongation along the *z*-axis would lift the orbital degeneracy even further, and orbitals with a higher density along the *z* direction would be stabilised at the expense of those which privilege the *x* and *y* directions. As a result, the t_{2g}² state would break into a (d_{xz}¹d_{yz}¹)d_{xy}⁰ (or e_g²) state, and such elongation would reduce the system's O_h symmetry into D_{4h} square planar one. A compression along the *z*-axis (planar expansion) would have the opposite effect on the t_{2g} orbitals. This phenomenon is also known as Jahn-Teller (JT), which manifests as a distortion of the electronic structure of a species to lower the energy by removing degeneracy in its electronic configuration.

The degeneracy of the JT-driven electronic states can suffer additional lifts. For transition metals, a zero (quenched) orbital momentum is expected. However, the virtual excitation to the empty states can be considered as a second-order perturbation, leading to non-zero momenta values [41]. The presence of a non-negligible orbital momentum in V³⁺ has been proven in spinel vanadate compounds [19]. The orbitals momenta can interact with the cation's spin momentum through a process known as Spin-orbit coupling (SOC) and would lift the orbital degeneracy again [24]. In **Figure I.3**, a scenario has been proposed in which the SOC-driven lift would make the JT-driven e_g state go from a high-spin state into a low-spin one. In reality, the SOC would partially change the occupation of JT-degenerate orbitals, leading to a situation where mixed orbital occupation occurs.

These two effects, JT and SOC, are in constant competition and cooperation in the spinel vanadate family. Their coexistence explains why this vanadate subgroup have a natural tendency to exhibit geometrical distortions, and it is therefore frequent to find compounds from the vanadate family with a distorted spinel-based structure. Along with these distortions, the break in degeneracy of the three-fold degenerate t_{2g} state can result in a preferential occupation of one or some of the energy levels. If this phenomenon manifests in the long range order, an orbital ordering (OO) then occurs [26].

An orbital ordering indicates the emergence of a broken symmetry state in which localised occupied orbitals form a long-range regular pattern, analogous to spin momenta orderings in magnetically ordered structures [27]. In an OO, as the one schematised in **Figure I.4** for CoV₂O₄ (by Ishibashi et al. [28]), the orbital occupation follows a symmetry pattern along specific crystal directions. In the figure's example, there is a planar ferro-OO and an antiferro-OO along the *z* direction. The OO occurs as alternating (d_{xy}d_{yz}) and (d_{xy}d_{zx}) planes of occupied orbitals.

This ordering brings about a so-called "orbital degree of freedom" which may coexist with magnetic and/or charge orderings inside the materials. The interplay between spin, charge, lattice and orbital degrees of freedom is one of the reasons behind the research interest in spinel vanadates [29].

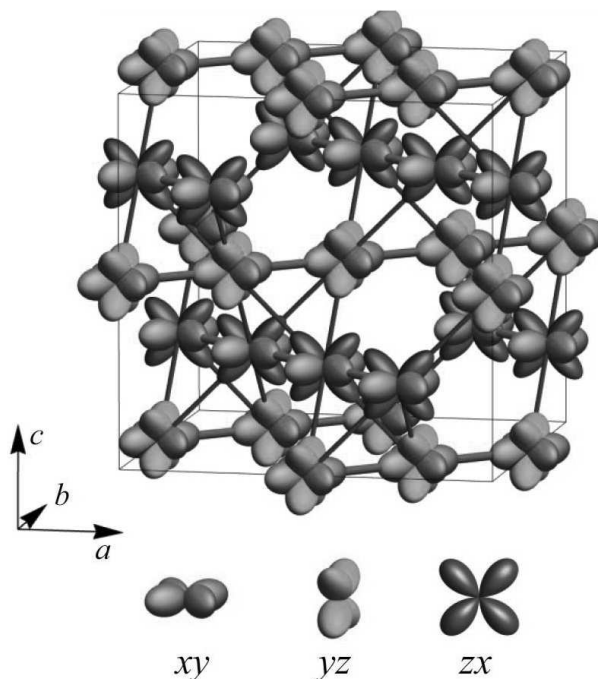


Figure I.4. Orbital occupancy in CoV_2O_4 , showing a long-range pattern known as orbital ordering. This orbital ordering is the same in the xy planar direction (ferro-OO) but alternates along the z direction. Taken from Ishibashi et al. [28].

In terms of the magnetic structure, V^{3+} is magnetically active ($S = 1$), resulting in a ferrimagnetic/antiferromagnetic behaviour in many $\text{A}^{\text{II}}\text{V}_2\text{O}_4$ compounds. The crystal and magnetic structures mainly depend on the nature of the A^{II} cation located at the tetragonal site. In the case of the cation being diamagnetic (e.g., A^{2+} : Mg^{2+} , Zn^{2+} , Cd^{2+}), A^{II} has a complete electronic shell and any structural distortion or magnetic behaviour will solely originate from the V atoms. In these compounds, there is a single structural transition from a room temperature cubic to a low-temperature tetragonal ($I4_1/amd$) structure ($T_s = 65, 51$ and 90 K for MgV_2O_4 , ZnV_2O_4 and CdV_2O_4 ; respectively), and a magnetic transition from room-temperature paramagnetic to low-temperature antiferromagnetic ($T_s = 42, 40$ and 30 K; respectively) [30]–[32]. The structural transition removes frustration effects, making the low-temperature magnetic long range antiferromagnetic order favourable [31].

These phenomena have been explained by Tsunetsugu and Motome [33] as an interplay of $dd\sigma$ superexchange interaction and geometrical frustration: they showed that an antiferromagnetic ordering of orbitals (antiferro-OO) can partially remove magnetic frustration and explain the experimentally observed magnetic structure which is composed of antiferromagnetic chains running in $[110]$ and $[1\bar{1}0]$ directions. Later, Tchernyshyov [34] proposed a purely ionic model where SOC plays the major role and the V orbital occupation takes place alongside a combination of xz and yz orbitals as a ferromagnetic orbital ordering (ferro-OO). The exact OO structure of these materials is still elusive, but the ferro-OO models seem to better match the experimental results [35].

If A^{II} has an incomplete electronic shell, both cations will play a role in the crystal, magnetic and orbital structure of the compound, and more intriguing phenomena may arise. That is the case of MnV₂O₄, (Mn²⁺: d⁴) which displays a magnetic transition from paramagnetic to collinear ferrimagnetic at 57 K, followed by a structural transition from cubic to tetragonal at 53 K [36]. At this temperature, the spin structure becomes non-collinear, and this phase transition can also be induced by an external field [37]. Additionally, an OO is believed to occur alongside the structural change. MnV₂O₄ exhibits a large magneto-caloric effect, which is believed to be linked to the change of the orbital state of V³⁺.

Another example is CoV₂O₄, (Co²⁺: d⁷), which displays two magnetic transitions with temperature, but no structural transition involving a lattice distortion. Initially, CoV₂O₄ transitions from a paramagnetic to ferrimagnetic at 142 K, then another phase transition occurs at 92 K [38]. The origin of the latter is still being discussed, but it might come from the emergence of a spin glass state or a short-range OO [39]. As previously described in **Figure I.4**, CoV₂O₄ shows a complex OO texture with a planar ferro-OO and an antiferro-OO along the *z* direction [28].

1.2. Spinel vanadates and Mott insulators

Mott-Hubbard insulators are materials in which valence electrons are strongly localised in their atomic orbitals, allowing no electrical conduction. These materials are characterised by strong interatomic Coulomb energies (*U*) that are much larger than the spin-dependant excitations (*t*) for charge transfer between sites, a situation known as strong-coupling limit: $U \gg t$. The completely opposite scenario, paramagnetic metals, corresponds to a completely delocalised electronic state. Electrons can propagate without feeling the opposition of Coulomb forces, situation which receives the name of weak-coupling limit: $U \ll t$ [40], [41]. The ease in which a material's electrons can hop from one site to another can be quantified by the spin-spin superexchange interaction (*J*) which, as seen in **Equation (I.1)**, depends on the two aforementioned parameters [42].

$$J \propto \frac{t^2}{U} \quad (\text{I.1})$$

The spin-spin superexchange interaction depends on the interatomic distance and, therefore, on the material's lattice volume. This volume dependence has been calculated by Harrison [43] for direct exchange between d orbitals to be $J \propto V^{-10/3}$. As a result, *J* decreases when lattice volume increases. This conclusion is anticipated because shorter interatomic distances facilitate electron charge transfer between sites.

The spinel vanadate family provides an excellent example of how lattice parameters, which are determined by the ionic radius of A, the cation at the tetrahedral site, can influence a material's conductivity, as shown in **Figure I.5**. Within this subgroup, one can find both conductive paramagnets

(such as LiV_2O_4) and Mott insulators (such as MgV_2O_4), with most other compounds falling between these two regimes. Additionally, the conductivity of a spinel vanadate can be modified from a Mott insulator to a paramagnetic metal by varying J , either through the application of mechanical strain or the introduction of a foreign atomic species (chemical doping) [41]. Strain can induce a first-order quantum phase transition between the Mott insulator and paramagnetic metal phases, known as the Mott transition. The electrical conductivity of spinel vanadates can be adjusted by manipulating the interatomic distances, making it useful for applications where the control of the electrical conductivity is critical [42].

In the vanadate family, there is a critical cation-cation distance $R_c \approx 0.262$ nm which marks the frontier between the localised and itinerant-electron regimes, proposed by Goodenough et al. [44, p. 266], [45] for similar octahedral-site cations in a close-packed oxygen sublattice. This value was later updated to 0.294 nm [46]. If the critical cation-cation distance R_c is such that $R < R_c$, then the cation sublattice d-electrons are collective, and if $R > R_c$, the cation sublattice d-electrons are localised [45]. These two scenerarios were distinguished as strong and weak interactions [47]. The conductivity (represented as the activation energy for conduction) vs. the interatomic V-V distances have been represented in. Values for interatomic distances and activation energies were obtained from the work of Rogers et al. [48], Kiswandhi et al. [49] and Kondo [50].

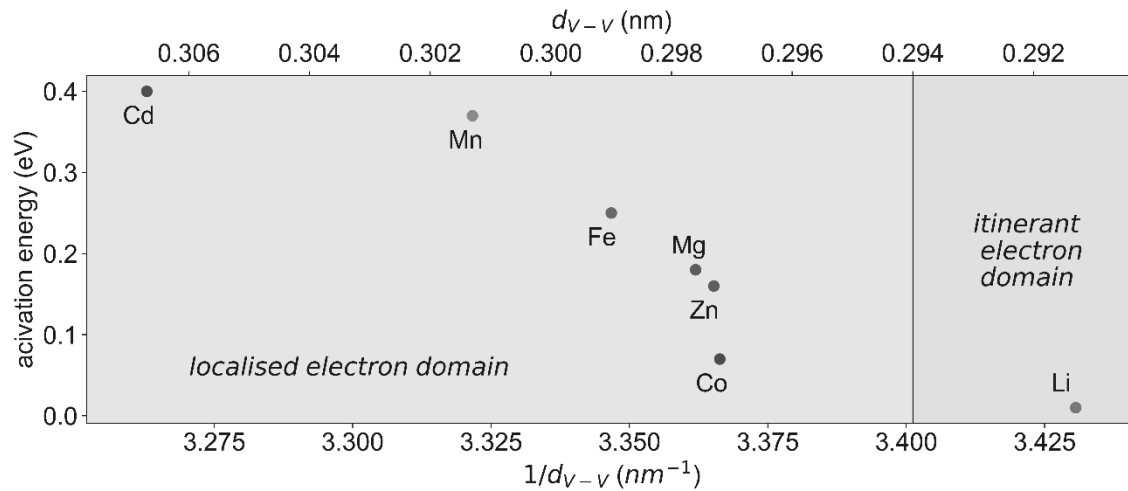


Figure I.5. Activation energy as a function of the V-V interdistance (top axis) or the inverse of the interdistance (bottom axis). Distance values corresponding to the localised electron domain are marked in red background, whereas distance values for the itinerant electron domain have a blue background. The critical V-V distance for conduction (R_c) corresponds to the frontier between these two conduction realms.

2. FeV₂O₄: spinel iron vanadate

2.1. Structural transitions and orbital ordering

Although all members of the spinel vanadate family would be worth studying, my PhD project has specifically focused on FeV₂O₄ (FVO), in which iron is the cation which occupies the tetrahedral site. In a T_d environment, the degenerate 3d orbitals split into the t₂ and e states. The electronic configuration of Fe²⁺ is d⁶, which leads to a doubly degenerate e³t₂³ state when placed in a tetrahedral crystal field, as schematised in **Figure I.6**. Similarly to V³⁺ in the O_h environment, Fe²⁺ in the T_d site can be stabilised by lifting the degeneracy to achieve D_{2d} symmetry. In the case of an elongation of the horizontal tetrahedra edges (as the one in the scheme), this would make the d_{z²} (a₁) contain the paired electron pair. An edge compression of these corners, however, would make this electron pair occupy the d_{x²-y²} (b₁), instead. The orbital occupation in Fe sites is therefore purely JT-driven.

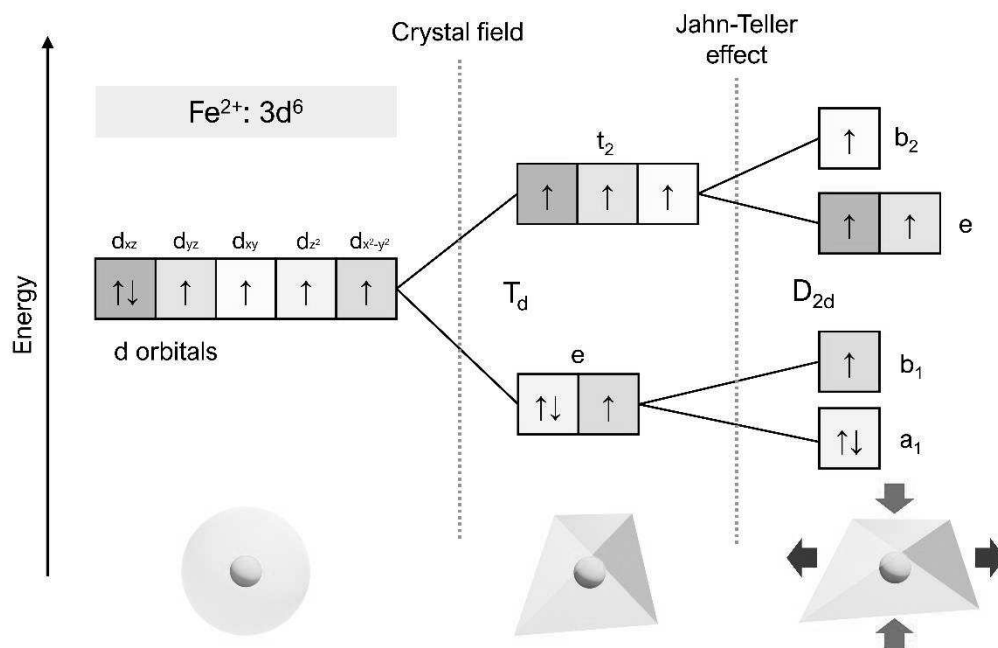


Figure I.6. Schematic representation of the energy stabilisation of Fe²⁺ in a tetrahedral electronic density, with the different splittings that can break the 3d degeneracy: i) crystal field splitting, ii) Jahn-Teller effect. Figures in the bottom correspond to electronic environments felt by the cation.

FVO is a special contender in the spinel vanadate family thanks to the presence of JT-active ions in both tetrahedral and octahedral sites, which sums up with the aforementioned SOC effects in V³⁺. All these assets make FVO a complex system in which the interplay (competition and or cooperation) of JT effects and SOC cause the system to adopt specific orbital arrangements depending on the dominant

phenomena. In general, if the SOC is predominant, the orbital occupation is forced along primary cubic axes, while in JT-predominant systems strong single-ion anisotropy forces spins to align along cubic $\langle 111 \rangle$ directions [19], [51]. Nevertheless, the phenomena interplay varies with temperature and this explain the varying nature of both FVO's OO and crystalline structure.

As temperature changes, FVO undergoes four phase transitions. At room temperature, it has a cubic spinel structure but, at $T_{S1} = 140$ K it transitions into a high-temperature tetragonal (HTT) compressed structure ($c < a$). This first transition is driven by the cooperative JT distortion on the FeO₄ tetrahedra, which cause a ferro-OO. Then, at $T_{N1} = 110$ K, FVO shifts into a high-temperature orthorhombic (HTO) structure, triggered by the SOC at the Fe²⁺ site. The transition changes the plane projection of the OO but it remains ferro-OO. Finally, at lower temperatures ($T_{N2} = 60$ K), FVO transitions into a low-temperature tetragonal (LTT) structure, and again into a low-temperature orthorhombic (LTO) structure at ($T_{S2} = 30$ K). These two last transitions have been associated with a JT-driven ferro-OO on V³⁺ sites. The different structures (symmetry groups and special positions of each atom) have been indicated in **Table I.1** on page 20, as well as the different ordering occurring at the diverse crystal phases [52], [53].

There seems to be academic consensus on the structure evolution with temperature, with a wide range of studies showing the same results [19], [52]–[54]. However, the OO structure and the triggers of each transition remain a subject of debate. The results presented above for the OO come from an analysis of normal-mode distortions from crystallographic data by Nii et al. [52] and equivalent results have been found using the same approach by Kawaguchi et al. [53]. The hypothesis of the cooperation of JT and SOC phenomena also matches with Mossbauer spectroscopy and X-ray magnetic circular dichroism (XMCD) results, which also suggest a coexistence of real and imaginary orbital states [55].

However, first-principle calculations of the orbital distribution give a completely different picture for the OO in FVO. According to Xie et al. [56], the orbital momenta of both ions would be too small to have any effect on the OO. Apart from JT effects, they suggest a strong Coulombic electron correlation effect in the unfilled d shells of both cations. The combination of these two phenomena result in a more complex OO than purely ferro-OO or antiferro-OO. Below T_{S1} , the ordering of the Fe²⁺ site seems to be purely ferro-OO and that on the V³⁺ site can be either ferro-OO or antiferro-OO depending on the crystal direction. This DFT-sourced orbital occupation also manages to explain the XMCD experimental data [57].

2.2. Magnetic orderings

Alongside this OO, FVO also exhibits a magnetic ordering at T_{N1} , transitioning from a paramagnetic to a collinear ferrimagnetic state. This collinear magnetic ordering then shifts into a noncollinear spin structure with canted vanadium (V³⁺) spin on the pyrochlore sublattice due to the strong coupling between magnetism and electric polarisation [58], [59]. A thorough investigation on FVO's magnetic

structure has been conducted by MacDougall et al. [19]. The collinear state is a non-compensated antiferromagnetic arrangement between the V³⁺ and Fe²⁺ atoms along the [001] cubic direction. In lower symmetry phases, the Fe²⁺ atoms align ferromagnetically along the longest orthorhombic axis with V³⁺ antiparallel. In the non-collinear magnetic arrangement, V³⁺ are tilted by 55° and align themselves along the centre-to-corner directions of the pyrochlore tetrahedra. As a result, V³⁺ ions present a “2-in-2-out” pattern with a net magnetisation along the [001] direction (or equivalent in lower symmetry phases) which is still antiparallel that of the Fe²⁺.

Both collinear and non-collinear magnetic states have been depicted in **Figure I.7**. This uncommon magnetic structure, also known as Yafet-Kittel (YK) arrangement, seems to follow the “ice-rules” in frustrated rare-earth antiferromagnets [60]. In such materials, the magnetic moments are arranged in a way that they satisfy the symmetry of the crystal lattice (Ising conditions). The V spins in FVO are subject to an equivalent Ising condition constraint which arises due to the significant trigonal distortion of the VO₆ octahedra. This distortion is further influenced by strong SOC effects [19].

The magnetisation at saturation was found to be 76.8 emu g⁻¹ (or 374.8 emu cm⁻³) at 5 K [58]. The magnetisation vs. applied field curves show distinct jumps, which can be associated with the presence of several domain systems with different anisotropies in the same crystal structure, each with different anisotropy and coercive field. Finally, a spin-glass-like state has been reported by Nishihara et al. [61] at T_g = 85.5 K. In other words, the magnetic moments become “locked-in” to a specific state of disorder, where they form a complex, disordered pattern that is known as a spin glass phase. This phenomenon has not been found by other groups and there is some controversy about its existence [29], [62]. As we will show later, our own SQUID AC measurements detected a much smaller spin-glass signature than Nishihara’s and did not confirm the spin glass behaviour in FVO.

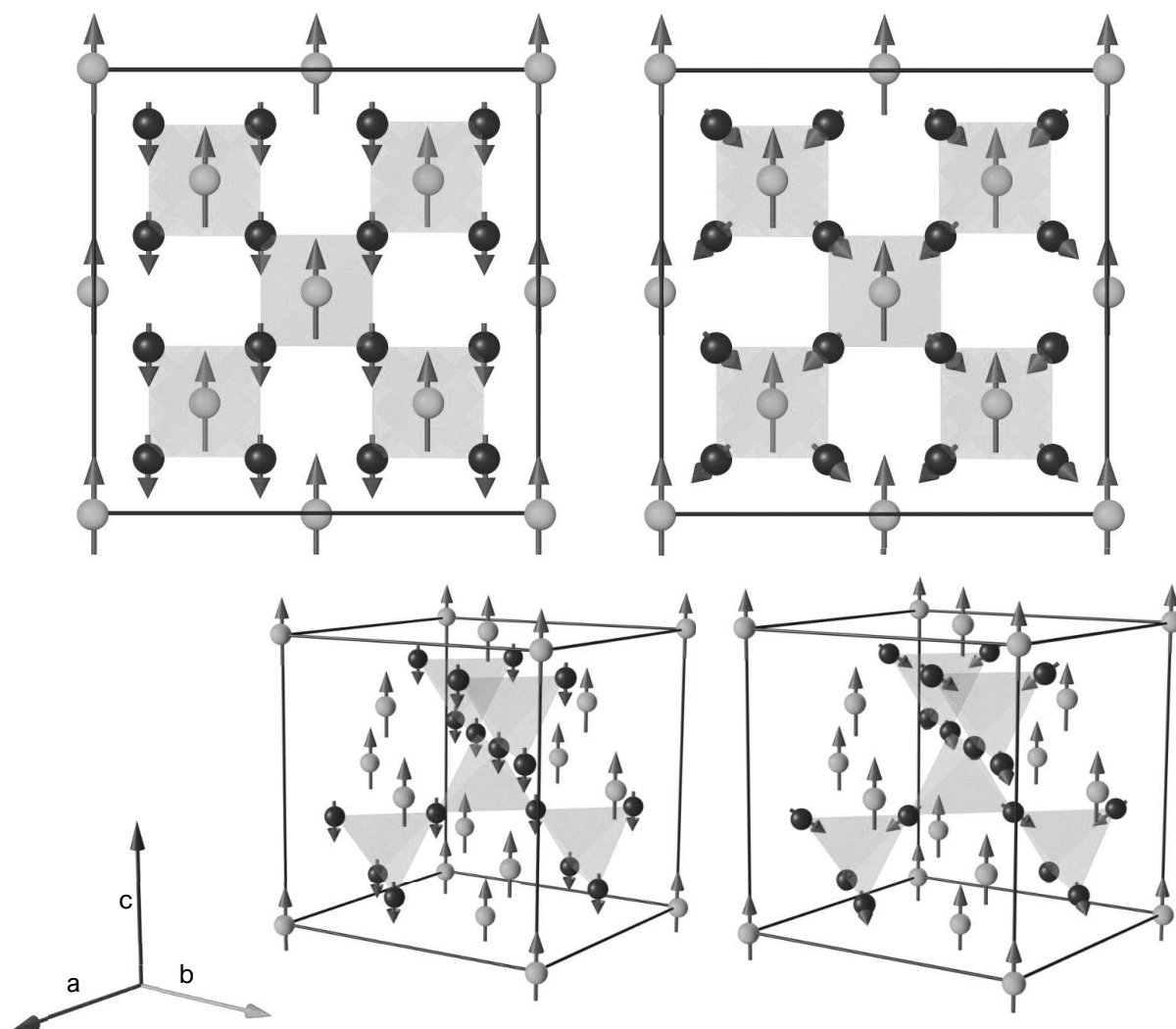


Figure I.7. Top: orthographic projections along $[\bar{1}00]$ direction representing the collinear (left) and non-collinear (right) magnetic states. Bottom: same image from a tilted perspective, depicting the crystallographic directions. Fe atoms are indicated in orange, while V atoms are in blue. Their antiparallel magnetic moments have been indicated in red and purple, respectively. Both structures have been drawn as cubic for the sake of the comparison. The magnetisation has been depicted along the $[001]$ direction. Adapted from FIG. 3 by MacDougall et al. [19].

2.3. Ferroelectric orderings

FVO displays not only a magnetic moment but also a net polarisation of approximately $63 \mu\text{C m}^{-2}$ [29], surpassing other well-known ferroelectric spinels like CdV_2O_4 ($P_s \approx 5 \mu\text{C m}^{-2}$) [63] or CoCr_2O_4 ($P_s \approx 2 \mu\text{C cm}^{-2}$) [64]. The structure at all temperatures is centrosymmetric and, therefore, the symmetry breaking occurs due to a secondary order parameter: the magnetic ordering. This makes FVO an improper ferroelectric and a naturally occurring multiferroic material.

To the author's knowledge, there are no reports on the polarisation reversal (ferroelectric hysteresis cycles) to date, or any direct imaging of the ferroelectric domains. The ferroelectric state has been characterised via indirect methods (e.g. pyrocurrent measurements) and it remains possible that FVO is an improper polar material rather than a true ferroelectric.

The polarisation seems to have two components. The first arises below T_{N1} (accompanied by the collinear magnetic ordering) and has been associated with an exchange striction mechanism. It has been suggested that the origin of this polarisation is caused by a V-V dimerisation, which would break the symmetry by making the different V atoms inequivalent. This phenomenon takes place in other ferroelectric spinel vanadates like CdV₂O₄ [63]. While predicted to exist, this component has yet to be experimentally measured, and its existence remains a topic of debate [12], [36]. The reason behind its non-measurement might be due to FVO's small gap and finite conductivity in the collinear ferrimagnetic region, which may screen the polarisation.

The second component appears below T_{N2} , coinciding with the non-collinear magnetic structure. There is scientific (experimental) consensus about its existence. The YK magnetic structure falls into the scenario of ferroelectricity in non-collinear magnets theoretically predicted by Katsura et al. [65]. In this structure of a noncollinear magnet, the magnetic structure of canted spins form a spin spiral structure of non-compensated electric dipoles [66]. Actually, a spin supercurrent \mathbf{j}_s emerges from the interaction of the spins of two neighbouring V atoms (i, j): $\mathbf{j}_s = \mathbf{S}_i \times \mathbf{S}_j$. This spin supercurrent induces a polarisation $P_{ij} = a\mathbf{e}_{ij} \times \mathbf{j}_s$ that is proportional to the strength of the spin-exchange interaction and the SOC (a). The spin spiral structure is therefore inherently polar.

The intrinsic magnetic origin of its polarisation, as well as the possibility of magnetically suppress its polarisation, make FVO a potential magnetoelectric material [67]. This strong magnetoelectric coupling even allows a tuning of FVO's polarisation via the application of external magnetic fields: $\Delta P = P_{H=0} - P_{H=14 \text{ kOe}} = 22 \mu\text{C m}^{-2}$ [29]. In conclusion, FVO is a type-II multiferroic material (ferrimagnetic + improper ferroelectric + orbitally ordered) surely below $T_{N1} = 60 \text{ K}$, and it is suspected to exhibit multiferroic properties at temperatures as high as $T_{N1} = 110 \text{ K}$.

The temperature evolution of FVO's structure, magnetic order, charge order and orbital order has been summarised in **Table I.1**. The different symmetry groups and special positions that each atom occupies have also been indicated. Structural data has been obtained from [53]. Following the authors' reported values, no errors have been indicated on the experimental data.

Table I.1. Temperature evolution compendium of FVO's structure and magnetic, charge and orbital orders in the bulk form, and crystallographic information about each phase.

Temperature	T _{S1} 140 K		T _{N1} 110 K	T _{N2} 60 K	T _{S2} 30 K	
Structure	Cubic spinel	HTT ($c < a_{cubic}$)		HTO	LTT ($c > a_{cubic}$)	
Magnetic order	Paramagnetic			Ferrimagn. colinear	Ferrimagnetic non colinear	
Charge order	Paraelectric			Ferroelectric (exchange striction)*	Ferroelectric (spin-supercurrent)	
Orbital order**	No OO	ferro-OO on Fe	ferro-OO on Fe	ferro-OO on V and Fe		
Crystallographic information (no errors considered)						
Space group	$Fd\bar{3}m$ (227)	$I4_1/amd$ (141)	$Fddd$ (70)	$I4_1/amd$ (141)	$Fddd$ (70)	
Setting***	2	2	1	2	1	
a (Å)	8.45361	6.0062	8.5278	5.9329	8.5277	
b (Å)			8.4703		8.4091	
c (Å)		8.3472	8.3398	8.5264	8.3687	
Cation positions						
Fe	8a $\frac{1}{8}, \frac{1}{8}, \frac{1}{8}$	4a $0, \frac{3}{4}, \frac{1}{8}$	8a $0, 0, \frac{1}{2}$	4a $0, \frac{3}{4}, \frac{1}{8}$	8a $0, 0, \frac{1}{2}$	
V	16d $\frac{1}{2}, \frac{1}{2}, \frac{1}{2}$	8d $0, \frac{1}{2}, \frac{1}{2}$	16d $\frac{5}{8}, \frac{5}{8}, \frac{5}{8}$	8d $0, \frac{1}{2}, \frac{1}{2}$	16d $\frac{5}{8}, \frac{5}{8}, \frac{5}{8}$	
Oxygen positions						
Position	32e x, x, x	16h $0, y, z$	32h x, y, z	16h $0, y, z$	32h x, y, z	
x	0.2617	0	0.3879	0	0.3910	
y		0.4747	0.3862	0.4843	0.3942	
z		0.2584	0.3823	0.2656	0.3831	

* disagreement about its existence

** by considering the lattice distortions (normal mode studies)

*** most common in the literature

Finally, in terms of its dielectric properties, FVO has been shown to present a field-dependent dielectric response. The capacitance of FVO as a function of the magnetic field has a hysteresis behaviour, and it changes even above the magnetic saturation field. This phenomenon may be related to an alteration of the non-collinear spin structure with increasing magnetic field [68].

2.4. FeV₂O₄ thin films

As demonstrated so far, bulk FVO exhibits interconnected spin, charge and orbital degrees of freedom. FVO's magnetic, charge and orbital orders vary with its structure and, as a result, these orderings are expected to be very sensitive to structure distortions and strain states. Because of the inevitable lattice mismatch between the films and the substrates, epitaxial thin films are a suitable platform to study the strain effects on the material's properties. This brings into play the so-called "strain degree of freedom", which enriches the properties of FVO thin films beyond their bulk counterpart [69].

Epitaxial thin films enable precise control of properties through epitaxial strain and defined crystallographic orientations that result from the epitaxy process. By choosing a substrate with a larger (smaller) lattice parameter than FVO, a tensile (compressive) strain can be induced in the crystal, which will be proportional to the lattice mismatch (τ) between FVO and the substrate: $\tau = (a_{\text{substrate}} - a_{\text{FVO}})/a_{\text{substrate}}$. Therefore, the substrate choice creates new avenues for tailoring or producing new properties. Strain effects are also a possibility to achieve the aforementioned Mott transition in FVO thin films, since compressive strains would shrink the lattice and reduce the V-V distances. Thin films are also a suitable platform to introduce foreign species and shrink the lattice by applying a chemical pressure.

The thin film form also offers a novel opportunity, compared to the bulk, to manipulate ferroic order for practical device applications such as memory, logic, and sensor technologies [70]. Despite the significant potential benefits of studying the properties of FVO thin films, only two other research groups have published scientific papers on this topic: one at Tsinghua University (Beijing, China) and another at the University of New South Wales (Sydney, Australia), with two scientific articles on the topic each.

The first group authored the two first works on the subject [69], [71]. In the first work, FVO (001) was deposited into three different substrates, with the lattice parameters and lattice mismatches indicated in **Table I.2**. Lattice parameters correspond to values at 300 K. The cubic room-temperature lattice constant (8.4536 Å) [53] has been used for FVO's lattice parameter.

Table I.2. Substrates used in the literature, lattice parameters and calculated lattice mismatches. Data for the lattice parameters (a) has been obtained from [72]–[74]. No error intervals have been indicated since they are not provided in the cited works.

Substrate	Abbreviation	a (Å)	Mismatch – τ (%)
SrTiO ₃	STO	3.905	- 8.2
LaAlO ₃	LAO	3.811	- 10.9
MgAlO ₄	MAO	8.068	- 4.8

As shown in the **Table I.2** and as schematised in **Figure I.8**, all the substrates presented a smaller lattice constant than FVO and, therefore, the films presented compressive strains. FVO lattice is schematically represented in the middle, with the different substrates adjacent to it.

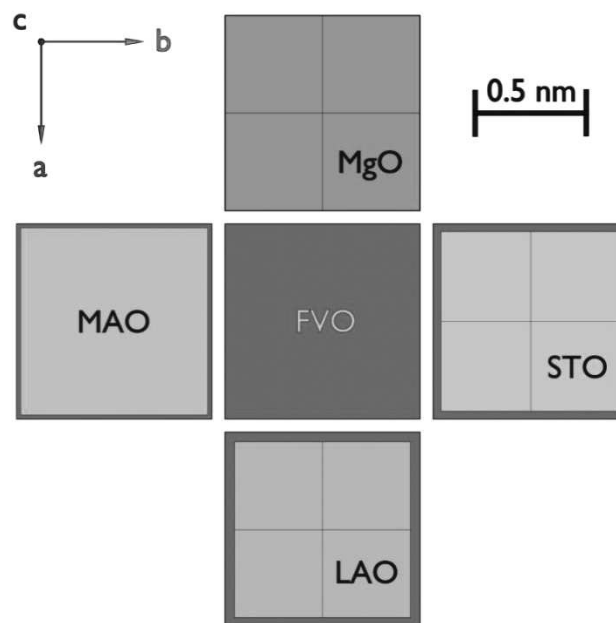


Figure I.8. Comparison between the lattice parameters of FVO and other common substrates. Projection along the [001] crystal direction. The red contour around the substrates corresponds to the difference in lattice parameter between FVO and the substrate. MgO has also been included ($a = 4.211$ Å [75], $\tau = - 0.4\%$) since the deposition of FVO//MgO films will be furtherly discussed.

Films were grown using pulsed laser deposition (PLD) with a laser fluence of 2.8 J cm^{-2} , a partial pressure of oxygen of $P_{\text{O}_2} = 3 \times 10^{-4} \text{ Pa}$, a temperature of 600°C and a repetition rate of 6 Hz. They report stoichiometric issues and an excess of iron: $\text{Fe}_{1+x}\text{V}_{2-x}\text{O}_4$ ($x = 0.1 - 0.3$). Their FVO thin films display

tetragonal symmetry at temperatures from 20 to 300 K, with the *c*-axis greater than the *a*-axis, in contrast to the cubic symmetry exhibited by the bulk material. The significant lattice mismatches prevented the formation of an in-plane epitaxial relationship. However, they provoked a strain-induced tetragonality which broke all the structural transitions with temperature. A single magnetic transition at $T_{N1} = 130$ K was found for the three films. This increase compared to the bulk value (10 K) might be due to the strain-induced shortening of the interatomic distances as well as the Fe excess.

The magnetic easy axis is discovered to be perpendicular to the film plane, and the film's high tetragonality causes out-of-plane magnetic anisotropy due to strong spin-lattice coupling. Additionally, X-ray diffraction reveals that the lattice constants of the film are influenced by the substrate on which it is grown, exhibiting different behaviour on different substrates. The strain on MAO has been associated to the in-plane lattice mismatch, while the strain on films grown on LAO and STO arises due to differences in the thermal expansion coefficients of the substrate and film.

In their follow-up study, they grew FVO (011) thin films on the same three substrates with a (011) crystal orientation. All of these films exhibit monoclinic symmetry, with β angles close to 90°: $\beta_{STO} = 89.91^\circ$, $\beta_{LAO} = 90.05^\circ$ and $\beta_{MAO} = 89.86^\circ$. Notably, the authors did not provide any uncertainty measurements for these angles nor did they explore the possibility that the angles could in fact be 90°. The films grown on STO and MAO are strongly compressed along the [001] direction and tensely strained along [110] – $[\bar{1}\bar{1}0]$ directions. However, the films grown on LAO only show slight distortion from cubic symmetry. The magnetic hard axis was located in the [001] direction, with the easy axis aligned along the [110] direction (for STO and MAO) or the $[0\bar{1}0]$ direction (for MAO). Additionally, the magnetoresistance anisotropy follows the magnetisation.

The second research group in the field focused on the characterisation of the transport, magnetic and magnetodielectric properties of FVO thin films [70] as well as imaging the temperature-dependent evolution of magnetic domains [76]. They deposited FVO onto STO at the (001)//(001) epitaxy, as well onto Nb-doped STO. Their optimised conditions included a laser fluence of 2 J cm⁻², a partial pressure of oxygen of $P_{O_2} = 1.3 \times 10^{-3}$ Pa, a temperature of 500°C and a repetition rate of 2 Hz. Their films also present an excess of Fe: Fe_{1.4}V_{1.6}O₄. Such a large off-stoichiometry hinders any relevant comparison with the work by Shi et al. [69], [71].

The material exhibits two magnetic transitions, occurring at $T_{N1} = 200$ K and $T_{N2} = 40$ K. Both Fe²⁺ and Fe³⁺ were detected by XMCD measurements and aberration-correctional scanning transmission electron microscopy (STEM) places the accommodation of excess Fe³⁺ ions on stacking faults as Fe₃O₄ along the {111} planes. The FVO:Fe thin films exhibit an anti-parallel alignment of spins between the Fe²⁺ and V³⁺ ions. Furthermore, two distinct phases with different coercive fields were identified, and a switching field of 3 T was observed on Magnetic Force Microscopy (MFM).

Ultimately, a Pd/FVO/Nb:STO heterostructure was used to measure the magneto-dielectric properties of FVO thin films. The magneto-capacitance loops showed weak hysteresis, indicating magneto-

dielectric coupling. The capacitance behavior was dominated by Maxwell-Wagner type relaxation due to the Schottky interface between FVO:Fe and Nb:STO. Unlike the material in the bulk form, their films showed no ferroelectricity.

Their subsequent study examined the temperature-dependent evolution of magnetic walls in FVO:Fe(001)//STO(001) thin films. Their main finding was that FVO:Fe magnetic structure organises in irregular and asymmetrical magnetic domains and that these domains coarse and shrink as a function of temperature.

In conclusion, at the beginning of the author's PhD project, there were only a few scientific publications on FVO thin films. Although structural and magnetic studies on the films were conducted, the films exhibited a significant vanadium deficiency. The limited scientific research on a material with such potential, where numerous degrees of freedom coexist and interact, serves as motivation for this thesis.

Chapter II. FeV_2O_4 : from the bulk form to the thin film

As its name anticipates, this chapter delves into the process of crafting FeV_2O_4 (FVO) thin films, tracing the journey from the raw bulk ceramic target to the final thin film deposition. The chapter unfolds in four distinct sections: two covering the synthesis techniques and characterisation methods and the other two presenting the results.

The initial part covers the synthesis methodologies employed to produce FVO ceramic targets by means of solid-state reactions. This is followed by an in-depth discussion on the Pulsed Laser Deposition (PLD) technique, highlighting the specific PLD setup utilised in this research.

In the subsequent section, we turn our attention to the characterisation techniques for both bulk samples and thin film materials. This includes a comprehensive overview of various X-ray characterisation methods that verify the desired crystal phase, as well as magnetic and transport measurements that characterise physical attributes of the thin film materials.

The third part of this chapter covers the results pertaining to FVO in its powder form. The confirmation of the correct crystal phase and stoichiometry of the bulk target serve as solid foundation for the latter fabrication of the films. Emphasis is placed on temperature-dependent studies, both structural and magnetic, which corroborate the structural transitions outlined in the opening chapter.

The concluding section is dedicated to the results on FVO thin films. It commences with a discussion on the fine-tuning of FVO deposition to achieve optimal conditions. Then, it presents the results of diverse characterisation strategies, affirming the superior quality of the deposited thin films. The chapter culminates with an exploration of the films' crystal structure through diffraction experiments and a comprehensive review of their physical properties. The content regarding the thin film optimisation process, the structural characterisation and the physical properties has been partially shared in the form of a scientific article [77].

This chapter serves a dual purpose: it not only explores the synthesis and characterisation methodologies essential for the deposition and evaluation of high-quality oxide thin films, but also showcases the results specific to our material of interest. By confirming the accurate crystal phase, we lay a robust foundation for the intricate analyses and advanced determinations that will be explored in the ensuing chapters.

1. Synthesis methods

1.1. Bulk target elaboration

1.1.1. The ceramic method

The ceramic method is a common technique for the obtention of ceramic powders in solid-state Chemistry. It involves the mixing of solid reactants (precursors) in the form of fine powders for their solid-state reaction in a high-temperature furnace. The ratio of the precursors enables the stoichiometric synthesis of the material of interest, and the reaction's conditions (temperature, atmosphere and reaction time) are key factors for the attainment of the correct phase with the desired crystallinity [78, p. 17].

For the elaboration of FVO in its powder form, the precursors were Fe₂O₃ and V₂O₅. It can be observed that, for both cases, the cations need to be reduced to match the oxidation state in the spinel form: Fe should pass from a +3 to a +2 state whereas V should go from +5 to +3. Therefore, the atmosphere should be reductive enough so that both cations undergo the reduction reaction. On top of that, V₂O₅ melts at 690°C [79] and can easily leak and incorporate the structure of other ceramic compounds. This is especially problematic because our tubular furnace is made of alumina (Al₂O₃) and, at high temperatures, it can be attacked by melted V₂O₅. To prevent this issue and besides the utilisation of a reducing atmosphere, the precursor mix was always placed in a platinum basket-shaped foil which was contained itself in an alumina combustion boat. An excessively reductive atmosphere, however, could reduce any of the species to lower oxidation states (or even the metallic form) and impede the obtention of the desired spinel phase. In conclusion, due to security issues and in order to obtain the adequate oxidation states, a long and careful optimisation process was needed to achieve the optimal reaction conditions. All the aforementioned tools used for the ceramic method have been schematised in **Figure II.1**.



Figure II.1. Scheme of the tools used for the ceramic method. From left to right: agate stone mortar, alumina basket with platinum foil and tubular furnace.

The bulk synthesis begins with the stoichiometrically weighing of precursor masses for the attainment of a molar ratio V/Fe of 2. Then, the mix of Fe₂O₃ and V₂O₅ powders is ground for 15 minutes in an agate stone mortar with a minimum quantity of ethanol. The mix is placed in the aforementioned combustion basket and introduced into the oven. A reductive gas flow of 150 sscm of H₂/Ar (2.5:97.5) was continuously applied in the oven chamber, as such gas mixture was found optimal in achieving the correct oxidation states. With a temperature slope of 100°C/hour, the mix was heated up to 600°C. A temperature dwell at this temperature occurred for 10 hours. This gives time to the precursor species to be reduced. Then, and with the same heating speed, the system is heated up to 1100°C, and the temperature is again maintained for 10 more hours. The spinel phase is then formed at these high-temperature conditions. Finally, the oven is cooled down at a rate of 200°C/min. The entire solid-state reaction process is represented in **Equation (II.1)**. Water has been added to the equation to respect the chemical balance.



In order to have a further proof on the aforementioned chemical processes and knowing the exact reduction temperatures of each reduction subprocess, a thermogravimetric analysis (TGA) could have been carried out. Unfortunately, the TGA which was available to us did not have any H₂/Ar gas input.

1.1.2. Attrition milling and sintering process

After obtaining the correct crystal phase via the ceramic method, targets for PLD were fabricated by sintering the obtained powder in the form of FVO pellets. Sintering is the process whereby particles bond together at temperatures below the melting point by atomic transport events, at a rate which is proportional to the temperature. Atomic diffusion caused by temperature-driven forces causes the particles to coalesce and increase their surface area of contact. This reduces the particles' surface area and surface curvatures, ultimately decreasing the system's free energy [80, p. 145]. The entire sintering process has been illustrated in **Figure II.2**.

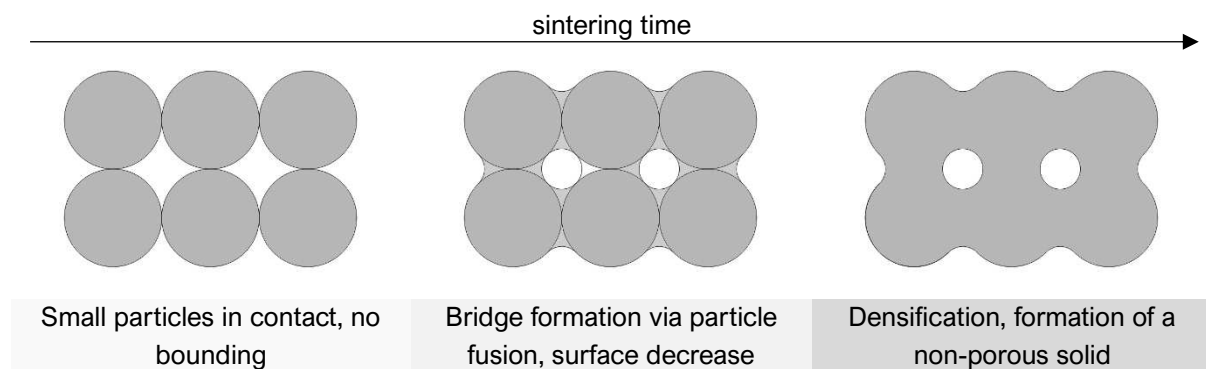


Figure II.2. Schematic representation of the sintering process for the obtention of ceramic targets.

Sintering takes place at higher temperatures than the solid-state reaction and serves also to improve the material's crystallinity. The resulting sintered material is a densified polycrystalline FVO target shaped as a cylinder-shaped pellet. The density of the pellet is heavily influenced by particle size. A smaller particle size facilitates more efficient particle coalescence, resulting in a denser ceramic with fewer unoccupied spaces. As a result, finer particles ease the densification process and lead to denser targets [81].

In order to quantify the density state of the target, a “sintering yield” (τ_s) comparing the target's density (ρ_{pellet}) in relation to the theoretical density ($\rho_{\text{theoretical}}$) can be defined, as shown in **Equation (II.2)**.

$$\tau_s = \frac{\rho_{\text{pellet}}}{\rho_{\text{theoretical}}} \quad \text{(II.2)}$$

As previously described, small-sized particles are needed to attain a successful sintering process. However, the powdery product of the ceramic method consists of particles with an uncontrolled and relatively large size. In order to reduce and control size, the FVO powder undergoes an attrition milling process. Attrition milling is a technique used to reduce the size of powdery materials by the gradual mechanical fragmentation of the powder particles. In this case, ball mill attrition was used, but other milling possibilities exist. In ball mill attrition, the powder is introduced into a container (attritor) accompanied with ceramic mill balls. A mechanical part stirs the slurry powder-balls mix, while the attritor is continuously refrigerated. The repeated impact and collision between the balls and the particles reduce the size of the latter, resulting in a narrower particle size distribution [82], [83].

A solvent is usually used to increase the particle dispersion, improve the milling efficiency and reduce the particle size, what is also known as solvent-assisted ball milling [84]. The solvent influences the particle's stability with size, and some may form aggregates beyond a critical size value, hindering thus a correct size shrinking [85]. Each solvent presents a critical size beyond which the free colloidal suspension is no longer stable.

The attrition efficiency can be characterised by a follow-up of the particle's size and also by the measurement of zeta potentials, which characterise the surrounding charge that develops at the interface between a solid surface and its liquid medium. Both parameters, size and potential, decrease with increasing milling time. However, the rate at which they decrease slows with time. After a certain milling time, the particles do not shrink anymore, or the agglomeration of particles occurs at the same rate as the particle subdivision. In conclusion, an optimal milling process is achieved by a proper choice of solvent type and milling time [86].

The bills were then washed with ethanol and the particle suspension was passed through a strainer. The resulting suspension was dried out overnight. The fine powder was manually ground the following day with a small quantity of polyvinyl alcohol. Following additional drying, the resulting slurry was introduced into a 1.5-inch (3.8 cm) mould and pressed in the form of a cylinder with a pressure of 60 bar. The pellet

was then placed on a platinum foil which was itself contained in an alumina combustion basket (just like the ceramic method). The whole system was introduced into a tubular furnace for the powder sintering. A reductive gas flow of 125 sscm of H₂/Ar (2.5:97.5) was applied while the pellet was heated up to 1300°C at a rate of 100°C/hour. Non-oxidative conditions were used so as not to lose the spinel phase and had to be optimised to prevent any cation reduction. A temperature plateau was maintained at this high temperature for 20 hours, after which the system was cooled down to room temperature.

1.2. Pulsed laser deposition (PLD)

1.2.1. Principles of PLD

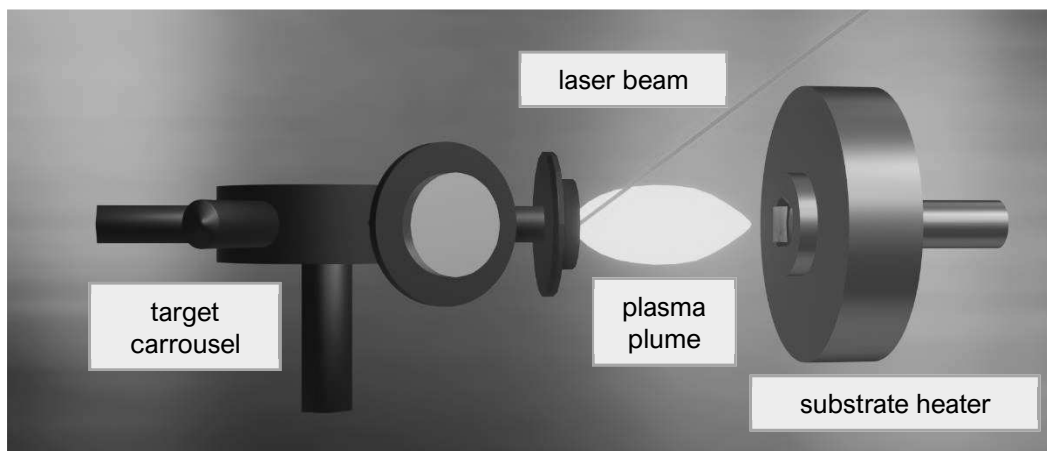
Pulsed laser deposition (PLD) is a physical vapour deposition technique for the deposition of thin films. As illustrated in

Figure II.3, PLD involves the use of a high-energy laser beam to ablate a target material in a vacuum chamber. When the high-power beam strikes the target, the material of interest is ejected in the form of a plasma plume towards a substrate, situated in close proximity to the target. As a result, there is a matter transfer from a bulk target onto a substrate on which the thin film grows.

The ablation process starts with the absorption of laser radiation by the bulk target. As the absorbed energy is transferred to the material, the temperature rises, and melting and vaporisation begin. Then, the melt front propagates deeper into the solid material, while the material ejection continues. The expelled material forms a dense cloud of material that interacts with the initial laser beam and the surrounding gas, leading to the formation of a plasma that is highly stimulated through scattering, photoexcitation, or multiphoton absorption mechanisms. This event generates layers of charged particles, including electrons, and a range of light and heavy plasma species, resulting in the creation of a field that accelerates the plasma species to energies ranging from several electron volts to thousands of electron-volts [87]. The plasma's high temperature and pressure cause additional material to vaporise, creating a plume that expands rapidly. The atoms composing the plume travel to the substrate which opposes the bulk target. Finally, the melt front recedes, leading to eventual re-solidification of the material [88]. The laser beam strikes the bulk target with a certain frequency (pulses) so this process repeats itself with a specific rate. The PLD method enables a precise control over the constituent elements of a film and enables the customisation of the chemical structure of the film according to specific requirements. The process outcome is influenced by the choice of various parameters beside the bulk and substrate selection.

The laser choice can have a significant influence in the deposition process. The whole ablation process starts with the absorption of laser photons by the bulk material. The photon absorption depends on the

material's band gap (and its light absorption properties) and on the laser wavelength. Different material types will have different optimal laser wavelengths and, therefore, one can choose the laser wavelength to cleave specific bonds in a material. Commonly used laser wavelengths in PLD include ArF (6.42 eV), KrF (4.99 eV), XeCl (4.03 eV), and Nd:YAG (1.16 eV) with KrF (248 nm – excimer, *excited dimer*) being the most common due to its long gas mixture lifetime, low absorption in air, and its ability to dissociate most chemical bonds in a solid through a single-photon absorption process [87]. Another parameter which affects the deposition is the laser fluence, which denotes how much energy the laser hits the target per surface of unit area. Laser fluence will influence the kinetic energy of the materials ejected from the target, which shortens the migration of species to the substrate and minimises the possibility of dissociation and form changes. The migration speed is directly related to the fluence value, and a



higher fluence provides materials ejected from the target with more kinetic energy, resulting in a higher deposition rate. Finally, the deposition rate will also be affected by the laser's pulse rate [89].

Figure II.3. Scheme for pulsed laser deposition. On the left, the different targets on a rotating carousel. One of them is being struck by the laser beam. This creates a plasma plume directed towards the substrate. The substrate is glued onto a heater's surface with silver paste.

The substrate temperature also plays a critical role in the deposition process. It refers to the temperature of the surface on which the film is deposited. The substrate temperature affects the quality of the film in several ways by determining the nucleation and growth kinetics of the film [90]. At low substrate temperatures, the mobility of adatoms on the substrate is limited, leading to slower nucleation and growth rates. This can result in a film with a rougher surface and poor adhesion to the substrate. Conversely, at high substrate temperatures, the mobility of adatoms increases, resulting in faster nucleation and growth rates. However, excessively high temperatures can also lead to the decomposition of the film, resulting in poor quality or even failure of the deposition process [90], [91].

PLD can be carried out in an ultra-high vacuum or in the presence of a background gas such as oxygen, argon, or nitrogen. The whole deposition process takes place in an isolated low-pressure chamber to prevent the pollution of the substrate. The choice of background gas can significantly affect the PLD process by controlling the kinetic energy of the ablated atomic species arriving on the substrate. This, in turn, determines the film nucleation and growth processes [92]. In the case of oxide materials, an oxygen atmosphere can be used to compensate the oxygen spell of the plume generation process. This enables a stoichiometric transfer by the appropriate choice oxygen partial pressures [93]. The chamber pressure also affects the deposition rate: higher pressures confine the plume to a smaller volume extent, limiting the material's ejection and subsequent deposition.

1.2.2. PLD set-up

The PLD set-up used in this PhD work was purchased from the *TSST* company. A 248 nm KrF laser was used, and the main chamber could reach pressures as low as 2×10^{-6} Pa. A secondary smaller chamber was used to insert the target carousel and the substrate heater into the main chamber, while preventing the main chamber from being constantly brought to atmospheric pressure. Rotary valve pumps were used to obtain primary vacuums, and ultra-high secondary vacuums were achieved using turbomolecular pumps. An electron gun and deflection units were used to perform Reflection High-Energy Electron Diffraction (RHEED) measurements for the *in situ* follow-up of the deposition. The complete PLD set-up has been modelled in **Figure II.4**.

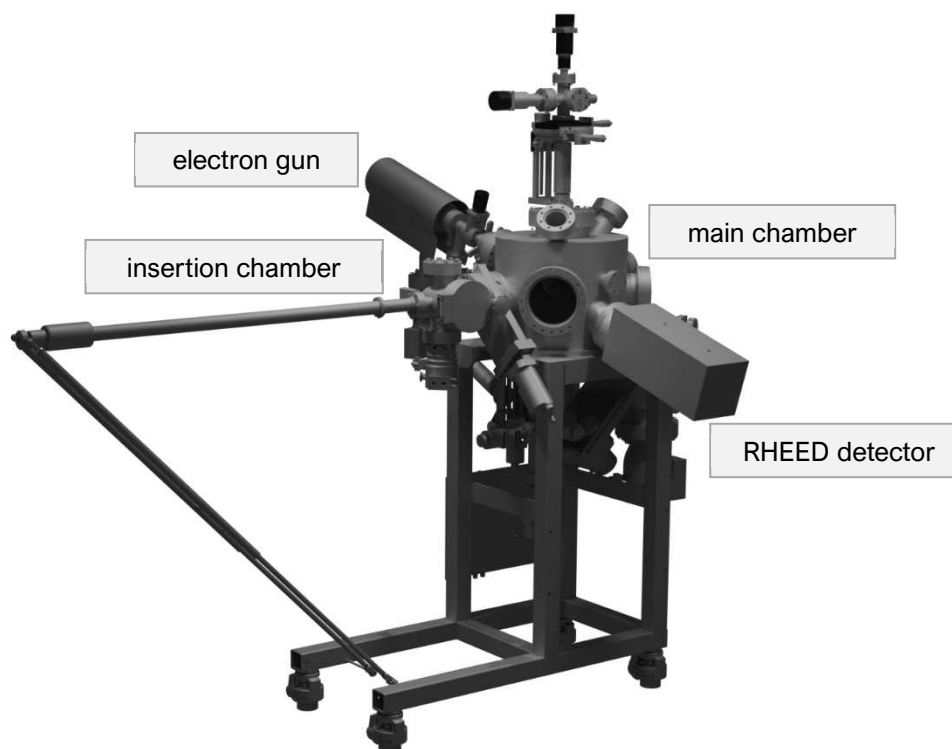


Figure II.4. 3D model of the used PLD set-up and its main components. The mirror set-up which was used to direct the laser beam into the chamber would lay on the right of the main chamber.

1.2.3. Substrate treatment

The PLD process starts with the substrate preparation. Once removed from their original containers, the substrates were methodically cleaned in ultrasound baths of isopropanol, acetone and isopropanol for 15 minutes each. In the case of large substrate wafers, some of them were cut using a diamond tip before the solvent cleaning. Afterwards, the substrates would undergo an annealing process to improve the surface roughness and to have the smoothest possible surface for the deposition.

Different substrates require specific annealing strategies, depending on how they respond to high temperatures. In the case of MgO samples, an optimisation study conducted by Youssef et al. [94] recommends annealing them in an open-air furnace at 800°C for 40 minutes. They performed annealing experiments in a high-purity O₂ atmosphere, which resulted in substrates with a smooth surface at the atomic level. Our laboratory did not possess a furnace equipment allowing pure O₂ heat annealing, so high-temperature treatments were conducted in open-air conditions. Although open-air annealing did not achieve the same level of smoothness, it did show a noteworthy enhancement in the surface condition.

The processing of STO involved a chemical treatment using a pH-controlled NH₄F-HF solution, followed by a high-temperature annealing process at 900°C for 2 hours. These procedures were inspired by the methodology outlined by Kawasaki et al. [95] and resulted in the achievement of an atomically smooth

TiO₂-terminated surface [96]. The combined application of chemical treatment and thermal annealing induces a distinctive stair-like pattern on the substrate surface, resembling a series of steps and terraces, commonly referred to as a “step-terrace” morphology.

After completing the annealing process, the morphology of the substrates was examined using Atomic Force Microscopy (AFM), a technique that will be elaborated on in the section “Atomic Force Microscopy” of this chapter – page 45. Subsequently, the substrate was affixed to the substrate heater using silver paste. This silver paste served the dual purpose of securely holding the substrate in place and ensuring efficient thermal contact between the substrate and the heater.

1.2.4. The deposition process

The substrate heater, along with the carousel containing the FVO target, was then introduced into the PLD chamber through the insertion chamber. Once both chambers were returned to their high-vacuum states, a controlled gas atmosphere was established within the chamber. Subsequently, the laser energy was measured and brought to the desired value for the ablation.

Prior to the deposition process, a preablation process is conducted in pulsed laser deposition to prepare the target surface. It consists of the laser ablation of the target surface without any actual deposition taking place – the substrate is protected with a mobile shutter. The purpose of preablation is twofold. Firstly, it removes any contaminants or surface impurities from the target material, ensuring the deposition of a pure film [97]. Additionally, it helps to establish a consistent composition and stoichiometry of the ablated material, leading to improved film quality and reproducibility [98].

Once the preablation process was complete, the substrate was heated to the desired deposition temperature. Once it reached this temperature, the substrate was maintained at this constant temperature for 30 minutes to ensure uniformity in the film's temperature. Following this, the RHEED setup was initialised, and the electron beam was aligned to bring the sample into diffraction condition. The RHEED technique will be detailed in the “RHEED” section of this chapter. The laser energy is again verified and, only after this verification, the deposition process commences.

2. Characterisation techniques

2.1. Scanning electron microscopy

Electron scanning microscopy (SEM) is an analytical technique that enables the imaging of the surface of samples using a high-energy focused electron beam. In SEM, the electron beam interacts with the sample and generates secondary electrons, backscattered electrons, and characteristic X-rays. These signals are collected by specialised detectors. Secondary electrons provide information about the surface morphology and topography, while backscattered electrons and characteristic X-rays offer data regarding the atomic composition and structure of the sample. These combined signals are processed and used to create a detailed and highly magnified image of the specimen's surface [99, p. 2].

Among the various functionalities offered by electron microscopy, SEM was used within the scope of this thesis to assess the state of the sintered pellets. This enabled us to obtain information about the grain homogeneity in the bulk target, as well as the grain size and morphology. Coupled with SEM, energy dispersive spectroscopy (EDS) was also used for the elemental analysis of the bulk and the thin films. EDS uses the interaction of the electron beam with the sample to generate characteristic X-rays, which are emitted from the sample and collected by a specialised detector.

When the electron beam from the SEM strikes the sample, it excites the electrons in the sample atoms' inner shells, causing them to be ejected. This ejection leaves a vacancy which is filled by an electron from a higher energy shell. The energy difference between these shells is released in the form of an X-ray. As each element has a unique atomic structure, the energy of the emitted X-rays is characteristic of the element, hence the name characteristic X-rays. The EDS detector measures the energy of these X-rays, enabling the identification of the elements present in the sample. By analysing the intensity of the characteristic X-rays, EDS can also provide quantitative information about the elemental composition of the sample. [100, p. 380]

In the context of our work, EDS was used in tandem with SEM to gain a comprehensive understanding of the stoichiometry of the samples. By leveraging EDS, it was possible to analyse the elemental composition of the bulk and the thin films, ensuring the atomic ratios of the constituent elements were correctly maintained, thus verifying the desired stoichiometry of the materials.

In the context of this work, the available equipment for the SEM-EDS analyses consisted of a *JEOL JSM 6700F* microscope equipped with a field emission gun operating at an accelerating voltage of 15 kV. SEM-EDS measurements were carried out in collaboration with the “Meb-Cro” platform at IPCMS.

2.2. X-ray characterisation

X-ray diffraction (XRD) techniques are a staple in the analysis of crystalline materials. The interaction between X-rays and matter gives valuable formation about the structural features of materials [101]. XRD can be used for the characterisation of materials in the bulk and the thin-film form, the latter implying technical challenges to be overcome. Firstly, thin films have a small quantity of matter, which leads to small intensities in diffraction experiments. This feature is also shared by other nanosized systems, such as nanoparticles or nanowires. On top of that, the substrate's diffraction signature can sometimes not be separated from the film's and, due to the difference in the quantity of matter, the substrate overshadows any signal coming from the material of interest. Secondly, thin films are inherently strong orientated systems, in which the crystalline orientation is determined by the growth epitaxy. Despite these difficulties and limitations, XRD on thin films can be used for a wide range of applications, including crystal phase identification [102], layer thickness evaluation [103], grain-size determination [104] and microstrain and residual stress analysis [105].

In this section, only the XRD-based lab routine characterisation techniques will be presented, all sharing a common principle: the incident photon energy is kept constant while the source-sample-detector angles vary. In “**Chapter III. Advanced structural characterisation of FeV₂O₄ films by resonant diffraction**”, more complex techniques on which the photon wavelength vary (and requiring a Synchrotron radiation source) will be furtherly developed.

These laboratory diffractograms share a consistent component layout, comprising several key elements that collaboratively yield accurate and precise measurements. The first element is the X-ray source, which consists of an electron beam of high voltage that strikes a metal target anode inside an evacuated tube. This produces an X-ray beam that is then collimated using a series of adjustable slits. The first of these slits is the soller slit, which is used to align the beam in the horizontal direction. A divergence slit is then used to control the size of the beam in the vertical direction. Then, an anti-scatter slit is used to reduce scattering from the sample holder or other components in the beam path. Once the beam has been collimated and scattered by the sample, the receiving slit is used to define the size and shape of the diffracted beam that is directed onto the detector. Finally, a detector measures the intensity of the diffracted beam, taking into account the diffraction angles [106, p. 69]. Unless indicated otherwise, a single X-ray wavelength of $K\alpha_{1,Cu} = 1.54056 \text{ \AA}$ has been used in the diffraction experiments of this PhD work.

By convention, the angle which forms the X-ray source with the sample's surface (or sometimes the (001) plane) is ω , and the angle which forms the incident beam with the detector is 2θ . Source, sample and detector form what is known as a “diffraction plane”, and it corresponds to the yz plane in **Figure II.5**. However, the sample can be rotated perpendicularly to this plane in two possible manners: it can be rotated azimuthally (rotation axis normal to the sample's surface), around the ϕ angle; and it can be rotated by tilting the sample (rotation axis along the sample's surface), around the χ angle. The three

different rotations have been represented in **Figure II.5**, and follow the General Area Detector Diffraction System (GADDS) geometric convention [107].

The measurement of the detected intensity as a function of one of the defined angles gives what is known as a diffractogram. By making an appropriate angular scan, the diffraction condition may or may not be respected (scattering vector at a reciprocal lattice point or not) and different structural information can be retrieved.

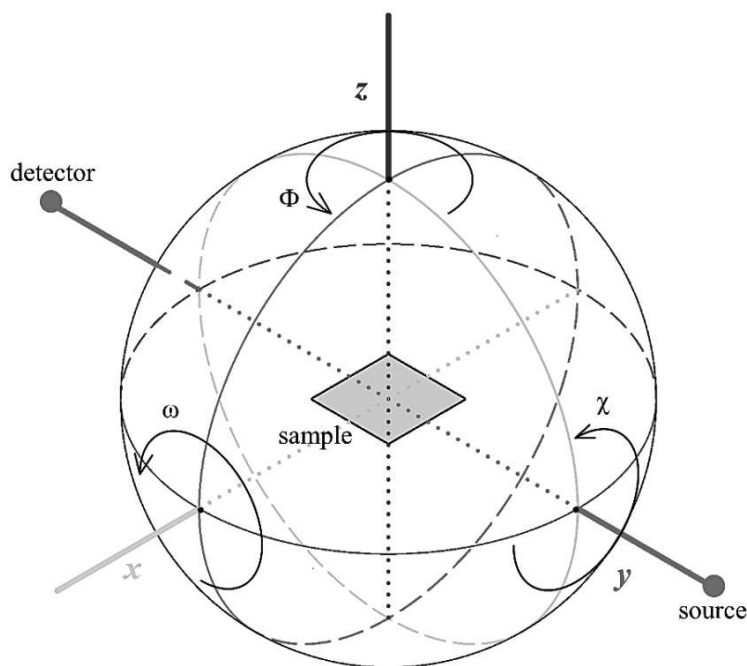


Figure II.5. Set-up for a XRD experiment with the main angles and possible rotations compared to the detector-sample-source layout. The scheme corresponds to $2\theta = 0$. Nonzero values would make the source, sample and detector not be aligned in the y axis.

The available equipment for the routine XRD characterisation consisted of, for the bulk samples, a D8 Brucker diffractometer in the Bragg-Brentano configuration equipped with a front monochromator, a copper anode ($K_{\alpha 1} = 1.54056 \text{ \AA}$) and an energy resolved Lynxeye XE-T linear detector. The characterisation of thin films was conducted using a Rigaku SmartLab diffractometer equipped with a Ge 220 x2 front monochromator and a copper anode ($K_{\alpha 1} = 1.54056 \text{ \AA}$). The XRD measurements have been carried out in collaboration with the “DRX” platform at IPCMS.

2.2.1. Powder X-ray diffraction

Powder is composed by crystallites which are randomly oriented in all possible directions. As a result, all possible ϕ and χ would be represented – the author acknowledges phenomena such as preferential

orientation, which have been omitted from the discussion for the sake of simplicity. All active reciprocal space points can be found in the normal direction of the sample's surface so, by keeping $\omega = 2\theta/2$ and performing a $\theta/2\theta$ scan, all active (and geometrically achievable) points can be reached by the scattering vector. The angle values for which the diffraction condition is met are those which respect Bragg's law: $n\lambda = 2d_{hkl} \sin \theta$, where λ corresponds to the X-ray wavelength and d_{hkl} to the interplanar distance of hkl planes. This scan mode is also known as "symmetric scan" and leads to a complete diffraction pattern conformed by diffraction peaks at specific $\theta/2\theta$ values. Among other information, the analysis of the $\theta/2\theta$ values at which diffraction occurs allows for the determination of d_{hkl} and, therefore, the crystal's lattice parameters.

This experiment usually takes place in the so-called Bragg-Brentano geometry, which is a specific configuration used in powder X-ray diffraction experiments. In this setup, the sample and detector are maintained at a constant distance from the X-ray source, ensuring that the incident and scattered beams form a fixed angle with the sample. This geometry maximizes the intensity of diffracted X-rays and provides a high signal-to-noise ratio for the diffraction pattern [108]. The Bragg-Brentano geometry will be ensuingly illustrated, for instance, in **Figure II.7** – page 39.

In the scope of this thesis, powder XRD experiments were mainly used to verify the crystal phases and obtain the lattice parameters via a Profile Matching analysis. Additionally, some powder-XRD diffractograms acquired at the Crystal line of SOLEIL Synchrotron will be presented later. The beam high intensity and its high resolution lead to diffractograms on which the relative intensities of the Bragg peaks can be fitted, being hence able to determine the atomic positions and/or site occupations, in a process also named as Rietveld refinement.

2.2.2. The structural characterisation of thin films

2.2.2.1. X-ray reflectivity (XRR)

When X-rays encounter a sample surface, they are reflected in a manner like any other electromagnetic radiation. The reflection of X-rays is described by the Fresnel equations, which explain the behaviour of light when it interacts with an interface between two media with different indices of refraction [109, p. 77]. X-rays possess a complex refractive index (n) with a real part smaller than 1. As a result, if the incidence angle is less than a critical angle defined by $\theta_c = \arccos(n)$, total external reflection occurs, and the X-rays do not penetrate the material. The range of the values for θ_c lies typically between 0.2° - 0.6° for X-ray wavelengths around 0.15 nm [101, p. 177]. Beyond this critical angle, the intensity of the reflected beam (also known as reflectivity) decreases proportionally to θ^4 . X-ray reflectivity (XRR) exploits the angle-dependence of the reflection intensity at low grazing angles and can be used to determine several structural parameters in thin-film materials [110].

Firstly, XRR can be used to measure the thickness of a thin film deposited on a substrate. The interference of X-rays reflected from the top surface of the film, with those reflected from the bottom surface of the film and the substrate, make the reflectivity decay in the form of oscillations. These oscillations are also known as Kiessig fringes [111], [112]. The period of the fringes is larger as the thin film's thickness decreases. By analysing the oscillation profile through a Fourier transform algorithm, the film's thickness can be precisely determined [113], [114].

Secondly, since the material's density directly influence its diffraction index, the film density can be estimated by using θ_c below which total reflection occurs. Similarly, the oscillations' amplitudes can be associated to the difference of density between the film and the substrate, with higher density differences leading to larger amplitude modulations [110]. Finally, the surface roughness, also defined as the physical "unevenness" of the surface, causes the reflected intensity to diminish more rapidly [109, p. 94]. The roughness of the interface between the substrate and the film can make the oscillations to disappear. Therefore, the decrease in the profile intensity with the angle, and the angle above which Kiessig fringes (θ_k) stop, can respectively be used to retrieve the film's and the interface's roughness. [110] A typical XRR profile as well as the influence of the different thin-film parameters have been shown in **Figure II.6**.

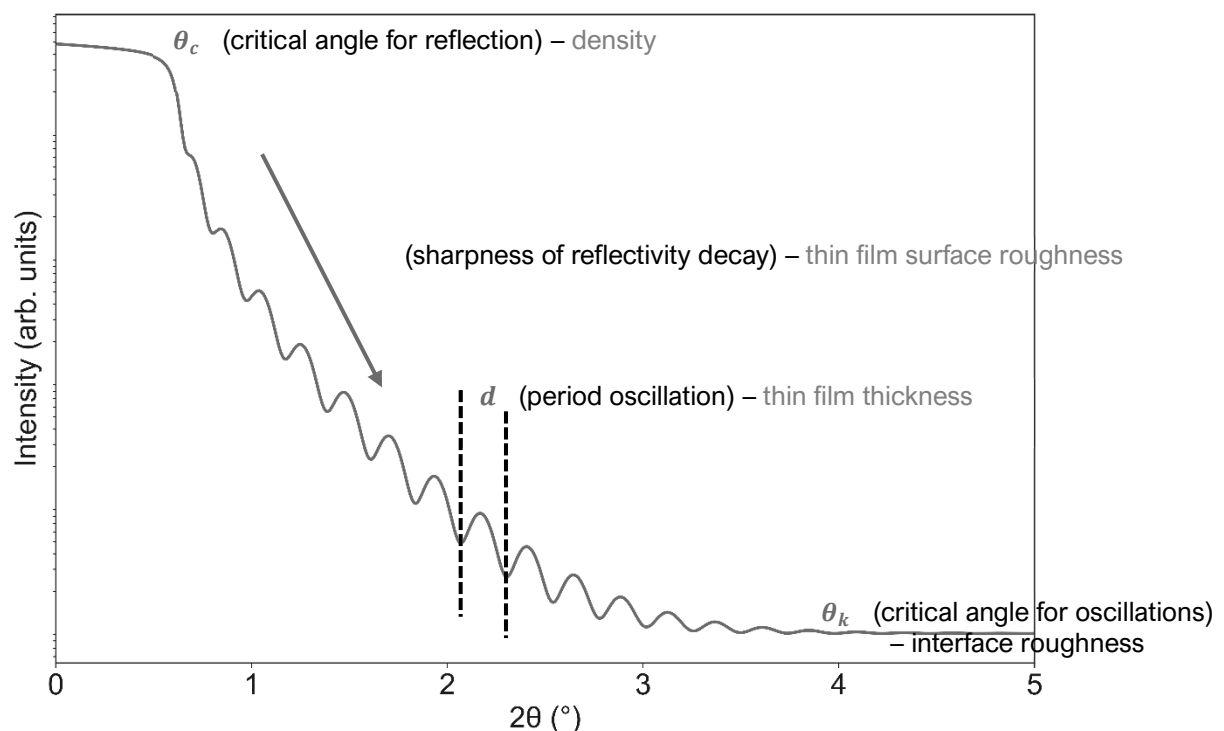


Figure II.6. Reflectivity profile showing Kiessig oscillations and the typical parameters which are obtained from an XRR analysis. Adapted from Yasaka [110].

2.2.2.2. $\theta/2\theta$ scans

Unlike multi-domain powdery samples, in thin films (or in any other oriented system, such as single crystals), there are no randomly oriented crystallites. Only special combinations of ω , θ , ϕ and χ allow the reaching of every Reciprocal Lattice Point (RLP). In most cases, the angles are no longer defined compared to the substrate's surface, but to a specific crystallographic direction. In this scenario, a $\theta/2\theta$ scan changes the modulus of the scattering vector along the direction defined by fixed ϕ and χ , and only $n(hkl)$ ($n \in \mathbb{Z}$) planes which respect the lattice symmetry will be observed. In our case, all thin films have been grown in the [001] direction. Angular $\theta/2\theta$ scans (defined compared to this direction) will give a diffractogram of the $00l$ reflections with preserved null χ . This scan of the scattered wave vector in the normal surface direction has been illustrated in **Figure II.7**. The positioning of the different $00l$ reflections will give information about the d spacing of the $\{00l\}$ planes and, as a result, $\theta/2\theta$ scans can be used to determine the out-of-plane lattice parameter of our thin films.

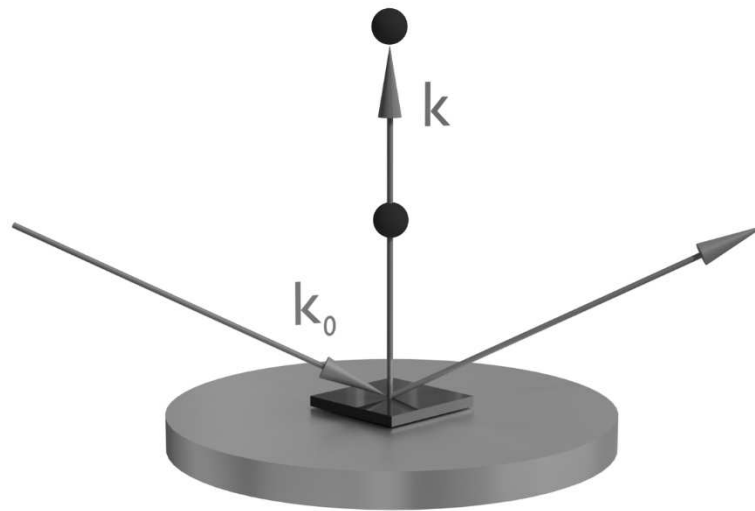


Figure II.7. Representation of a $\theta/2\theta$ scan on which the $00l$ RLP (depicted as blue objects) are reached by a scattered wave vector (\mathbf{k}) with a changing modulus in the normal direction. \mathbf{k}_0 represents the incoming wave vector.

The peaks in $\theta/2\theta$ diffractograms have a fringe-like profile of oscillations which are centred around the peak position. These oscillations are known as Laue oscillations. Laue oscillations are a type of X-ray diffraction phenomenon that occurs in a crystallographically aligned film or a crystal and which comes from the incomplete destructive interference of a finite number of unit cells [115], [116]. They appear when a sample consists of domains with the same number of unit cells across most of the area being probed. The presence of these oscillations is frequently used as evidence of high sample quality, indicating that grown films are highly crystalline, homogenous, have a low density of defects and possess a smooth substrate/film interface [117]–[119]. The term “crystallinity” is used in this work as the degree to which the atomic or molecular structure of the film exhibits a regular, ordered arrangement

characteristic of a crystal lattice. The Laue oscillations can be modelled by using the Laue interference function, which relates the number of unit cells in the diffracting crystal to the oscillations in the diffracted intensity. As a result, the analysis of the oscillation period can be used to determine the film's thickness [120], among other structural information.

In the scope of this PhD work, $\theta/2\theta$ diffractograms have been used not only to determine the out-of-plane lattice parameter, but also as an evaluation of the films' correct phase and good crystallinity - alongside the RHEED diffraction patterns after deposition. As a result, in the PLD optimisation process, the choice of the optimal conditions has been made according to these two criteria. Further analyses would later back up the fitness of the films that are deposited with the optimised conditions.

2.2.2.3. Rocking curve analysis

Rocking curve analysis, also known as an ω -rocking curve, is a diffraction technique used to examine the structural quality of a thin film or crystal. It involves rotating the sample (rocking) around the Bragg angle (ω) while keeping all other angles constant. This rotation results in a curve, the rocking curve, which represents the diffracted intensity as a function of the deviation from the perfect Bragg condition.

In a perfectly ordered single crystal, the rocking curve will be very narrow, indicative of all crystal planes simultaneously satisfying the Bragg condition. However, the sample's mosaicity and defects will cause a broadening of the rocking curve. Thus, the width of the rocking curve at half maximum intensity, known as full width at half maximum (FWHM), is a measure of the structural quality of the crystal. A smaller FWHM indicates a better crystalline quality, while a larger FWHM suggests a larger degree of crystal disorder.

In the context of this work, rocking curves were mainly used for the alignment of our samples on a specific hkl reflection. For that purpose, rocking curves around the expected Bragg position (in terms of ω and 2θ) were carried out, and the maximum of the ω -scan was chosen for further experiments. An adjustment of the azimuthal angle ϕ was also necessary for the proper reaching of RLP. Once the alignment was successful, other techniques such as $\theta/2\theta$ scans, ϕ scans or Reciprocal Space Mappings (RSM) were privileged for the judgement of the film's quality.

2.2.2.4. ϕ scans

The growth of a film on a substrate takes place in a particular direction, which is determined by the substrate's orientation and the interaction between the substrate's crystal's structure and that of the material growing on top of it. The relationship between the crystal alignment of the substrate and the film is also known as epitaxy. A growth is considered epitaxial if there is a defined registry between the crystal alignment of the substrate and the thin film material. In the interface of an epitaxial film, atoms of

both the substrate and the thin film occupy natural lattice positions of the other's crystal structure. Epitaxy is a desirable feature in thin film technology, since it enables the obtention of high-quality thin films. Furthermore, it makes possible the fabrication of materials with desirable properties that do not exist naturally or in the bulk form [121, p. 34].

When a crystal film is properly aligned at a specific reciprocal lattice point (satisfying the Bragg condition for a specific reflection), the equivalent reflections can be reached with a displacement in the azimuthal angle with a displacement in the azimuthal angle (Φ), which involves rotating the crystal around the zone axis. This experiment is also known as Φ scan and consists of the azimuthal rotation of the film with constant 2θ and ω values [122]. By performing a Φ scan and examining the distribution of the equivalent reflections, one can determine if the film is epitaxially grown with respect to the substrate. In an ideal epitaxial relationship, the crystallographic orientations of the film will correspond to those of the substrate at each azimuthal angle, manifesting as peaks with a coherent angular spacing as for a scan of the substrate.

As a result, the synthesised thin films were aligned at a specific reflection of the substrate. 2θ and ω were chosen in a way the tilt angle (χ) was null, making the zone-axis rotation a simple rotation around z , as shown in **Figure II.8**. The same procedure was then repeated on a reflection of the thin film material. Since the substrate's signal might eclipse the film's diffracted intensity, an appropriate reflection choice for the film would be an RLP permitted by the film's material structure but not the substrate. That same strategy would be repeated in the mapping of reciprocal space points, as continued hereunder.

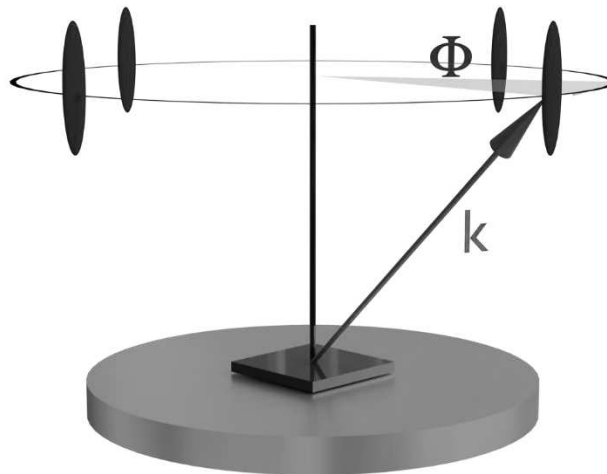


Figure II.8. Schematic representation of Φ scans. Since ω and 2θ are kept constant during the experiment, the scattering vector does not move. The sample is brought into diffraction conditions, and the scan in the azimuthal angle (Φ) allows the probing of the equivalent RLPs (represented a blue-coloured rods).

2.2.2.5. Reciprocal Space Mapping (RSM)

Reciprocal Space Mapping (RSM) is an X-ray diffraction technique that provides comprehensive structural information about thin films. It goes beyond the one-dimensional information obtained from traditional $\theta/2\theta$ scans and ϕ scans by creating a two-dimensional mapping of the scattering intensity in the reciprocal space. Moreover, in contrast to the previously described experiments, it can provide information about the thin film's in-plane lattice parameters.

In a typical 2D-RSM measurement, two angles are scanned simultaneously. The scattering angle 2θ is varied to change the magnitude of the scattering vector, while the angle ω is changed to scan different reciprocal lattice points in the out-of-plane direction. The χ and ϕ angles are fixed at the values that satisfy the Bragg condition for a specific reflection. As a result, a two-dimensional map of an area of the reciprocal space is generated, with the reciprocal lattice points presented as intensity peaks [123, p. 269]. This map corresponds to a 2D-cut of a 3D RLP alongside the diffraction (or measurement) plane, as illustrated in **Figure II.9**. The scan takes place in angular coordinates, but these can be converted into reciprocal space coordinates by the relationship shown in **Equation (II.3)**, where q_{\parallel} and q_{\perp} are normal vectors in the diffraction plane. In our source-sample-detector geometry, q_{\parallel} is orientated in the source-to-detector direction while q_{\perp} is vertically perpendicular to it.

$$\begin{aligned} q_{\parallel} &= \frac{2\pi}{\lambda} (\cos(\omega) - \cos(2\theta - \omega)) \\ q_{\perp} &= \frac{2\pi}{\lambda} (\sin(\omega) - \sin(2\theta - \omega)) \end{aligned} \quad (\text{II.3})$$

In the case of a null tilt angle, the diffraction plane would contain the surface normal and q_{\parallel} and q_{\perp} can be easily related to the reciprocal space components. In our films, the normal surface direction is the [001] crystal direction and q_{\perp} is equal to the reciprocal space vector q_z . Nevertheless, the q_{\parallel} vector would be a combination of both the q_x and q_y components. Proper choices of $h0l$ or $0kl$ reflections are needed to independently obtain the different reciprocal vectors. The relationships between the RSM normal vectors and the crystal reciprocal vectors, as well as with the crystal lattice parameters, has been made explicit in **Equation (II.4)**. Such straightforward relationships are only possible due to the fact that our system crystallises in a (pseudo)cubic configuration with $\alpha = \beta = \gamma = 90^\circ$, and more complex expressions would arise if the lattice vectors were not perpendicular to each other.

$$\begin{aligned} a &= \frac{h}{q_{\parallel}(h0l)} \\ b &= \frac{k}{q_{\parallel}(0kl)} \\ c &= \frac{l}{q_{\perp}(hkl)} \end{aligned} \quad (\text{II.4})$$

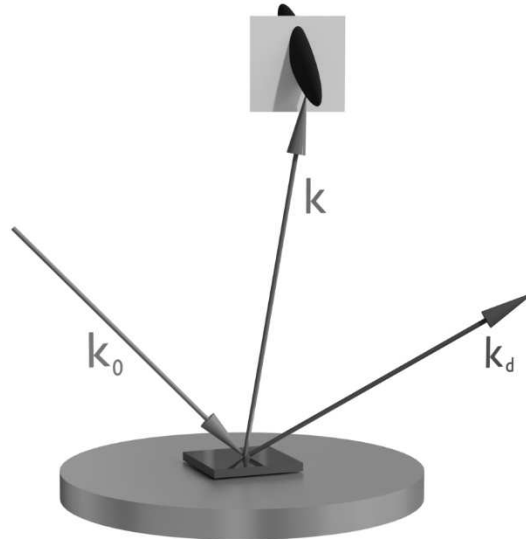


Figure II.9. Representation of a 2D-RSM. 2θ , ϕ and ω are adjusted so that the atomic scattering vector $\mathbf{k} = \mathbf{k}_d - \mathbf{k}_0$ is in diffraction geometry at a specific reflection. Small $\omega/2\theta$ variations lead to a 2D cut-area of the 3D RLP.

In our work, we have used RSM as a further confirmation of the film's correct phase and crystallinity (by the own presence and intensity of the diffracted peak), to confirm the out-of-plane lattice parameters obtained by $\theta/2\theta$ scans and to obtain the in-plane lattice parameters. For that purpose, RSM on reflections allowed by the film's symmetry but forbidden by the substrate's were chosen – specific choices are explicit in the “Results on FeV₂O₄ thin films” section of this chapter – page 69. RSM was also employed to study the precise crystal epitaxy through a scan of reflections shared by both the film and the substrate.

2.3. RHEED

Reflection high-energy electron diffraction (RHEED) is a widely used technique for surface structural analysis in monitoring epitaxial growth. RHEED is based on the use of an electron gun to project high-energy electrons (from 10 to 100 keV) onto a sample which are diffracted by the material into a detecting fluoresce screen. Electrons, unlike photons, undergo Coulomb interactions and cannot penetrate the material's bulk as easily. As a result and differently to XRD, RHEED only penetrates a few angstroms into the sample and the diffracted pattern corresponds to the material's surface and not to its bulk [124]. By analysing the diffraction pattern, information about the crystallographic orientation, lattice spacing, and surface morphology can be obtained [125].

The electron beam hits the material's surface at low incident (tilt) angles, usually less than 4° , in order to study the surface disorder of the growing film. An electron deflection unit is typically used to change

the incident angle of the incoming electrons by applying magnetic fields. The azimuth angle is also adjusted in order to satisfy the diffraction angle condition.

The *in situ* monitoring of thin-film growth through RHEED is achieved by analysing the periodic intensity changes in the diffraction pattern. These RHEED oscillations are caused by the interference between the electrons diffracted by the growing thin film and those reflected by the substrate. Each oscillation period corresponds to the time required to deposit a single layer of the material of interest (frequently of a unit-cell thick, but not necessarily) [126], [127]. By monitoring the oscillations, one can determine the growth rate and film thickness during deposition, enabling precise control over the growth process and the achievement of the desired film thickness.

Apart from the intensity evolution as a function of time, the diffracted pattern itself can also give valuable structural and morphological information. The position of the diffraction spots compared to the substrate's shows whether the growth occurs epitaxially or not. Furthermore, the shape of the diffraction spots can determine if thin-film growth occurs in a two-dimensional (2D) or three-dimensional (3D) mode. During 2D (layer-by layer) growth, the atoms added to the surface of the thin film layer are able to diffuse laterally before forming new islands. The high horizontality of the crystal film results in rod-like unidirectional RLPs. This results in a RHEED pattern that is characterised by sharp, distinct streaks that are parallel to each other, indicating a flat surface [128], [129]. Conversely, during 3D growth, the arriving adatoms lack sufficient time to diffuse laterally, leading to the formation of new islands that grow vertically. This results in a RHEED pattern that is characterised by point-shaped diffraction spots with a diffuse intensity distribution, indicating the presence of rough surfaces [130], [131]. The RHEED setup, as well as the different patterns associated to the diverse growth modes, have been illustrated in **Figure II.10**. The RHEED measurements for this thesis have been conducted using a RHEED system from *STAIB instruments* with a voltage of 35 kV.

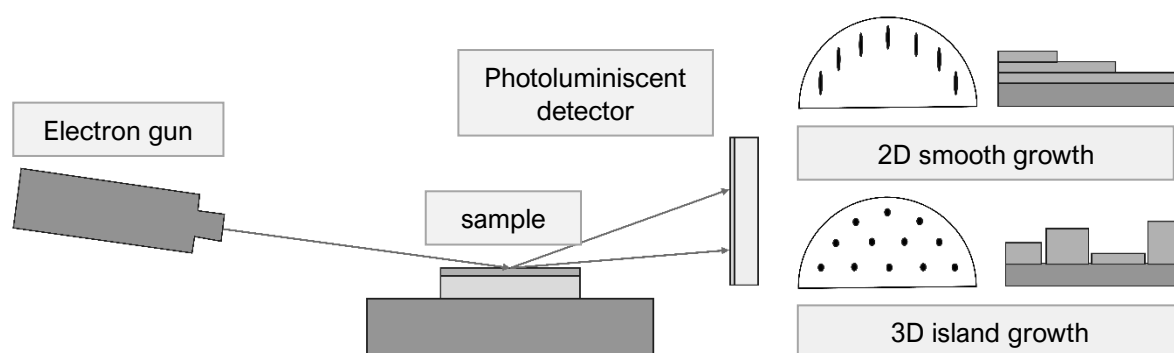


Figure II.10. Left: schematic representation of the RHEED set-up. Right: Illustration of RHEED patterns according to the different growth modes. Inspired by Krieger [132, p. 42] and Gellé [133, p. 57].

2.4. Atomic Force Microscopy

Atomic Force Microscopy (AFM) is a technique employed for the characterisation of the topology of thin films at the nanometre scale. This technique is based on the principle of scanning probe microscopy, where a sharp probe attached to a flexible cantilever scans the surface of the sample. The basic setup of an AFM involves a micro-machined cantilever probe with a sharp tip. This tip is mounted on a piezoelectric actuator. The cantilever's deflection is tracked by a laser beam, reflected off the endpoint of the beam, and received by a position-sensitive photo detector.

In AFM, the cantilever is equipped with a sharp tip that interacts with the surface of the material. The cantilever oscillates and, when the tip is brought close to the surface, atomic-scale forces such as van der Waals forces, electrostatic forces, and mechanical contact forces, cause the cantilever to deflect. This deflection is measured by a laser that is reflected off the top surface of the cantilever and detected by a photodiode. The movements of the probe across the sample surface and the corresponding deflection of the cantilever create a precise map of the surface topology [134, p. 908]. The archetypical layout of an AFM set-up has been schematised in **Figure II.11**.

In the topology measurements that we carried out, the tip did not touch the surface. Such a scanning approach, also known as “non-contact mode,” allows surface analysis without inflicting any mechanical damage to either the sharp tip or the sample's surface [135, p. 242].

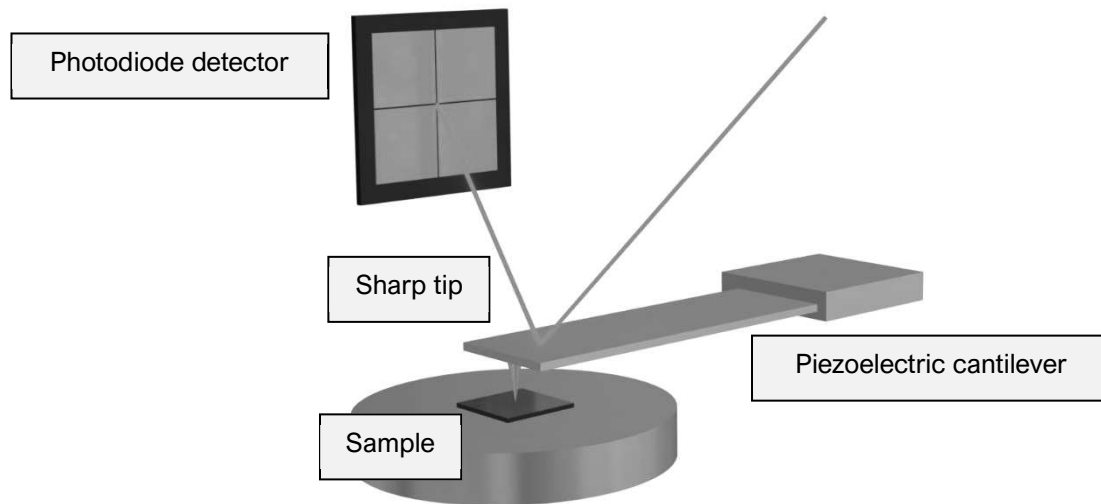


Figure II.11. Schematic representation of an Atomic Force Microscopy set-up with its main components.

AFM analyses aim at giving information about the quality and smoothness of the sample's surface, which can be related to the sample's roughness. The term “roughness” quantifies how much a given area

deviates from a perfect planar surface and increases as the surface's relief becomes more prominent [136]. A common mathematical definition of the roughness is the root mean square roughness (R_q) and refers to the extent of change in the surface's height. As shown in **Equation (II.5)**, R_q is defined over a certain surface area of dimensions $l_x \times l_y$, and quantifies the average square difference between the sample's height $z(x, y)$ and the mean height \bar{z} [137].

$$R_q = \sqrt{\frac{1}{l_x l_y} \int_0^{l_x} \int_0^{l_y} (z(x, y) - \bar{z})^2 dx dy} \quad \text{(II.5)}$$

2.5. Magnetometry measurements

The magnetic characterisation of both the powder and the thin film samples has been carried out in a superconducting quantum interferometer device (SQUID) from *Quantum Design*. The basic architecture of a SQUID involves a superconducting loop, often made from thin films of materials such as niobium or lead, interrupted by two extremely thin insulating barriers known as Josephson junctions. These junctions allow for the tunnelling of Cooper pairs and create the conditions for quantum interference to occur. A change in magnetic flux passing through the loop modulates the critical current of the SQUID, which is tracked by an ultra-sensitive amplifier. The high sensitivity of the SQUID magnetometer enables magnetic characterisation of both bulk-sized and nanosized samples (e.g. thin films) [138], [139].

In SQUID magnetometry, the superconducting loop is exposed to a magnetic field. This magnetic field induces a change in the magnetic flux within the loop, which then affects the phase difference across the Josephson junctions. The interplay between these two effects allows the SQUID to oscillate between different superconducting quantum states, producing an output signal that is highly sensitive to the field's intensity. This signal can then be processed to give a precise measure of the magnetic state of the sample [140].

Two distinct types of measurements have been routinely performed in SQUID magnetometry. The first involves measuring magnetisation (M), which is the extent of a material's magnetism, in relation to temperature, all while under a fixed magnetic field (H). In essence, magnetisation represents the collective behaviour of magnetic moments within a substance, showing how they align with or oppose an external magnetic field. M vs. T analyses are performed to the Curie temperature (T_c), the specific temperature at which certain materials lose their permanent long-range magnetic ordering. Magnetisation as a function of temperature ($M(T)$) is measured during an increase in temperature under a small magnetic field. However, this can be done following one of two different methods: either after cooling the sample in zero magnetic field, known as Zero Field Cooled (ZFC) measurements, or after cooling the sample in the presence of a non-zero magnetic field, known as Field Cooled (FC) analyses.

The second type of measurement is the execution of hysteresis cycles, where magnetisation is measured against the strength of the external magnetic field at a set temperature ($M(H)$). The external magnetic field is applied in two different ways during these tests. Firstly, in an in-plane (IP) configuration, the magnetic field is introduced parallel to the surface of the thin films. For such measurements, a quartz sample holder is often used. Conversely, in a out-of-plane (OOP) configuration, the magnetic field is applied at a right angle to the surface of the sample. Both measurements are conducted on thin films that have been cut into small 3 x 3 mm² pieces and placed within a non-magnetic plastic tube or stuck onto a quartz sample holder. An illustration of the two sample configurations has been shown in **Figure II.12**.

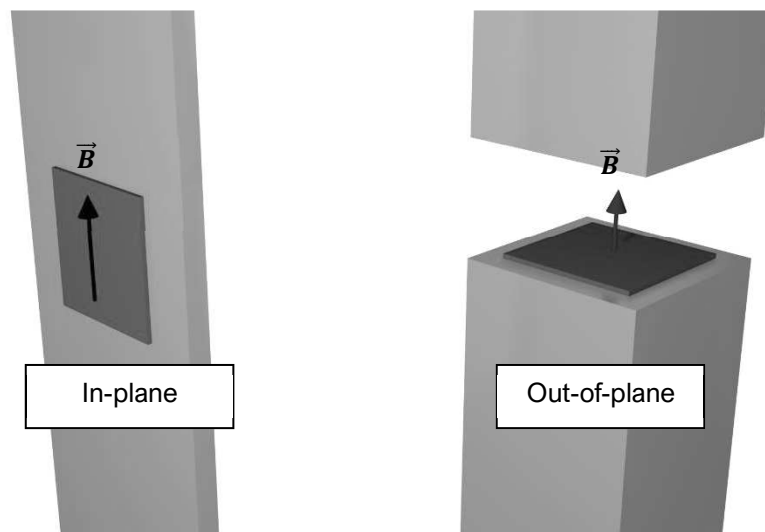


Figure II.12. Schematic representation of the in-plane and out-of-plane configurations for magnetometry analyses. The two conformations are defined according to whether the magnetic field (\vec{B}) is applied along the sample's surface (in-plane) or in the sample's normal direction (out-of-plane).

These two configurations allow for the determination of the easy magnetisation axis, which is the direction that most easily allows for the material to become magnetised. This in turn provides information about the magnetic anisotropy of our systems, which refers to the degree to which the magnetic properties of a material depend on the direction of magnetisation.

Even if our films present a considerable magnetic component, the substrate manifests itself in SQUID measurements due to its diamagnetic contribution. The sample holder, whether plastic straw or quartz semicylinder, also gives a non-negligible diamagnetic signal. A diamagnetic correction was by default carried out in all $M(H)$ curves, by fitting the negative slope of the high-field magnetisation data. In some cases (with depositions using MgO substrates), a paramagnetic contribution was also detected in the substrates, and such component would be removed in order to isolate the film's magnetisation. Any removal of this paramagnetic contribution will be explicitly documented in the magnetometry measurements of this PhD work.

2.6. Transport measurements

The final routine characterisation of thin films involved the study of their transport properties, i.e., the films' response to a stimulus in the form of an electric current. The study of the conduction properties gives an insight about the film's conductivity and the efficiency with which it can transfer electrical charges. In the section "Spinel vanadates and Mott insulators" of **Chapter I** – on page 13, we showed that the conduction properties in the vanadate family are directly related to the V-V atomic distance. Transport measurements enable the categorisation of the obtained films into one of the conduction realms (semiconducting, insulating or pseudometallic) and assist in the study of the influence of the strain on the films' conduction properties.

Transport measurements took place in a physical properties measurement station (PPMS) by *Quantum Design*. Electric currents (I) would be applied, and the voltage response (U) would allow the calculation of an electric resistance ($R = U/I$) by using Ohm's law. To compare different devices, resistance values are converted to resistivities $\rho = 1/\sigma = R \times S/l$, representing the inverse of the electric conductivities (σ) and nullifying the influence of the sample's length (l) and its surface (S) on the measured resistance value.

Measuring a sample's resistance through the ohmic response to a current input is a common strategy for bulk materials. In thin films, however, the sheet resistance (R_s) is often more used to characterise the planar transport response of the film as a whole. Sheet resistance measures the lateral resistance per square area of a film with uniform thickness, quantifying the ability of electrical charge to traverse within the plane of the film [141]. R_s relates to the film's resistivity by the relationship $R_s = \rho \times t$. It can be measured following different strategies, such as using a colinear four-contact mode [142] or the corner-to-corner van der Pauw method.

The strategy proposed by L. J. van der Pauw in 1958 [143] is the most commonly used technique for the measurement of sheet resistances in thin films. It is based on a four-contact resistance measurement, in which these contacts (1, 2, 3, 4) must be on the edge of the sample and be small in relation to the surface, as illustrated in **Figure II.13**. Once these requirements are met, the "horizontal" and "vertical" resistances are measured, as indicated in **Equation (II.6)**. The subscripted values correspond to the pads where the current (voltage) is applied (measured).

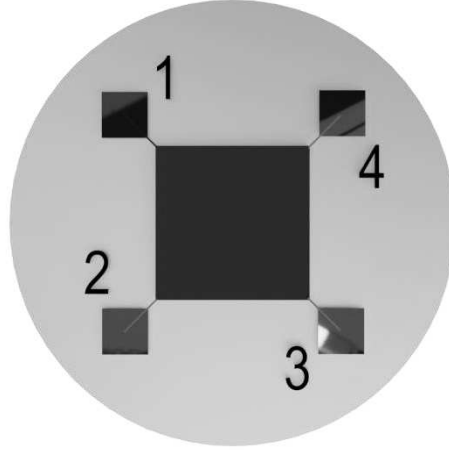


Figure II.13. Schematic illustration of the van der Pauw method set-up, with four contacts connected to the outer edges of a thin film.

$$R_{horizontal} = \frac{U_{23}}{I_{14}} \quad R_{vertical} = \frac{U_{12}}{I_{43}} \quad (\text{II.6})$$

The resistivity can be then measured by the expression shown in **Equation (II.7)**, where t is the film's thickness and $f\left(\frac{R_{horizontal}}{R_{vertical}}\right)$ is a geometric factor which takes into account the deviation from the perfect non-square shape geometry [144]. This factor is often graphically obtained or using tabulated values in the literature [145], but numerical solutions have been also provided by what is known as "Chan's method" [146]. In the case of this PhD work, the graphical solution was used because of its simplicity.

$$\rho = \frac{\pi t}{\ln 2} \left(\frac{R_{horizontal} + R_{vertical}}{2} \right) f\left(\frac{R_{horizontal}}{R_{vertical}}\right) \quad (\text{II.7})$$

The van der Pauw method does not necessitate a specific shape for the sample, provided it is approximately two-dimensional and has a uniform thickness. Additionally, the effects of contacts must be negligible in comparison to the overall resistance values [147]. The method involves making four small contacts at the perimeter of the sample, with areas negligible compared to the sample's surface.

As the current is driven between one pair of contacts and the voltage is measured between a separate pair, contact resistance does not significantly influence the measured resistivity, circumventing a major issue when measuring thin films [148]. Besides, the van der Pauw method is highly accurate because it averages over multiple measurements taken in different configurations, which helps to mitigate errors and the effects of non-uniformities in the sample.

3. Results on bulk FeV₂O₄

3.1. Granulometry

As previously mentioned, a small particle size is a requirement for the obtaining a dense PLD target after sintering the powder in the form of pressed pellets. After the first annealing process, the FVO powder underwent a mill ball attrition with ethanol as the solvent. Among the available solvents in our lab, ethanol seemed to give the smallest particle size. A study of the size distribution as a function of time has been carried out, i.e., samples from the attrition process have been periodically analysed during the ball mill process, as seen in **Figure II.14a**. The size distributions have been fitted using a Gaussian distribution function: $f(x) = \frac{1}{\sigma\sqrt{2\pi}} e^{-(x-\mu)^2/(2\sigma^2)}$. The particle size has been described by the centre of the Gaussian distribution (μ) or expectation, whereas the amplitude of the size distribution has been characterised by the standard deviation (σ). The evolution of these two parameters has been indicated in **Figure II.14b**.

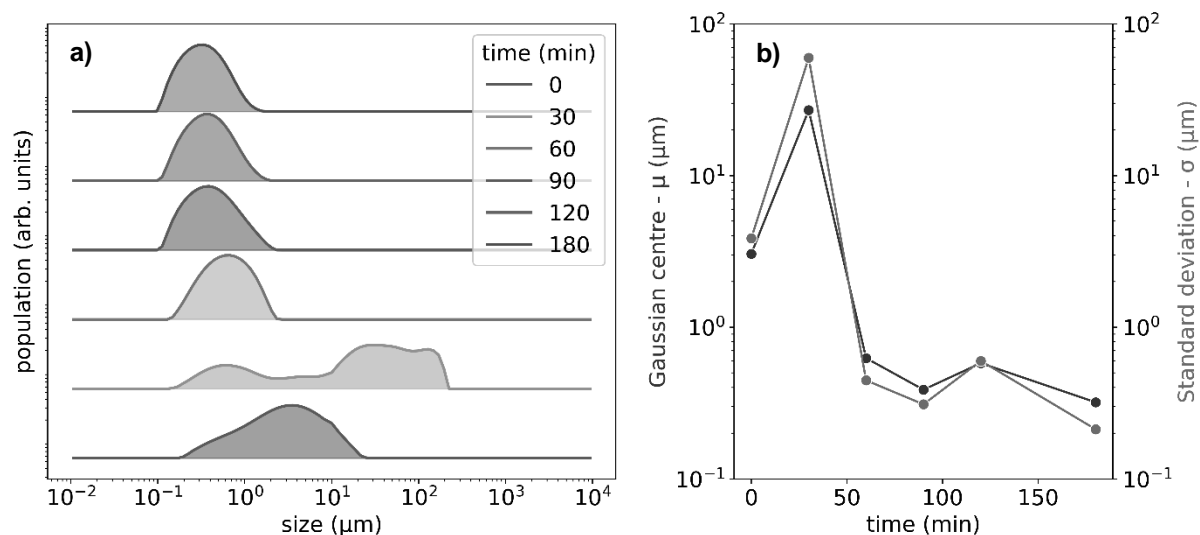


Figure II.14. Size evolution with time for the ball milling of FVO powder with ethanol as dispersant. (a) Population distribution for each given time is shown as a function of size. (b) Parameters of the Gaussian fit of the size distributions: in blue, the Gaussian centre; in red, the amplitude of the distribution.

Just before the ball mill process, the particles have a size of around 3 μm. Then, the attrition process starts breaking particles down, but they seem to agglomerate into bigger particle clusters. This causes both the mean size and the standard deviation to increase. At a certain time, the particles are broken down into stable sizes, and both μ and σ take a low value. Beyond 60 minutes, the particles reach a submicron size with a narrow size distribution. As a matter of prudence, ball milling processes were carried out up to 120 minutes.

3.2. Scanning electron microscopy

The dense target pellet ($\tau_s = 0.85$) was cut to expose its inside, and both the target surface and the inner part were imaged using SEM, as shown in **Figure II.13**, for an electron energy of 3 keV.

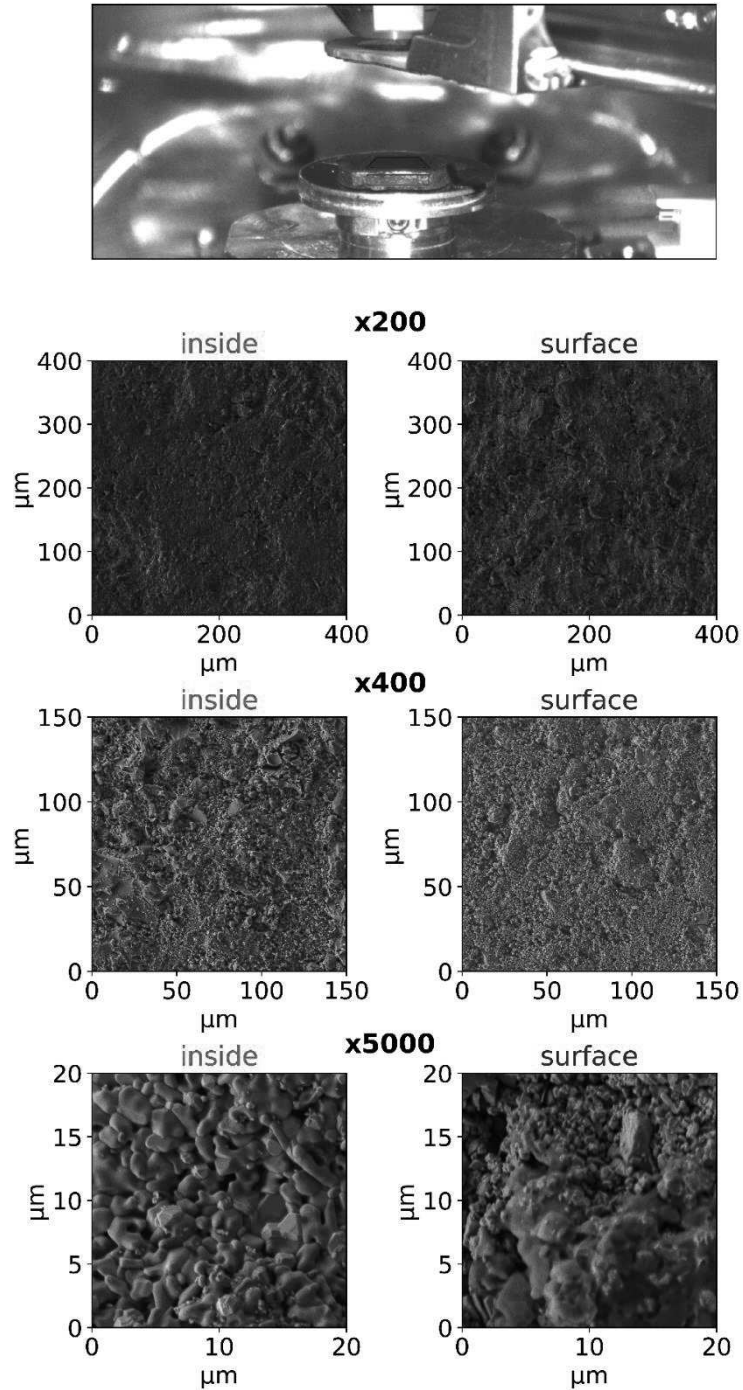


Figure II.15. SEM images of the FVO target's surface and the cut on its inside, with different objective lens magnifications: x200, x400 and x5000.

The SEM images did not show enormous differences between the surface area and the inner part of the target, suggesting that the target pellet has a homogeneous microstructure. The images at a smallest resolution reveal more texture relief on the surface image, which may be related to some surface contamination during the sintering process or due to air exposure. These images furtherly prove the micron-sized nature of the grains, and the uniform size distribution observed in the granulometry measurements.

In terms of the target stoichiometry, the elemental analysis via EDS revealed a V:Fe ratio of 1.97(7) for the target pellet, close to the expected value of 2. This proves the correct stoichiometry of the targets of the PLD targets, fulfilling the first requirement for the obtention of stoichiometric FVO films.

3.3. Powder XRD

The crystallographic structure of the sintered pellet was verified by room-temperature powder XRD experiments. Profile matching analysis of the diffractograms confirmed the $Fd\bar{3}m$ cubic space group at room temperature, with a lattice parameter of $a = 8.4575(1)$ Å on the diffractogram acquired at a Synchrotron radiation facility (CRISTAL Line, SOLEIL Synchrotron). As seen in **Figure II.16**, the simulated diffractogram (red) matches the experimental data (grey), with relatively small differences (blue) between both profiles. Rietveld refinement furtherly confirmed the correct crystal stoichiometry and found that the oxygen atoms were placed at the crystal position $x = 0.262(2)$. Small parasitic phases were detected, but they did not hinder the structural resolution, since the refinement is done on the Bragg-active peaks. All these findings match the values reported in the literature for FVO at room temperature [53] and confirm the obtention of the correct spinel phase.

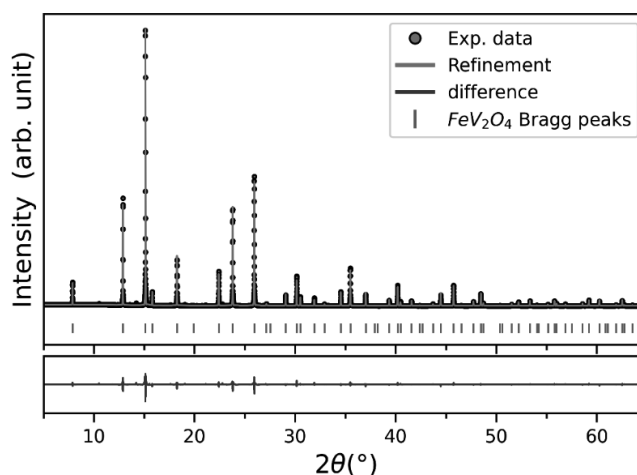


Figure II.16. Experimental powder-XRD data (grey) and best refined diffractogram (red) using Profile Matching and Rietveld refinement strategies. The difference between the experimental and simulated diffractogram has been indicated in blue, whereas the Bragg peak positions are shown as green lines.

This same analysis was performed in a routine laboratory diffractometer at temperatures ranging from 90 to 300 K for 2θ between 10 and 120°, to study the profile evolution with temperature, as depicted in **Figure II.17** – with **a** showing the whole angular range, and **b**, **c** and **d** being zooms at specific ranges.

The diffractogram at room temperature did not suffer any remarkable change until temperatures around 130 K, when peak splitting starts happening. This change, subtle around the transition temperature but more visible as the temperature decreases, corresponds to the cubic-to-HTT structural transition. When the temperature is decreased, the HTT-to-HTO transition is also detected as a split in the peaks around 110 K. The two remaining transitions (HTO-to-LTT and LTT-to-LTO) were not detected, as the available diffractometer could not reach temperatures lower than 80 K.

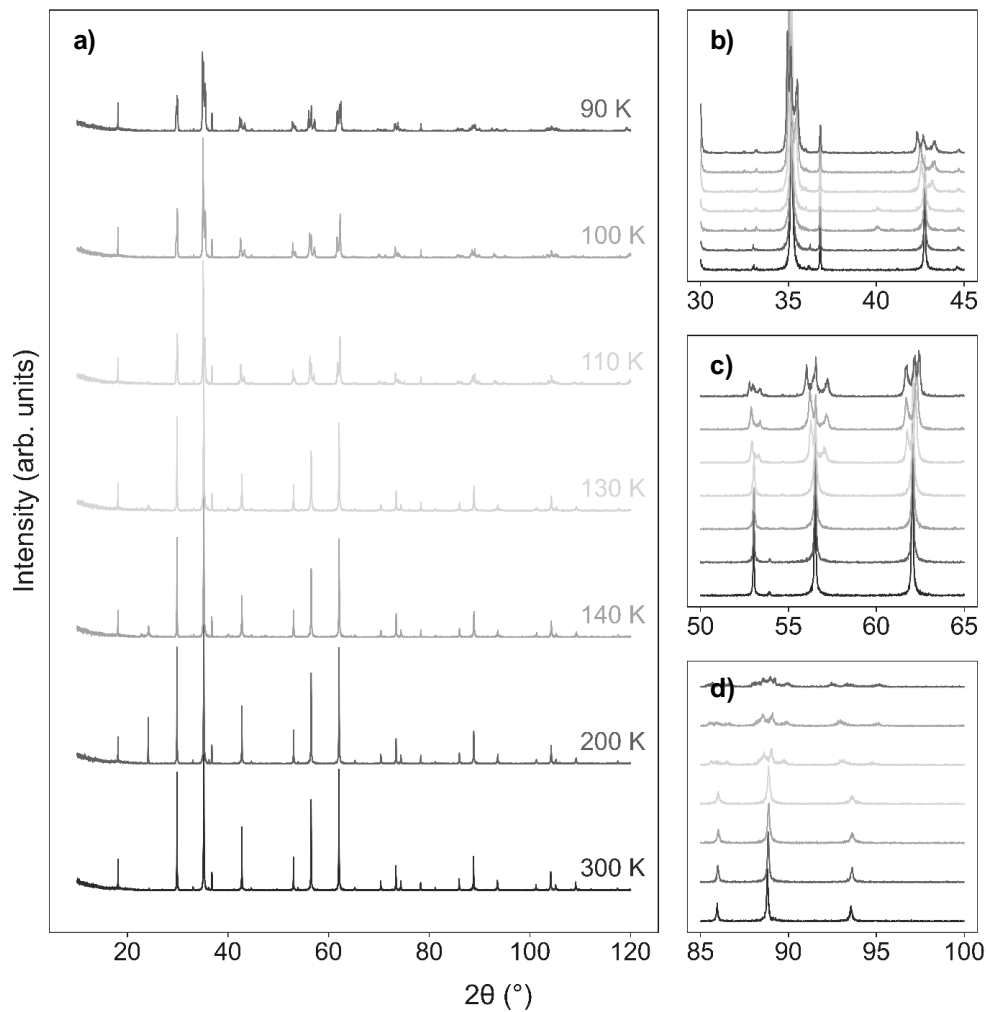


Figure II.17. Diffractograms at decreasing temperatures **(a)**. On the right, zoomed regions of interest – **(b)**, **(c)** and **(d)**, where the peak splits are visually clear.

All the peaks could be associated with the spinel FVO phase, but a foreign peak at $2\theta = 25^\circ$ seemed to appear at temperatures around 230 K, accompanied by two smaller satellite peaks on its right and left sides. Its intensity increases with decreasing temperature, and suddenly disappears at 140 K along the

cubic-to-HTT transition. This observation can be clearly seen in **Figure II.18**, on which the intensity of the peaks has been represented as colours in a colourmap as a function of the temperature. This foreign peak does not correspond to the sample holder (it is not present in other measurements) and cannot be associated with any spurious phase (since it appears and disappears). Through the study of its harmonic counterparts, it could not be linked to any of the already present peaks. A phenomenon occurring in the cubic phase beyond the already-reported structural changes might be behind this foreign peak.

On top of that, the cubic-to-tetragonal and tetragonal-to-orthorhombic peak splitting can be clearly seen in **Figure II.18**. Taking the peak at 42° as an example, one can see that a first separation occurs at around 130 K, which corresponds to the break of lattice degeneracy between $a = b$ and c . Later, at around 110 K, a second splitting occurs when the orthorhombic phase occurs. The same observations can be clearly observed in the peaks at 56° and 92°.

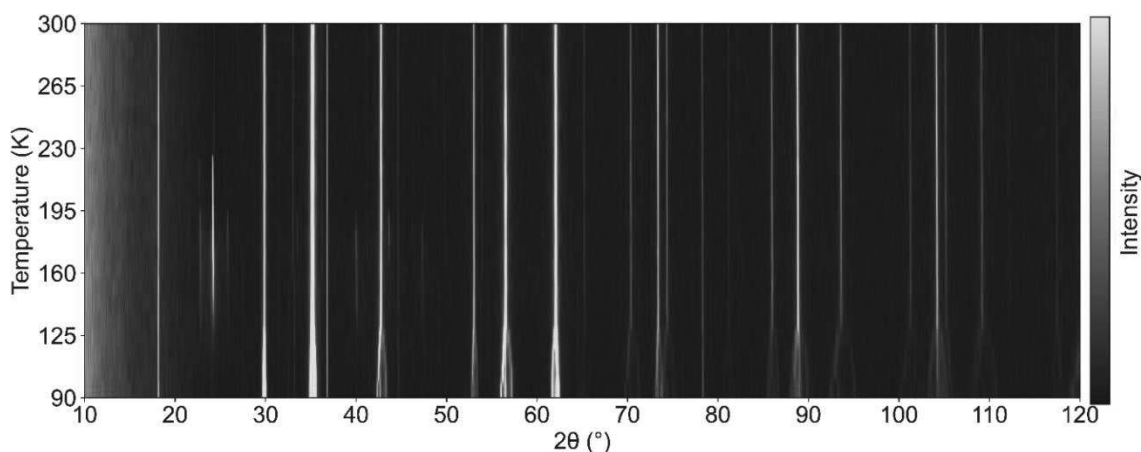


Figure II.18. Intensity (colour, legend on the right) as a function of the angle and the temperature.

The diffractograms acquired at each temperature were fitted with cubic ($F d \bar{3} m$), tetragonal ($I 4_1/a m d$) and orthorhombic ($F d d d$) models to study the evolution of lattice parameters with temperature. Fits were carried out using the Python package *xrayutilities* [149]. The results of the fits can be seen in **Figure II.19**. The tetragonal structure has a 45° tilt compared to the cubic and orthorhombic structures: $\mathbf{a}_{tetra} = 1/2(\mathbf{a}_{cubic} + \mathbf{b}_{cubic})$; $\mathbf{b}_{tetra} = 1/2(\mathbf{a}_{cubic} - \mathbf{b}_{cubic})$ so the $a = b$ values for the tetragonal structures have been corrected with a $\sqrt{2}$ factor.

At room temperature and down to 130 K, all three fits lead to the same result: $a = b = c$, confirming hence the cubic structure. The value of the lattice parameter (a) slightly decreases (- 0.04% from 300K to 150K) with the decreasing temperature as the lattice shrinks. The appearance of the foreign peak at 230 K provides no indication of a change in the lattice parameter. Analogously, other groups did not observe any transition sign on their temperature-dependent single-crystal XRD with Synchrotron

radiation [53]. The difference between the experimental value for the structural transition and its theoretical value (140 K) [28], [53] can be solely attributed to the thermal inertia.

Below 130 K, c splits away from the other two lattice parameters, and their difference becomes more significant with decreasing temperature. Differently to the cubic fit, the orthorhombic and tetragonal fits in this temperature range give the same result: $a = b \neq c$. c is smaller than the other two lattice parameters, and a planar lattice contraction occurs. As previously described in the section “Structural transitions and orbital ordering” of **Chapter I** – page 15, this transition is driven by the cooperative JT distortion on the FeO₄ tetrahedra, which causes a ferro-OO in the lattice [19].

At temperatures below 110 K, a and b split again, and the orthorhombic fit ($a \neq b \neq c$) is the only model able to explain the diffractogram’s profile. As mentioned in the state of the art on FVO’s research, his structural change is triggered by the SOC at the Fe²⁺ site. The OO changes its plane projection but remains ferro-OO.

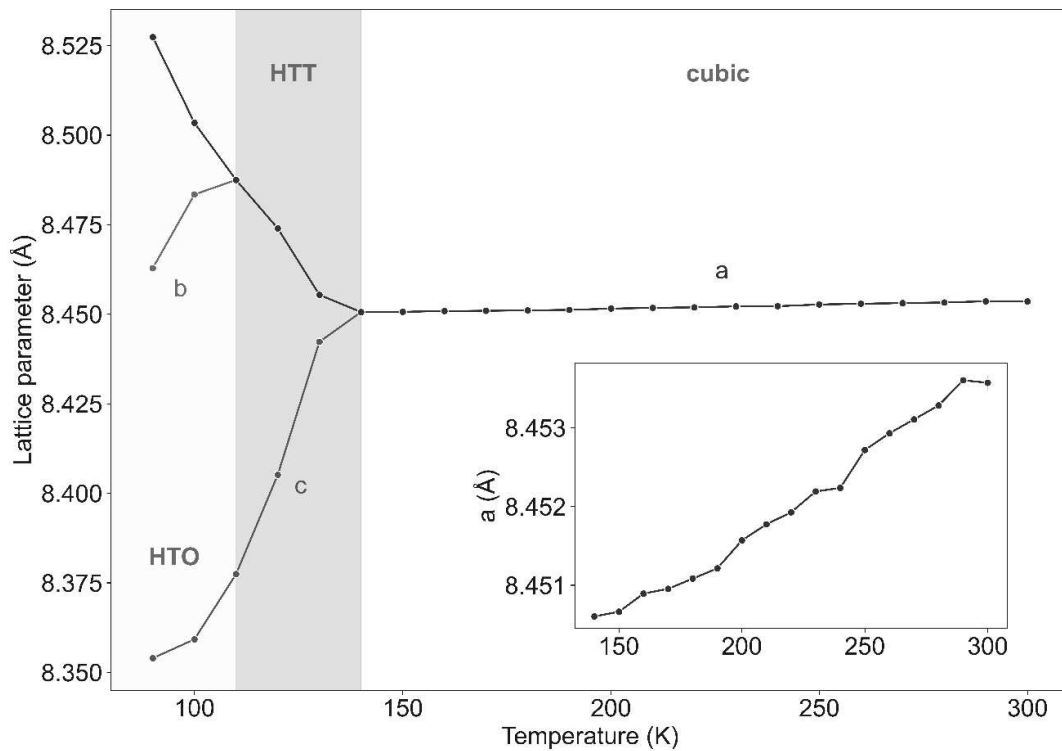


Figure II.19. Evolution of lattice parameters as a function of temperature. The temperature domain on which cubic, tetragonal and orthorhombic fits lead to $a = b = c$ (cubic structure) has been left in white colour. On the bottom right part of the graph, the evolution of lattice parameter as a function of temperature. The region when c broke apart from a and b (tetragonal) has been shadowed in blue, and the yellow zone corresponds to a total split between a , b and c (orthorhombic).

3.4. Temperature-dependant magnetism and specific heat

The appearance of a magnetic ordering has a distinct shape in the magnetisation evolution. In the same manner, as the material undergoes a magnetic ordering transition, there is a transfer of energy between the magnetic moments and the lattice vibrations of the material. This transfer of energy results in a change in the specific heat of the material. Actually, during any phase transition, a undergoes a change in its internal energy and/or entropy and its specific heat may exhibit a discontinuity, a singularity, or a sharp peak.

As a result, the temperature evolution of the powder's magnetisation and specific heat capacity ($C = \frac{1}{m} \frac{dQ}{dt}$) enables the determination of the transition temperatures in FVO for both magnetic and non-magnetic phase changes. The magnetisation vs. temperature analysis was carried out via field-cooling mode ($H_{ext} = 5000$ Oe) Quantum Design SQUID measurements, whereas the specific heat capacity measurement took place in a Quantum Design PPMS (Dynacool).

As shown in **Figure II.20**, the evolution of C as a function of temperature allows the detection of the several phase transitions: the cubic-to-HTT transition ($T_{S1} = 138.1(4)$ K) the HTT-to-HTO transition ($T_{S1} = 111.8(1)$ K) and the HTO-to-LTT transition ($T_{N2} = 60.1(2)$ K). The found temperatures match with the values found in the literature (140 K, 110 K and 60 K) [19], [28], [53].

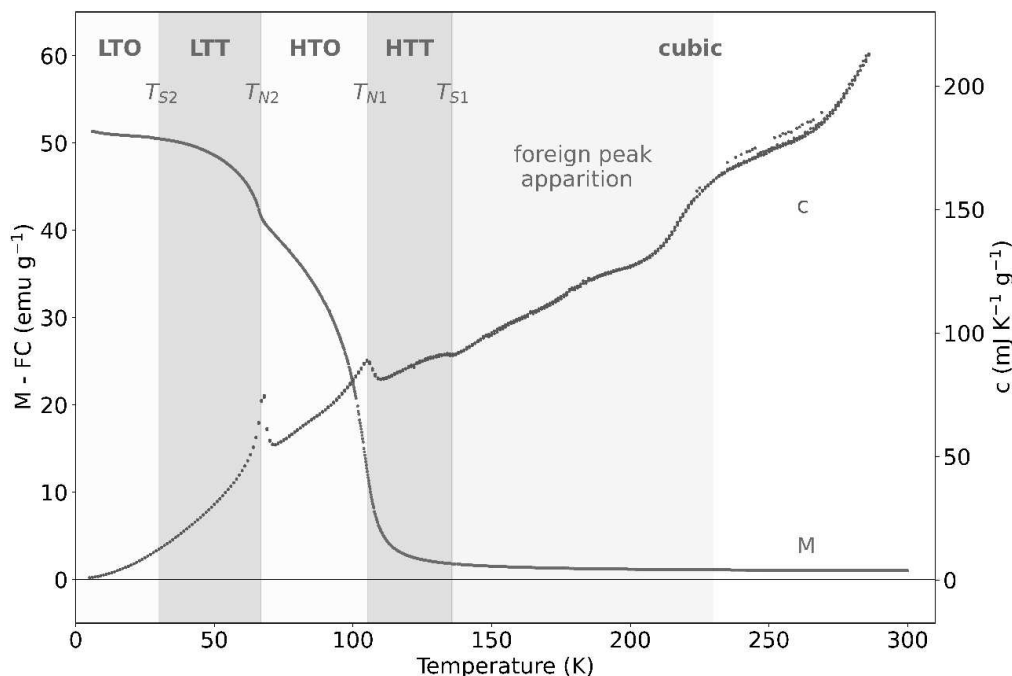


Figure II.20. Magnetisation and specific heat capacity as a function of temperature, in the 2 – 300 K temperature domain. The different phases have been highlighted in blue (tetragonal) and yellow (orthorhombic), and the temperature domain on which the foreign XRD peak appears is shown in grey.

This further confirms the obtention of the correct FVO phase in the bulk form. The transition at 110 K corresponds to the magnetic ordering (paramagnetic to linear ferrimagnetic), and it shows a clear magnetic signature in the magnetisation vs. temperature curve. Furthermore, the pass from a collinear to non-collinear magnetic structure is evidenced by the step in the magnetisation at 60 K, below which the vanadium spin canting reduces the opposition of the vanadium's sublattice magnetism and increases the overall magnetisation of the lattice.

The last structural transition, from LTO to LTT at 30 K (T_{S2}), has not been observed in either the SQUID or specific heat measurements. Works in the available literature also report the non-detection of this transition by such techniques [19], [54]. The low-temperature resolution of the crystallographic structure (e.g. low-temperature powder diffraction) would be useful to further confirm the presence of this transition. Even if the previous reports did not detect this transition using similar approaches, we have no information about the kinetic conditions (temperature scan rate of their measurements).

The temperature domain at which the foreign XRD peak appears shows some bumps which do not have the same distinct shape of the other transitions. The XRD analysis discarded any drastic structural change, and the magnetisation studied confirms that no magnetic transition occurs at such temperatures. Therefore, the nature of the phenomena taking place at the cubic phase below 230K remain unclear, and further temperature-dependant studies (Rietveld refinements, Neutron Diffraction (ND), X-ray Magnetic Circular Dichroism (XMCD), etc.) might be needed to fully understand the processes happening at such temperatures.

3.5. Hysteresis curves

The magnetisation (M) of the powder FVO as the function of the applied magnetic field (H) has been measured at temperatures ranging from 2 K to 130 K, as shown in **Figure II.21a**. The evolution of the magnetisation at saturation (M_s) with temperature has been represented in **Figure II.21b**. A consistent colour scheme has been employed to delineate each temperature domain when the different FVO phase occur.

The powder presents a permanent reversible magnetic behaviour up to 110 K, which is consistent with the M vs. temperature (T) measurements. Below this temperature, the powder presents a coercive field of approximately 1000 Oe, with no significant variation with the temperature. Saturation occurs at fields below 0.5 T, which explains the equivalence between the M_s vs. T (**Figure II.21b**) and the M vs. T (**Figure II.20**) curves.

At the LTO and LTT phases, the powder presents a M_s of ≈ 56 emu g⁻¹ or 2.3 μ_B per formula unit (f.u.), and no difference in the magnetic behaviour is observed between the two phases. Along with the LTT-to-HTO transition, the M_s value falls to ≈ 43 emu g⁻¹ or 1.7 μ_B /f.u. and it becomes zero with the HTO-to-HTT transition.

If the magnetism of FVO magnetism were to be explained solely through the spin-only contribution of each individual species, an antiparallel alignment of Fe^{II} ($S = 2$, $\mu_{\text{spin-only}} = 4 \mu_B$) and V^{III} ($S = 1$, $\mu_{\text{spin-only}} = 2 \times 2 \mu_B = 4 \mu_B$) would result in a null net magnetic moment. Actually, V^{III} shows a non-quenched orbital momentum, and its net contribution to the overall magnetisation has been proved to be much smaller ($\approx 0.85 \mu_B$ at 4 K) [19]. Considering for Fe^{II} a spin-only scenario and for V^{III} a spin-orbit-coupling-affected moment, we can retrieve the the low-temperature value for $M_s = 4 - 2 \times 0.85 = 2.3 \mu_B$.

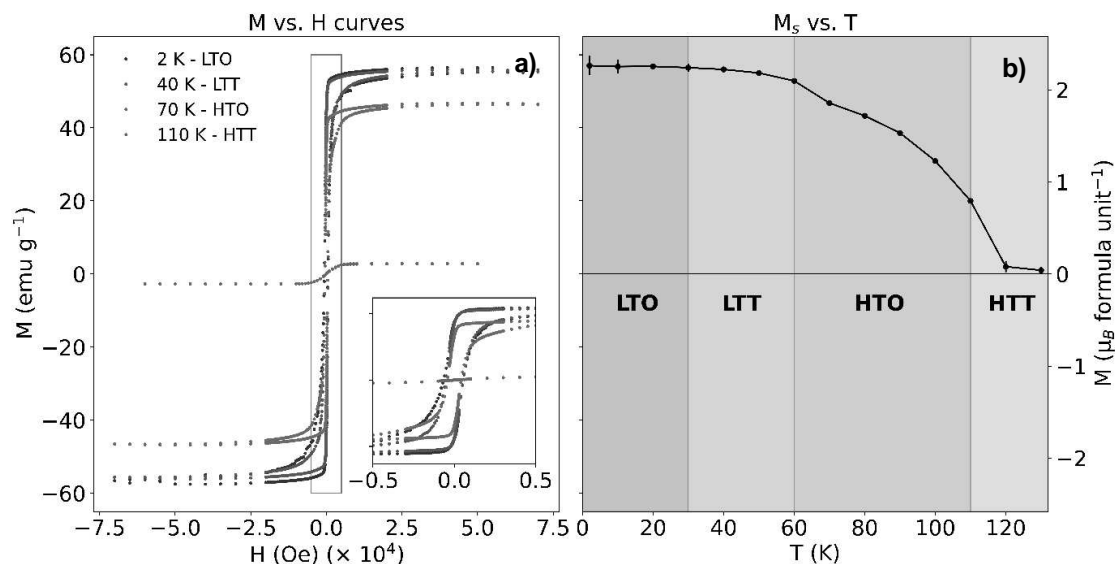


Figure II.21. (a) M vs. H curves for four different temperatures at the LTO, LTT, HTO and LTT phases. A zoom has been made at the range $[-5000 \text{ Oe}, +5000 \text{ Oe}]$. (b) M_s vs. T from 2 to 130 K. Both graphs have the same y-scale.

The difference between the M_s values in the LTO-LTT and HTO phases is due to the temperature-dependence of each cation's contribution and the transition from a non-collinear to a collinear magnetic state, increasing the opposition of V^{III} moments when the structure passes from a YK-structure of canted spins into a perfectly collinear one. The M_s variation with temperature is not enough to determine the contribution of each cationic species, or to quantify the spin canting in the noncollinear structure (since both phenomena vary at the same time). ND analysis would add the element sensitivity needed to determine the contribution of both Fe^{II} and V^{III}, and would help us determining the spin-canting in the LTO-LTT phases [19].

3.6. High-temperature measurements

The high-temperature stability of the spinel phase was studied at temperatures ranging from 20 to 1000°C via a thermogravimetric analysis (TGA) and differential scanning calorimetry (DSC) conducted under a N₂ atmosphere, as depicted in **Figure II.22**. TGA and DSC scans were carried out

simultaneously at a heating rate of 2°C/min. At the end of the experiment, the powder sample had converted into a black slurry which was completely stuck to the Pt sample holder, not allowing any verification of the final phase after the heating process.

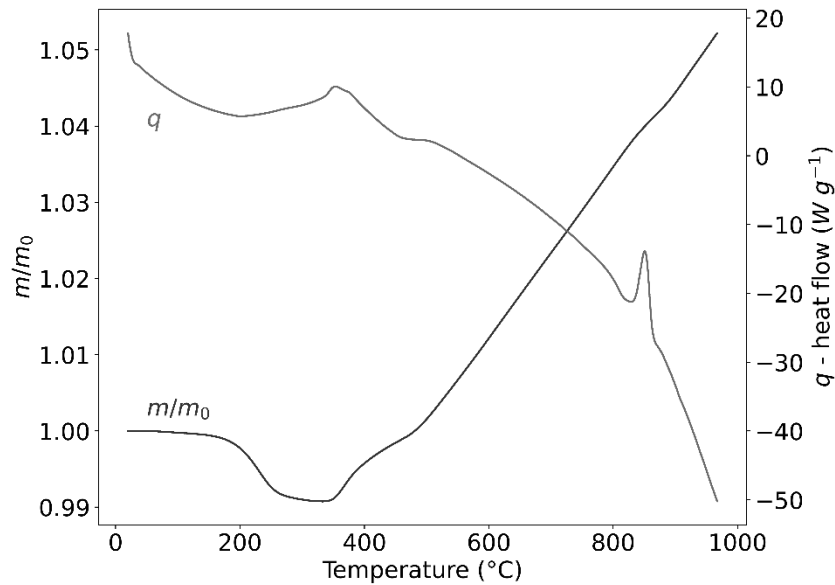


Figure II.22. Relative mass (blue) and heat flow (red) evolution as a function of temperature in the 30 to 1000°C temperature range.

FVO remains stable up to 200°C, a temperature at which a net mass loss occurs. The volatilisation of the cationic species at such low temperatures is improbable, so such mass loss might be attributed to the evaporation of some water absorbed or to an unknown chemical reaction. At around 400°C, the mass starts to increase, which indicates the oxidation of the cations. Since all the process takes place in an inert atmosphere, the origin of the oxygen input for the oxidation cannot come from ambient air.

Comparing the formula unit mass of FVO (221.73 g mol⁻¹) with that of the oxidised precursors V₂O₅ (181.88 g mol⁻¹) and Fe₂O₃ (159.69 g mol⁻¹), we observe that the oxidation of the cations within the spinel phase would result in a net mass gain of 18.0% (considering the mass of the solid material, since the total mass would naturally be conserved). This mass gain, however, is only around 5% for the TGA experiments at its topmost temperature. We can conclude that there is not a total oxidation of both cationic species and, despite getting out of the spinel structure, they do not reach their highest possible oxidation states. After the TGA + DSC experiments, the powder is transformed into a slurry which is completely stuck onto the measurement crucible, becoming irrecoverable for any further structural characterisation. This slurry must contain Fe and V in intermediate oxidation states, with the oxygen coming from residues from the N₂ itself. The formation of nitrogen-based compounds is also a plausible hypothesis, but impossible to verify. Conducting the same experiment under an oxygen or ambient gas atmosphere could enhance our understanding of the high-temperature stability of FVO's phase, but such an experiment might jeopardise the TGA/DSC equipment.

3.7. AC susceptibility measurements

A spin-glass-like state was announced in the material by Nishihara et al. [61] at $T_g = 85.5$ K but other groups have failed in reproducing this phenomenon in the material [29], [62]. Spin glass behaviour is a phenomenon observed in disordered magnetic materials, where the magnetic spins of atoms or ions are frozen in a random arrangement. This state is characterised by a lack of long-range order, competing interactions, and frustration among the magnetic moments, culminating in a highly complex energy landscape with numerous metastable states. [150], [151]

Alternative current (AC) magnetic susceptibility measurements are a way to detect spin glass states in materials. In these measurements, an alternating magnetic field is applied to the sample, and its response in terms of magnetic moment is measured. The response can be decomposed into two components: the in-phase (χ') and the out-of-phase (χ'') components. The in-phase component corresponds to the magnetic moment aligned with the applied field, whereas the out-of-phase component is related to the magnetic moment lagging behind the applied field due to the energy dissipation.

In the work by Nishihara et al., the authors performed AC magnetic susceptibility measurements at various frequencies (1000, 333, 100, 33, 10, 3, and 1 Hz) and temperatures (70 - 120 K) with an applied AC field of 3 Oe. They reported a maximum in the χ' component at 106 K at all frequencies. The maximum of the χ'' component, however, showed to be frequency dependent: from 98.3 K at 1 Hz to 104.7 K at 1000 Hz (a temperature shift of 6.5 K). These peak top temperatures were used to calculate the temperature variation of the relaxation time: $\tau = 1/2\pi\nu_{AC}$. The spin relaxation vs. temperature data at low frequencies was then fitted with the relationship shown in **Equation (II.8)**, where T_g is the spin-glass transition temperature, τ_0 is the spin flipping time and $z\nu$ is the dynamical exponent, which reflects the rapidness of the deviation from τ_0 [152], [153].

$$\frac{\tau}{\tau_0} = \left(\frac{T - T_g}{T_g} \right)^{-z\nu} \quad (\text{II.8})$$

The same measurements – same temperature and frequency range, for the same applied field – were repeated on the sintered FVO powder, as shown in **Figure II.23: a** for the real part and **b** for the imaginary part. The χ' maximum for all frequencies was measured at 104.2(1) K, close to the transition temperature identified by specific heat measurements (≈ 110 K). The shift of the χ'' maximum with frequency was less pronounced than Nishihara's: from 100.8 K at 3 Hz to 101.5 K at 1000 Hz (4.7 %).

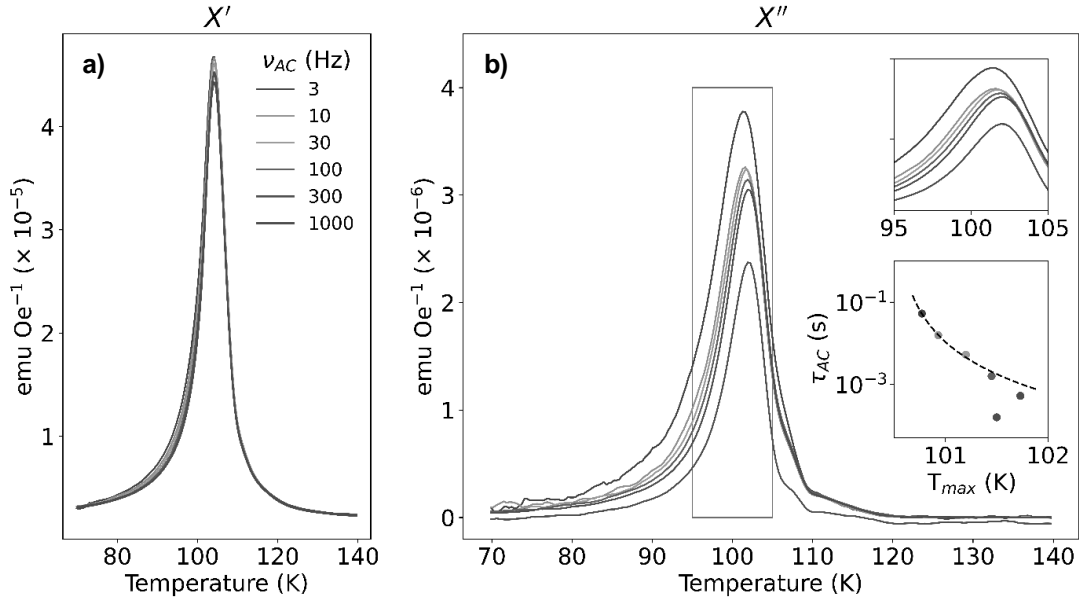


Figure II.23. (a) Real (χ') and (b) imaginary (χ'') parts of the magnetic susceptibility as a function of temperature for different magnetic field frequencies. A magnetic field of 3 Oe was applied for the measurements.

The low-frequency ($\nu_{AC} < 1000$ Hz) data was fitted with the model shown in **Equation (II.8)**, leading to a value for the spin-glass transition temperature $T_g = 100(1)$ K and $\tau_0 = 9.5(9) \times 10^{-7}$ s and $z\nu = 2.6(3)$ for the other parameters. These values are distinct from those reported by Nishihara et al.: $T_g = 85.5$ K, $\tau_0 = 6.32 \times 10^{-8}$ s and $z\nu = 7.82$. Besides, Nishihara's fits were performed at a second peak occurring at lower temperatures (around 80 K).

The presence of a spin-glass-like state in FVO cannot be confirmed; however, this constitutes the first report of temperature-varying χ'' maxima since Nishihara's work. Further experiments would be needed in order to unequivocally attribute these phenomena to a spin-glass behaviour. One possibility would be ND experiments, since in a spin glass the random magnetic momenta lead to a diffuse recognisable scattering pattern [154].

4. Results on FeV₂O₄ thin films

4.1. Optimisation of FeV₂O₄ thin-film deposition

All the FVO thin film depositions reported in the literature before the commencement of this PhD work [69]–[71], [76] used an oxygen atmosphere during the deposition. As previously mentioned, all these groups report an excess of iron on their films. Beside this out-of-stoichiometry, our group was unable to detect the spinel phase when growing the thin films with an oxygen atmosphere: the vanadium seemed to evacuate the FVO structure in the form of an oxidised V₂O₅ layer [77]. A first optimisation of the conditions using an inert (Ar) atmosphere had already taken place, with an optimal deposition at 400°C, with a fluence of 1 J cm⁻², a target-to-substrate distance of 5 cm and a repetition rate of 10 Hz. MgO substrates were chosen for this optimisation process, due to the small lattice mismatch between FVO and MgO ($\tau = -0.4\%$).

The optimisation process, however, was completely repeated. The existing FVO target was almost destroyed at the author's moment of arrival and the elaboration of a new target would necessarily imply to reoptimise (or at least adjust) the existing conditions. Secondly, the best conditions often matched with the limits of the varying parameter. For instance, only temperatures from 400°C to 600°C were tried, and the lower limit was found to be the best.

As a result, depositions at different conditions were again carried out to obtain the most crystalline spinel FVO phase. θ - 2θ scans were then carried out on the 004 reflection. The presence of a clear peak with defined Laue oscillations was used as an indicator of a correct FVO deposition, as it served as a criterion for the choice of the best optimisation conditions. Further characterisation would confirm the presence of the correct FVO phase in those films deposited with the optimised conditions.

FVO thin films were deposited at temperatures from 325°C to 525°C, at argon partial pressures from 0.001 to 0.1 mbar, laser fluences from 1.3 to 4 J cm⁻² and laser frequencies from 2 to 10 Hz. The θ - 2θ scans for each film can be seen in **Figure II.24**. The best conditions were found to be 400°C, 0.01 mbar, 4 J cm⁻² and 5 Hz.

The temperature was shown to have a large influence on the film's quality, as shown in **Figure II.24a**. The best temperature value (400°C) is of the same magnitude than that of other spinel compounds grown on PLD such as Fe₃O₄ (400°C) [155] and Mg_{1.5}FeTi_{0.5}O₄ (500°C) [156]. Lower temperatures (325°C) showed no oscillations in the XRD analysis. When slightly increasing the temperature (475°C), a crystalline spinel phase is also kept, but the films show worse quality when the temperature is increased beyond this threshold.

As showcased in **Figure II.24b**, the pressure also seemed to play a major role in the film's deposition, with a small pressure interval being able to lead to correct depositions. Tests were made with both an O₂ and an Ar atmosphere, and those with some O₂ pressure suggested the oxidation of V(III) into V(V)

and the formation of a V_2O_5 sublayer [77]. There can be a few reasons for the presence of such a narrow valid pressure window.

Firstly, the pressure can affect the dynamics of the plasma plume. When the pressure is higher, there are more gas molecules present and therefore, the ablated material can be scattered more by collisions with the gas atoms. This may lead to a more diffusive plume and potentially a less controlled and non-uniform deposition. Conversely, at very low pressures, the plume can become too directional, which can also affect the uniformity of the film [157].

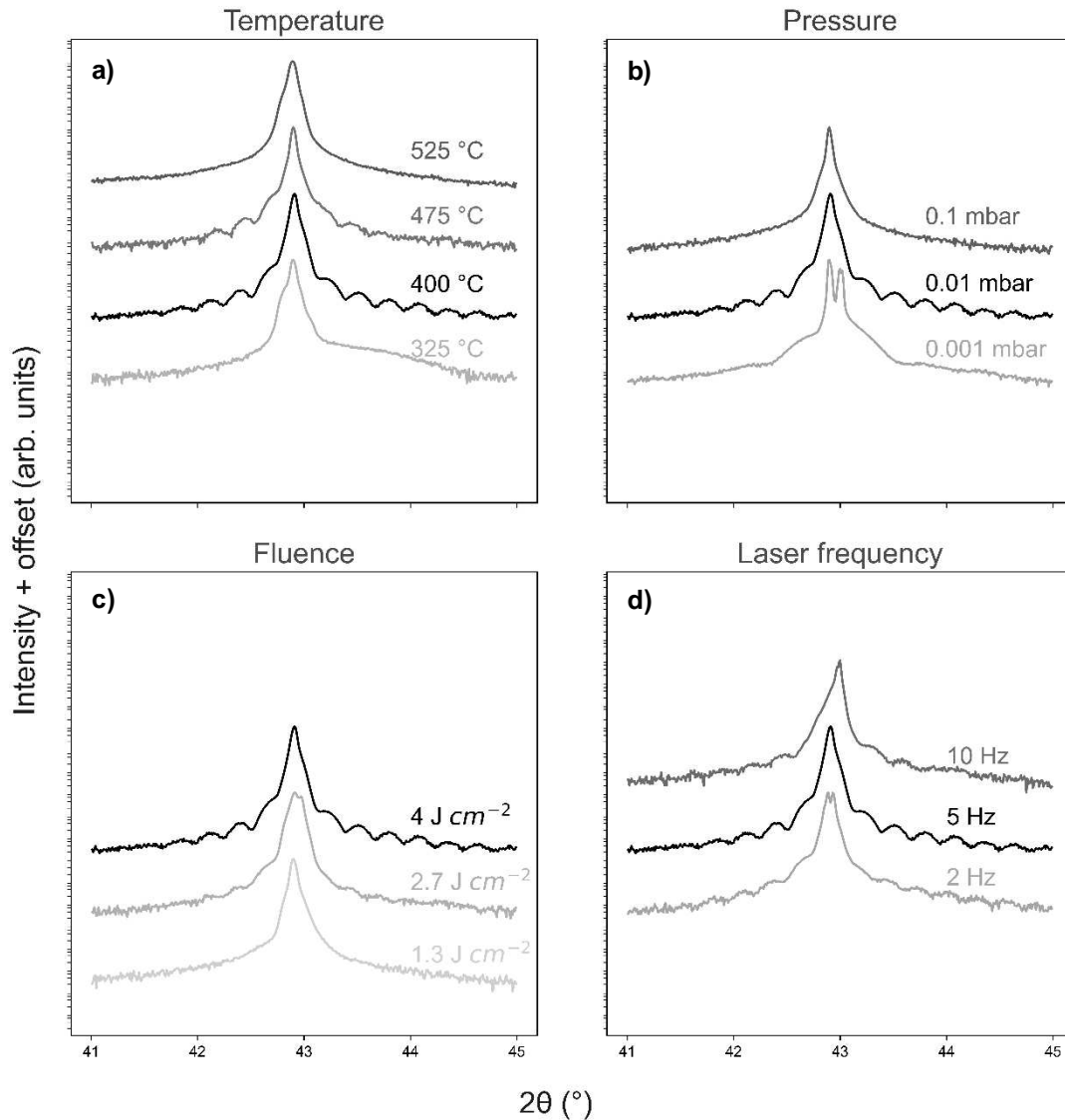


Figure II.24. θ - 2θ on the 004 peak for FVO//MgO films at different conditions. Each plot corresponds to different films in which all parameters are kept the same but the parameter which heads the plot: (a) temperature, (b) pressure, (c) laser fluence and (d) laser frequency. The film which presents the best crystallinity has been placed in the middle of the plot in black colour.

Secondly, the deposition pressure can have an influence on the energy of the deposited particles. Higher pressures can lead to more collisions, which can lower the energy of the arriving particles. This, in turn, can influence the growth and quality of the film. At lower pressures, there might not be enough collisions to lower the energy of the arriving particles, which could result in a non-uniform film or one with undesirable properties [158].

In terms of the laser fluence, the permitted interval was however wider, as **Figure II.24c** displays. Higher fluence values seemed to improve the films' quality and, as a result, the highest stable fluence value (4 J cm⁻²) was chosen. The fluence value was drastically changed from the preoptimised fluence value: the film's quality at such energy was far from ideal.

Finally, as showed in **Figure II.24d**, the laser frequency showed not to play a large part in the film's quality, and an intermediate value of 5 Hz was chosen.

4.2. X-ray reflectivity results

Using the optimised conditions, depositions at different number of hits (n_h) were carried out and each film was analysed through XRR. The data was fitted using the reflectivity tools provided by *xrayutilities*, as shown in **Figure II.25a**. As expected, and as displayed in **Figure II.25b**, the films' thicknesses linearly increase with the number of hits with a rate of 1 nm per 130(5) hits – or 7.7(3) nm for every 1000 hits.

The fit of the XRR oscillations also enabled the characterisation of some physical properties in the thin films, as described its dedicated section: “X-ray reflectivity (XRR)” – page 37. For the 35 nm FVO thin film, the XRR fit gave a thickness of 35.12(5) nm, a density of 4.89(7) g cm⁻³ and a roughness of 0.399(6) nm. Apart from the thickness, the fitted values did not vary much with an increase in the number of hits. The density is close to the theoretical value for the bulk 4.833 g cm⁻³, and the compressive strain due to the substrate constraint justifies a small increase compared to the bulk density value.

Using the optimised conditions as a starting point, various conditions were tried on FVO films deposited onto STO substrates. The same conditions were found for FVO//STO films, so we could conclude that the substrate choice does not have a significant influence in the deposition conditions. The XRR experimental results and fit for a 60 nm-thick film are shown in **Figure II.26**.

The XRR best fit corresponds to a film of 61.67(9) nm, density of 4.88(2) g cm⁻³ and a surface roughness of 0.27(9) nm. The density value is close to the one of MgO films and also corresponds to the scenario of a net lattice shrinking due to the substrate's compressive strain. The surface roughness is lower and matches with the best surface state of the STO substrates compared to MgO. The relationship between the thickness and the number of hits (not shown here) is also respected by films deposited onto STO substrates.

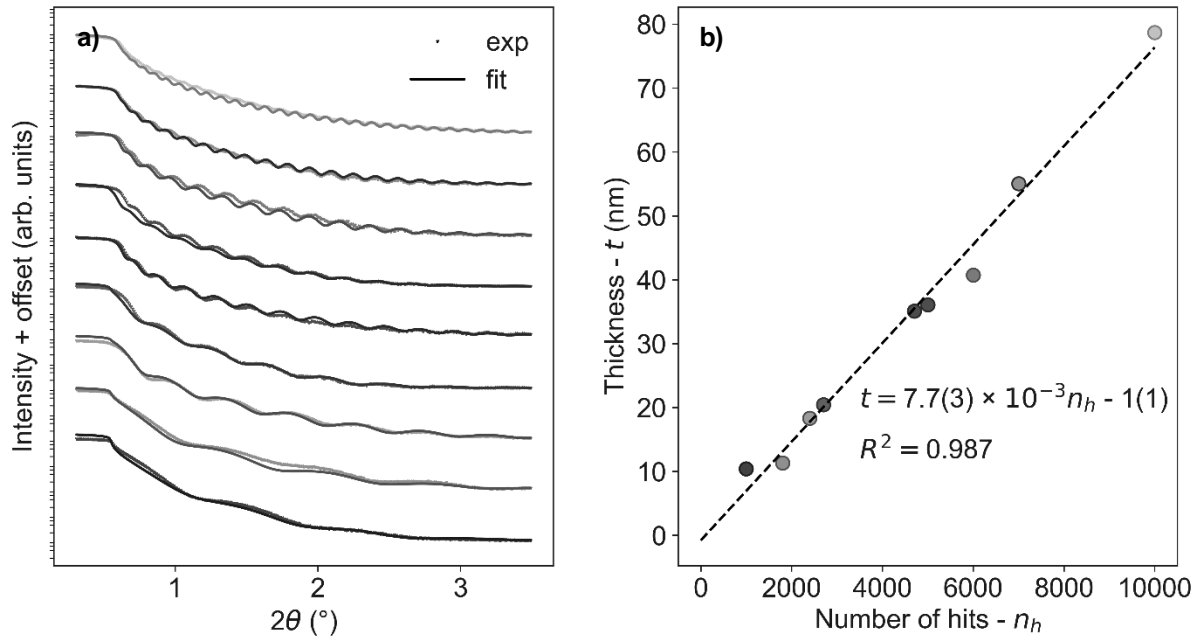


Figure II.25. (a) experimental (dotted) XRR curves and fits (solid lines) for FVO//MgO films of increasing thicknesses. (b) relationship between the number of hits for the PLD deposition and the XRR fitted thicknesses. Each of the XRR curves of the left correspond to a solid dot on the right – same colour code.

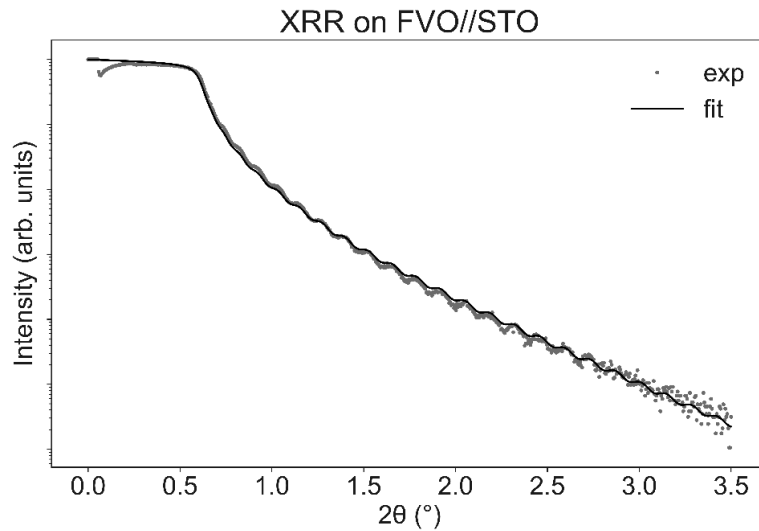


Figure II.26. XRR results for a 35 nm-thick film of FVO onto a STO substrate. Experimental results are shown in red dots, and the best XRR fit as a solid black line.

4.3. Scanning electron microscopy

As shown in **Figure II.27**, SEM images were acquired on FVO//MgO (**a**) and FVO//STO (**b**) films deposited with the optimal conditions. The images display a smooth and uniform surface, where a few micron-sized 3D objects are present. While the majority of the surface lacks these distinctive features, specific areas with defects were intentionally selected where these objects are present to facilitate the surface alignment process.

These micron-sized objects can originate from two sources. Firstly, they may result from ambient air pollution, where dust particles adhere to the surface after the deposition and during all the different characterisations. Secondly, the objects can be attributed to a splashing phenomenon in PLD, where small fragments or material chunks from the PLD target are forcefully ejected and land on the surface. Since the AFM measurements does show a smooth surface, the presence of these relief features is considered to be anecdotal.

Regarding the stoichiometry of the film via an EDS elemental analysis, the FVO//MgO thin films exhibited a V/Fe ratio of 1.9(3), whereas the FVO//STO thin films showed a ratio of 2.1(4). These stoichiometry values are consistent with the bulk value of 1.97(7) and are in close proximity to the expected ratio of 2 for FVO. However, it is worth noting that the films displayed a wider range of ratio distribution compared to the bulk material, resulting in less precise statistics and larger margin of error for these stoichiometry measurements.

Nonetheless, the results indicate that there has been a transfer of stoichiometric mass between the bulk target and the thin films and they confirm that our FVO thin films have the desired V/Fe ratio.

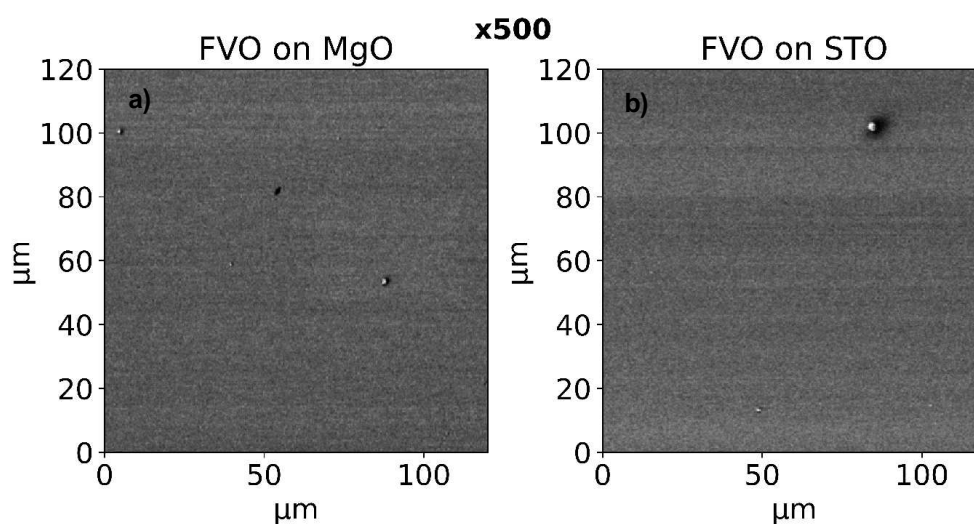


Figure II.27. SEM images on FVO//MgO (**a**) and FVO//STO (**b**) thin films after deposition with x500 magnification. Zones with relief features were deliberately chosen for an easier sample alignment.

4.4. RHEED pattern analysis

The RHEED pattern before deposition consisted of a series of bright spots arranged in streaks, attributable to the single-crystal-like nature substrates before deposition. As it can be observed in **Figure II.28**, this pattern is better observed in MgO (**a**) substrates than in STO (**c**). The RHEED images display the so-called “Kikuchi lines”, a pattern observed in electron diffraction caused by incoherent scattering of incident electrons due to thermal vibrations in a crystal [159], [160]. Since the electron-diffraction Kikuchi lines can be associated with specific planes in the material, their positioning and orientation can provide valuable insight into the crystal's orientation and assist in attributing the diffracted spots to reflections in the reciprocal space [161].

Additionally, the sole presence of this diffraction phenomenon is an indicator about the superior quality of the crystal surface. In well-ordered crystals, the Kikuchi lines are more defined and sharper. If the crystal exhibits defects or is less well-ordered, the lines will appear less distinct and more diffuse [162]. In conclusion, the RHEED pattern showed that the MgO and STO substrates presented a smooth and crystalline surface state.

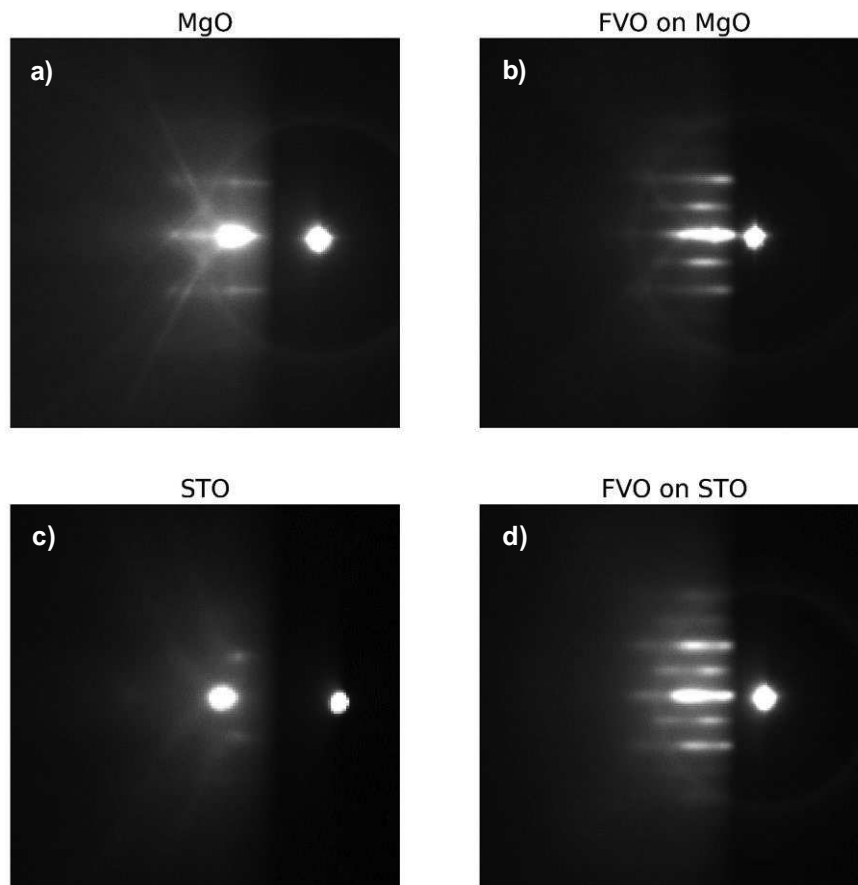


Figure II.28. RHEED pattern before and after deposition: MgO (**a/b**), STO (**c/d**). The “before” image corresponds to the archetypical image of a single-crystal RHEED pattern, whereas the “after” image corresponds to a 2D smooth film.

The RHEED pattern after deposition onto MgO (**Figure II.28b**) consisted of rod-shaped spots which, as previously explained, is associated to a 2D smooth surface. No oscillations were recorded in the follow-up of the spot intensities during the deposition process, and layer-by-layer growth was not detected *in situ*. However, the elongated shape of the nodes and the presence of the Kikuchi lines indicates both a good surface state and a correct crystallinity inside the material.

Regarding the deposition onto the STO substrate (**Figure II.28d**), the RHEED pattern reveals a combination of rod-shaped and single-spot patterns. This suggests that the FVO//STO films stay in between a complete total morphology and a 3D-island one. The unidirectional rod-shaped nodes are still visible, confirming the “2D-ness” of the films. The Kikuchi lines are much fainter than on FVO//MgO, but they were not highly visible either in the substrate prior to the deposition.

4.5. AFM results

The topography of the films was studied through AFM measurements, as shown in **Figure II.29**. $5 \times 5 \mu\text{m}^2$ square surfaces were imaged in non-contact mode before deposition (only MgO – **a**, or STO – **c**) and after deposition (FVO//MgO – **b**, and FVO//STO – **d**).

Roughness values were obtained after a region analysis study on different zones of the samples: $R_{q,MgO} = 0.21(3)$ nm and $R_{q,FVO//MgO} = 0.23(4)$ nm for FVO//MgO and after deposition; $R_{q,STO} = 0.12(3)$ nm and $R_{q,FVO//STO} = 0.15(4)$ for FVO//STO films.

The AFM images show a relatively smooth surface for both the substrate and the thin film. MgO and FVO//MgO do not present a step-terrace-like pattern, but STO substrates and FVO//STO films do have such atomically smooth pattern. The roughness value for the films after deposition obtained through topographical region analysis shows some discrepancy with the value obtained via XRR (page 65). The reasons behind the differences largely stem from the inherent differences in the methodologies of the two techniques. XRR uses a large X-ray beam that covers an area of a few square millimeters on the sample, capturing a macroscopic perspective of the surface. In contrast, AFM probes a much smaller, localised area, providing a more microscopic perspective. This disparity in the sampled area can lead to variations in the measured roughness, with AFM often revealing a smoother surface, owing to the convolution of the AFM tip shape and the short wavelength of the probing X-rays. Finally, XRR can probe buried interfaces beneath the top surface layer, which is beyond the reach of AFM [163].

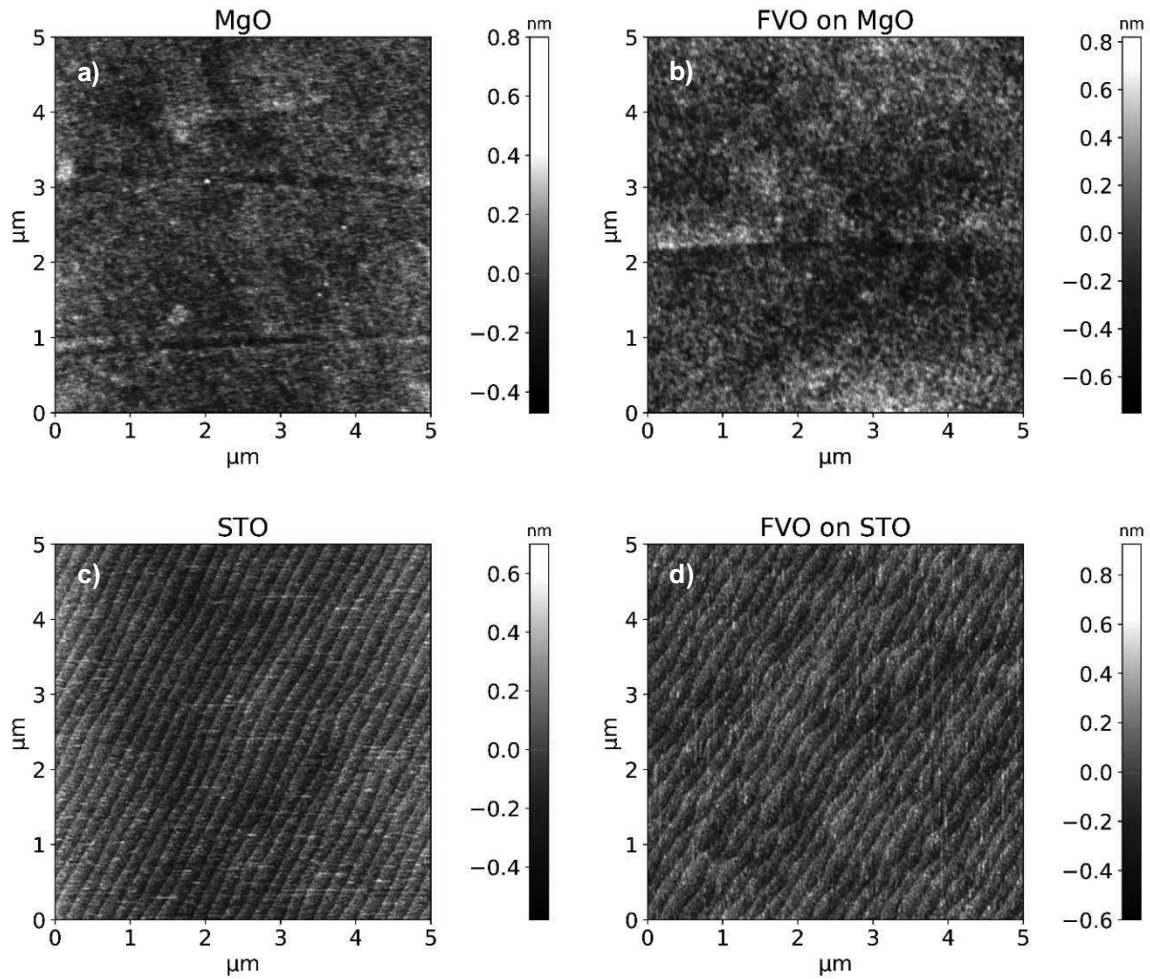


Figure II.29. Topography images of $5 \times 5 \mu\text{m}^2$ size before deposition on MgO (a) and STO (c) substrates, and on FVO//MgO (b) and FVO//STO (d) films after deposition.

4.6. The structural characterisation of thin films

4.6.1. $\theta/2\theta$ scans

The $00l$ reflections have been investigated using $\theta/2\theta$ scans for 40 nm-thick FVO films. For the FVO//MgO films (XRR thickness = 39.2(1) nm), as depicted in **Figure II.30**, the 004 and 008 reflections of FVO show at very close angular values to the 004 reflections of MgO. The substrate presents a signature of a sharp peak, whereas the FVO film presents a broad pattern of oscillating Laue fringes, which suggests a good material crystallinity. The intensity profile has been fitted using the layer module of *xrayutilities*, and the refined curves clearly match the experimental ones. The fit of the oscillations yielded a sample thickness of 38.7(2) nm – close to the XRR value – and an out-of-plane lattice parameter of $c = 8.453(1) \text{ \AA}$.

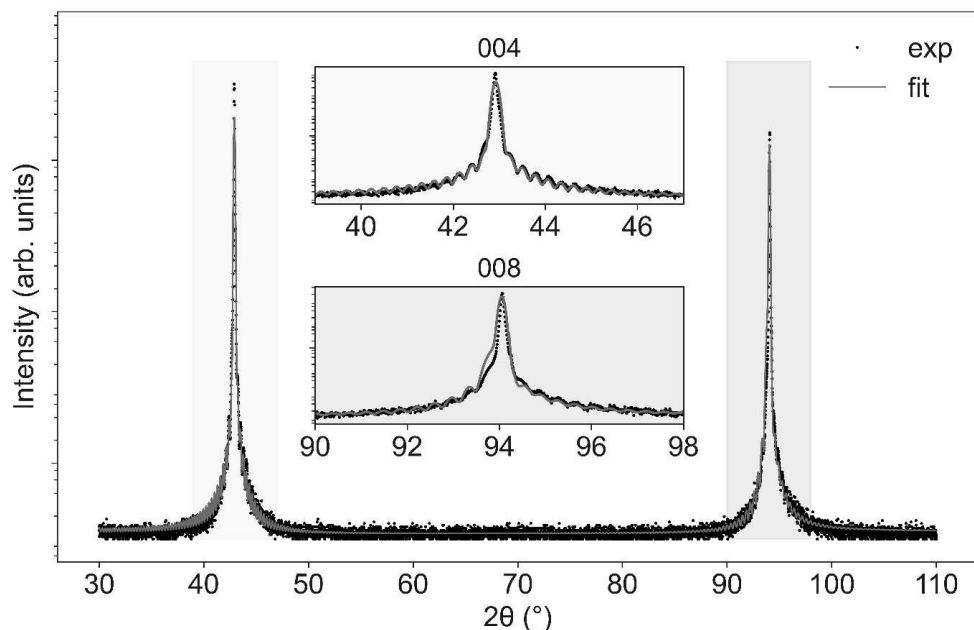


Figure II.30. $\theta/2\theta$ diffractograms for FVO//MgO thin films for a 2θ range of 30 – 100° with the experimental data (black) and the *xrayutilities* best fit (red). Zooms have been made in the ranges [39°, 47°] and [90°, 96°] for the better observation of the 004 and 008 reflections on FVO, respectively.

A thickness-dependance study has been conducted to study the evolution of the out-of-plane parameter with the thickness. Ultrathin films did not exhibit an intensity profile with sufficient intensity to be fitted, and the oscillations above 60 nm were too small to make any refinement. In those thickness values with exploitable data, no consistent trend was observed, so the results will not be hereby presented.

The same procedure has been carried out on FVO//STO films with a XRR thickness of 39.6(1) nm, as shown in **Figure II.31**. Remarkable differences can be seen from the FVO//MgO diffractogram. First, there is a clear substrate-film peak separation, indicating a larger disparity in their out-of-plane lattice parameters. Secondly, the film's pattern does not show a fringe-like pattern. The absence of Laue oscillations was also reported on previous works on FVO(001)//STO(001) [70], [71] and FVO(110)//STO(110) [69] thin films.

This disparity with MgO depositions comes from the difference in lattice mismatches between the two substrates: $\tau_{MgO} = -0.4\%$ and $\tau_{STO} = -8.2\%$. The significant lattice mismatch between FVO and STO compromises the structural integrity of FVO films. As a result, relaxation in FVO//STO starts at much thinner layers than on FVO//MgO. Misfit dislocation is expected for FVO grown on STO, which results in a more significant crystal mosaicity. Several crystal domains would be diffracting under Bragg diffraction conditions, but their diffracted waves might interfere destructively with each other and suppress the oscillations. Analogous observations have been documented and explained in large-mismatch Fe//MgO films [164].

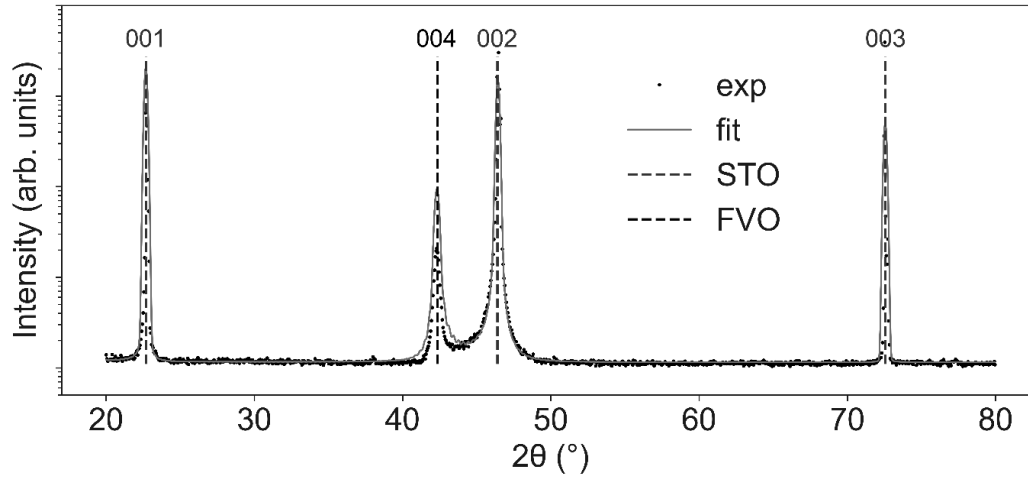


Figure II.31. $\theta/2\theta$ diffractograms for FVO//STO thin films for a 2θ range of 20 – 80° with the experimental data (black) and the *xrayutilities* best fit. The fitted positions for FVO reflections have been indicated in black dashed lines, and for STO reflections in blue.

These discrepancy between FVO//MgO and FVO//STO films also shows in the aforementioned RHEED results – page 67, where the film relaxation and mosaicity in STO manifests as a more 3D-island-like pattern than on MgO. Nevertheless, and as seen in the AFM results, a worse crystallinity does not translate into a worse surface state and the substrate’s good initial roughness is inherited by the thin film.

The absence of fringes hindered any fit of the film’s thickness, but the peak’s position yielded an out-of-plane lattice parameter of $c = 8.50(1)$ Å, close to the values found in the literature by Shi et al. ($c \approx 8.52$ Å) [71] and by Zhou et al. ($c = 8.50$ Å – no error given) [70]. The small differences might arise from the out-of-stoichiometry state of their films.

The same $\theta/2\theta$ scans were conducted in the d2am line of the European Synchrotron Research Facility (ESRF), as shown in **Figure II.32** for both FVO//MgO (a) and FVO//STO (b). The diffractograms were acquired at X-ray wavelength of 1.74331 Å, in contrast to the previously used wavelength of 1.54056 Å. The high intensity of the synchrotron radiation significantly improved the resolution of the diffractograms.

Similar to the measurements acquired with a laboratory diffractometer, the Laue-fringe pattern only appeared for the FVO//MgO film. The oscillation fit led to a film thickness of 39.05(2) nm, close to the previously found value of 38.7(2) nm but closer to the thickness obtained via XRR – 39.2(1) nm. The fit of the peak position resulted in the out-of-plane lattice parameters $c = 8.4525(2)$ Å for FVO//MgO and $c = 8.505(1)$ Å for FVO//STO, which are consistent to the previously found values of 8.453(1) Å and 8.50(1) Å, respectively. In both measurements, the presence of a fringe-profile facilitated the peak position (as the centre of the oscillations), and that explains the better accuracy for the c value on FVO//MgO. A

high-resolution thickness-dependent analysis would be worth conducting if the time and resources allowed such a study.

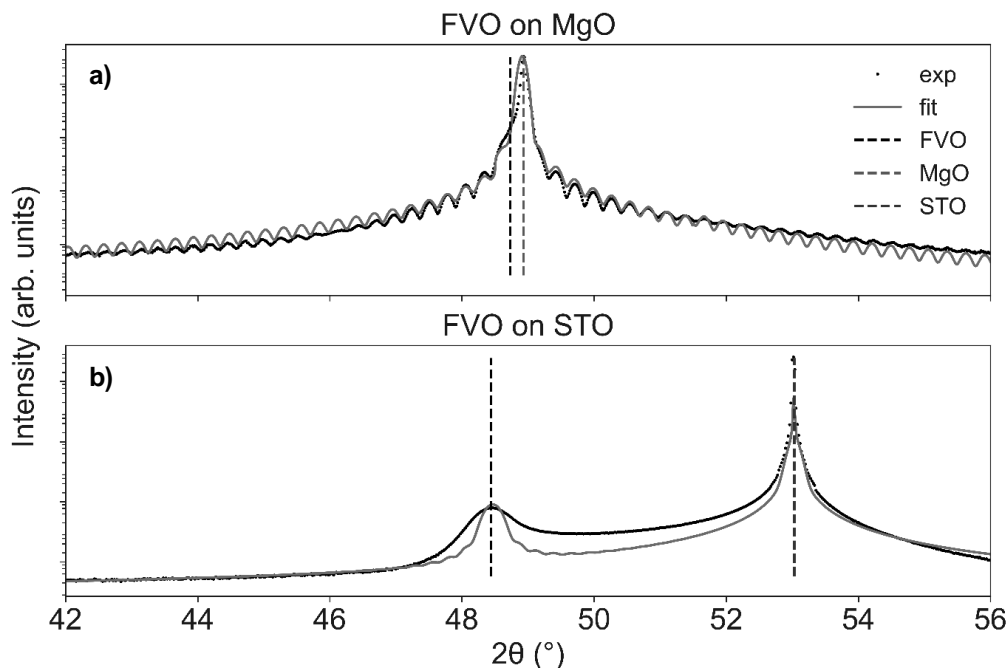


Figure II.32. $\theta/2\theta$ diffractograms for FVO//MgO (a) and FVO//STO (b) acquired at the d2am line of the ESRF. The black dots represent the experimental diffractograms, and the red solid line the best fit. The centre of the peaks of FVO(004) has been indicated in black dashed lines for both films, whereas MgO(002) and STO(002) peaks have been indicated with a green and blue dashed lines, respectively.

4.6.2. ϕ scans

ϕ scans were carried out on FVO//MgO and FVO//STO films. The reflections 024 and 013 were chosen for MgO and STO, respectively, due to their high intensities. For FVO, the reflection 026 was chosen for FVO//MgO films since 013 (its equivalent for MgO) is not allowed by the F crystal symmetry; and 448 was chosen for FVO//STO films because of its high intensity. ϕ was chosen so that $\phi = 0$ corresponds to the film's edge direction, also aligning with one of the in-plane lattice directions. As shown in **Figure II.33 – a** for FVO//MgO, **b** for FVO//STO, four peaks appear in each of the angular scans, confirming the expected presence of the equivalent reflections.

Peaks for 024 (for MgO), 026 (for FVO on MgO) and 013 (for STO) reflections appear at ($\phi = 90 \times n$, $n \in \mathbb{Z}$) degrees, and peaks for 448 reflections (FVO on STO) appear at ($\phi = 45 + 90 \times n$, $n \in \mathbb{Z}$) degrees. The films' reflections and the substrates' appear at consistent angular differences. This proves the crystallographic coherence between the substrate's structure and the films' and, in other words, the films' epitaxial state.

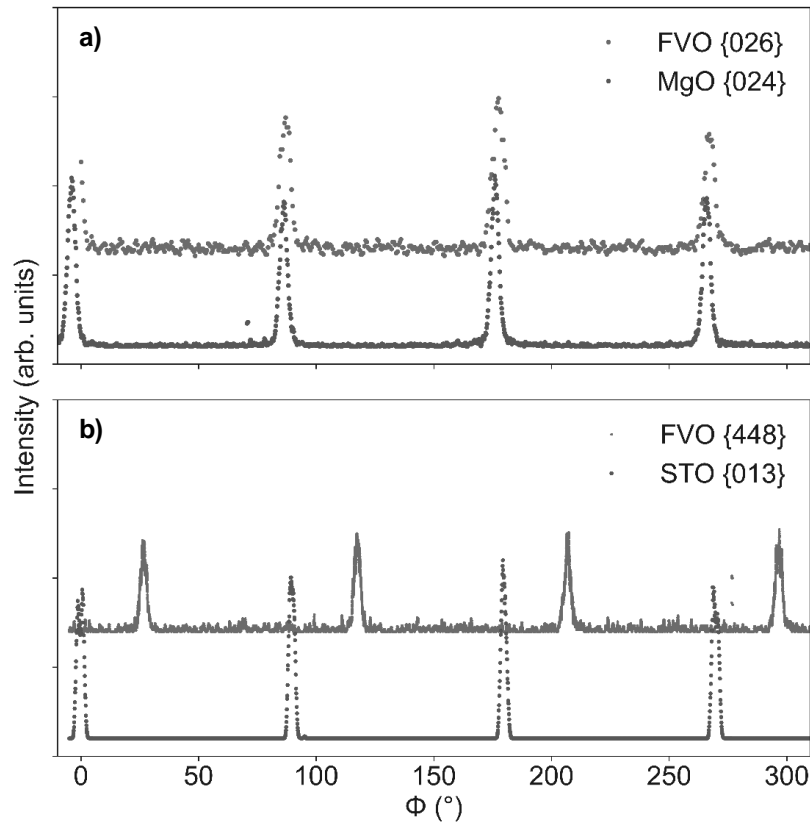


Figure II.33. (a) ϕ scans on FVO//MgO films on the 024 peak of MgO and the 026 reflection of FVO. (b) ϕ scans on FVO//STO films on the 013 reflection for STO and the 448 reflection for FVO.

4.6.3. Reciprocal Space Mapping (RSM)

2D-cuts of the reciprocal space have been made on the FVO films, as previously explained in the description of the RSM technique – page 42. The same reflection choice has been made for RSM and ϕ scans. The results hereby shown correspond to 40 nm-thick films, and small variations were observed with changing thicknesses. Nonetheless, no regular or significant trends in the lattice parameters were observed with varying thicknesses.

On FVO//MgO films, and as shown in **Figure II.34**, the 206 and 026 reflections can be clearly distinguished, confirming again the attainment of a crystalline spinel phase. Gauss fits around the peaks position led to lattice parameters of $a = 8.427(4)$ Å, $b = 8.425(5)$ Å and $c = 8.451(1)$ Å. The value for the lattice parameter matches the one obtained by $\theta/2\theta$ analysis: $8.4525(2)$ Å. Taking into account the uncertainty, the two in-plane lattice parameters can be considered to be equal, which is supported by the fact that the 206 and 026 reflections were shown to be perfectly equivalent in ϕ scans. The equivalence of the a and b parameters is also anticipated by the epitaxial deposition onto a cubic substrate. The crystal structure is therefore tetragonal.

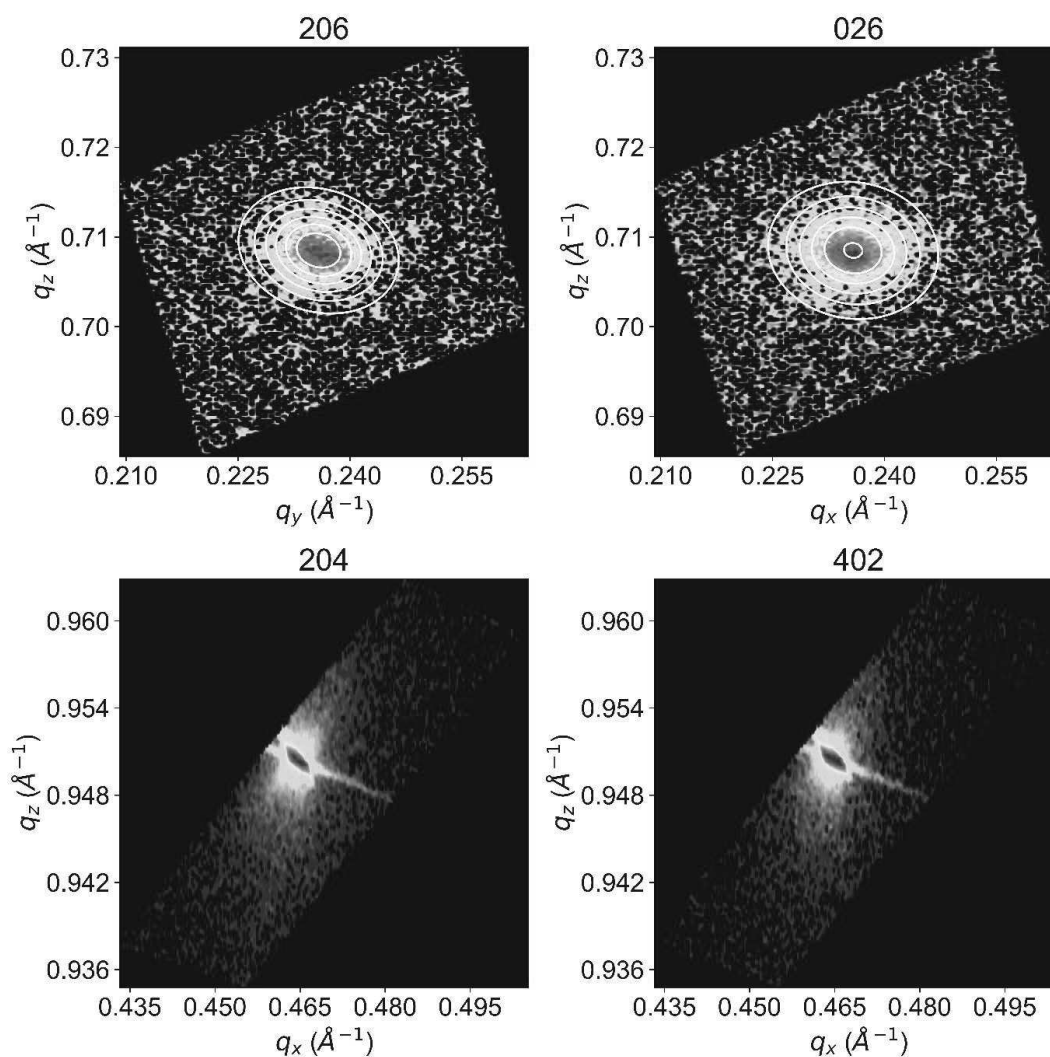


Figure II.34. RSM results for FVO//MgO films. Top: 2D-RSM conducted in two {206} reflections for FVO. Bottom: 2D-RSM at the {204} reflections of MgO, showing the contributions of both the substrate and the film material.

The lattice tetragonalisation is caused by the substrate, from a cubic structure in the bulk, the thin film becomes tetragonal with c being $\approx 0.28\%$ larger than a . The value for the in-plane lattice parameters is virtually the same as twice that of MgO: $2 \times 4.4212 = 8.4224 \text{ \AA}$. This suggests that there is a perfect accommodation of one unit cell of FVO onto four unit cells of MgO, as depicted in the section “FeV₂O₄ thin films” of **Chapter I** – page 22. The analysis of the {048} reflections (024 reflections for MgO, as marked in the graph), shows both the peaks of the film and the substrate. MgO’s intensity eclipses FVO’s due to the lattice parameter proximity, and no fit of the peak centre could be conducted. However, the distinct rod-like peak shape is a proof of the strained nature of the FVO//MgO thin films [165]. On FVO//STO films the {448} reflections were analysed, as illustrated in **Figure II.35**. The sole peak presence confirms the correct crystal phase. However, the peak intensity was not as bright, and four reflections were measured for the determination of the in-plane lattice parameters.

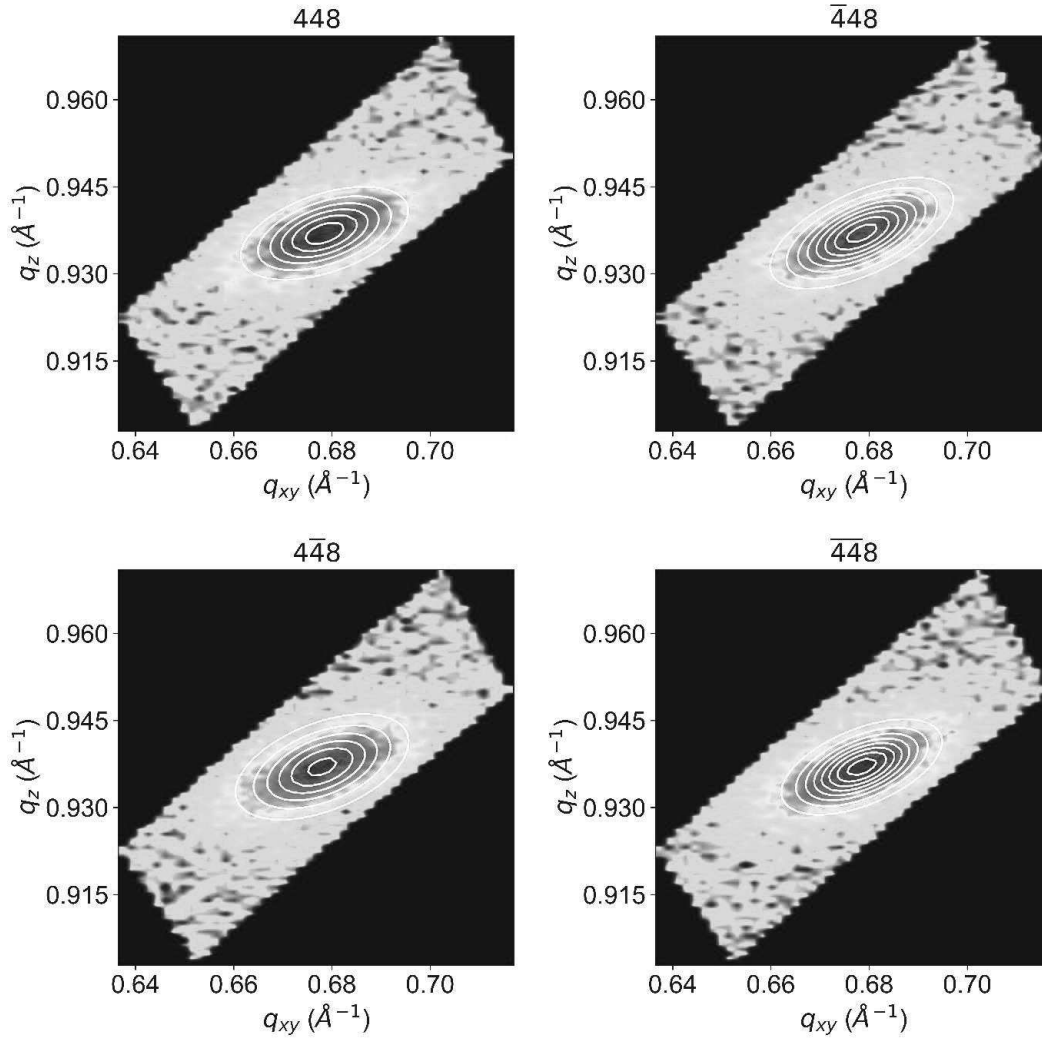


Figure II.35. 2D-RSM images on the {448} reflections of FVO//STO films.

The choice of reflections makes that the “parallel” reciprocal space component is a linear combination of the two in-plane reciprocal space vectors: $q_{||} = q_x + q_y$. The found in-plane lattice parameters were $a = b = 8.356(7)$ Å and the out-of-plane parameter $8.520(2)$ Å, close to the $\theta/2\theta$ value $8.505(1)$ Å.

In FVO//STO the structure tetragonalisation is even more accentuated than on FVO//MgO, with $c \approx 1.8\%$ larger than a . The lattice shrinking due to the substrate compressive strain is more significant, but this compression does not reach the fully strained state in the system, since the four-fold STO base would have in-plane lattice dimensions of $2 \times 3.905 = 7.810$ Å. This suggests that the substrate exerts a compressive strain on the film but it is not able to accommodate the strained structure. Due to the disparity in lattice parameters, no RSM capturing both the film and the substrate simultaneously was acquired.

The structural information for both thin film systems FVO//MgO and FVO//STO has been summed up in **Table II.1**. A tetragonality factor $f_{tetra} = (c - a)/a$ (%) describing the “out-of-cubic” state of the film has been included alongside the in-plane and out-of-plane lattice parameters. The previously defined lattice mismatches (τ) have also been included. In addition, the effective Poisson ratio (ν^*) has been calculated for both structures, whose calculation for epitaxial thin films with biaxial (symmetric) in-plane stress is described in **Equation (II.9)**. Its value depends on ν , the Poisson coefficient $\nu = -\epsilon_t/\epsilon_l$ which is the ratio between the strain in the transverse ($\epsilon_t = (c_{film} - a_{bulk})/a_{bulk}$) and the longitudinal ($\epsilon_l = (a_{film} - a_{bulk})/a_{bulk}$) directions [166], [167].

$$\nu^* = \frac{2\nu}{1 - \nu} \quad (\text{II.9})$$

Table II.1. Structural compendium for the FVO//MgO and FVO//STO systems compared to the bulk powder. Values for the in-plane lattice parameter have been obtained by RSM, for the out-of-plane lattice parameter via $\theta/2\theta$ scans and for the bulk values through powder-XRD. Theoretical lattice parameters have been used for the lattice mismatch values, and experimental for the rest.

	FVO//MgO	FVO//STO	Bulk
$a = b$ (Å)	8.426(4)	8.356(7)	8.4575(1)
c (Å)	8.4525(2)	8.505(1)	
V (Å ³)	597.2(1)	592.3(1)	603.22(2)
τ (%)	- 0.4	- 8.2	-
f_{tetra} (%)	0.31(2)	1.79(1)	0
ν^*	- 0.27(7)	1.7(1)	0

The deposition of FVO onto both STO and MgO substrates resulted in a shrinking of the total lattice volume: $\approx 2.0\%$ for FVO//STO and $\approx 0.8\%$ compared to the bulk target. This observation can be attributed to the compressive strain effects of both substrates and explains the difference between MgO and STO depositions and is supported by the significant tetragonality of both systems. This lattice shrinking leads to smaller interatomic distances, which will later be used to elucidate the differences in magnetic and transport properties between the films and the bulk, and also between both FVO//MgO and FVO//STO thin film systems.

The effective Poisson coefficient ν^* describes the structural response to the strain effects caused by the substrate on the thin film material. For compressive strains, an in-plane strain usually leads to an out-of-plane lattice extension in order to relax the cell structure. Such is the case of FVO//STO, when the lattice parameters are compared to the bulk: $a_{FVO//STO} < a_{bulk}$ and $c_{FVO//STO} > a_{bulk}$, and it reflects in a positive Poisson ratio.

In FVO//MgO, however, we have evidenced a simultaneous lattice compression in both the in-plane and out-of-plane directions: $a_{FVO//MgO} < a_{bulk}$ and $c_{FVO//MgO} < a_{bulk}$. This unique lattice behaviour gives rise to a negative value for the effective Poisson coefficient ν^* , leading to an unconventional mechanical response known as "auxetic" behaviour. Unlike the conventional materials that expand in one direction when compressed in another, auxetic materials exhibit a counterintuitive phenomenon where they expand in both directions when subjected to compression. Auxetism in oxide materials is rare but it has also been reported in other spinel thin film systems like CoFe₂O₄//MgO [168] and NiFe₂O₄//STO [169]. To our knowledge, FVO//MgO is the only documented auxetic vanadate thin film system so far.

4.7. Magnetic properties of FeV₂O₄ thin films

4.7.1. Magnetism as a function of temperature

The magnetic properties of the films as a function of temperature (T) were studied by measuring the magnetic response (magnetisation, M) under the application of a magnetic field (H) of 5000 Oe from 300 K to 2 K – FC mode in a SQUID setup. The results are depicted in **Figure II.36**. The data correspond to 40 nm-thick FVO films on STO and MgO, and are accompanied by the M vs. T curve for bulk FVO.

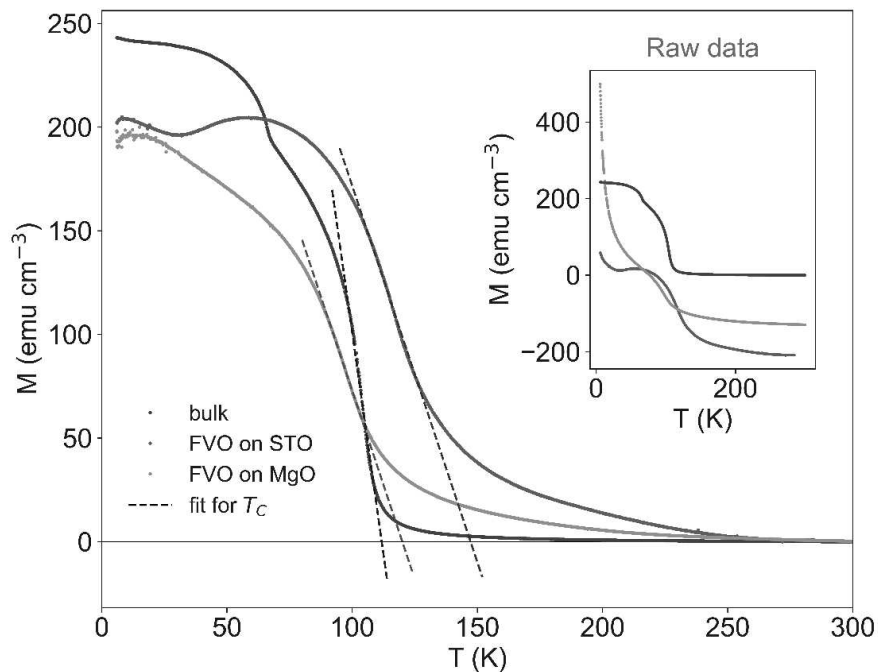


Figure II.36. M vs. T in the temperature range 2 – 300 K in FC mode, under $H = 5000$ Oe. On the right, the raw data has been plotted, whereas the main plot corresponds to data with a paramagnetic correction. Linear fits for the transition temperature are indicated by dashed lines, whereas the dotted plots represent the experimental values: blue for bulk FVO, red for FVO//STO and orange for FVO//MgO.

Magnetisation values have been normalised with the sample's volumes. The films presented a significant paramagnetic behaviour, as it can be seen in the upper right plot of **Figure II.36**, which is more remarkable for FVO//MgO films than for FVO//STO films, and which comes solely from the substrates. Besides, both substrates showed a diamagnetic component which results in a negative displacement of the M vs. T curve.

Raw magnetisation curves were fitted using a modified version of Curie's law $\chi = -d + C/T$ in the paramagnetic temperature domain ($T > 200$ K), with d being the strength diamagnetic contribution (constant with temperature) and C quantifying the paramagnetic part. Corrected magnetisation curves take this paramagnetic contribution away and lead to the curves in the figure's main plot. The correction is not perfect, and a small paramagnetic bump is left in the low-temperature range – more notorious for FVO//STO. After correction, the curves present the profile of a ferr(i/o)magnetic material which becomes paramagnetic at a certain temperature. Differently to the bulk material, a single magnetic transition is observed at T_C (T_{N1} for bulk FVO). The magnetisation per volume value is also smaller for the films, which suggests a collinear ferrimagnetic ordering in the low-temperature magnetic structure of FVO films. More advanced studies (e.g. XMCD) could be conducted in order to unveil the magnetic structure of the films.

Linear fits have been conducted in the temperature realm around which a curvature change occurs in the M vs. T data, and the T_C values have been obtained by intersection with $M = 0$. The transition temperatures suffer a significant shift compared to the powder sample: from 111.8(1) K in bulk FVO, to 120.1(6) K in FVO//MgO and 147.5(7) K in FVO//STO for the 40 nm-thick films. With the deposition onto a substrate with a smaller lattice parameter, FVO's lattice shrinks, and the interatomic distances decrease. This enhances the orbital overlapping, increasing the magnetic exchanges between the different magnetic species and allowing the system conserving this magnetic ordering until a higher temperature value [49], [170]. This explains why the transition temperature of FVO//STO ($V \approx 593 \text{ \AA}^3$) is higher than that of FVO//MgO films ($V \approx 600 \text{ \AA}^3$), and why these two values exceed the bulk's ($V \approx 605 \text{ \AA}^3$). The increase in the transition temperature could be also due to an out-of-stoichiometry of the FVO films. However, the already shown EDS-SEM study (page 66) and further analyses conducted in Synchrotron facilities (page 104) made us discard that hypothesis.

The transition temperature for FVO//STO films is higher than that obtained by Shi et al. (≈ 130 K) [69] and by Zhou et al. [70] (≈ 120 K) on their $\text{Fe}_{1+x}\text{V}_{2-x}\text{O}_4$ //STO films, and the latter group observed a second transition temperature at around 60 K – just like in bulk FVO. These studies lack deep structural characterisations, and the few information which they report suggests that their films had a poor crystallinity and a suboptimal surface topology. The main deposition difference comes from the use of an O_2 partial atmosphere instead of Ar, which could be behind the poorer crystallinity and magnetic properties of their films. The lower transition temperature could also be associated to a poor substrate morphology, or by the presence of magnetic dead layers [171]. Because of this, and owing to the stoichiometry issues that they report, we cannot compare our FVO films with the work in the literature.

The thickness was found not to play an important role in the transition temperature of FVO//STO films, with values in the range 140 – 148 K and no observable trend in T_c vs. thickness. Nevertheless, the transition temperature for FVO//MgO did show a thickness-dependant behaviour, as depicted in **Figure II.37**, and is probably due to the fully strained nature of FVO//MgO films.

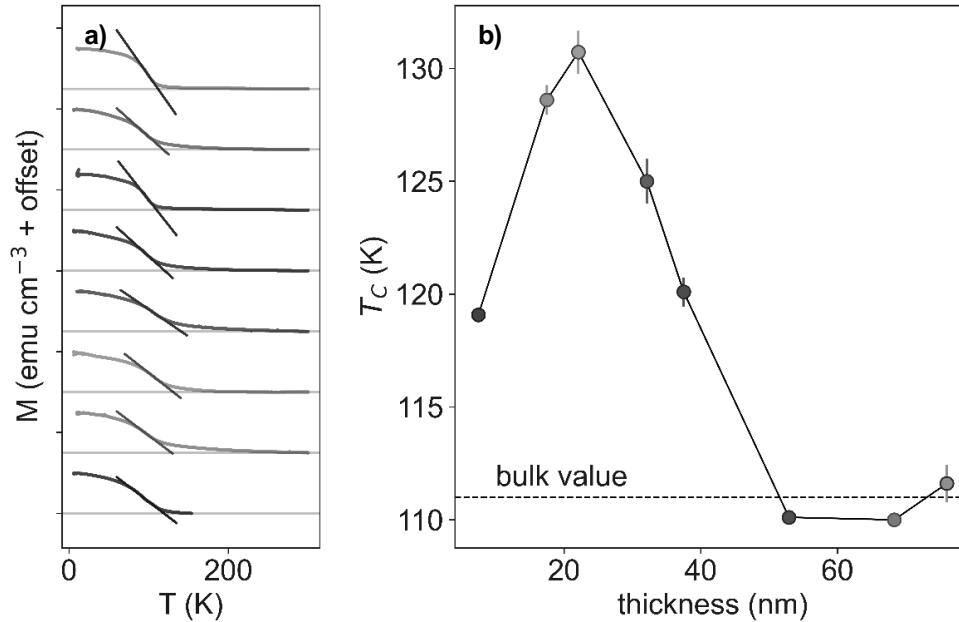


Figure II.37. (a) Magnetisation as a function of temperature for films of increasing thicknesses for FVO//MgO, with linear fit for the obtention of the magnetic transition temperature. (b) Magnetic transition temperature as a function of the thickness. The colour code has been respected, and M vs. T curves in the left plot correspond to filled dots on the right.

In the low thickness domain, the transition temperature increases with the thickness up to around 22 nm where it reaches its maximum: 131(1) K. When the films are thin, an increase in the number of layers enhances the overall strength of the magnetic interactions, which can translate into an increase in the magnetic compensation temperature [172]. As films get thicker, the volume interactions increase, which strengthens the magnetic exchanges and augments the value of the temperature needed to vanish the magnetic order.

For thicker films, however, other effects must come into play to explain the drop in the transition temperature. The increase in the number of layers might increase the mosaicity of the film's magnetic structure, and several magnetic domains might occur along the film's thickness. The films' increasing thicknesses might also come along with an accumulation of defects in the structure, and an augmentation of the film's polycrystallinity. All these effects would result in an overall weakening of the magnetic interactions. Beyond a certain thickness threshold, the temperature reaches a bulk-like value, and the strain effects of the thin-film layout no longer enhance the magnetic properties of the films as a function of the temperature.

Another hypothesis for this decrease in the magnetic transition temperatures comes from the emergence of two magnetic phases as the thickness increases, as the hysteresis curves in the next section of this chapter show. FVO films in both MgO and STO substrates seem to develop a complex magnetic structure of two different phases, one hard and another soft, alongside a same crystal phase. Similar findings have been reported in $\text{Fe}_{1+x}\text{V}_{2-x}\text{O}_4$ //STO films [70]. As the thickness increases, this magnetic mosaicity becomes more visible – appearance of magnetisation “jumps”, and the material’s coercivity increases. The magnetic exchanges weaken in this harder magnetic structure, and the magnetic interaction between and inside these two magnetic phases fades away at lower temperatures.

4.7.2. Magnetic hysteresis

As carried out previously in the bulk, SQUID magnetisation vs. applied field measurements were conducted in FVO films to characterise both their magnetic hysteresis and their anisotropy. The diamagnetic contribution of the substrates has been taken away by a linear fit at the high-field (after saturation) values. Results for FVO//MgO for different thicknesses at 60 K are depicted in **Figure II.38**.

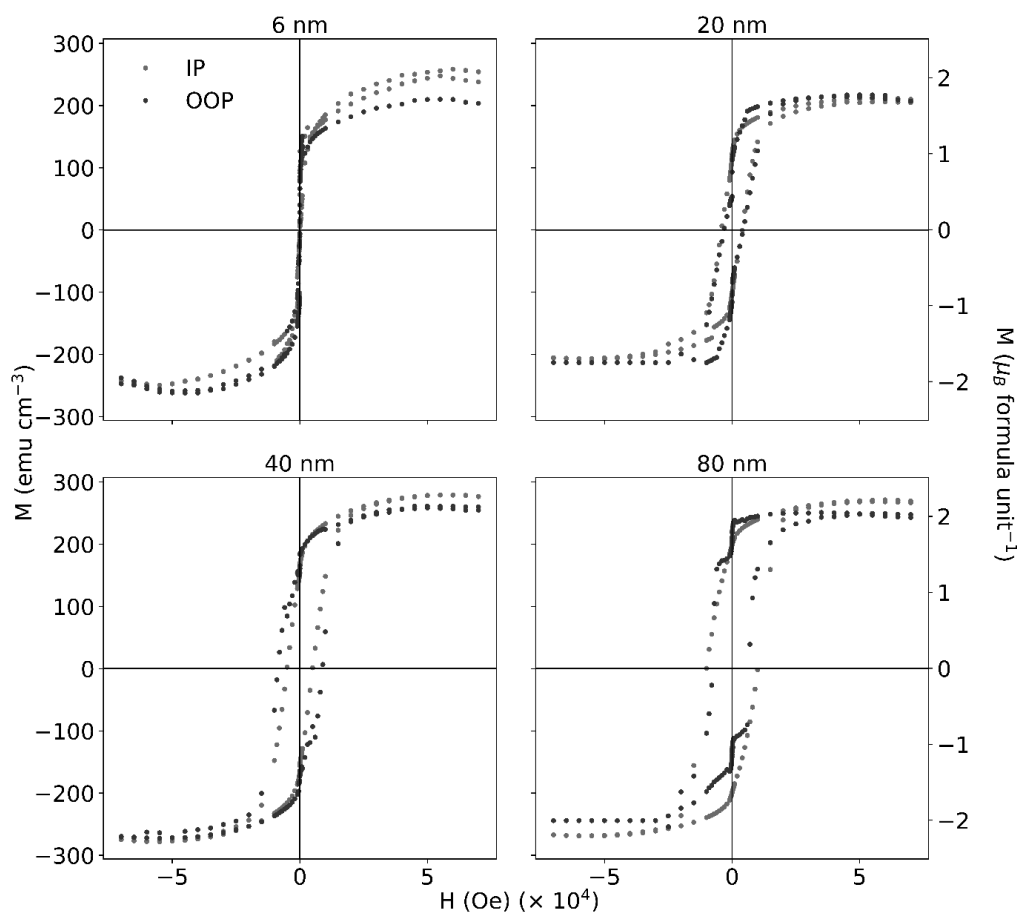


Figure II.38. 60 K magnetisation vs. applied field in the (- 70000, 70000 Oe) range for FVO//MgO thin films of four different thicknesses (calculated by the $t(n_h)$ relationship). All plots share the same scales. Red dots correspond to in-plane measurements, and blue dots to out-of-plane.

At very low thicknesses, M vs. H loops present a non-noticeable hysteresis. Since the films are composed by just a few layers, the magnetic interactions are not strong enough to resist an opposing magnetic field, so the magnetisation aligns itself with the applied field. The films present a strong paramagnetic behaviour as well. In thicker films (around 20 nm), magnetic coercivity begins to manifest, with indications of perpendicular magnetic anisotropy (PMA), i.e., the easy axis in the out-of-plane direction. The hysteresis loops start to show the aforementioned “two-jump” profile, signature of the emergence of two magnetic phases of different coercivities.

Both the PMA effect and the two-jump profile become more prominent with thicker films (≈ 40 nm). As the films grow thicker, the crystal mosaicity increases with the accumulation of structural defects, making the films more magnetically robust. The adding of neighbouring magnetic moment also strengthens the overall magnetic ordering, and hardens the magnetic response of FVO films. The films reach an out-of-plane coercive field of $\approx 1 \times 10^4$ Oe at 60 K, making the material significantly harder than bulk FVO (c. f. **Figure II.21** – page 58).

The two-jump magnetic behaviour is only evident in the out-of-plane lattice measurements, suggesting that the two magnetic phases (one being a harder ferrimagnet, the other softer) are coupled in the in-plane direction but decoupled in the out-of-plane direction. Such behaviour is only observed in thicker films, so it could be due to the emergence of magnetic textures in the OOP direction, phenomenon only permitted when the films are thick enough to allow it.

After reaching a certain thickness, FVO//MgO films attain a bulk-like status, losing the PMA, and films of approximately 80 nm in thickness no longer show any difference in coercivity between the in-plane and out-of-plane directions. The two-jump behaviour becomes more prominent, supporting the hypothesis of it being a thickness-dependent phenomenon. The magnetic structure of the films can be simplified as a combination of a soft magnetic phase, predominant in the next-to-the-substrate fully strained region, and a harder magnetic phase which is more visible in the bulk-like part. The actual scenario, however, seems to be more complicated: this does not explain the difference between the in-plane and out-of-plane couplings, the bulk-like contribution is harder (whereas the bulk itself is softer) and there is no structural evidence which suggests the presence of these two magnetic phases (as crystal phases with different anisotropies). More advanced studies are needed in order to unveil the magnetic structure of FVO//MgO films.

Finally, in terms of the magnetisation at saturation, the films present a value of $\approx 1.9 \mu_B$ per formula unit, which matches that of bulk FVO in the collinear magnetic phases. No significant variation with the thickness has been observed. If we suppose a perfect antiparallel alignment of Fe^{II} ($S = 2$, $\mu_{\text{spin-only}} = 4 \mu_B$) and V^{III}, that would make V have a net magnetic contribution of $\approx 2.1 \mu_B$ – far from the $4 \mu_B$ if their magnetic moments came solely from the spin contribution. This is another confirmation of the predominance of the orbital momentum in V^{III}, and of the importance of considering the spin-orbit-coupling in the full comprehension of FVO’s magnetic properties. Further studies should be conducted

to fully understand the magnetic contribution of each cation, to confirm the collinear arrangement of the magnetic spins and to unveil the orbital influence in FVO's magnetism.

M vs. H measurements have also been carried out in FVO//STO films, as **Figure II.39** shows. Only thicknesses ranging from 40 to 80 nm have been studied.

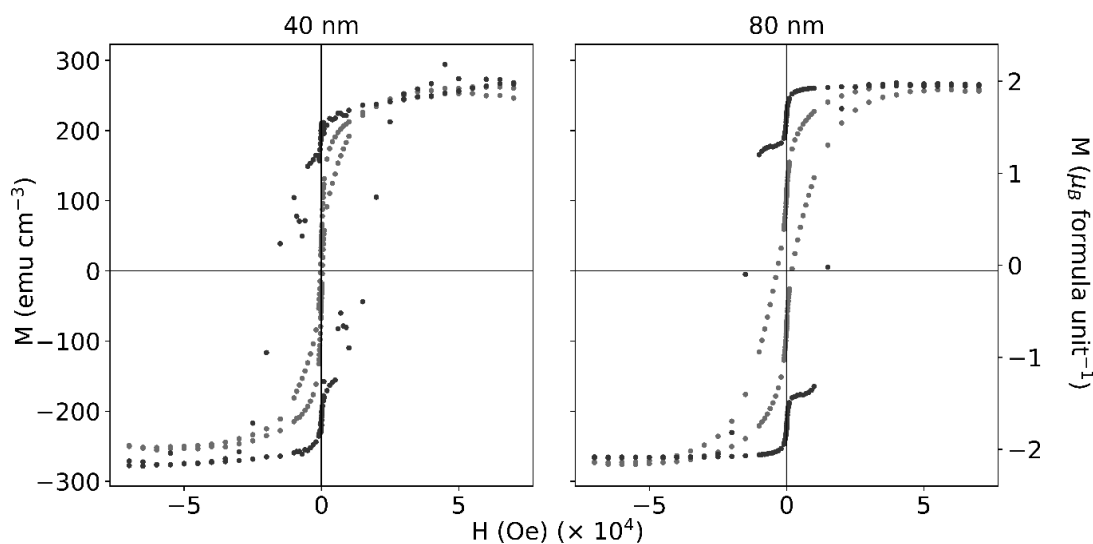


Figure II.39. 60 K magnetisation vs. applied field in the (- 70000, 70000 Oe) range for FVO//STO thin films of two different thicknesses. The two plots share the same scales. Red dots correspond to in-plane measurements, and blue dots to out-of-plane.

The FVO//STO films show a larger PMA than FVO//MgO films. This justifies why FVO//STO films have been chosen in “**Chapter III. Advanced structural characterisation of FeV₂O₄ films by resonant diffraction**”, the chapter of this thesis where this PMA feature is used for spin transport applications. The substrate-to-film strain can modulate the PMA behaviour, with PMA becoming more predominant as the strain increases [173]. Since the compressive strain is significantly larger in FVO//STO, PMA is therefore more notorious in this thin-film system.

The PMA can also be explained due to the films' tetragonality. The films elongation in the out-of-plane direction facilitates the orbital occupancy along the z direction, working as a “strain-driven” Jahn Teller effect. This results in a preferential occupation along the z -oriented orbitals which enhances the orbital moments along z [174]. An anisotropic orientation of the orbital moments can explain the magnetic anisotropy in systems with strong orbit coupling [175], as it is the case for FVO. As a result, since the out-of-plane direction possesses a stronger orbital occupancy (and orbital moments), it becomes the easy magnetisation direction, whereas the hard axis falls into the in-plane direction. This would also explain why FVO//MgO films, with a more “cubic-like” structure, do not show such a strong PMA.

FVO//STO films, just like FVO//MgO and Fe_{1+x}V_{2-x}O₄//STO films [70], show the distinct two-jump behaviour in M vs. H measurements. The profile is clearer than in FVO//MgO films. The XRD characterisation and the RHEED results already showed that FVO grows in a more “3D-like” manner onto STO. If we associate the soft ferrimagnetic phase with a bulk-like structure, the M vs. H profile should not have such a large proportion of the hard ferrimagnetic phase. Therefore, the two magnetic phases cannot be attributed to “fully-strained” and “bulk-like” growth modes.

The stronger crystal mosaicity manifests as a more important magnetic hardness and coercivity in FVO//STO. The curves present similar values for M_s , suggesting again an antiparallel collinear arrangement – which needs to be furtherly confirmed. The same explanation for the spin-orbit coupling and the magnetisation per formula unit can be given.

As shown in **Figure II.40** for the 40 nm FVO//STO film, both the magnetisation at saturation (**a**) and the coercive field (**b**) decay with the temperature. M_s stays at $\approx 2 \mu_B$ up to 60 K, then slowly drops with the temperature. When it comes to the H_c , its decline is continuous with temperature, and reaches almost zero values above 100 K. The values have been obtained through M vs. H cycles at varying temperatures.

The material’s coercivity is approximately $H_c \approx 1.5 \times 10^4$ Oe at 60 K and reaches values up to $H_c \approx 3.5 \times 10^4$ Oe at 2 K, for FVO//STO. The M vs. H measurements could not be conducted at very low temperatures for FVO//MgO, due to the huge paramagnetism that they showcase. However, we can conclude that FVO//STO films present a more pronounced perpendicular anisotropy and a harder magnetic behaviour than FVO//MgO films, which adds to their higher magnetic transition temperature.

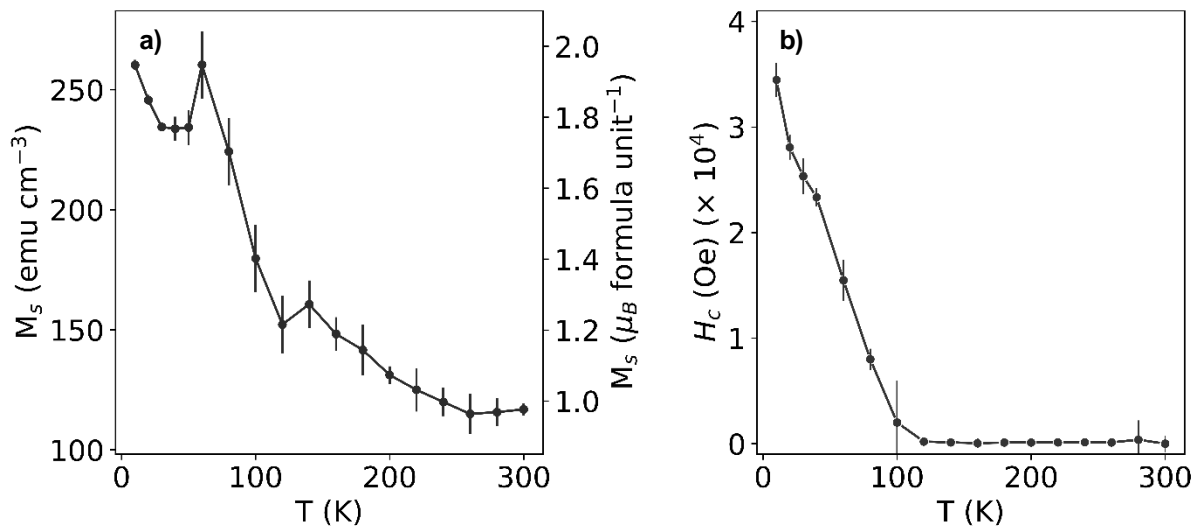


Figure II.40. (a) Magnetisation at saturation as a function of temperature. (b) Coercive field for the magnetisation reversal vs. temperature. Both data have been obtained via M vs. H SQUID measurements for a 40 nm FVO//STO film at varying temperatures.

4.8. Transport properties of thin films

FVO thin films underwent a cornered wire-bonding process following the scheme previously presented for the van der Pauw method – c.f. **Figure II.13**. The “horizontal” and “vertical” resistances were measured – as defined in **Equation (II.6)** – as a function of temperature, and the films’ resistivities were calculated using the expression in **Equation (II.7)**. The resistivity behaviour as a function of the temperature is shown in **Figure II.41**. Measurements were conducted in the temperature ranges of 175 – 375 K for FVO//STO and 200 – 375 K for FVO//MgO. At temperatures below those lower limits (175 K for FVO//STO and 200 K for FVO//MgO), resistance values were above the detection threshold of our PPMS.

For both types of thin films—FVO//STO and FVO//MgO, each 40 nm thick—the resistivity decreases as the temperature increases. This indicates that the materials act as semiconductors or insulators. Additionally, in neither of these two types of films does the strain-induced reduction in the V-V distance trigger a Mott transition in the material. FVO//STO films showed to be more conductive: at 300 K $\rho_{\text{FVO//STO}} = 5.4(2) \times 10^{-3} \Omega \text{ m}$ compared to $\rho_{\text{FVO//MgO}} = 2.8(1) \times 10^{-2} \Omega \text{ m}$, with a resistivity ratio of around $\rho_{\text{FVO//MgO}}/\rho_{\text{FVO//STO}} \approx 5.2$.

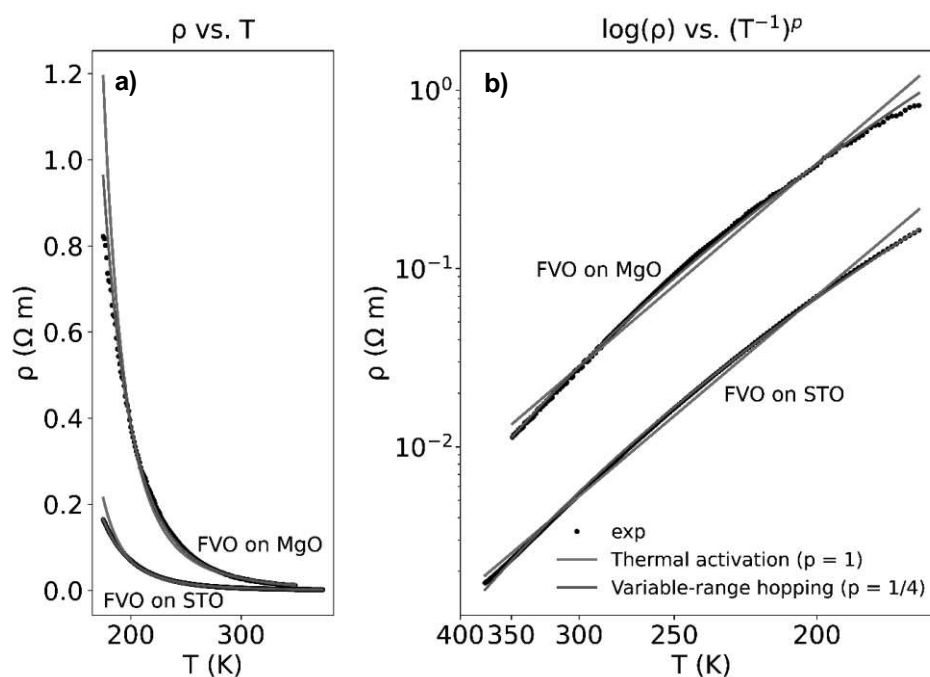


Figure II.41. Resistivity as a function of temperature. (a) Nominal values. (b) Resistivity (log scale) as a function of the temperature (inverse scale). The black dots correspond to the experimental values. The solid lines correspond to fits using the thermal activation model (red) and the variable-range hopping model (green).

These room-temperature values can hardly be compared to previous studies, as no work in the literature reports the data for FVO//MgO films, and the only study so far on FVO//STO (by Zhou et al. [70]) does not document temperatures above 200 K. The films present a substantially higher room-temperature resistivity than films of spinel Fe₃O₄ (FFO) on MgO of comparable thickness: $\rho_{\text{FFO}/\text{MgO}} \approx 5 \times 10^{-5} \Omega \text{ m}$ [176], [177], which is expected due to the half-metal behaviour and high spin-polarised electron conduction of FFO [178].

The 200 K resistivities of the films are $\rho_{\text{FVO}/\text{STO}} = 7.1(1) \times 10^{-2} \Omega \text{ m}$ and $\rho_{\text{FVO}/\text{MgO}} = 3.8(2) \times 10^{-1} \Omega \text{ m}$, larger than the value reported by Zhou et. al: $\rho_{\text{FVO}/\text{STO}} \approx 2 \times 10^{-2} \Omega \text{ m}$ [70]. This disparity in the resistivity results could be due to the out-of-stoichiometry state of their films and the contribution of the excess of iron in the overall conductivity.

The resistivity vs. temperature curves were fitted using two different approaches. Firstly, the electron conduction was described using a thermal conduction model. In semiconductors, the high temperature conduction usually comes from the electrons hopping from the valence band to the conduction band, in a process acknowledged as thermal activation (TA). The relationship between the material's resistivity (or inverse reasoning with the conductivity) is therefore explained as an Arrhenius activation process of charge carriers whose presence in the conduction band becomes more notorious with the increasing temperature [179]. In such a conduction scenario, the resistivity variation with the temperature can be described with the expression shown in **Equation (II.10)**, where ρ_0 is a pre-exponential factor – theoretical resistivity at infinite temperature, E_a is the activation energy for the thermal activation of electrons and k is the Boltzmann's constant.

$$\rho = \rho_0 e^{-\frac{E_a}{kT}} \quad \text{(II.10)}$$

Nevertheless, the TA model fails in describing the whole conduction process in systems whose electrical conduction vs. temperature cannot be fully explained by an increasing population of electrons in the conduction band. In fact, FVO has a Mott insulator behaviour with strongly localised electronic states, and the variable-range hopping (VRH) model provides a more suitable approach. This model describes the low-temperature electrical conduction in Mott insulators, where electrons hop between the different localised states. It is applicable in situations where the electron-electron interactions are strong enough to hinder the motion of electrons and form localised electronic states. The likelihood of the electronic hops occurring is determined by both the distance between states and the energy difference between them. In the VRH model, the resistivity as a function of temperature is described by **Equation (II.11)**, where ρ_0 is again a pre-exponential factor and T_0 is a characteristic temperature related to the density and the degree of localisation of the electronic states. The T_0 value, also known as Mott temperature, is a measure of the hopping energy scale of the electron hopping process between the localised electronic states [179], [180].

$$\rho = \rho_0 e^{-\left(\frac{T_0}{T}\right)^{1/4}} \quad (\text{II.11})$$

As seen in **Figure II.41**, both models succeed in describing the temperature behaviour of FVO films, with the VRH model leading to better fits ($R^2_{VRH-FVO//STO} = 0.9997$, $R^2_{VRH-FVO//MgO} = 0.9994$) than the TA model ($R^2_{TA-FVO//STO} = 0.996$, $R^2_{TA-FVO//MgO} = 0.990$). Both fits have been conducted using equation forms $\ln \rho = a + b \times (1/T)^p$, where a is the natural logarithm of the pre-exponential factor, b equals $(-E_a/k)$ for the TA model and $(-T_0)$ for the VRH mechanism and p is a factor which considers the system's dimensionality, differentiating between the two models.

Converting the equations into their exponential forms, the TA model led to resistivities of $\rho_{FVO//MgO} = 1.48(4) \times 10^{-4} e^{-0.136(1)/k_{ev}T}$ and $\rho_{FVO//STO} = 2.97(5) \times 10^{-5} e^{-0.133(1)/k_{ev}T}$, k_{ev} being the Boltzmann constant in eV K⁻¹. Despite the limitations of the model, it succeeds in describing the higher electrical resistivity of FVO//MgO, which results from their larger activation energy: 0.136(1) eV for FVO//MgO, compared to 0.133(1) eV for FVO//STO. For the VRH model, the resistivities as a function of the temperature take the form $\rho_{FVO//MgO} = 6.79(2) \times 10^{-13} e^{-1.07(1) \times 10^8/T}$ and $\rho_{FVO//STO} = 3.48(1) \times 10^{-13} e^{-9.145(3) \times 10^7/T}$. The value for the Mott temperature are $T_{0-FVO//MgO} = 1.07(1) \times 10^8$ K and $T_{0-FVO//STO} = 9.145(3) \times 10^7$ K which indicates larger energies needed for electron hopping in FVO//MgO films. As described in **Table II.1** – page 76, FVO//STO presents a lower lattice volume and shorter interatomic distances, so the distance between hopping sites and the energy needed for the hopping process are also expectedly lower.

In the study by Zhou et al. [70] resistivity curves were also fitted via the VRH model, and the found Mott temperature value was 2.488×10^8 K, unexpectedly higher than ours, since their films were considerably more conducting than ours. The VRH model in their case, however, did not seem to fit well the low-temperature values, so another model might have been more appropriate to explain the electronic conduction in their Fe_{1+x}V_{2-x}O₄ films.

In conclusion, the transport properties of FVO films have been modelled using a simple approach (TA), common to semiconducting materials, and a more holistic strategy (VRH), suitable for Mott insulators. The second model fitted better the temperature dependance of the films' resistivity, but the parameters of both models were able to explain the more resistive nature of FVO//MgO films.

Chapter III. Advanced structural characterisation of FeV_2O_4 films by resonant diffraction

The arrangement of atoms within a crystal material can play a critical role in its properties and functionalities. As a result, the understanding of the crystallographic structure, which includes precisely locating its atoms, is sometimes a preliminary step before the implementation of a functional material into technological devices.

This is the case of many functional oxides. One example is magnetically active or ferroelectric oxides, where knowing the oxygen position is needed to explain the arrangement responsible for the material's behaviour [63], [181]. Equally, in oxides with orbitally ordered states, locating oxygen atoms allows understanding the lattice deformations which lead to the orbital order inside the material [53]. In our material of interest, FeV_2O_4 (FVO), the orbital order has been studied through an analysis of the lattice distortions, which have been obtained via the relative locations of the neighbouring oxygens around the two central cations [52].

Such study has been conducted with either Synchrotron X-ray Diffraction (S-XRD) and Neutron Diffraction (ND) techniques. In bulk materials, these strategies are commonly used to locate the different atoms which compose the crystal [182]–[184]. However, these methods have difficulties in giving a whole picture of the crystal structure of thin-film samples. Thin films have much less matter to probe, limiting a potential crystallographic unveiling via ND. Furthermore, they possess a strongly oriented crystal orientation, which hinders a complete crystallographic study through conventional S-XRD.

A possibility for such systems is Precession Electron Diffraction (PED), a technique coupled with Transmission Electronic Microscopy (TEM) which allows solving the structure of thin-film materials [185], [186]. Despite its potency in obtaining accurate structure models, this technique brings about a tedious and destructive sample preparation process. Therefore, a friendlier approach for the crystallographic unveiling of thin films is desirable.

For that purpose, in this chapter we introduce resonant (or anomalous) diffraction as an alternative for the presented issues, with the ultimate goal of locating the atoms in FVO thin films. We begin by deriving the atomic scattering factors from the classical diffraction problem, whose energy dependence is the key to understand anomalous diffraction. Secondly, we explain how the energy dependence of these

factors is exploited by resonant diffraction in order to retrieve information about the material's atomic and electronic structure.

A focus is made on resonant elastic x-ray scattering (REXS), technique which is furtherly explained, as well as its application in thin films. Using theoretical simulations, REXS is shown to be a successful technique for the determination of the atomic positions, and experimental results (by confrontation with other methods in the bulk) validate this approach. Both validations are carried out in the showcase material FVO.

In order to facilitate REXS experiments, an entire methodology in the form of a computer program has been developed: *inserexs*, whose main aspects are detailed in this chapter. This software, alongside an *ad hoc* developed approach, are used to characterise the cationic species in FVO thin films following the approach of REXS studies in the near-edge energy range (DANES). Besides, REXS analyses in the extended energy range (EDAFS) enable the determination of the position of the oxygen atoms as a function of the temperature. The *inserexs* software [187] and the determination of oxygen atoms in FVO thin films [188] have already been shared in the form of peer-reviewed scientific articles.

Finally, both the positions of the cations and of the oxygen atoms are obtained from REXS spectra using artificial neural networks. The machine-learning-powered refinement of DANES spectra leads to same results for the cation positions as the other described methodology. The attribution of oxygen positions via the treatment of EDAFS spectra still needs to be improved, only leading to approximative results.

This chapter is a compendium of the different utilities and strategies which, by the means of anomalous diffraction experiments, lead to the structural resolution of FVO thin films. Beside the meaningful results which will be presented hereafter, this chapter contains numerous novel approaches that can be futurely used in the study of oxide thin films.

1. Fundamentals of resonant diffraction

1.1. From the classical diffraction problem to the atomic scattering factor

The diffraction problem, which refers to the scattering of photons by a material, can be studied from the perspective of photon-electron interaction. In classical physics, the motion of photons as a function of time (t) is described as an electric field $E = E_0 e^{i\omega t}$ possessing an oscillating frequency (ω) and an amplitude (E_0). When a photon interacts with an electron, the motion of the electron undergoes a response which is governed by the differential equation expressed in **Equation (III.1)**.

$$\frac{d^2x}{dt^2} + kx + \omega_s^2 = \frac{eE_0}{m} e^{i\omega t} \quad (\text{III.1})$$

This equation characterises the electronic displacement (x) caused by the photon-electron interaction, where k is a damping factor (indicating the resistance to the motion of the electron ω_s the natural frequency of the electron and m and e are the mass and the charge of the electron, respectively). The solution of this differential equation provides the displacement of the electron in response to the oscillating electric field and can be expressed as the relationship indicated in **Equation (III.2)**:

$$x = \frac{eE_0}{m} \cdot \frac{e^{i\omega t}}{\omega_s^2 - \omega^2 + ik\omega} \quad (\text{III.2})$$

From this displacement, one can calculate the amplitude of the motion (A) as expressed in **Equation (III.3)**, which quantifies the extent of the motion after the photon-electron interaction:

$$A = \frac{e^2 E_0}{mc^2} \cdot \frac{\omega^2}{\omega_s^2 - \omega^2 + ik\omega} \quad (\text{III.3})$$

In the case of a free electron, the natural frequency and damping factor terms would be zero. Therefore, the amplitude of the displacement of that free unbound electron (A_e) would take the value indicated in **Equation (III.4)**:

$$A_e = -\frac{e^2 E_0}{mc^2} \quad (\text{III.4})$$

One can then define a ratio between the amplitude scattered by the diffracting electron and that diffracted by a free electron, also known as the atomic scattering factor [189]. The atomic scattering factor characterises the scattering power of a considered electron and can give valuable information

about the material's atomic structure. The expression for the atomic scattering factor has been made explicit in **Equation (III.5)**:

$$f = -\frac{A}{A_e} = \frac{\omega^2}{\omega^2 - ik\omega - \omega_s^2} \quad \text{(III.5)}$$

The atomic scattering factors contribute significantly to the structure factor, which is a mathematical description of how a particular crystal scatters incident X-rays. The structure factor, denoted as F_q , is essentially a sum over all the individual contributions of the atoms present in the crystal structure. Each atom contributes a term that is the product of its atomic scattering factor and a phase factor that depends on the position of the atom within the unit cell. The structure factor has been mathematically expressed in **Equation (III.6)**, where \mathbf{q} represents the scattering vector, \mathbf{r}_j the vector coordinates of the j^{th} atom located in the x_j, y_j and z_j fractional coordinates, hkl are the Miller indices and f_j the atomic scattering factor. The scattered intensity, I , is proportional to the square of the absolute value of the structure factor $|F_q^* F_q|$.

$$F_q = \sum_j f_j e^{-i\mathbf{q} \cdot \mathbf{r}_j} = \sum_j f_j e^{2\pi i(hx_j + ky_j + lz_j)} \quad \text{(III.6)}$$

The complete form of the atomic scattering factor takes the form of $f = f_0(\sin 2\theta / \lambda) + f'(\lambda) - if''(\lambda)$, with f_0 being the Thomson scattering factor (non-resonant), which represents the scattering of X-rays by a free electron and whose main dependance comes from the scattering angle θ ; and f' and f'' being the real and imaginary anomalous (resonant) terms [190]. The expression for each anomalous term has been indicated in **Equation (III.7)** and **(III.8)**, while the derivation of both expressions from **Equation (III.5)** has been detailed in **annex 2** – page 180.

$$f' = \frac{\omega_s^2(\omega^2 - \omega_s^2) - k^2\omega^2}{(\omega^2 - \omega_s^2)^2 + k^2\omega^2} \quad \text{(III.7)}$$

$$f'' = \frac{k\omega^3}{(\omega^2 - \omega_s^2)^2 + k^2\omega^2} \quad \text{(III.8)}$$

Considering both resonant and non-resonant terms, the whole expression for the structure factor takes the form of **Equation (III.9)**.

$$F_q = \sum_j \left(f_{0j} + f'_{0j}(\omega) + f''_{0j}(\omega) \right) e^{-i\mathbf{q} \cdot \mathbf{r}_j} \quad \text{(III.9)}$$

Extending upon this expression for the structure factor, it is possible to understand why reflections that are forbidden in classical diffraction experiments ($\sum_j f_{0j} e^{-i \mathbf{q} \cdot \mathbf{r}_j} = 0$) are “allowed” in resonant diffraction. The resonant terms bring about different scattering amplitudes in equivalent atoms occupying also equivalent crystallographic positions. This phenomenon manifests as an anisotropic behaviour of the crystal's X-ray susceptibility. Forbidden reflections take on particular significance in proximity to X-ray absorption edges, where the anisotropy of susceptibility can yield discernible effects in scattering patterns [191].

Tackling the diffraction problem by using classical Physics, we have reached both anomalous terms f' and f'' , whose variation settles the foundations of resonant diffraction – as explained in the next section of this chapter. A similar outcome can be obtained by treating the diffraction problem from a quantum perspective as, for instance, performed by Grenier and Joly [192].

Nevertheless, the equations provided above correspond to the excitation of an electron, and it does not offer a complete understanding of the resonant diffraction process within a material. The complete expression for the resonant terms of the atomic scattering factor receives the form shown in **Equation (III.10)**, providing a more comprehensive understanding of the resonant diffraction process within a material [192]. This equation considers the dependence of the diffraction process on the material's electronic structure (φ_n) and the incoming ($\boldsymbol{\varepsilon}_i$) and outgoing ($\boldsymbol{\varepsilon}_s^*$) polarisations. $\sum_{n,g}$ is the summation over all relevant quantum states, $\langle \varphi_g | \boldsymbol{\varepsilon}_s^* \cdot \mathbf{r} | \varphi_n \rangle$ and $\langle \varphi_n | \boldsymbol{\varepsilon}_i \cdot \mathbf{r} | \varphi_g \rangle$ describe the interaction of the material with the incident and scattered light, \hbar is the reduced Planck constant, $(E_n - E_g)$ the energy difference between the quantum states and η is damping term.

$$f'(\omega) - i f''(\omega) = m\omega^2 \sum_{n,g} \frac{\langle \varphi_g | \boldsymbol{\varepsilon}_s^* \cdot \mathbf{r} | \varphi_n \rangle \langle \varphi_n | \boldsymbol{\varepsilon}_i \cdot \mathbf{r} | \varphi_g \rangle}{\hbar\omega - (E_n - E_g) + i\frac{\eta}{2}} \quad \text{(III.10)}$$

1.2. Anomalous diffraction

The previously presented terms, f' and f'' , are also called dispersive or anomalous atomic scattering factors. Differently to the Thomson scattering term f_0 , the dispersive terms are dependent on the frequency of the incident photon and, therefore, on the wavelength (and energy) of the X-ray radiation. As schematised in **Figure III.1**, the anomalous terms suffer significant variations around the absorption edges of resonance, whereas the non-anomalous term f_0 keeps a constant profile.

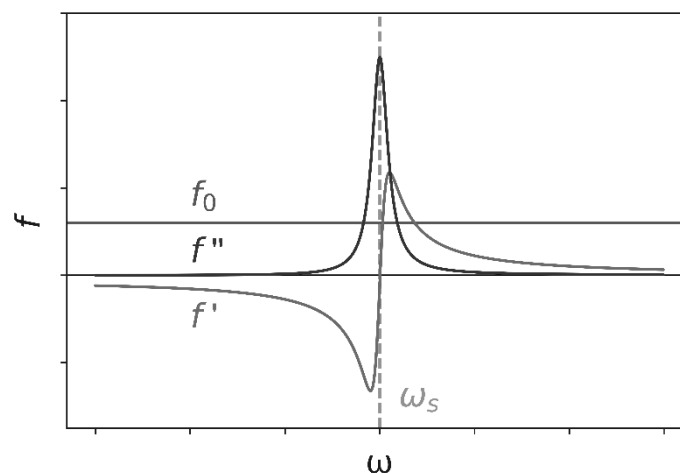


Figure III.1. Variation of the terms of the atomic scattering factor, f_0 , f' and f'' , as a function of the frequency (ω) around the resonance frequency (ω_s) edge.

On the one hand, f' is the real part of the anomalous scattering factor. It accounts for the shift in the phase of the scattered X-ray due to the interaction of the incident X-ray with the bound electrons in the atom. f' is energy-dependent and becomes significant near the absorption edges of the atom. On the other hand, f'' is the imaginary part of the anomalous scattering factor. It accounts for the absorption of the incident X-ray by the atom, which leads to the re-emission of the X-ray with a phase shift of 90 degrees. Similar to f' , f'' also is energy-dependent and acquires significance near the atom's absorption edges.

In conventional diffraction experiments, the wavelength of the radiation used is typically kept constant. The sample is therefore irradiated with a monochromatic beam with which the diffraction patterns are collected. The atomic scattering factors are considered constant since the energy is unchanged. Nevertheless, in resonant (or anomalous) diffraction, the energy dependence of the atomic scattering factors is taken into account. The incident energy of the x-rays is tuned to match the energy of one of the electronic transitions within the material, thus allowing its "resonance". As a result, and in contrast to conventional diffraction experiments, anomalous diffraction aims at studying the variation of the atomic scattering factors as a function of energy, and the scattered patterns take the shape of X-ray spectra [193].

Resonant diffraction combines the potential of both x-ray absorption spectroscopy (XAS) and x-ray diffraction (XRD) in one single experiment [194]. The XAS part provides information about the electronic states involved in the crystal ordering, while the XRD part gives information about the spatial order. There are two main types of resonant diffraction experiments: resonant elastic x-ray scattering (REXS), fully covered in the next section of this chapter, and resonant inelastic x-ray scattering (RIXS).

RIXS experiments aim at measuring the dynamic response of electrons in the material to the incoming X-rays. The energy of the incident radiation is absorbed by the material, causing an electronic transition to higher energy levels. The energy of the scattered radiation does not match that of the incident energy and is therefore not conserved (inelastic process) [195], [196]. By measuring the energy loss of the scattered x-rays, information about the electronic excitations within the material can be retrieved. Such alterations in energy, momentum, and photon polarisation can correlate with corresponding excitations in the studied materials [197]. RIXS possesses an enormous potential and can be used to obtain a wide range of information, such as the material's density of states [198], the magnon generation and propagation [199], spin waves [200] polarons [201] and the more elusive orbiton quasi-particles [202].

1.3. Resonant Elastic X-ray Scattering

In a REXS experiment, an incident photon (of varying energy) excites a bound core electron into an unoccupied state, close to the Fermi level, while the material's orientation respects the diffraction condition – with the scattering vector being targeted towards a specific reciprocal lattice point (RLP). The electronic transition, from a ground to an excited state, strongly depends on the electronic structure of the valence shell. The electron reverts into its core ground level, re-emitting a photon of the same energy as the incoming photon [203]. In contrast to RIXS, the electronic excitation in REXS is an elastic process, i.e., there is no net energy loss in the excitation-deexcitation processes.

Since the transition takes place at a specific edge of a specific atom (among those present in the crystal), REXS is both element and orbital sensitive [193]. The entirety of this process, along with a visual scheme of the experimental setup, is depicted in **Figure III.2**. The spectroscopic response of a REXS experiment comes in the form of energy-dependent oscillations which serve as a distinctive representation of the electronic structure of the resonant atom.

The spectral position and intensity of REXS oscillations can be used to construct a three-dimensional picture of the electronic density within the material. If classical (non-resonant) diffraction corresponds to the Fourier transform of the lattice's electronic density, its resonant counterpart is considerably more sensitive to the projection of the state density over the resonant atoms. Furthermore, the choice of the examined spectral region can provide distinct insights: focusing on certain regions can yield information about the resonant atom itself, such as its electronic configuration and atomic structure, while other regions can reveal details about its electronic environment.

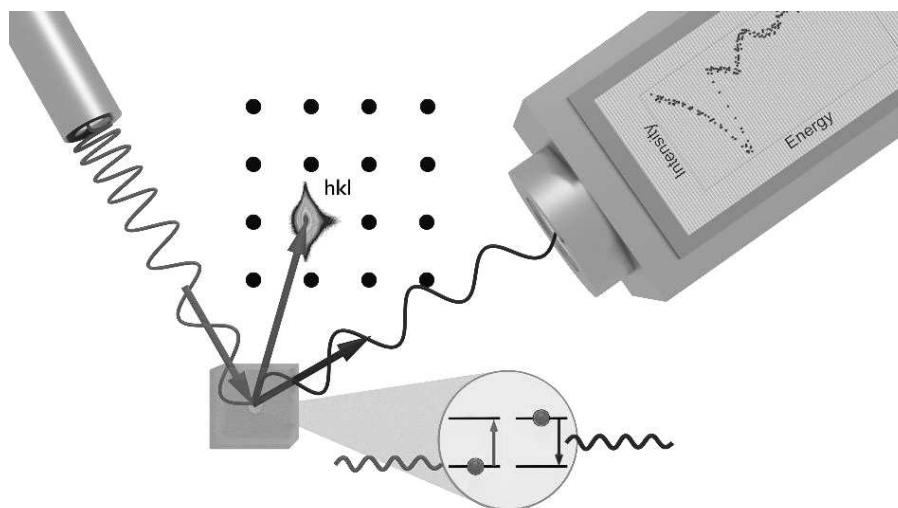


Figure III.2. Schematic representation of a REXS set-up and experiment. In green, the incident beam; in blue, the diffracted beam. The X-ray source, the target material and the X-ray detector are oriented so that the diffraction condition is respected for the desired reflection (hkl).

The x-ray absorption near the edge structure (XANES) is characterised by a sharp rise in absorption immediately preceding the absorption edge (energy at which the electrons of an atom are excited). The exact shape of the XANES spectrum is dependent on the electronic configuration of the resonant atom and its chemical environment, and therefore provides information about the nature and coordination of the resonant atom [204], [205].

Beyond the resonance energy, at the extended absorption fine structure (EXAFS) part of the REXS spectrum, information can be retrieved regarding the neighbouring atoms of the resonant atom. a photoelectron (virtually generated) probes a molecular state (or a band) that encompasses the excited resonant atom and the nearby atoms. This process perturbs the electronic orbitals of the resonant atom and its neighbours, leading to alterations in the phase and amplitude of the scattered X-rays. These changes are contingent on interatomic distances and coordination numbers. Consequently, the EXAFS spectrum can be scrutinised to extract information concerning the electronic states of atoms neighbouring the resonant atom [206]–[208].

REXS in the near-edge energy range is also known as “Diffraction Anomalous Near Edge Structure (DANES)” and REXS in the extended energy range (+20 eV beyond the edge) is also known as “Extended Diffraction Absorption Fine Structure” (EDAFS).

1.4. Fitting of REXS spectra

EDAFS measurements are often analysed via a Fourier transformation of the acquired spectra which can lead to the interatomic distances and other structural information [190], [209]. Conducting such an

analysis, simply referred as “EXAFS”, can assist in placing the neighbouring atoms in a sphere around the central cation. When it comes to DANES analysis, the experimental spectra are often compared either to established standards or theoretically simulated spectra [205].

In the context of this work, the latter strategy has been used for the study of both the EXAFS and XANES parts of the REXS spectrum. The experimental spectra have been directly compared to theoretical spectra generated using the *ab initio* software FDMNES [210]. FDMNES uses time-dependent Differential Functional Theory (TD-DFT) with the Hubbard correction (LDA+U) for the spectra generation. The Green’s function formalism has been used. The calculus radius was set to 5 Å, which appeared to be an appropriate choice when compared to the system’s lattice parameter (approximately 8 Å). Larger values showed negligible differences in the shape of the generated spectra but heavily increased the simulation time. Lower radius values, however, led to significant changes in the spectra.

In each refinement process, one or more parameters of interest have been investigated, and a theoretical spectrum has been generated with every unique set of parameters. For each individual set of parameters, the difference (χ^2) between the intensity of the experimental spectrum (I_{ES}), and that of the theoretical spectrum (I_{TS}) generated with those parameters is calculated, as expressed in **Equation (III.11)**. The difference is calculated along all the energy (E) range, from E_{start} to E_{end} .

$$\chi^2 = \int_{E_{start}}^{E_{end}} (I_{TS}(E) - I_{ES}(E))^2 dE \quad \text{(III.11)}$$

All the χ^2 calculated differences, alongside the n varying parameters, form a mathematical space of $(n + 1)$ dimensions. Its absolute minimum (in terms of χ^2) marks the parameter combination which leads to a theoretical spectrum which best matches the experimental. Using this strategy, one can unequivocally refine one or more parameters of interest.

Finally, as previously mentioned, the scattering process in REXS occurs with the detected intensity corresponding to a specific RLP hkl , for a designated atomic species and a particular electronic transition of the selected atom. In an ideal case, in order to solve a crystallographic structure, one could just measure the REXS spectra at all non-null reflections. In actual experiments, the acquisition of REXS spectra at all RLPs would not be practical. Access to instruments able to perform such experiments is costly and infrequent, and beam time slots are time-limited.

Prior the measurement itself, an experimentalist should know whether REXS experiments are suitable for their aim and should make a choice of the most adequate reflections. The “usefulness” of a reflection on a specific energy range $[E_{start}, E_{end}]$ has been defined according to two parameters. Firstly, the more intense a reflection, the better the signal-to-noise ratio for the measurement, and the superior the spectra fitting and the refinement. The intensity (I_{hkl}) must therefore be taken into consideration for the choice of the best reflection. The value of the intensity can be estimated via the structure factor: $|F_q^* F_q|$.

Secondly, the REXS spectrum must be sensitive to the parameters of interest: if these parameters change, the spectrum acquired at that certain reflection must change as well, and the spectrum modification must allow detecting the parameter's variation. For this, one can define a second parameter called "sensitivity" (S_{hkl}) which considers how much a spectrum is altered when the desired parameter changes. Mathematically, the sensitivity takes the form shown in **Equation (III.12)** for a single varying parameter x which takes values varying from x_{min} to x_{max} . Its value is the difference between the intensity of each theoretical spectrum and the average intensity of all the generated spectra (I_{av}).

$$S_{hkl} = \int_{x_{min}}^{x_{max}} \int_{E_{end}}^{E_{start}} \left(I_{TS(x)}(E) - I_{av}(E) \right)^2 dE dx \quad \text{(III.12)}$$

The two parameters that have been used to evaluate REXS reflections are represented in the form of S vs. I plots where all reflections are evaluated based on their sensitivity and intensity values. The intensity and sensitivity alongside a S vs. I plot have been schematised in **Figure III.3**.

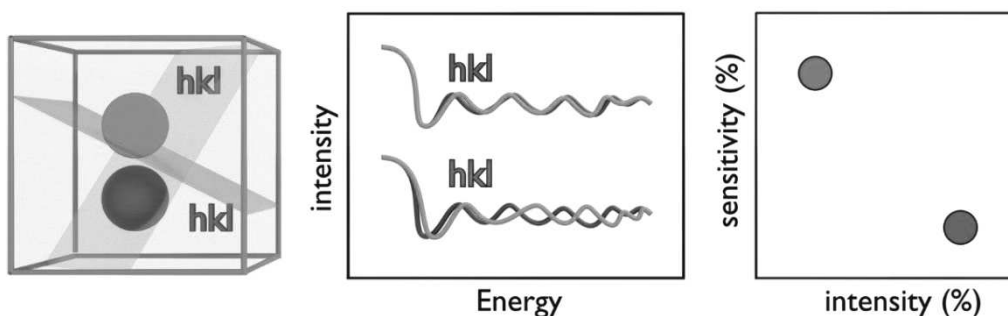


Figure III.3. Left: scheme of two possibilities for an atomic position (blue and purple) and two possible hkl reflections (red and green) at which REXS experiments can be carried out. Middle: comparison of REXS spectra acquired at both reflections. The red hkl is shown to be more intense, whereas the green hkl is more sensitive to the change in the atomic position. Right: comparison in the sensitivity vs. intensity plot for the two reflections.

In the mathematical expression of the sensitivity, one can see that it is proportional to the intensity since it aggregates the absolute variation in spectra intensities. A "normalised" sensitivity can also be proposed, which, on the contrary, considers the relative variation in spectra, as shown in **Equation (III.13)**. Notwithstanding, the normalised sensitivity tends to be overestimated for reflections with very low intensity.

$$S_{hkl} = \int_{x_{min}}^{x_{max}} \int_{E_{end}}^{E_{start}} \left(\frac{I_{TS(x)}(E) - I_{av}(E)}{I_{av}(E)} \right)^2 dE dx \quad \text{(III.13)}$$

In all the REXS experiments hereafter, we have previously conducted a study of the intensity and sensitivity of the reflections. This has been extremely helpful in determining the best conditions for the study of a parameter of interest in a desired energy range. In order to rapidly obtain I vs. S plots of all reflections of any given system and for any set of parameters, a computer program has been conceived: *inserexs*, which is fully detailed in the next section of this chapter.

2. *inserexs*: reflection choice framework for REXS experiments

2.1. Motivation and general description

The *inserexs* (*I*ntensity and *S*ensitivity comparator for *REXS*) framework has been developed as a side project of this PhD work [187]. The program has been designed to help REXS users in knowing which reflections should be explored, in order to determine a certain parameter of their interest. *inserexs* has an open-source code which has been protected under a BSD license at the Agence de Protection de Programmes (French Agency for software protection), with the deposition number IDDNFR001490010000SP202200031325. It is free to use or modify with the proper authorship recognition and can be found in the following link: <https://github.com/antpeacor/inserexs>. *inserexs*' visual identity can be observed in **Figure III.4**.



Figure III.4. *inserexs* visual identity. The light blue curve represents a REXS spectrum, “in” stands for the intensity, “se” for the sensitivity and “rexs” for the homonymous diffraction technique.

The program has been written in Python and consists in several modules that communicate between each other, as ensuingly detailed. Implemented multithreading capability allows the simultaneous operation of the several modules which compose the general program. The interaction with *inserexs* is made through an intuitive graphical user interface (GUI), as shown in **Figure III.5**, from which one can load all the crystallographic data, insert which parameters are desired from REXS and visualise the program's output. The option of inserting the data without the GUI is also given. *inserexs* has been tested on Windows 10 and Ubuntu 20.040 LTS. At its current stage it already accomplishes the goal for which it has been designed for: being able to choose a reflection for the determination of an atomic position

or occupancy, before any real experiment takes place. Future releases will expand its current functionalities. An expanding user manual has been included in the software distribution.

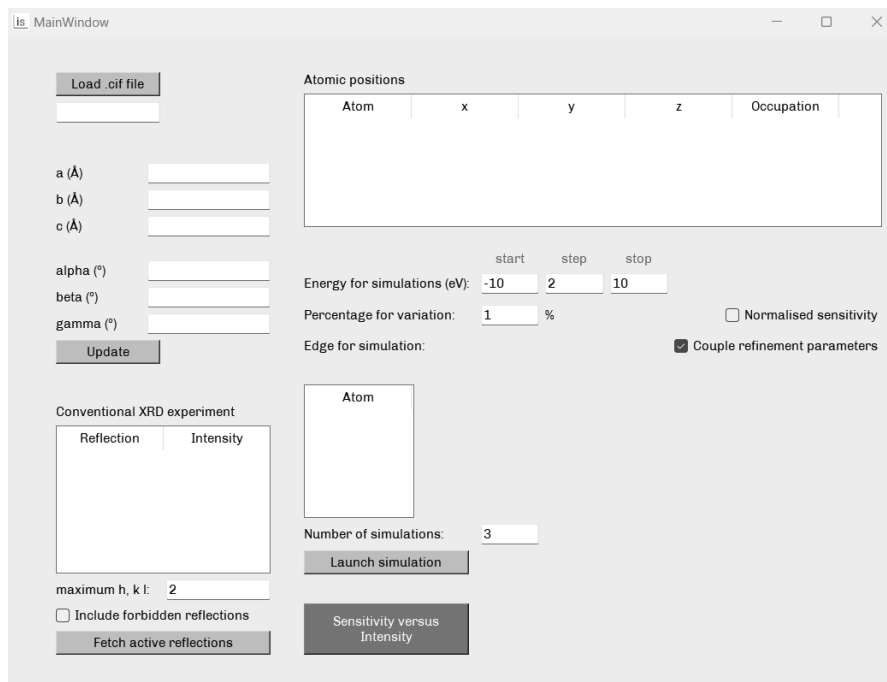


Figure III.5. User interface for *inserexs*, showing its main functionalities.

As previously described and as suggested by its name, the reflection evaluation in *inserexs* is conducted by assessing their relative intensity and sensitivity. For the intensity value, *inserexs* calculates the crystal's structure factor $F_{hkl} = \sum_i f_i e^{2\pi i(hx_i + ky_i + lz_i)}$ and approximates the intensity to $I_{hkl} \propto F_{hkl} \times F_{hkl}^*$. This enables the program to discern which reflections are allowed (nonzero intensity). *inserexs* generates all possible atomic positions (from the symmetry operations and the positions' information on the .cif file) and calculates F_{hkl} , considering each atom's atomic scattering factor (f_i). By default, *inserexs* designates a reflection as active when its intensity is larger than 0.1% of the intensity of the most intense reflection. This value can be manually changed in the intensity module.

For short and fast simulations, *inserexs* employs a rough approximation of considering the atomic scattering factor to be the atom's number of electrons. However, when specifically requested (by selecting "Include forbidden reflections" on the GUI), the program precisely calculates each atom's f_i by using the numerical tables of anomalous scattering factors calculated by the Cromer and Liberman's method [211]. For this method to function correctly, the file *Sasaki_anomalous* (distributed alongside *inserexs*) must be present in the directory where the code is executed. If the specific atom whose edge will be used for the simulations is identified, that atom's edge energy is the one used for the calculation of the atomic scattering factor. Otherwise, *inserexs* calculates the atomic scattering factors for an energy of 10 keV – order of magnitude of most cations' K-edges (not recommended). Independently of choosing

or not to consider the forbidden reflections, the plotted intensity will correspond to the one generated by FDMNES, for which each atomic scattering factor is individually calculated again.

The sensitivity and normalised sensitivity are calculated using the expressions given in **Equations (III.12) and (III.13)**. The former is the default value displayed by *inserexs* but the user can switch between these two measures upon request – by checking the available option on the GUI.

2.2. Program composition and module interactions

The program is comprised of three main modules which interact with the outer program FDMNES, as shown in **Figure III.6**. The first is the central module, whose function is to connect the rest of the modules and provide a structural foundation for the entire application. It is also directly linked to the user interface, from which the input takes place. It is also responsible for the data assembling and final display. The other two modules are in charge of obtaining the intensity and sensitivity values, respectively.

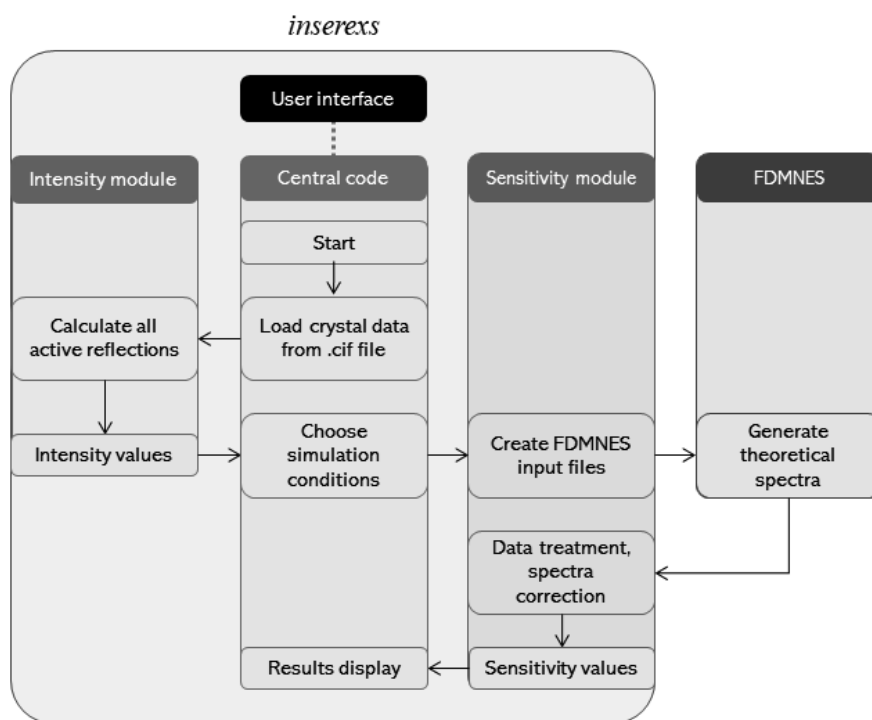


Figure III.6. Data flowchart for the calculation of the intensity and sensitivity values from an input file, showing the interaction between the program’s modules and between them and FDMNES.

From the GUI, one can load the crystal data as a .cif file. Alongside *inserexs* main code a “cif builder” tool has been distributed, for those cases where a .cif file is not available. The .cif file should follow the conventions indicated in the International Tables of Crystallography [212]. The code makes a line

recognition and attributes the different crystal parameters, which can be subsequently modified and updated directly from the GUI. Several .cif files have been successfully tested, each one with different writing styles and amount of information. However, some lines are essential for the proper operation of *insexs*. The whole list can be found in the user guide.

All the .cif information is transferred to the intensity module, which uses the crystal information to obtain the intensity of the non-null reflections. To this end, the program generates all the atomic positions from the .cif file's atomic positions and symmetry operations. Then, it removes redundant positions and, uses each unique position to calculate the structure factor for each reflection. By using the lattice parameters, it verifies whether the reflections are equivalent, and outputs those which are not. From the GUI one can choose either to neglect all forbidden reflections or to take them into account (despite not being seen in conventional XRD experiments they can sometimes be measured in REXS). A maximum value for the h , k and l values must be inserted (2 by default). In order to calculate all the possible reflections, a large number should simply be entered. The consideration of forbidden reflections significantly increases the calculation time.

For the intensity calculation, the module calculates the Thomson component of the atomic scattering factor, as well as its anomalous components [213]. Then, it calculates the structure factor, considering both the atomic scattering factors and the atomic positions. The output intensity has been approximated to the square of the structure factor.

The code considers a general triclinic case when angle-dependent calculations are needed for the atomic scattering factor. The set of intensities for each reflection can be retrieved from all these steps, although it gives similar results (and is faster) to ensuingly use the intensities given by FDMNES.

The code requires the user to make selections from the GUI which parameter will vary, how much it will vary, the energy range (start, stop and step) and the edge on which the simulation will take place. It is also possible to choose whether all parameters will vary simultaneously or independently. All this information, alongside the list of active reflections, is sent to the sensitivity module so that it generates proper FDMNES input files. Then, FDMNES and generates the simulations.

If the chosen edge or the chosen parameter do not respect the crystal structure, an error arises at this stage. If the process has been successful, the sensitivity module loads and processes the FDMNES output data and calculates the sensitivity, as previously defined. Finally, a sensitivity versus intensity plot is shown directly on the GUI. The plot is also automatically saved in the folder where the .cif was found.

2.3. Output showcase

Three examples will be shown in this section. As furtherly explained, in all of three structures the studied parameter directly affects the material's properties, and the best reflections for examining these parameters are plotted in a S vs. I plot.

All the parameters have been modified 1%. The results are shown in **Figure III.7**. An energy step of 2 eV has been chosen for the simulations, for percentual variation of the indicated parameters of 1%. A maximum value of 4 for h , k and l has been chosen. The first example pertains to a DANES experiments and aims at locating the cation which is directly explored, while the two others correspond to EDAFS experiments in which a cation is probed to indirectly determine the position or occupancy of the oxygen atoms.

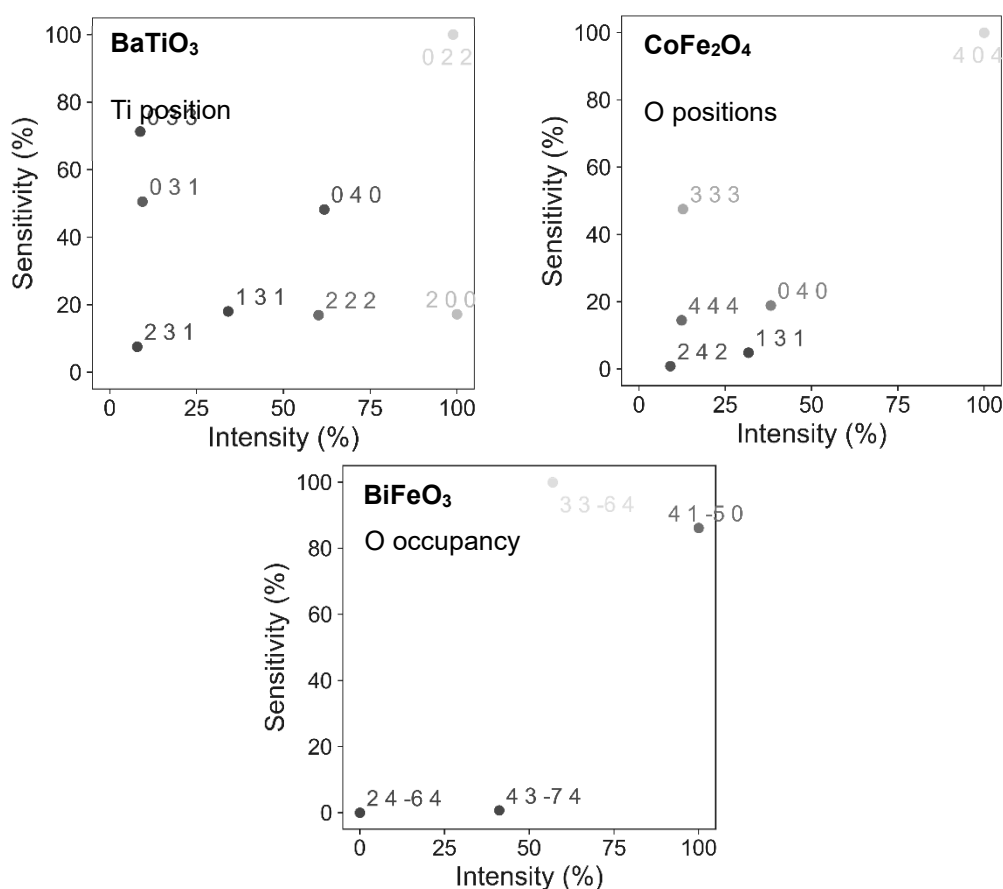


Figure III.7. Result display for the different systems (and varying parameters): BaTiO_3 (Ti position), CoFe_2O_4 (O positions), BiFeO_3 (O occupancy).

Firstly, the ferroelectric oxide BaTiO_3 ($P 4 m m$), whose polar behaviour arises from the displacement of the Ti^{4+} cation in the perovskite structure [214], [215] along the z direction. The XANES region of Ti (-50, +50 eV around the edge) has been selected, since it is sensitive to the cation's position. The 022 reflection proves to be the most sensitive to the Ti position and the most intense as well, whereas the

200 reflection is just as intense but not as sensitive. Another suitable reflection would be the 040, being both sensitive and intense; or 033, also sensitive to the regarded parameter.

The second system is the spinel oxide CoFe₂O₄ ($Fd\bar{3}m$), a hard ferrimagnetic spinel exhibiting excellent electromagnetic performance [216] and catalytic properties [217]. To determine the x position, the EXAFS part of one of the cations could be chosen (e.g. +20, +120 eV). For this material, and differently to the already studied FeV₂O₄ [188], the 404 reflection emerges as the most intense and highly sensitive to the oxygen positions.

The third studied crystal is the ferroelectric BiFeO₃ ($R3c:H$), whose electrical polarisation and switching dynamics are largely dependent on oxygen vacancies [218], [219]. In order to determine the occupation of the oxygen site, the same conditions for the EXAFS domain have been chosen on the Fe edge. The $33\bar{6}4$ is clearly the most sensitive to the occupation of the oxygen atoms and it is also intense enough to be considered. The $41\bar{5}0$ is the most intense reflection and it also possesses an important sensitivity. In this example, these two reflections are so intense and sensitive in relation to the oxygen's occupancy factor that the other reflections demonstrate almost negligible relative intensities and sensitivities.

In the subsequent section of this chapter, we will utilise *insexes* to identify the optimal reflections for the examination of both the cations in the spinel structure and the positions of oxygen atoms in FeV₂O₄ thin films.

3. DANES on FeV₂O₄ films: cationic distribution

As previously mentioned, the oscillations in the XANES part of a resonance spectrum can be used to study the electronic environment of the resonant atom. Due to the coordination difference in O_h and T_d sites, DANES be used to locate a specific atom, i.e., study its distribution between one or the two crystal sites. As it will be furtherly detailed, the direct observation of resonant atoms cannot be used for lighter ligand atoms (such as oxygen in our system), but DANES can be used for the location and site occupation of the cationic species. There already exist literature reports on DANES experiments being used for such a purpose on thin film systems [168], [220], [221]. The objective of this section is the study of the cationic distribution in FVO//MgO thin films.

The cation distribution in the Fe-V-O system can be expressed in the form of the following grid: (Fe_{1-x}V_x)_{Td}[V_{2(1-y)}Fe_{2y}]_{Oh}O₄, with x (y) representing the vanadium (iron) insertion in the T_d (O_h) sites. These parameters capture the occupancy factor of Fe in the T_d (1 - x) and O_h (y) sites, and V in the O_h (1 - y) and the T_d (x) sites, and explain the deviation from a perfect direct spinel structure (Fe^{II})_{Td}[V^{III}]_{Oh}O₄ (x = y = 0). The possibility of unoccupied crystal sites has not been treated in this work, since it would increase the dimensionality of the study (overcoming our available simulation resources) but, as furtherly shown, an unequivocal cationic distribution can be attributed despite the limitations that this assumption arises. Finally, in this DANES study, the oxygen position has been kept as that of the bulk documented in the literature ($x = 0.2617(1)$) [53]. Variations from this value are not expected to significantly alter the simulated REXS profiles.

The *insexe*s S vs. I, illustrating the occupancy of the cationic sites, is represented in **Figure III.8**, and has been obtained via small variations (5 %) of both (x, y) for each cationic species, simulated in the [- 20 eV, + 20 eV] domain around the absorption edges.

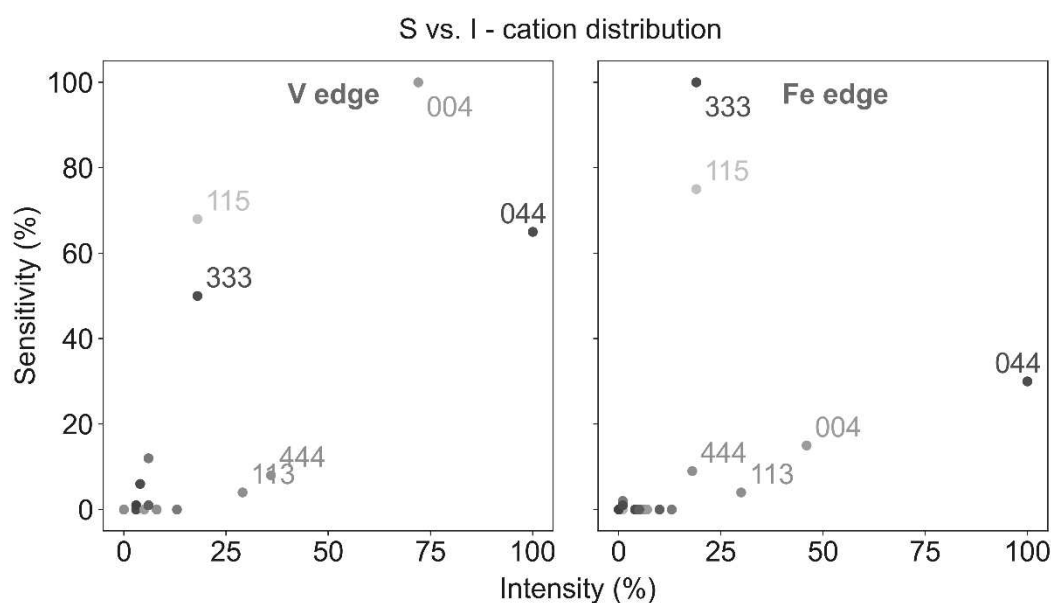


Figure III.8. S vs. I plot for the cation distribution simulated for both edges (V and Fe).

In spite of the structural tetragonality of the thin films, a pseudo-cubic crystallographic setting will be used to refer both the bulk cubic structure and the tetragonal structure of the films. The structural information for the simulation has been taken from the crystallographic parameters obtained in the second chapter of this thesis – **Table II.1** on page 76.

The plots at both edges (Fe and V) do not differ significantly. Both edges appear suitable for the characterisation of the cationic occupation. The main difference lies in their energy levels: 5481 eV for V [222] and 7111 eV for Fe [223], [224]. Due to the smaller wavelength of the incident X-rays, this latter edge will present fewer self-absorption issues and a better signal-to-noise ratio, leading to finer and clearer REXS spectra. The Fe K-edge has been therefore chosen for all the REXS experiments.

In terms of the reflection choice, the reflection sensitivity has been prioritised because of the considerable intensities obtained in Synchrotron radiation facilities: 333 and 115. The more intense reflections (004 and 044) also present the drawback of being shared by the substrate (as 002 and 022). Despite REXS being an element-sensitive technique, the presence of Fe traces in the much more massive MgO substrate (confirmed by EDS) might interfere the spectra acquired in the near-edge energy range. This phenomenon is also enhanced by the fact that the beam penetration in the hard X-ray region (as it is for Fe K-edge) strongly probes the substrate. In conclusion, the reflections 333 and 115 both present the advantages of high sensitivity to changes in the cationic distribution and they produce oscillations that can be entirely attributed to the spinel thin film.

EDAFS spectra have been acquired at the D2AM beamline of the ESRF Synchrotron Radiation Facility. The difference (χ^2) between the experimental (ES) and theoretical (TS) spectra was determined according to **Equation (III.11)** for both reflections: $\chi^2 = \chi^2_{333} + \chi^2_{115}$. The ES presented an energy shift (E_s) in the overall spectrum profile, alongside a slope caused by the air's absorption (m). The TS and ES have been normalised (with $I_{corrected} = (I - I_{min}) / (I_{max} - I_{min})$) so that their intensity values fall into the [0, 1] range. A scale factor ($\times s$) and a baseline ($+ b$) were employed to align the TS with the ES profiles, alongside the E_s values. Both experimental and theoretical spectra have been acquired/simulated in the EXAFS region: from -20 to $+20$ respect to the iron's K-edge.

For each (x, y) combination in the [0, 1] range – with steps of 0.05 – the smallest χ^2 has been calculated with free varying (E_s, s, b, m) parameters. The χ^2 values as a function of (x, y) have been shown in **Figure III.9**. Upon initial observation, it is noticeable that the region in the lower bottom corner presents the smallest χ^2 . Theoretical spectra in this zone have been simulated with a smaller step between each successive x and y values step (0.02).

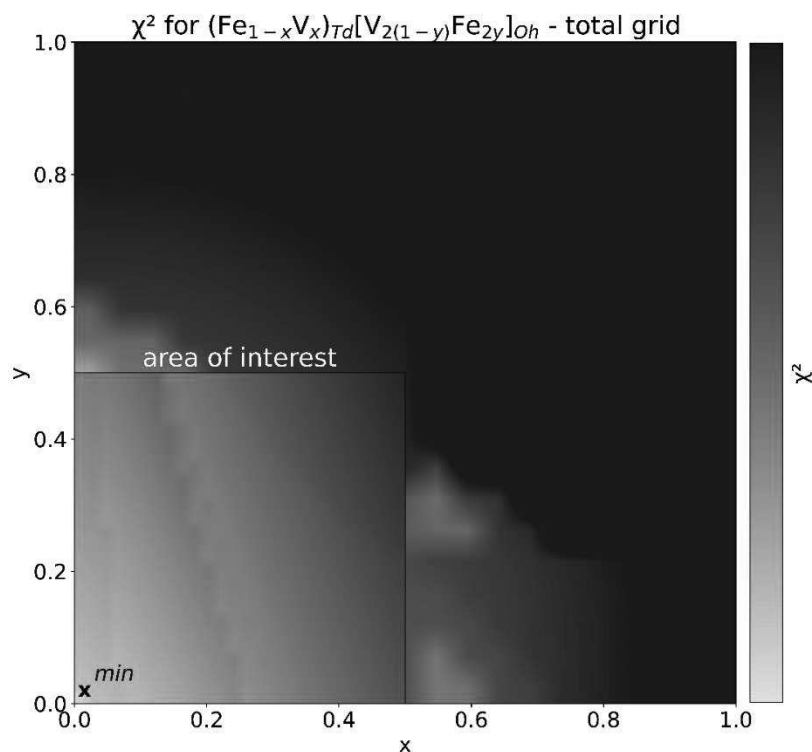


Figure III.9. χ^2 as a function of x and y (both from 0 to 1) in order to determine the cationic occupation at the crystal sites, with a close-up look on the region with the smallest χ^2 .

A mathematical minimum for χ^2 has been found for $x = 0.015(5)$ and $y = 0.020(3)$. However, the determination of this minimum is constrained due to the abrupt termination at $x = 0$ and $y = 0$ in the 3D space defined by (x, y, χ^2) . The TS which matches the ES the best is the one simulated for $(x = 0, y = 0)$, as represented in **Figure III.10**.

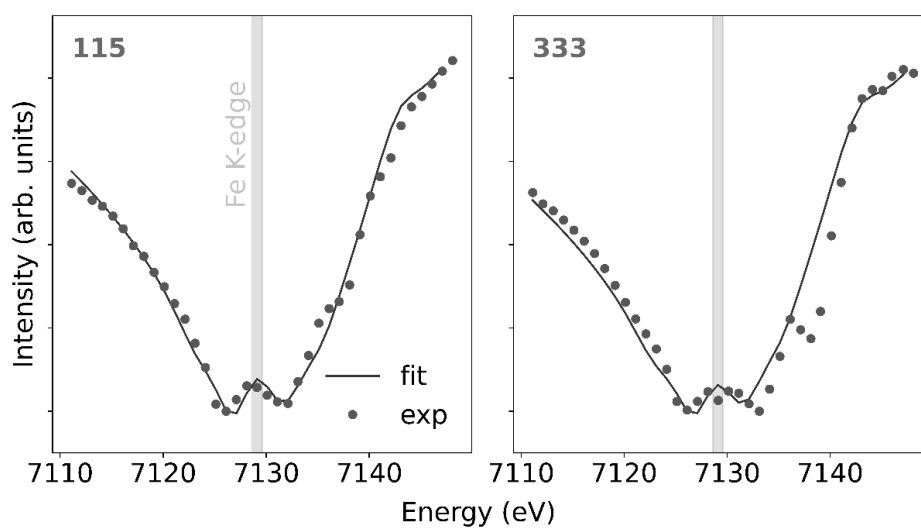


Figure III.10. DANES spectra around the Fe K-edge (-20, +25 eV) for the 115 (left) and (333) reflections: experimental (green-dotted) and simulated with $(x = 0, y = 0)$ (blue lines)

The Fe-V-O system has been described using a $(\text{Fe}_{1-x}\text{V}_x)_{\text{Td}}[\text{V}_{2(1-y)}\text{Fe}_{2y}]_{\text{Oh}}\text{O}_4$ mesh, which represents variable cationic occupancies. The cationic distribution that yields the best match between the TS and acquired ES would be $(\text{Fe}_{0.985(5)}\text{V}_{x0.015})_{\text{Td}}[\text{V}_{1.960(6)}\text{Fe}_{0.040(6)}]_{\text{Oh}}\text{O}_4$ if the mathematical minimum is considered or $(\text{Fe}_{1.00}\text{V}_{0.00})_{\text{Td}}[\text{V}_{2.00}\text{Fe}_{0.00}]_{\text{Oh}}\text{O}_4$ by taking the individual (x, y) combination with the smallest TS-ES χ^2 .

Such cationic contribution can adopt two forms, depending on whether the divalent species occupies the T_d or O_h sites: $(\text{Fe}^{\text{II}})_{\text{Td}}[\text{V}^{\text{III}}_2]_{\text{Oh}}\text{O}_4$ (direct spinel) or $(\text{Fe}^{\text{III}})_{\text{Td}}[\text{V}^{\text{III}}\text{V}^{\text{II}}]_{\text{Oh}}\text{O}_4$ (inverse spinel). The former scenario is the most probable, since iron is more easily reduced than vanadium. In addition, the divalent form of vanadium has stability issues, the direct spinel structure is electronically more stable and the $(\text{Fe}^{\text{II}})_{\text{Td}}[\text{V}^{\text{II}}_2]_{\text{Oh}}\text{O}_4$ is also favoured by Jahn-Teller phenomena in both T_d and O_h sites.

These results can be confronted with the magnetic characterisation part of this thesis, by taking into account the magnetisation at saturation (M_s) of the films, as presented in the section “Magnetic properties of FeV₂O₄ thin films” of the second chapter of this thesis – page 77. Unfortunately, vanadium atoms present a non-negligible orbital momentum and the measured M_s cannot be used to leverage the antiparallel alignment of O_h and T_d species with their spin-only momenta. Subsequent experiments will concentrate on the degree of cation oxidation to definitively confirm the anticipated direct spinel structure.

4. EDAFS on FVO films: oxygen positions

In the previous section, a DANES-based approach has been used to characterise the cationic species of a thin film by resonant experiments at the K-edge of one of the own resonant atoms (Fe). Formerly, other experiments conducted on thin films systems had already been shown successful in probing the metallic cations through resonance at their K-edges [220], [221].

Unfortunately, this approach cannot be directly applied to probe oxygen atoms in oxide thin films. Resonance at the absorption edge of oxygens is not practically feasible, due to the low energy (530 eV) [225] and hence long wavelength (2.3 nm) of this edge. These values imply too strong absorption issues [226] and the impossibility to study small-sized crystallographic cells, such as those of most oxides. The direct probing of oxygen atoms is not straightforward.

EDAFS has already been used for the solving of crystallographic structures by the analysis of the EXAFS oscillations, which can be related to the interatomic distances [227], [228]. Scanning beyond a cation's edge, one can place its surrounding ligands in a sphere whose radius is the interatomic distance. If the ligands are in a position (x, y, z) that depends on several parameters, more than one solution will place them in the described sphere, and it will be hard to unequivocally locate them by this approach

We hereby propose to directly fit the EDAFS spectra for the refinement of the oxygen positions, using the aforementioned approach for DANES spectra. This strategy, however, would be only valid if the beyond-the-edge REXS profile is sensitive enough to a change in the oxygen atoms, and if the simulated intensities can be attributed to specific oxygen positions. Firstly, the methodology for validation involved theoretically demonstrating that EXAFS spectra are indeed sensitive to oxygens' positions. Prior to the experimental validation, we have proven that it is feasible to unequivocally determine these positions through a fitting procedure of REXS spectra intensities with FDMNES [210].

Secondly, the entire procedure underwent experimental validation. For that purpose, a bulk sample has undergone both the classical strategy for the determination of the atomic positions (S-XRD and Rietveld refinement [229]) as well as the approach that we present. As ensuingly shown, the values found using EDAFS are equivalent to the classical method. Then, the whole procedure has been carried out on the thin film sample.

For the bulk sample, REXS measurements were carried out at the DIFFABS beamline of SOLEIL Synchrotron, covering an energy range of (-40 eV, +240 eV) around the Fe K-edge (around 7130 eV) [223], widely scanning thus both XANES and EXAFS parts of the Fe absorption spectrum. A dedicated Python code was developed for the treatment and refinement of these EDAFS data. S-XRD measurements with $\lambda = 0.67122$ nm were performed at the Cristal beamline. The refinement of the S-XRD data was carried out using the FullProf-WinPLOTR software [230]. For the thin film, REXS experiments were performed at the d2am beamline of ESRF Synchrotron with the same energy range as the powder sample. Unless indicated otherwise, all measurements have taken place at room temperature.

4.1. Theoretical validation

Spectra simulations have been carried out in the range [-50, + 250] around the absorption edge. A 0.2 step has been chosen for the [- 50, + 50] part (more sensitive) and a 0.5 step for the [+ 50, + 250] part. The XANES part has been kept to facilitate the intensity normalisation of the TS (and even more useful later for the comparison with the ES). Atomic coordinates were fixed for the cations, which occupy fixed special positions ($F d \bar{3} m$, setting 2): Fe at the 8a (1/8, 1/8, 1/8) and V at the 16a position (1/2, 1/2, 1/2). The theoretical lattice parameter value was chosen for the simulations. Repeating the process with the value found through S-XRD led to practically no change in the final result.

As displayed in **Figure III.11**, the sensitivity versus intensity plot (generated using *inserexs*) indicates that both the 115 and 333 reflections are yet again the most responsive to the positions of the oxygen atoms. Owing to the powdery nature of the sample, when measuring the 333 reflection, the acquired intensity would also include the 511 reflection (for both: $h^2 + k^2 + l^2 = 27$). Consequently, we considered a composite of 333+511, in addition to the 004 reflection, which is the third most sensitive and also the most intense.

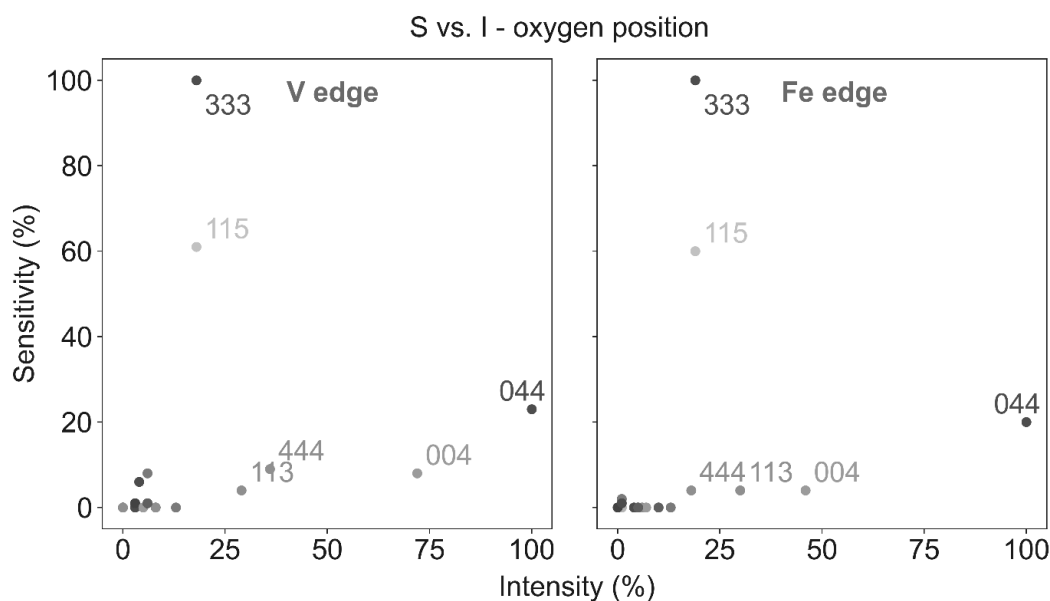


Figure III.11. Sensitivity vs. Intensity plot to the oxygen position for all actively diffracting for FVO, for both the V and Fe K-edges.

All parameters were kept constant, including the lattice parameter and the positions of the cations, with the exception of the oxygen atoms' positions (x). For this simulation part, structure parameters were taken from the literature [53]. Besides, owing to geometry reasons, x is expected to have a value close to 0.25 and spectra were therefore simulated in the range x : [0.230 – 0.280].

To validate the potential of fitting EXAFS spectra to determine oxygen positions, an initial fitting process was conducted on a pseudo-experimental spectrum (p-ES). For that aim, a Gauss-centred random noise

was added to the simulated theoretical spectra, as shown in **Figure III.12**. This figure clearly illustrates the pronounced sensitivity of the 333 to the positions of the oxygen atoms. At a later stage, a random Gauss-centred energy shift was introduced, simulating the experimental conditions encountered in REXS measurements.

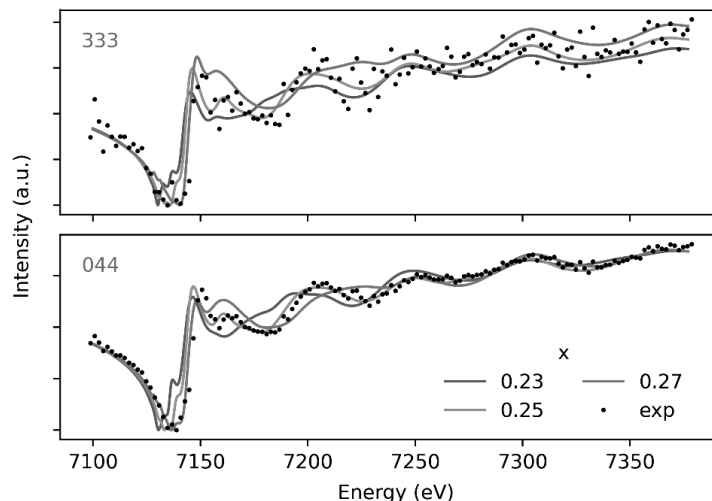


Figure III.12. p-ES for $x = 0.25$ (black) and TS (colored) for various x values, around Fe K-edge for the 333 and 044 reflections.

Through repetition of the noise generation and fitting processes 10,000 times, it was possible to estimate an error bar via the Bootstrap method [231], [232]. The resulting p-ES, generated with $x = 0.25$ and zero energy shift, was then fitted by comparison with the theoretical spectra. For each x and energy shift (E_i) values, a difference (χ^2) between the intensity of p-ES, $I_{p-ES}(E)$, and the TS, $I_{TS(x=x_i)}(E + E_i)$, is calculated, as defined in **Equation (III.14)** – based on **Equation (III.11)**. This process is repeated for all considered reflections (j).

$$\chi^2_{j(x_i, E_i)} = \int_{E_{min}}^{E_{max}} \left(I_{p-ES}(E) - I_{TS(x=x_i)}(E + E_i) \right)^2 dE \quad (\text{III.14})$$

When considering the whole set of reflections which are studied, the total error takes the form of: $\sum_j \chi^2_{j(x_i, E_i)}$. The fitting of the Fe edge p-ES leads to a minimum $x = 0.2500(2)$, as displayed in **Figure III.13**. Therefore, the theoretical feasibility of determining the position of the oxygen atoms through a fitting procedure of the EDAPS spectra has been demonstrated.

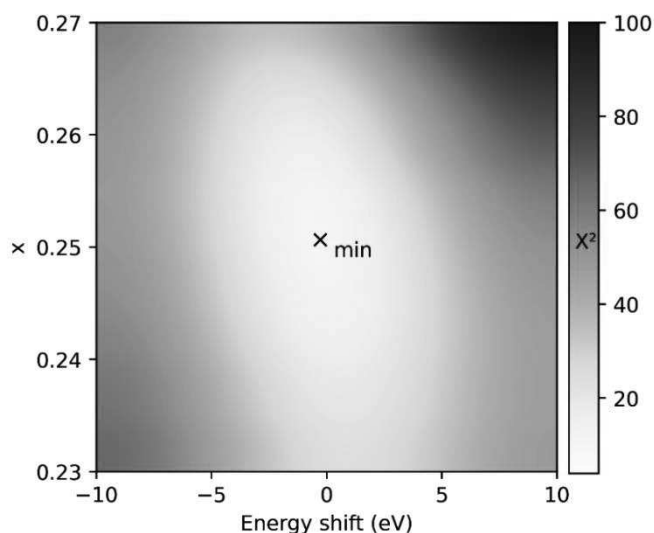


Figure III.13. χ^2 as a function of the oxygen position, x , and the energy shift. The cross named “min” represents the x and energy shift coordinates leading to the smallest χ^2 .

4.2. Experimental results

4.2.1. Results on powder sample, proof of concept

The S-XRD diffractogram measured for the synthesised FVO powder is shown in **Figure III.14**. While a negligibly small parasite phase attributed to the Fe₂O₃ precursor is noticeable, it doesn't interfere with our study's results as the refinement focuses on the position and relative intensities of FVO peaks.

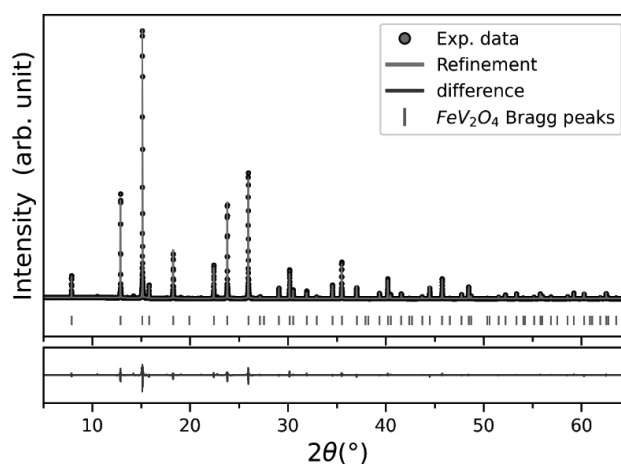


Figure III.14. XRD experimental diagram for $\lambda = 0.67122 \text{ \AA}$ (black) and the best refinement obtained with Fullprof (red).

By employing a profile matching analysis, the lattice constant was found to be $a = 8.4575(1) \text{ \AA}$, which aligns with previously reported results [53]. Using this value, a Rietveld refinement was done, which led to an outcome of $x = 0.262(2)$ for the oxygen atoms positions. The complete set of refined atomic positions has is listed in **Table III.1**.

Table III.1. Atomic positions of bulk FVO. $Fd\bar{3}m$ space group (origin choice 2).

Atom	Position	Atomic coordinates
Iron	8a	0.125, 0.125, 0.125
Vanadium	16d	0.5, 0.5, 0.5
Oxygen	32e	0.262(2), 0.262(2), 0.262(2)

REXS spectra were acquired on the same capillary as the one used for S-XRD measurements. FDMNES was again used to simulate spectra for a complete meshing of oxygen positions and energy shifts. Our simulations also took into account the substantial self-absorption displayed by the powder sample. Ideal occupancy factors (Fe: 8/192, V: 16/192, O: 32/192) were considered. A fitting of these factors shows that the experimental occupancy factors are close to the ideal values.

The experimental REXS spectra were compared to the simulated ones, as shown in **Figure III.15**. Slope and intensity normalisation corrections, not depending on the material itself but on the measurement conditions, were performed before data analysis.

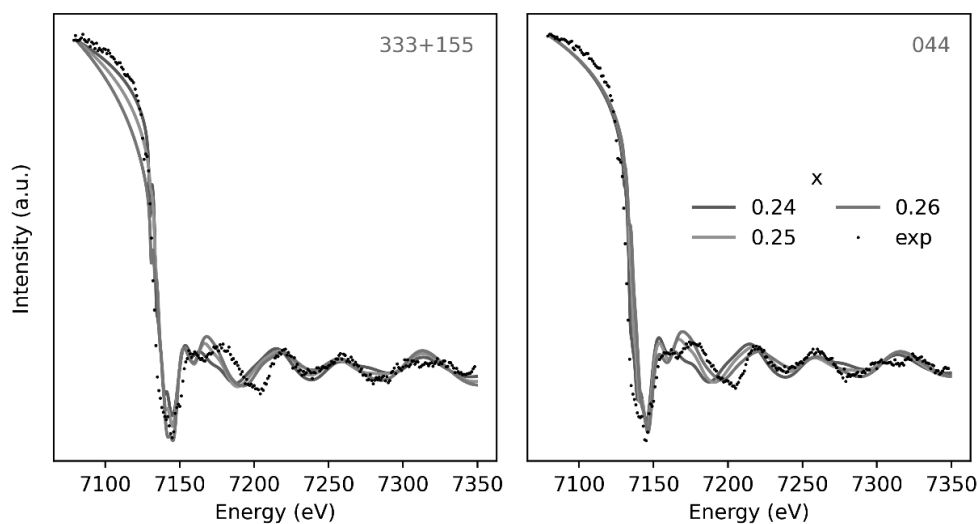


Figure III.15. REXS spectra acquired at the Fe edge for the 333+115 and 044 reflections, compared to the simulated TS at different x .

The procedure used on the p-ES was repeated with the experimental spectra. The results of the refinement procedure can be seen in **Figure III.16**, with $x = 0.2625(2)$. This value found for the oxygen positions perfectly matches the one obtained via the Rietveld refinement of the S-XRD. The procedure was reiterated, varying the starting energy value for the refinement (7200 eV) by ± 20 eV. This led to negligible changes in the oxygen position value or the energy shifts.

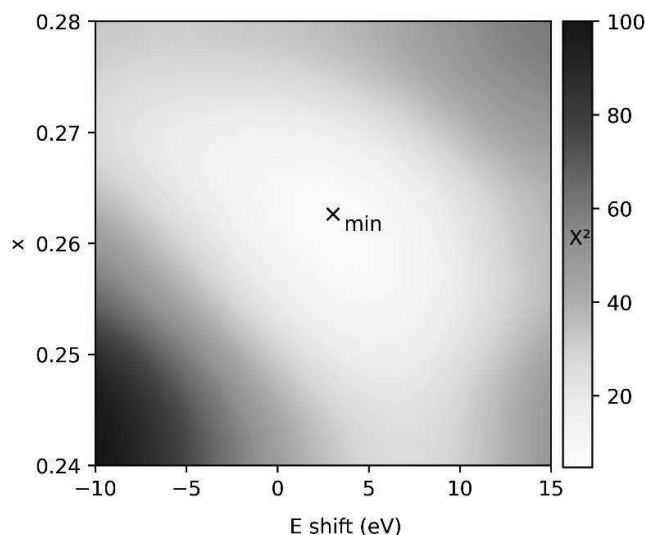


Figure III.16. χ^2 as a function of x (oxygen position) and the energy shift, for the experimental spectra in the FVO bulk sample.

Another refinement was performed on the XANES part of the Fe absorption spectrum (7050 to 7200 eV) using the previously described procedure. Oppositely to EDAFS fitting, the refinement conditions highly affected the found value for the oxygen positions. In addition, the error was too high to consider the results reliable. Scanning the EXAFS part of the spectrum, which mostly depends on the oxygens (neighbouring ligands), seems hence necessary for an exact determination of their positions.

4.2.2. Oxygen positions in a thin film system

The complete EDAFS procedure was subsequently applied to a 25 nm MgO//FVO thin film sample. Due to the substrate strain, FVO presents a distorted spinel tetragonal structure, crystallising in the $I4_1/amd$ space group. As a result, the oxygens' positions in the thin film (0, y , z) depend on two parameters. Analogously to what done for the bulk sample, in the χ^2 minimisation the energy shift was considered as a third parameter, minimising it for each (y , z) set.

MgO crystallises in the $Fm\bar{3}m$ space group ($a = 4.21$ Å) and has 022 as an active reflection. Since the substrate presents much more matter than the thin film, it completely eclipses the 044 reflection of FVO,

which becomes unexploitable. The chosen RLPs are then 311 and 511. This prevents any error caused by Fe inserted in the much more massive MgO substrate – whose presence has been verified via EDS.

The FVO film's lattice parameters are $c = 8.441(7)$ Å and $a = b = 8.463(3)$ Å, as presented in the second chapter of this thesis – **Table II.1**, page 76. This structural information has been used for the generation of the theoretical spectra. The χ^2 minimum was found for $y = 0.467(1)$ and $z = 0.267(1)$, as shown in **Figure III.17**. This minimum falls in a χ^2 valley of (y, z) values leading to small differences, and the error values seem underestimated. The found (y, z) , however, fit well the 311 and 511 spectra, as shown in **Figure III.18**. The complete set of atomic positions for the thin film has been listed in **Table III.2**.

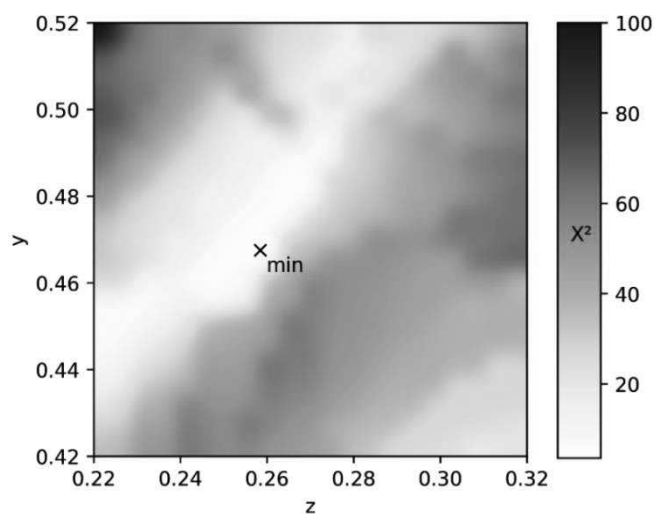


Figure III.17. χ^2 as a function of z and y , parameters defining the oxygen positions, for the FVO//MgO thin film. The “min” represents the (y, z) set leading to the lowest χ^2 .

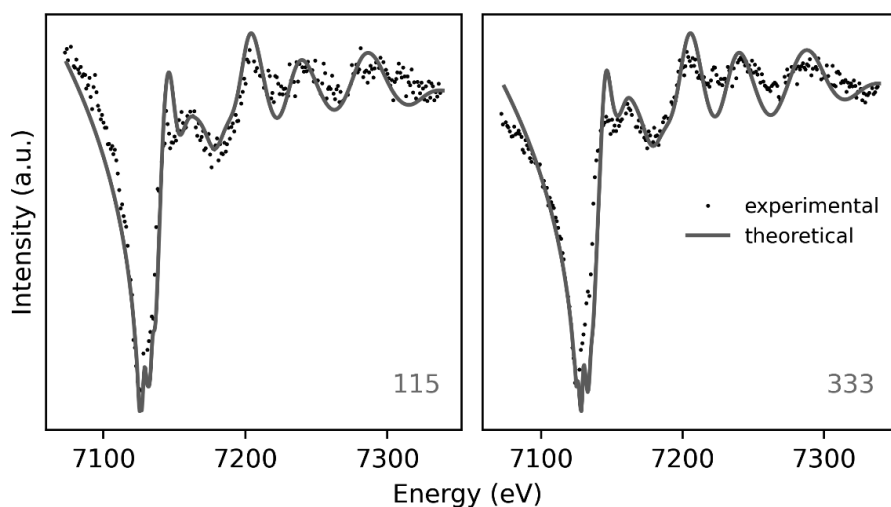


Figure III.18. REXS spectra for the experimental 511 and 333 reflections compared to the theoretical data, for the FVO//MgO thin film.

Table III.2. Atomic positions of FVO thin films. $I 4_1/am d$ space group (origin choice 2).

Atom	Position	Atomic coordinates
Iron	4a	0, 0.75, 0.125
Vanadium	8d	0, 0, 0.5
Oxygen	16h	0, 0.467(1), 0.267(1)

Although the signal-to-noise ratio isn't as good as for the bulk, a mathematical minimum was found, facilitating the location of the oxygen atoms. Scanning additional RLPs could improve calculation statistics and lead to a more accurate determination. However, and despite the limited amount of matter, we managed to determine the positions of the oxygen atoms in a 25 nm thin film.

To summarise, the position of the oxygen atoms, defined by the x parameter in the bulk FVO sample, has been found the same for the Rietveld refinement of the S-XRD data – 0.262(2) and the approach we have presented in this study – 0.2627(2), which constitutes a proof of validation for our approach. As we demonstrated with FVO//MgO, this method is applicable to thin-film systems. Despite the small quantity of matter, the oxygen positions have unambiguously been determined in a non-destructive way.

Our approach, extending the methods of structural studies that use DANES to probe cations in thin films [168], now also allows indirect probing of the ligands surrounding the cations. It can naturally be generalised to any system other than a spinel oxide. However, lower symmetry systems may have more parameters to fit, requiring more simulation time and making the refinement process harder. In dealing with multiple parameters, instead of employing a complete meshing strategy, an appropriate choice of simulation conditions could be made for the χ^2 minimisation process until the refinement process converges unequivocally into a singular result.

In conclusion, this study has demonstrated the adequacy of a non-destructive REXS-based approach in determining the position of oxygen atoms, as proven by the study conducted on a bulk sample. We have then applied the method to a thin film to prove its efficiency in the case of a small amount of matter. The honing of this technique will enable the complete probing of the atomic positions in nanosized systems and will surely ease the conception of future thin-film based devices.

4.3. Oxygen positions as a function of temperature

In the spinel structure, the position of the oxygen atoms corresponds to the corners of the polyhedral in both octahedral and tetrahedral sites. In bulk FVO, previous studies have linked the changes in the

oxygen positions with the geometrical distortions inside the lattice as a function of temperature [28], [53].

These geometrical distortions are quantitatively analysed via a study of the normal modes, i.e., the patterns of vibration that encompass the whole crystal lattice. These normal modes are quantified by the difference of position between the ligand in the ground state (or high-symmetry structure) and its position in each state [27], [52]. These distortions along certain directions can be linked to shifts in the electron cloud distribution, which naturally induce a change in the energy of the electronic levels. Such phenomena can be explained by the interplay of JT and SOC effects in the lattice. Besides, these distortions can steer the arrangement of electron orbitals over long distances, which can manifest in the form of an orbital ordering. In conclusion, changes in the oxygen position can be connected to the lattice distortions in the sites, which could result in more stable orbital occupations and long-range orbital orderings.

In a different run from the work presented so far, REXS spectra covering both XANES and EXAFS [- 20 eV, + 200 eV] have been acquired as a function of temperature at both 115 and 333 reflections, as shown in **Figure III.19** and **Figure III.20**, respectively.

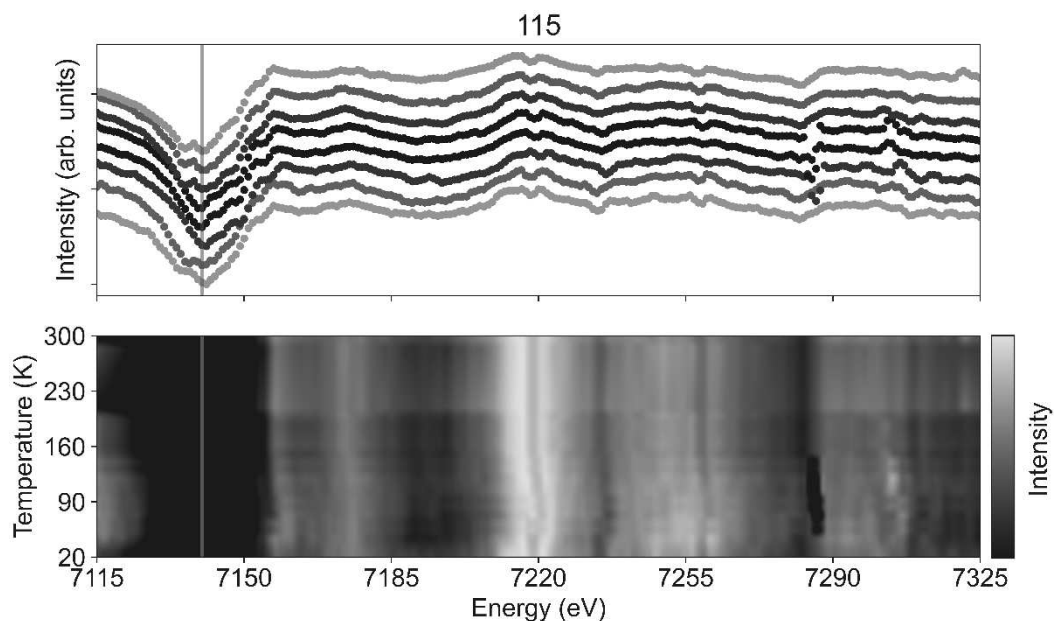


Figure III.19. 115 reflection. Top: Intensity vs. Energy for different temperatures (warmer colours indicate higher temperatures). Bottom: colourmap of intensity as a function of temperature and energy.

Neither of the two reflections displays dramatic changes in their spectra as the temperature varies. The χ^2 minimisation process was repeated with the same theoretical spectra previously generated, leading to the minima which are showed in **Figure III.21**. The study of oxygen positions with temperature presents a major drawback: the theoretical spectra are generated with lattice parameters which

correspond to room-temperature measurements on the thin films, and they can suffer substantial changes with temperature.

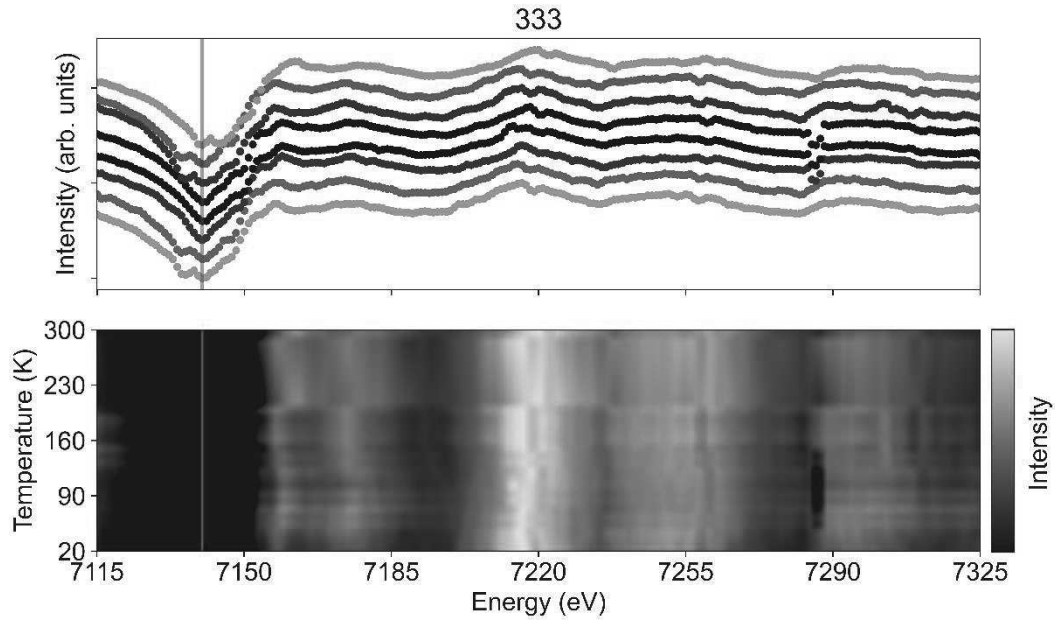


Figure III.20. 333 reflection. Top: Intensity vs. Energy for different temperatures (warmer colours indicate higher temperatures). Bottom: colourmap of intensity as a function of temperature and energy.

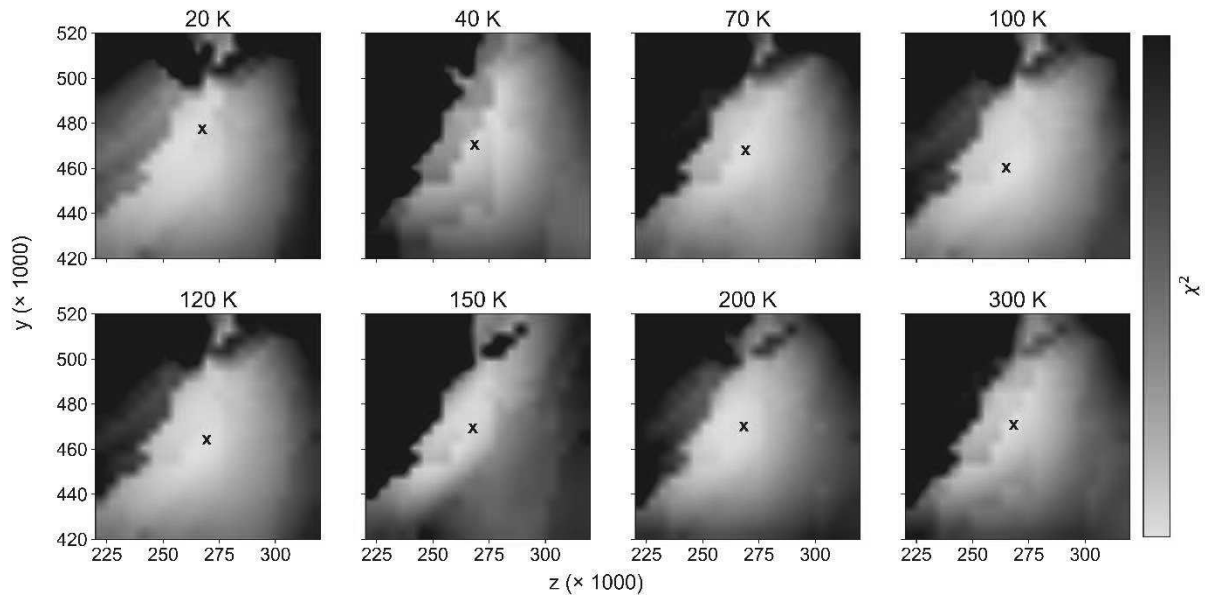


Figure III.21. χ^2 as a function of z and y , parameters defining the oxygen positions, for different temperature values. y and z values have been multiplied $\times 1000$. The “x” represents the (y, z) combination leading to a minimum χ^2 .

A solution to this issue would be to acquire RSM images at different temperatures to obtain the actual lattice parameters at each temperature. This work is currently underway. These temperature-dependent values could be used as input for FDMNES for further spectra generation, which would significantly increase the already high computational needs of this study. Despite acknowledging the limitations of this analysis, χ^2 values were calculated for spectra acquired at different temperature values, using spectra simulated with room-temperature lattice parameters.

A minimum χ^2 can be found for all the spectra, located within the χ^2 -valleys of (y, z) values. The evolution of $(0, y, z)$, representing the oxygen positions in the thin films, as a function of the temperature is shown in **Figure III.22**. The value found at 300 K in this second run is $y = 0.468(1)$ and $z = 0.266(1)$, while the values found in the first run were $y = 0.467(1)$ and $z = 0.267(1)$, which can be considered equivalent when considering the uncertainties. Small variations can come from the fact that the first run's thin film was substantially thinner (25 nm instead of 40 nm) and the strain effects might play a more important role.

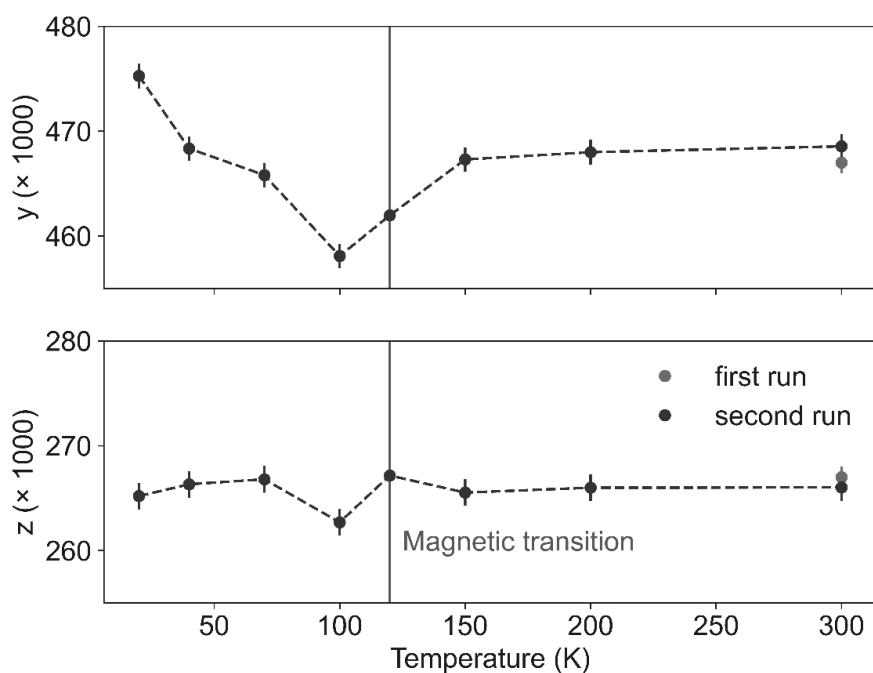


Figure III.22. Evolution of y and z parameters – with oxygen atoms being at $(0, y, z)$ as a function of temperature.

The values for z remain constant with temperature, except for an anomalous behaviour at 100 K, which could be an outlier. For y , however, the values seem to decrease with temperature and then increase after a temperature which coincides with the magnetic transition in the thin film, until reaching a plateau for higher temperature values.

In conclusion, this second experimental run affirmed the findings of the first analysis by identifying the same values for the oxygen position. It demonstrates the reproducibility of the technique utilised, and the ability of using EDAXS analyses for the location of oxygen atoms in oxygen thin films. The refinement of temperature-dependent spectra remained constrained in this study due to the limitations arising from a lack of knowledge about the lattice parameters. Future work will revisit this data, taking these limitations into account.

Additionally, it should be noted that, despite the success of the current technique, the χ^2 minimisation process is computationally demanding: a single minimisation process can take several hours or days to complete and each minimisation trial must be independently launched. As a result, the aforementioned approach cannot be used for *in situ* analyses (while the spectra are being acquired). In the next section of this chapter, a more efficient alternative procedure for spectra refinement will be introduced, leveraging machine learning tools to accelerate the process.

5. Neural networks for the refinement of REXS spectra

5.1. Artificial neural networks and REXS spectra

Python programming, and more specifically, its built-in Data Science libraries, have played a critical role in all the analysis presented in this thesis so far. Several methodologies in the form of *Jupyter notebooks* have been conceived for diverse purposes: the treatment of magnetic and transport data, the refinement of x-ray diffractograms, etc. The notebook compendium has been shared in the form of a repository project: “*junoda*, notebook codes for the treatment of scientific data”, which can be accessed in <https://github.com/antpeacor/junoda>.

Regarding the refinement of REXS spectra, *numpy*'s vectorisation utilities proved instrumental in facilitating χ^2 minimisation processes, as it can be seen in the ad hoc *junoda* notebook. This minimisation involved calculating n -dimensional χ^2 matrices, with n being the number of free parameters. This task required substantial computation time, often stretching into hours or even days with our current computational resources (64-core computer). The “mesh” or “grid” system of TS-ES comparison also necessitates the simulation of all possible TS points with FDMNES. Given our available computing resources, this also required an extensive amount of time. Despite the success of the aforementioned techniques, their high computational cost presents a significant obstacle, making real-time data analysis impractical.

Artificial Neural Networks (ANNs) offer a potential resolution to the aforementioned computational challenge. Drawing their name and inspiration from the biological neural networks present in our brains, ANNs belong to a class of algorithms within the expansive field of Machine Learning (ML). ANNs can be envisioned as a network of nodes, or “neurons,” interconnected by “synapses.” [178] Each neuron i in a given layer l receives an input from the previous layer (\vec{x}^{l-1}). Then, it processes it using a function determined by the model's design (the activation function – $g(h_i)$), and sends the output (x_i^l), to the next layer. The strength of the connections, also known as weights (\vec{w}_i), are initially random and are adjusted during training to help the network learn and make accurate predictions. Each neuron presents also a “bias” (b_i) which helps control the sensitivity of the neuron's response. Taking into account all these elements, a neuron's output takes the form of $x_i^l = g(\vec{x}^{l-1} \cdot \vec{w}_i + b_i)$ with $h_i = \vec{x}^{l-1} \cdot \vec{w}_i + b_i$ being the net input to the neuron.

An ANN model is constituted by a diversity of neuron layers: a single input layer, multiple hidden layers (with their number and complexity influencing the model's performance), and a final output layer. This architectural construct has been schematically represented in **Figure III.23**. The network refines its efficacy through a training process that entails learning from a pre-established dataset, termed the training set. This set comprises known inputs and their corresponding desired outputs. The goal of the training is to reduce an error function - typically the sum of the squared differences between the network's outputs and the desired ones - by tweaking the weights between connected neurons. To

assess different neural network architectures, an independent validation set is used, also known as cross-validation (CV) set. The CV set helps selecting the highest-performing architecture. Lastly, a separate test set is employed to evaluate the finalised neural network's performance level, providing a confidence measure for its utility [233]–[235].

The chief advantage of ANNs is their capacity to learn and adapt without the need for explicit programming, a vital characteristic when contending with tasks of significant complexity and computational intensity. They effectively learn to recognise patterns within the data by training on a multitude of examples, which can be particularly advantageous for large-scale data analysis.

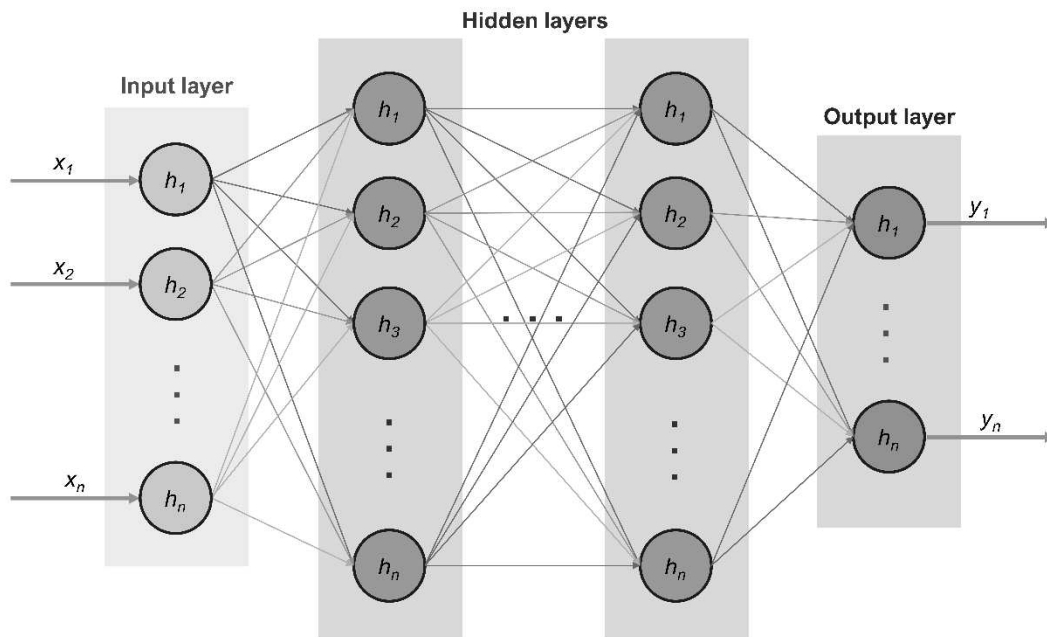


Figure III.23. Schematic representation of an ANN architecture with an input layer, several hidden layers and an output layer. The h_i factor on each neuron represents the net input which is passed to the activation function, and which considers the weights and bias of the neuron: $h_i = \vec{x}^{l-1} \cdot \vec{w}_i + b_i$. The scheme has been inspired by Fernández-Cabán et al. [236].

Within the context of REXS spectra analyses, an ANN model can be trained utilising a set of relevant parameters (one or more) in conjunction with the theoretical spectra generated for these parameters. Then, it learns to associate the different oscillation patterns to changes in the crystal structure. Unlike the “mesh” method mentioned earlier, a well-trained ANN model can provide immediate output in the form of interest parameters and eliminates the need for prior simulation of all possible combinations of parameter sets.

ML-based algorithms have already been used for the refinement of REXS spectra. For instance, the *PyFitIt* Python framework provides ML strategies for the treatment of XANES spectra [237]. Furthermore,

there are prior instances of ANN-based methods employed in the refinement of XANES spectra, but these reports pertain to systems that differ from our current context [238], [239].

5.2. Model training and choice of best ANN architecture

Our objective is to extract structural information from REXS spectra, that is, to correlate Intensity versus Energy profiles with distinct structural data. The 115 and 333 reflections have been utilised independently with their outputs set to be contrasted.

According to the Universal Approximation Theorem, any arbitrary continuous function of a bounded set can be, within a given accuracy, approximated by a suitable ANN model [240]. The ability of a model to approximate a given data set largely depends on the complexity of the model's architecture, apart from other variables not depending on the model itself (data quality, quantity of samples, etc.). More complex models can fit the data more effectively. As a result, it might be anticipated that supplementing new hidden layers or escalating the number of neurons within existing layers would augment a model's performance. However, a model that learns the training data too perfectly runs the risk of failing to generalise to unseen data, a problem known as overfitting. Overfitting results in the model capturing noise along with the underlying pattern in the data, leading to suboptimal performance when predicting on new data [241].

The choice of the activation function ($g(x)$) also assumes a significant role in shaping the performance of an ANN model. Activation functions introduce non-linearity into the model, allowing it to learn and model more complex patterns in the data. Two commonly used activation functions are the Rectified Linear Unit (ReLU) and the sigmoid function. The ReLU function, defined as $g(x) = \max(0, x)$ is one of the most widely used activation functions in deep learning models due to its simplicity and efficiency. It effectively eliminates negative values during the forward pass of the model, introducing non-linearity without expensive computational operations. On the other hand, the sigmoid function, defined as $g(x) = (1 + e^{-x})^{-1}$, outputs a value between 0 and 1, effectively interpreting the input as a probability. Its computational cost is significantly larger than ReLU, but it inherently brings all outputs into given borders [242]–[244].

Within the context of the objectives mentioned earlier, forty distinct models varying in number of layers, neurons per layer, and activation functions have been contemplated. The architectural details of the used models have been indicated in the annexes (**Table A.1**). Theoretical spectra, produced with the FDMNES software, have had a Gaussian-centred noise and an artificial slope introduced to simulate p-ES that closely resemble the acquired ES. For each varying set of n parameters – (x, y) for the cationic distribution; (y, z) for the oxygen positions, this process has been repeated ten times, leading to $10 \times n$ pseudo-experimental samples with $10 \times n$ associated sets.

Subsequently, 80% of the created instances are employed to train the ANN models. The training process takes place 50,000 times per model. Throughout these iterations, the Adam optimiser [245] is deployed to minimise the Mean Square Error within the training set (comparing predicted values with the actual ones). The 20% unseen samples are equally divided into a CV and a test datasets. The CV dataset is utilised to compare various models and make a considered selection of the optimal model architecture. The primary purpose of CV is to avoid overfitting, which can be detected by divergent trends in the mean square error (MSE) of the CV and training sets. Once the best model has been chosen, the test set is used for a final and unbiased evaluation of the train model [246], [247]. The instances are split in a way that all the different PES coming from the same TS fall into the same dataset (training, CV or test) and, as a result, the confrontation with CV and test datasets is completely new for the models. The entire process, commencing from the TS simulation to the acquisition and assessment of an optimal ANN model, is depicted in **Figure III.24**.

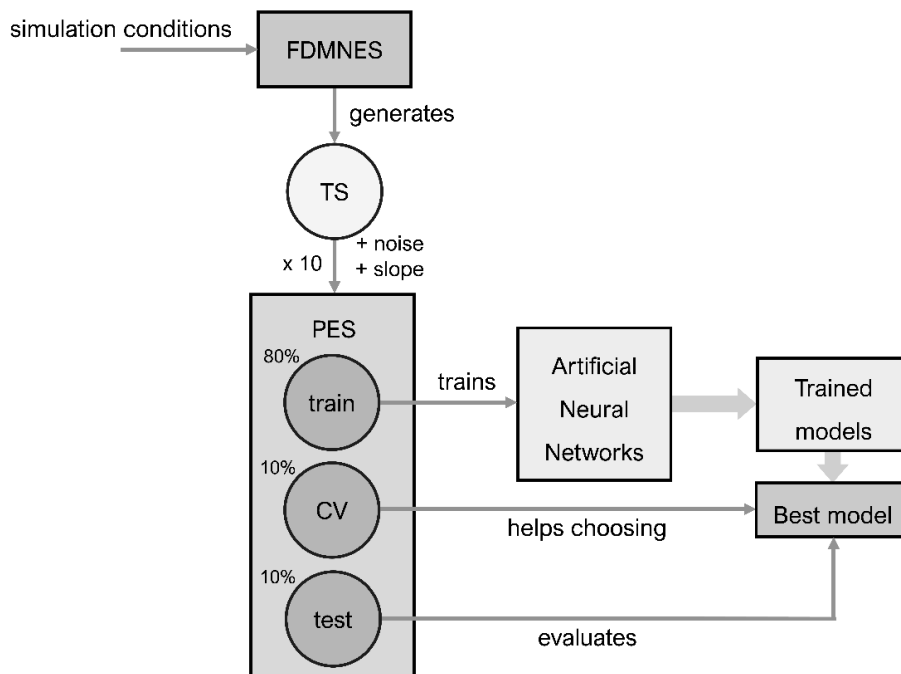


Figure III.24. Diagram representing the following steps: i) generation of theoretical spectra (TS) using FDMNES, ii) obtention of pseudo-theoretical spectra (PES) by mimicking experimental conditions, iii) split of PES into training, cross-validation (CV) and test datasets, iv) training of artificial neural networks (ANN) using the training dataset, v) choice of best model using the CV dataset, vi) evaluation of the optimal model using the test dataset.

5.3. ANNs for the cationic distribution in the Fe-V-O system

As previously explained, the varying cationic occupations in the Fe-V-O system can be modelled as $(\text{Fe}_{1-x}\text{V}_x)\text{Td}[\text{V}_{2(1-y)}\text{Fe}_{2y}]\text{OhO}_4$ with x and y taking values from 0 to 1. REXS spectra, with x and y values spanning

from 0.00 to 1.00 in increments of 0.02, have been generated within the energy range of [- 25, + 50 eV] relative to the Fe K-edge. The noise and slope adding process (ten times on each different spectrum) then lead to 25,000 different PES.

The ensuing results pertain to spectra at the 115 reflection – those for 333 are presented in the annexes: **Figure A.3** – page 183. MSE values of all different models after their respective training are shown in **Figure III.25**, as a function of the number of neurons which compose each model.

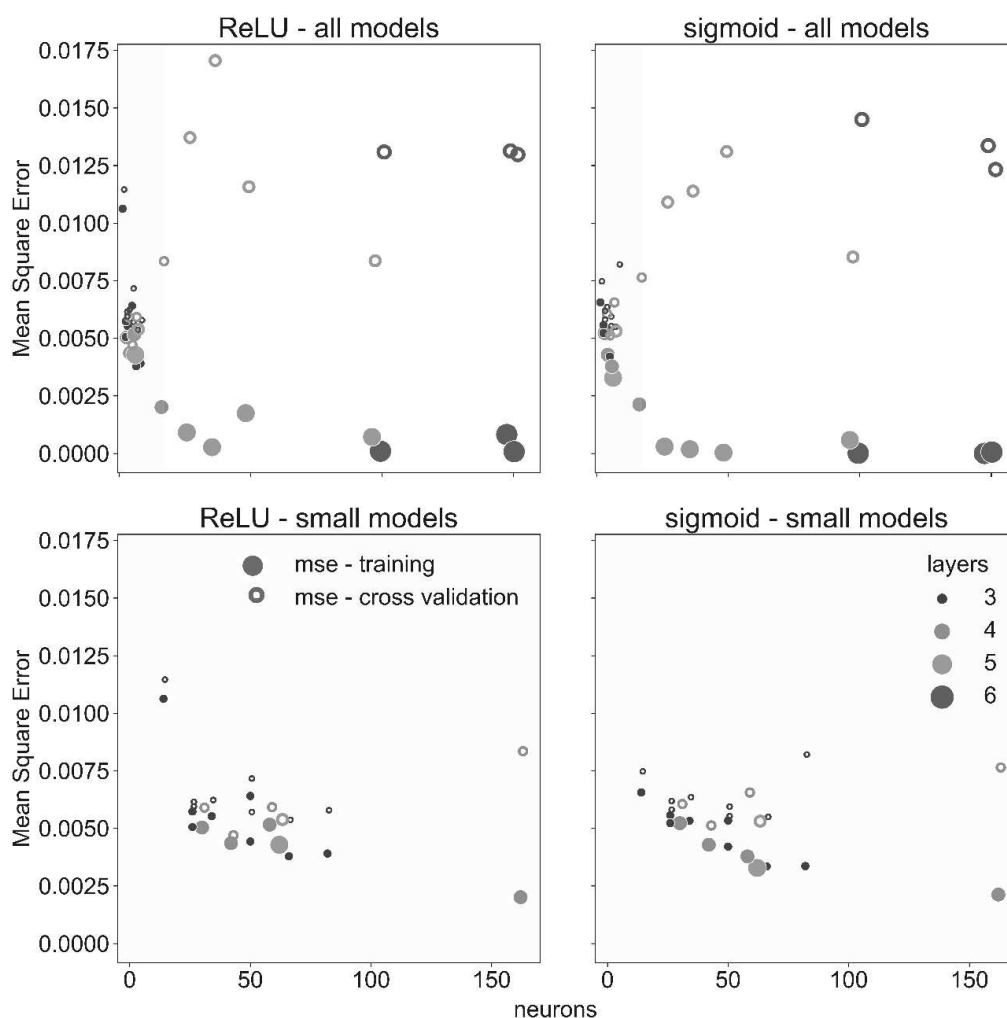


Figure III.25. Top: MSE as a function of neurons of the model for the training (full circle) and CV (hollow) datasets. The circles' size and colour correspond to the number of layers of each model. Bottom: same plot but for models under 200 neurons (highlighted zone in the top). Models have been split according to their activation functions: ReLU (left) or sigmoid (right). These results correspond to the 115 reflection.

The efficiency of each model has been verified by comparing them with the CV dataset and determining the difference between the anticipated and actual values, as portrayed in the **annex 3.1** – page 181.

As anticipated, the MSE of the training dataset declines as the model's complexity augments in all instances. For the CV set, MSE values follow the same trend for simple ANN architectures, but they drastically increase after the 200-neuron threshold. This train-CV divergence is a clear sign of overfitting and can be better observed by observing the MSE ratio between the CV and train datasets, as shown in **Figure III.26**.

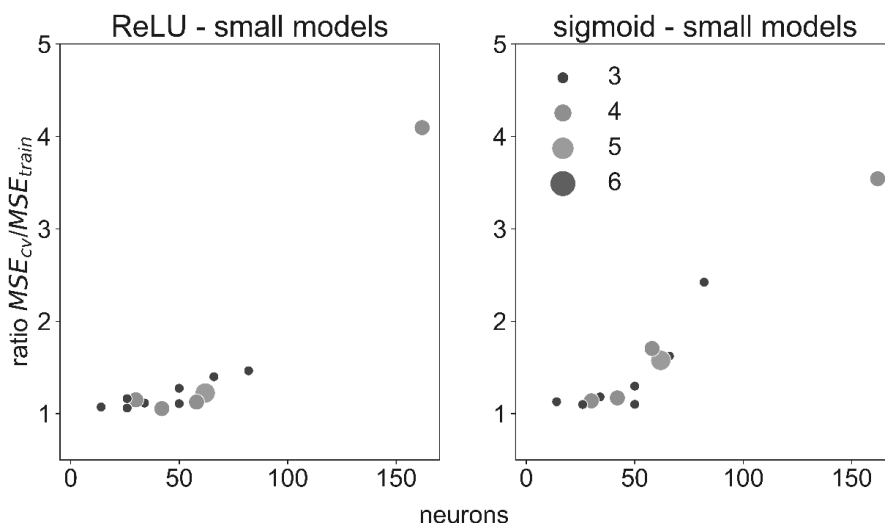


Figure III.26. Ratio of MSE for models under 200 neurons, as a function of the number of neurons. Models have been split according to their activation functions: ReLU (left) or sigmoid (right). Results for the 115 model.

The performance of ReLU and sigmoid models bear similarities for this particular case. The lowest MSE-CV value is obtained for the models with a (16, 16, 8, 2) neuron architecture, while keeping a low MSE ratio. This same result is shared by both 115 and 333 reflections.

Finally, the experimental spectra have been submitted to the optimal models. For the 115 reflection, the model trained with a ReLU activation function leads to $x = 0.03(3)$ and $y = -0.01(3)$, while the one trained with a sigmoid activation function gives $x = 0.01(4)$ and $y = 0.04(3)$. For the 333 reflection, the optimal ReLU model has led to $x = 0.07(4)$ and $y = 0.01(3)$ and the sigmoid to $x = 0.06(2)$ and $y = 0.04(4)$. Errors have been calculated using the σ value of the difference distribution on the test dataset.

We can see that the top models for each reflection (when looked at separately) give us the same predicted values for the experimental spectrum. Using the smallest CV MSE, the best ReLU model did better than the sigmoid for the 115 reflection, while the sigmoid did better for the 333 reflection. ReLU models also had the benefit of being quicker to train, while sigmoid models were good at keeping the output between 0 and 1. Regardless, irrespective of the activation function employed, the models' efficiency was akin when the optimal neuron structure was deployed.

Considering the finest model for each reflection, the mean output values would equate to $x = 0.05(4)$ and $y = 0.02(3)$. These values perfectly align with the ones found via the χ^2 minimisation process: $x = 0.015(5)$ and $y = 0.020(3)$ (c.f. **Figure III.9** on page 92) which, as shown in **Figure III.10**, are able to fit the REXS experimental spectra. The (Fe)_{Td}[V₂]_{Oh}O₄ cationic distribution is therefore again confirmed.

Although the error stemming from this method is significantly larger than that yielded by the previous analysis, the output is virtually immediate once the models are trained. Performance enhancement can be accomplished by refining the quality of the training dataset (for instance, by tweaking noise and slope adding parameters, simulating more spectra, etc.), or by amassing more experimental spectra. However, and more importantly, the success of this study underscores the potential of ANNs as a robust tool for fitting DANES spectra.

5.4. ANNs for the oxygen positions in FVO thin films

The same methodology was employed for the localisation of oxygen atoms at the coordinates $(0, y, z)$, utilising the EXAFS section of the spectrum. REXS spectra were generated with y and z values ranging from $[0.450, 0.550]$ and $[0.200, 0.320]$ respectively, in increments of 0.002. This occurred within an energy range of $[+20, +120 \text{ eV}]$ relative to the Fe K-edge. A process that involved adding noise and slope to each unique spectrum (repeated ten times) resulted in 25,000 distinct pseudo-experimental spectra (PES). A similar evaluation of model performance was undertaken, the results of which are detailed in the **annexes 3.5** and **3.7** for the 115 reflection, and the **annexes 3.6** and **3.8** for the 333. The most effective models identified for both reflections were the ReLU-activated model (32, 64, 128, 128, 2) and the sigmoid-activated model (32, 32, 2).

Subsequently, the optimal models were provided with experimental data, corresponding to the spectra obtained at varying temperatures, as depicted in **Figure III.27**.

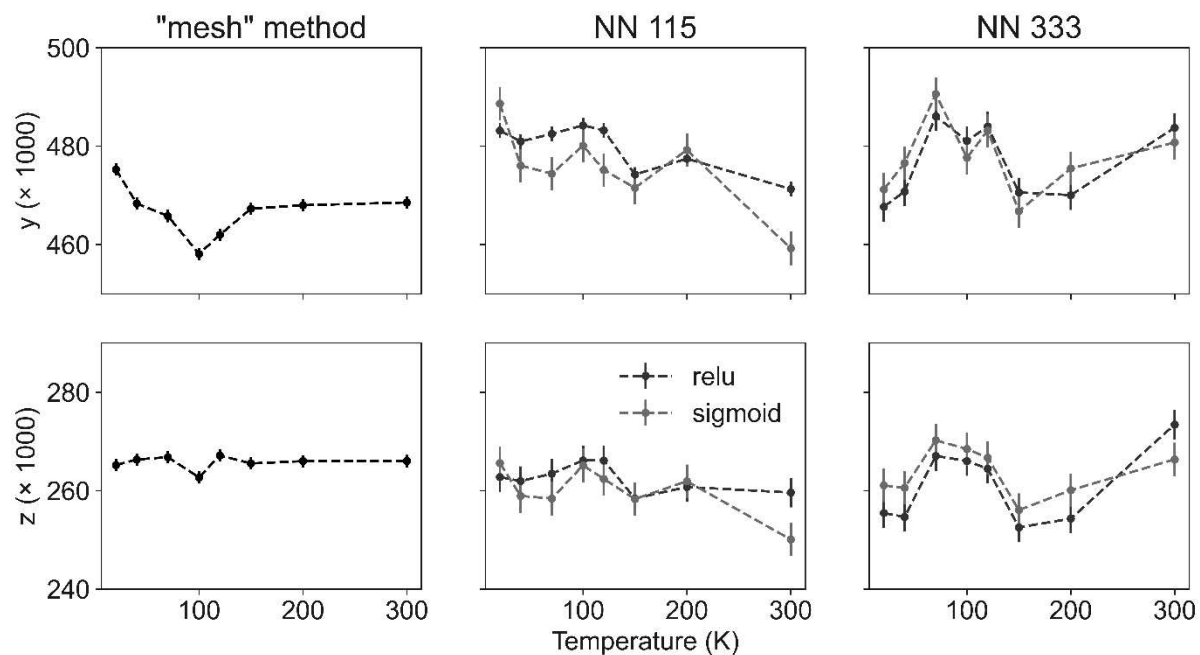


Figure III.27. Predicted values for y (top) and z (bottom) as a function of temperature: values obtained by χ^2 minimisation (left), by ANN trained on the 115 reflection (middle) and on the 333 reflections (right). The ANN results correspond to the best ReLU (red) and sigmoid (black) models, i.e., those conducting to the smallest CV MSE.

Unlike the ANNs employed for the XANES spectra, those used for the EXAFS fail to deliver consistent values, resulting in substantial discrepancies between the predictions generated by each model for different reflections. The temperature evolution of the parameters follow an erratic trend. Even though the outcomes have some resemblance to the expected values (with the reference being the ones computed through χ^2 minimisation), this strategy necessitates further refinement.

This research has certain constraints that are worth noting. Firstly, the theoretical files used for generating spectra were simulated using room-temperature lattice parameters. However, and as shown for the bulk sample, these parameters are subject to significant variation with changes in temperature. The observed variations in the spectra profiles could be attributed to alterations in the lattice structure rather than being exclusively due to oxygen positions. Albeit erratic, the variations of the y and z parameters follow similar temperature trends for the 115 and 333 reflections, and between ReLU and sigmoid models. Due to the sensible and consistent evolutions, our ANN models might capture the evolution in the crystal lattice structure. This is also a limitation that the χ^2 -based methodology presents. The resolution of the temperature-dependent structure with temperature, and the subsequent simulation of theoretical spectra (with the updated parameters), is a requirement for the honing of both approaches.

Secondly, the utilisation of ANNs for EDAXS spectra comparison might not be the most optimal method. This is due to inherent discrepancies in ANNs when dealing with these spectra. The network's difficulty in delivering consistent values could stem from the complex and multidimensional nature of the EXAFS data, making the traditional ANN model less equipped for this type of analysis.

To enhance the results of this research, various ML algorithms could be investigated. For instance, Convolutional Neural Networks (CNNs), known for their efficiency in image and pattern recognition [248], might yield better results when applied to the complex and feature-rich EXAFS spectra. CNNs have already been proven successful in the quantitative analysis of spectra [249], but their computational cost exceeds our available means. Alternatively, the use of ensemble methods, which leverage the power of multiple ML models, could improve the accuracy of the predictions. Furthermore, adapting the models to account for temperature-dependent parameters in the theoretical files could also lead to a more precise correlation between the predicted and actual values.

In summary, the refinement of REXS spectra utilizing ANNs has showcased its effectiveness, particularly in the case of XANES. Here, it yielded results comparable to the more time-consuming χ^2 minimisation process. The performance ANN will be further validated in the last chapter of the thesis, pertaining the spinel vanadium ferrite, where ANNs will be shown successful in a different stoichiometry. In the section “Cationic distribution in the thin film” – page 169, these ANN models are employed to characterise a Fe-V-O spinel with a totally different stoichiometry.

Nevertheless, when dealing with the EXAFS domain for the localisation of the oxygen atoms, extra efforts are necessitated to facilitate the successful deployment of rapid and reliable ML tools for the refinement of REXS spectra.

Chapter IV. Pt/FeV₂O₄

heterostructures for spintronics

The two previous chapters have focused on the fundamental properties of FeV₂O₄, settling the foundations for the obtention of high-quality epitaxial thin films, the study of their physical properties and the resolution of their crystal structure by means of anomalous diffraction.

This fourth chapter aims at chasing the technological applicability of the iron vanadate-based thin films, in the form of Pt/FeV₂O₄ heterostructures, for spintronic applications. The chapter starts with a broad introduction to the realm of spintronics and, more specifically, the spin-driven control of magnetic states. Then, it introduces the effects of the spin-caused phenomena on the magnetotransport properties of materials and describes the quantification of spin-orbit torques for the reversal of the magnetisation.

This chapter also covers the fabrication of Pt/FeV₂O₄ devices and an in-depth study of the spin transport properties of the heterostructures. Part of this work has already been published in Applied Physics Letters [250]. Our main finding is that the spin-driven effects dominate the magnetoresistance signal with a maximum value of 0.12% at low temperatures, only comparable to properly optimised oxide-based systems.

Furthermore, a thickness-dependent study has been employed to study the variation of the spin transport parameters with temperature. Links have been established between changes in the transport parameters and corresponding transformations within the FMI. The variation of the longitudinal and transverse resistivities have been explained via a competition of spin-driven events and other phenomena caused by magnetic anisotropy. Finally, a harmonic study has been used to quantify the torque response for the reversal of the magnetisation. The results, albeit requiring further confirmations, highlight the potential of iron vanadate as a promising candidate for future multifunctional spintronic devices.

1. Introduction

1.1. Spin-driven control of magnetic states

The pursuit of energy-efficient devices has become a focal point in Materials Science research. Traditional charge-based electronics, while forming the backbone of current technology, have inherent limitations such as energy dissipation, overheating, and scale constraints [251], [252]. Among the many approaches to overcoming these drawbacks, the utilisation of the intrinsic spin of the electron as a vector of information has emerged as a particularly promising avenue to reduce power consumption and overcome some of the barriers faced by traditional methods. This field, known as spintronics, offers a fundamental shift from the conventional charge-based paradigm.

Historically, spin-based information has been used to record magnetic data through the utilisation of ferromagnetic metal alloys, commonly composed of Fe, Co and Ni. The manipulation of these magnetic states was achieved by applying magnetic fields, generated by charge current lines. This approach gave rise to the first generation of non-volatile magnetic random-access memories (MRAMs). While first-generation MRAMs were a step forward, they possess substantial design limitations that limit their technological potential: write selectivity, thermal stability and size constraints; beside their considerable power consumption [253], [254] Therefore, the quest for more efficient and scalable solutions continued.

A pivotal moment in spintronics occurred with the discovery of Giant Magnetoresistance (GMR) effect. This phenomenon relates to changes in electrical resistance within layered metallic systems when the magnetisations of separate ferromagnetic layers align differently due to an external magnetic field. The discovery of GMR inaugurated new horizons for data storage and retrieval, revolutionizing the capabilities of magnetic memories [255], [256].

However, as the field of spintronics has matured, new research efforts focus on the manipulation of magnetic states via the application of electric currents, also known as current-induced magnetisation switching (CIMS). Differently to classical MRAMs, CIMS approaches aim at a reversal of the magnetisation through physical phenomena based on spin torques. Two CIMS strategies outstand for enabling energy efficient and spin current-driven magnetisation switchings: the spin-transfer torque (STT) and the spin-orbit torque (SOT) phenomena, which are schematised in **Figure IV.1**.

The STT effect comes from the transfer of spin angular momentum between two adjacent magnetic layers, typically engineered as a multilayer structure with a non-metallic layer as separator. When a non-polarised current is injected into a magnetic layer (also named “fixed layer”), the layer’s magnetisation predominantly filters one of the spins directions, generating a spin-polarised current (j_{sp}). This j_{sp} passes through the non-metal separator and reaches the second (“free”) layer. The spin angular momentum exerts a torque onto the free layer’s magnetisation, ultimately changing the direction of the magnetisation [257].

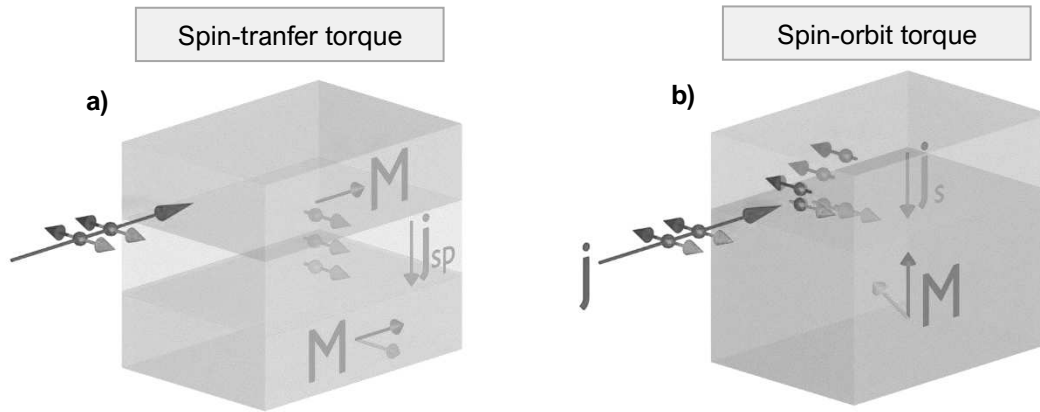


Figure IV.1. (a) schematic representations of the STT phenomenon, showcasing – from top to bottom – the fixed layer – separator – free layer heterostructure. (b) illustration of the SOT effect, with the upper non-magnetic heavy metal and the bottom magnetic material. Inspired by Kato et al. [258].

The SOT effect, on the other hand, arises from the coupling between the spin of conduction electrons and their orbital motion within the material. This section aims at presenting a comprehensive comparison between SOT and STT, but a more detailed explanation of the phenomenology behind the SOT-based systems is given in the next section of this chapter. Unlike STT, where the torque is exerted by the transfer of spin angular momentum between the two magnetic layers, SOT relies on the interaction of the spin with strong spin-orbit coupling (SOC) materials. This coupling leads to an effective magnetic field, which is translated in the form of a torque on the magnetisation of a nearby magnetic layer [259], [260].

The efficiency and behaviour of the SOT effect are dependent on the choice of materials, the thickness of the layers, and the interface quality. Unlike STT, the SOT effect can induce magnetisation switching without the need to pass current directly through the magnetic layer, potentially reducing Joule heating and improving energy efficiency [261].

In a typical SOT device, a heavy metal (HM) with strong SOC (such as Pt or Ta) is placed adjacent to a ferromagnetic layer. When a charge current is passed through the heavy metal layer, the SOC induces a transverse spin current due to the spin Hall effect (SHE) or the Rashba-Edelstein effect – depending on the case. This transverse spin current then impinges on the adjacent ferromagnet (FM), exerting a torque on its magnetisation [260]. Our focus will be directed towards SOT-based systems and, more specifically, those using the SHE effects.

1.2. Spin transport and magnetoresistance

As previously described, common strategies for SOT-based systems require the use of a HM with a SOC. When a charge current is injected onto the HM, a spin current density (\mathbf{j}_s) is generated due to the SHE. As shown in **Equation (IV.1)**, the value of this transverse spin current depends on the charge current density (\mathbf{j}), the spin Hall angle (θ_{SH}) – ratio between the spin Hall conductivity (σ_s) and the material's conductivity (σ); and the spin polarisation (\mathbf{s}) – unit vector perpendicular to \mathbf{j}_s and \mathbf{j} [262].

$$\mathbf{j}_s = \theta_{SH} \left(-\frac{\hbar}{2e} \right) \mathbf{j} \times \mathbf{s} \quad (\text{IV.1})$$

The spin current generated in the HM moves towards the interface with the FM. At the interface, the flow of the spin current is typically hindered due to various mechanisms, leading to a build-up or accumulation of spins at the interface [263]. The accumulated spins at the interface can exert a torque ($\boldsymbol{\tau}$) on the magnetisation of the FM. **Equation (IV.2)** describes this interaction, which depends on the spin current density (\mathbf{j}_s) and the direction of the FM's magnetisation – \mathbf{m} being its unit vector, also known as reduced magnetisation: $\mathbf{m} = \mathbf{M}/|\mathbf{M}|$ [264].

$$\boldsymbol{\tau} = \frac{\hbar}{2e} \mathbf{m} \times \mathbf{j}_s \quad (\text{IV.2})$$

When the magnetisation direction is parallel to the spin current density, their cross product becomes zero: $\mathbf{m} \times \mathbf{j}_s = 0$. In this case, no torque is exerted on the FM's magnetisation, and this latter is not affected by the spin current. In this configuration, the spin current is reflected at the FM-NM interface. As the NM with a strong SOC transforms a charge current into a spin current via the SHE, the reflected spin current is transformed into a charge current through the inverse spin Hall effect (ISHE). This generated charge current reduces the NM's resistivity, whose variation can be experimentally measured.

However, when the magnetisation direction is perpendicular to the spin current density, their cross product reaches a maximum: $|\mathbf{m} \times \mathbf{j}_s| = |\mathbf{m}||\mathbf{j}_s|$. In this perpendicular configuration, the spin current is absorbed by the FM layer at the interface, transferring its angular momentum and exerting a maximum torque on the FM's magnetisation. This phenomenon can provoke a tilt on the magnetisation and, ultimately, reverse its direction. The spin absorption at the interface causes the HM's conductivity to be smaller than when the magnetisation direction is parallel to the spin current (no charge current generated via the ISHE). This scenario has been illustrated in **Figure IV.2** using a Pt/FVO heterostructure.

Consequently, the HM's resistivity is affected by the direction of the FM's magnetisation. This magnetoresistance (MR) phenomenon, specifically linked to the absorption or reflection of the spin current at different magnetisation angles, is known as the Spin Hall magnetoresistance (SMR) effect [264]–[266]. SMR plays a crucial role in identifying materials that have the potential for an efficient SOT

switching, which is a fundamental requirement for the development of future energy-efficient and high-speed spin-orbitronic devices [267]–[269].

The changes in the HM's longitudinal (ρ_{xx}) and transverse (ρ_{xy}) resistivities due to the SMR effect are described by **Equation (IV.3)** and **(IV.4)**, respectively [262]. ρ_0 represents the longitudinal resistivity of the HM without any applied magnetic field, $\Delta\rho_{SMR\parallel}$ is the parallel contribution to the resistivity by the SMR effect and $\Delta\rho_{SMR\perp}$ quantifies the perpendicular component. Finally, m_x , m_y and m_z represent the components of the reduced magnetisation in the x , y and z directions.

$$\rho_{xx} = \rho_0 + \Delta\rho_{SMR\parallel}m_y^2 \quad (\text{IV.3})$$

$$\rho_{xy} = -\Delta\rho_{SMR\parallel}m_xm_y + \Delta\rho_{SMR\perp}m_z \quad (\text{IV.4})$$

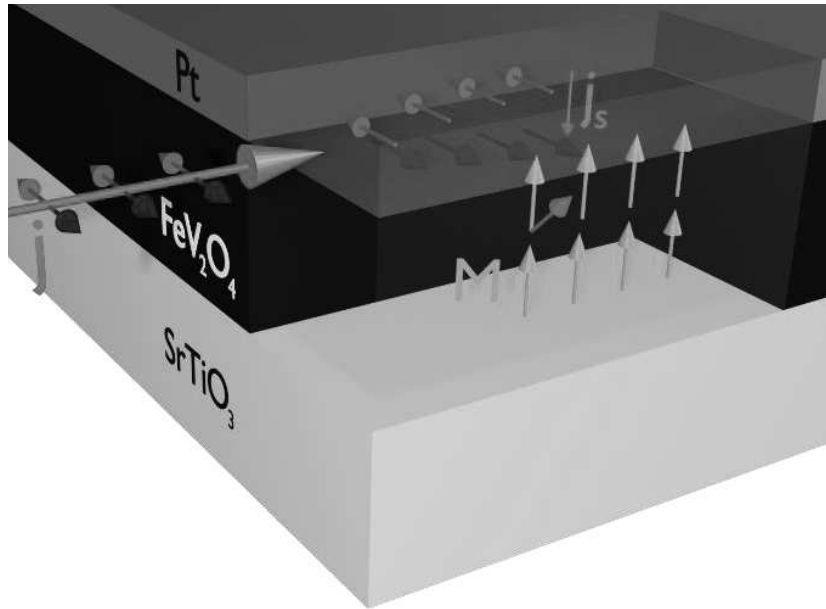


Figure IV.2. Spin Hall magnetoresistance phenomenon in a heavy metal/ferrimagnetic insulator heterostructure, with the action of a spin-orbit torque on the ferrimagnet's magnetisation.

On top of that, in a heterostructure where a non-magnetic HM is in contact with a FM layer, the HM suffers an induced interfacial magnetism due to the magnetic proximity effect (MPE). This means that the magnetic moments within the FM layer can induce a sort of “magnetic imprint” into the adjacent HM layer [270]. This induced magnetisation also influences the transport properties of the HM.

When the magnetisation direction is parallel to the current flow, the spin of conduction electrons aligns more easily with the magnetisation, resulting in less scattering and a lower resistivity. Essentially, the electrons find a path of least resistance along the direction of the magnetic field, and energy is not lost in the process of realigning the spins. This alignment allows the current to flow more easily. Conversely,

when the magnetisation direction is perpendicular to the current flow, the misalignment between electron spin and magnetisation leads to higher resistance state. The different scattering rates of the electrons, depending on their spin alignment relative to the material's magnetisation direction, manifests as a magnetoresistance phenomenon. This magnetic-driven magnetoresistance receives the name of anisotropy magnetoresistance (AMR), and is a well-known phenomenon in ferromagnetic conductors [271]–[273].

The values of the longitudinal and transverse resistivities under the AMR effect are described by **Equation (IV.5)** and **(IV.6)**, respectively [262]. Firstly, $\Delta\rho_{AMR}$ represents the variation of the longitudinal resistivity due to the AMR effect. Secondly, $\Delta\rho_{PHE}$ refers to the resistivity change due to the planar Hall effect (PHE), which occurs in ferromagnetic materials when an electric current flows in a direction perpendicular to both the magnetisation and the applied magnetic field. This effect stems from the spin-orbit interaction in conducting ferromagnets. Finally, $\Delta\rho_{AHE}$ is the resistivity change due to the anomalous Hall effect (AHE), which is a Hall effect that occurs even without an applied magnetic field and stems from the spin-orbit coupling in a magnetic material [274], [275].

$$\rho_{xx} = \rho_0 + \Delta\rho_{AMR}m_x^2 \quad (\text{IV.5})$$

$$\rho_{xy} = \Delta\rho_{PHE}m_xm_y + \Delta\rho_{AHE}m_z \quad (\text{IV.6})$$

The two aforementioned MR effects, SMR and AMR, coexist within a HM-FMI heterostructure. As a result, the transverse and longitudinal resistivities can be described by the global expressions shown in **Equation (IV.7)** and **(IV.8)**. In the transverse resistivity, the different contributions have been regrouped into an in-plane (IP) term: $\rho_1 = \Delta\rho_{PHE} - \Delta\rho_{SMR||}$; and an out-of-plane (OOP) term: $\rho_2' = \Delta\rho_{AHE} + \Delta\rho_{SMR\perp}$. The ordinary Hall effect (OHE), which is often overlooked in bulk metals, can have significant contributions to the latter term [274]. This effect introduces a linear field dependence to the external magnetic field. The overall out-of-plane transverse contribution is expressed in the form of $\rho_2 = \Delta\rho_{AHE} + \Delta\rho_{SMR\perp} + \Delta\rho_{OHE}$, with the “anomalous” component being the formerly defined ρ_2' .

$$\rho_{xx} = \rho_0 + \Delta\rho_{AMR}m_x^2 + \Delta\rho_{SMR||}m_y^2 \quad (\text{IV.7})$$

$$\begin{aligned} \rho_{xy} &= (\Delta\rho_{PHE} - \Delta\rho_{SMR||})m_xm_y + (\Delta\rho_{AHE} + \Delta\rho_{SMR\perp} + \Delta\rho_{OHE})m_z = \\ &= \rho_1m_xm_y + \rho_2m_z \end{aligned} \quad (\text{IV.8})$$

1.3. Magnetotransport studies

As described by **Equations (IV.7)** and **(IV.8)**, the nominal values of the resistivities in the HM are influenced by the orientation of the FM's magnetisation. Applying magnetic fields selectively in certain directions allows for an intricate study of each of the components. Such a study is conducted by angle-dependent magnetotransport measurements and enables the evaluation of the specific terms of the MR tied to the different magnetic orientations.

The magnetotransport studies of the HM-FM heterostructures have been conducted in devices engineered with a Hall bar geometry, as schematised in **Figure IV.3**. The device fabrication process is detailed in the section "Elaboration of Pt/FeV₂O₄ heterostructures" of this same chapter. The Hall bar geometry has been chosen because it allows for independent and reliable evaluation of the transverse and longitudinal resistances. Resistivity measurements have been carried out using a four-contact mode on the devices. A Cartesian coordinate system can be defined on the Hall bar: the plane along the heterostructure surface is xy , with x defined in the direction of the injected current density (j) and y perpendicular to it; whereas z corresponds to the OOP direction.

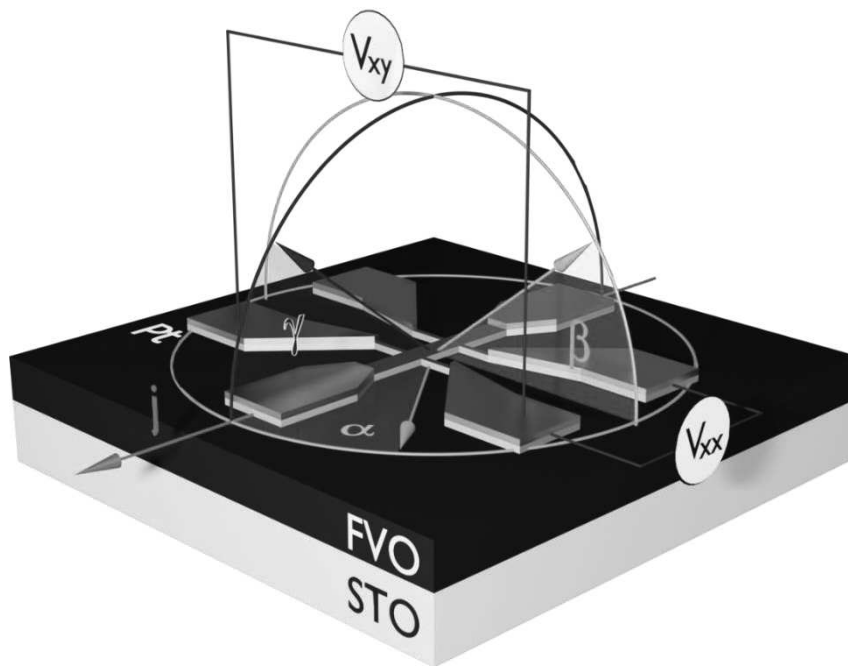


Figure IV.3. Representation of the Hall bar device, indicating the three different angular scanning configurations (α , β and γ) and the two different measured voltages (V_{xx} and V_{xy}).

Three angles are defined to indicate the relative orientation of the applied magnetic field (H) with the electric current. When the field reaches a certain threshold (the FM's coercive field), it can orientate the FM's magnetisation. For fields substantially larger than the material's coercivity, the FM's magnetisation can be assumed to follow the magnetic field direction. The angles are α , the angle formed by H applied

in-plane direction respect to the x axis (or \mathbf{j}); β , the angle between y and \mathbf{H} , the latter perpendicular to x ; and γ , the angle between x and \mathbf{H} when the field is applied perpendicular to the y axis. The variations of these three angles constitute the angle-dependant studies that will be furtherly discussed, and which enable the evaluation of the different MR components. The three angles are illustrated in **Figure IV.3**, along with the longitudinal (V_{xx}) and transverse (V_{xy}) voltage responses to a current density injected in the Hall bar.

The longitudinal magnetoresistance (c.f. **Equation (IV.7)**) has two components: one caused by the FM's magnetism, and another caused by the spin-driven interfacial effects. The former varies with m_x^2 whereas the latter depends on m_y^2 . Both projections of the reduced magnetisation can be written in terms of the previously defined angles: $m_x = |\mathbf{m}| \cos \gamma$, $m_y = |\mathbf{m}| \cos \beta$. Consequently, a γ -scan can be used to quantify the AMR effect: $\rho_{xx} = \rho_0 + \Delta\rho_{\text{AMR}} \cos^2 \gamma$ and a β -scan can be employed to isolate the SMR component: $\rho_{xx} = \rho_0 + \Delta\rho_{\text{SMR}} \cos^2 \gamma$. In both cases, \mathbf{H} is applied in a way that one of the magnetisation components varies while the other becomes zero.

Even if γ - and β -scans are useful to discern both components of the longitudinal magnetoresistance, such angle-dependent measurements do not allow isolating the different terms of the transverse resistivity (c.f. **Equation (IV.8)**), since both m_x and m_y have an influence on ρ_1 . The $m_x m_y$ product vary in the form of $\cos^2 \alpha$ and, as a result, an α -scan is used to study the in-plane component: $\rho_{xy} = \rho_1 \cos^2 \alpha$. The out-of-plane component, solely dependent on m_z , can be quantitatively studied by varying \mathbf{H} along the out-of-plane direction, i.e., by measuring $\rho_{xy}(H_z)$.

1.4. FeV₂O₄ as ferrimagnetic insulator for spintronics

In terms of material choice, there exist different strategies for material layouts enabling SOT-based devices. Recent efforts have focused on ferromagnetic insulators (FMI) where a pure spin current can propagate without dissipation while exerting a torque on the magnetisation itself [276], [277].

Robust SOTs-related phenomena are found in heterostructures that include materials with large SOC, large SHE and small spin diffusion length (λ_{sd}), such as the 5d metals [278]. As a result, in terms of material choice, platinum (Pt) is the most employed non-ferromagnetic HM for charge-to-spin conversion. To study this phenomenology with minimum proximity effects, the garnet ferrite Y₃Fe₅O₁₂ (YIG) is the most commonly chosen material, and Pt/YIG is the system where the SMR phenomenon was first experimentally reported [265]. Since then, several spinel ferrites (Fe₃O₄, CoFe₂O₄ or NiFe₂O₄) have also been chosen as FMI [118], [279]–[281], and more recently, multiferroic compounds, such as Ga_{0.6}Fe_{1.4}O₃ and Bi_{0.9}LaFeO₃ [282]–[284], have been investigated on the basis of a possible electric-field control of the magnetisation, *i.e.* to challenge mainstream materials by adding extra functionalities in future FMI-based spin-orbitronic devices.

In the scope of this PhD work, we introduce for the first time the spinel iron vanadate FeV₂O₄ (FVO) as an FMI material in the form of thin films. In the bulk, FVO shows ferrimagnetism [19], [285], ferroelectricity [29], [286] (and hence a multiferroic behaviour [58], [287]), an orbital-ordered state due to the presence of Jahn-Teller active cations (both Fe²⁺ and V³⁺) and a strong SOC [53], [54], [56]. All these attributes have been explained with detail in the section “Structural transitions and orbital ordering” of the first chapter of this thesis – page 15.

One of the limitations of oxide magnetic materials for spintronics is that few of them present a PMA [288]. In this sense, and as shown in “Magnetic properties of FeV₂O₄ thin films” (**Chapter II**, page 77), FVO thin films exhibit a large PMA when grown onto STO single crystals as substrate. This mostly results from an enhanced tetragonality of the bulk cubic structure as caused by the STO-induced compressive strain and the strong magnetoelastic coupling, as shown in the case of FVO [70] and for other complex oxides thin films [173].

The effect of the compressive strain of the STO substrate modifies the crystal structure from a cubic spinel in bulk ($Fd\bar{3}m$) to a distorted tetragonal spinel ($I4_1/amd$) in the thin-film form. The paramagnetic-to-ferrimagnetic transition temperature is also modified by dimensionality effects and it is usually found at a larger value than the bulk (ca. 110 K) [69], [71], [76], as previously confirmed.

In this chapter, we present an in-depth study of the magnetotransport properties of Hall-bar patterned Pt/FVO//STO heterostructures. SMR effects dominate the MR signal, with a maximum value of 0.12% at low temperatures, which is of the same order of magnitude as the best values obtained with archetypical Pt/YIG system [262]. Links have been established between changes in the transport parameters and corresponding transformations within the FMI. The variation of the longitudinal and transverse resistivities have been explained via a competition of spin-driven events and other phenomena caused by magnetic anisotropy.

1.5. Quantification of the spin-orbit torque

The spin accumulated in the HM-FMI interface exerts a SOT on the FMI’s magnetisation. This torque can be quantified by an analysis of the first and second harmonic responses of the transverse voltage when submitting the HM-FMI device to AC angle-dependent measurements.

The Pt/FVO devices present a considerable PMA and, as a result, one can assume that the equilibrium orientation for the FVO’s magnetisation will be around the OOP direction at appropriate temperatures. By performing small angle variations along this position, the IP components of the magnetisation can still be neglected: $m_x \approx m_y \approx 0$. Considering the global expression for the transverse resistivity (c.f. **Equation (IV.8)**), the transverse response of the resistivity would only depend on the z component of the reduced magnetisation, which can be approximated to $m_z \approx \cos \theta_M$, θ_M being the angle formed by the FMI’s magnetisation and the OOP direction. In this scenario, the nominal transverse response would

take the form presented in **Equation (IV.9)**. This constitutes the first harmonic response of the transverse resistivity [25].

$$\rho_{1\omega} \approx \rho_2 \cos \theta_M \quad (\text{IV.9})$$

When AC currents are applied to a system, the current oscillations induce oscillations in the magnetisation due to the interactions between the injected electrons and the magnetic moments. The system's dynamic response comes in the form of torques, which can be categorised as damping-like (DL) and field-like (FL) [289].

DL torques arise due to the non-collinearity between the magnetisation and the effective field induced by the spin accumulation. The torque tends to realign the magnetisation with this effective field. This torque acts similarly to the intrinsic damping present in the magnetic system, causing a change in the angle of the magnetisation. The DL effect can be quantified as a DL-type field (H_{DL}) and can tilt the magnetisation out of its equilibrium position.

FL torques are generated due to the effective magnetic fields arising from the spin accumulation. However, unlike DL, FL torques doesn't seek to realign the magnetisation. Instead, it operates perpendicular to both the magnetisation and the effective field, i.e., it influences the precession of the magnetisation around its equilibrium position without causing it to tilt or change its angle [289], [290]. The field associated to the effect of this torque is known as H_{FL} .

When determining SOT using AC second harmonic measurements, it is the combination of these two torques that paints a comprehensive picture, as described by **Equation (IV.10)**. $\rho_{2\omega}$ depends on θ_M , the DL and FL fields (H_{DL} and H_{FL}), the external applied field (H_{ext}), the effective out-of-plane anisotropy field (H_k), the thermoelectric resistivity (ρ_T) and the current-induced Oersted field (H_{Oe}).

$$\rho_{2\omega} = \left(\frac{1}{2} \rho_2 \frac{H_{DL}}{H_{ext} + H_k} + \rho_T \right) \sin \theta_M + 2\rho_1 (2 \sin^3 \theta_M - \sin \theta_M) \frac{H_{FL} + H_{Oe}}{H_{eff}} \quad (\text{IV.10})$$

In cases where the magnetisation is along the OOP direction and, by performing γ -dependent scans, the **Equation (IV.10)** can be furtherly simplified into **Equation (IV.11)**, with ρ_{ANE} being the anomalous Nerst effect resistivity. This is due to the fact that the DL torque is larger when the magnetisation is oriented in the xz plane, whereas the FL torque tends to align the magnetisation towards the applied field. We have ignored the PHE correction, since ρ_1 tends to be negligible compared to ρ_2 in OOP-oriented systems and it would lead to incorrect values even if it could not be neglected [291], [292].

$$\rho_{2\omega} \approx \left(\frac{1}{2} \rho_2 \frac{H_{DL}}{H_{ext} + H_k} + \rho_T \right) \sin \theta_M + \rho_{ANE} \quad (\text{IV.11})$$

As hinted by **Equation (IV.11)**, the anisotropy field intervenes in the $\rho_{2\omega}$ value. H_k represents the internal magnetic field required to reorient the magnetisation of the FMI layer from its preferred, or "easy", direction of magnetisation to a direction that's perpendicular to it, or "hard". It can be expressed in terms of the applied field and the angles in respect to the magnetisation (θ_M) and the applied field (θ_H), as shown in **Equation (IV.12)** [293].

$$\sin \theta_M = \frac{H_{ext}}{H_k} \sin(\theta_H - \theta_M) \quad (\text{IV.12})$$

This expression can be simplified considering the equilibrium equation for the magnetisation: $H_{ext} \sin(\theta_H - \theta_M) = H_k \sin(\theta_M) \cos(\theta_M)$ [294], [295], leading to **Equation (IV.13)**. Therefore, H_k can be extracted as the inverse of the slope of the linear relationship between $\sin \theta_M$ and $2 \sin(\theta_H/\theta_M) H_k$.

$$\sin \theta_M = 2 \frac{H_{ext}}{H_k} \sin\left(\frac{\theta_H}{\theta_M}\right) \quad (\text{IV.13})$$

The objective of the two harmonic study is to quantify the SOT response to the current injection in the HM, with the ultimate goal of causing a magnetisation reversal on the FMI due to the DL torque. The relative influence of the DL torque into the FMI's magnetisation can be quantified via the torque's efficiency (ξ_{DL}), which depends on the magnetisation at saturation (M_s), the film's thickness (t) and the current density (j), as described in **Equation (IV.14)**.

$$\xi_{DL} = \frac{2\mu_0 e}{\hbar} M_s t \frac{H_{DL}}{j} \quad (\text{IV.14})$$

The analysis of the two harmonic responses have started by the angle-dependent fitting of $\rho_{1\omega}$ curves, in order to study the anomalous component of the transverse resistivity (ρ_2). Then, the relationships between the applied field's angle (θ_H) and the actual magnetisation angle (θ_M) have been used to quantify the anisotropy field (H_k).

The second harmonic resistivity response has been then fitted for small θ_M , where $\sin \theta_M \approx \theta_M$. $\rho_{2\omega}$ has been fitted as a function of θ_M with $H_{DL}/H_{ext} + H_k$ being the linear relationship's slope and ρ_{ANE} the y -intercept. The influence of thermal effects has been neglected.

2. Elaboration of Pt/FeV₂O₄ heterostructures

2.1. Elaboration procedure

The fabrication of the Pt/FVO heterostructures involved a Pulsed Laser Deposition (PLD) procedure, as the one described in “Pulsed laser deposition (PLD)” in **Chapter II** – page 29. The deposition took place onto SrTiO₃ (001) (STO) single-crystal substrates, and treated according to the standard Kawasaki procedure [95].

The deposition of the FVO layer was carried out at the previously optimised conditions: at 400°C, in an Ar pressure of 10⁻² mbar, by ablating the target with a laser fluence of 4 J cm⁻² at a repetition rate of 5 Hz; followed by a cooling down process in the same Ar partial pressure. For all heterostructures, the thickness of the epitaxial and stoichiometric FVO layer was of approximately 40 nm.

The deposition of the upper Pt layer was also conducted using PLD but, differently to FVO, the process took place at room temperature to avoid any inter-diffusion at the Pt/FVO interface. The optimised conditions correspond to a laser fluence of 4 J cm⁻², at a repetition rate of 5 Hz and in an Ar pressure of 10⁻³ mbar. Unless indicated otherwise, the results presented here refer to samples with a Pt thickness of 3 nm.

2.2. Hall-bar patterning

After the elaboration of the heterostructure, a Hall bar geometry is etched on the Pt layer. This process was conducted at the Jean-Lamour Institute (IJL) in Nancy, in collaboration with the “Équipe Spintronique et Nanomagnétisme – SPIN”. The procedure was reproduced at the facilities of the IPCMS, but the results shown hereafter solely correspond to devices fabricated at the IJL. The entire conditions for the device patterning will be detailed for the sake of device reproducibility.

The procedure begins with the spin-coating deposition of a positive photoresist “1813 resist” (*SHIPLEY*) at 10,000 rpm for 40 seconds, with an acceleration of 4,000 rpm per second, followed by annealing with a hotplate at 115°C for 60 seconds. Then, a mask with the desired pattern is applied to the Hall bars. The mask is exposed on an MJB4 aligner for 20 seconds at 154.6 mJ cm⁻² in a contact vacuum. The development process is carried out with MF319 for 40 seconds at 20°C without ultrasonics, followed by rinsing with DI water for 20 seconds at 20°C with ultrasonics. The outcome is a protective polymeric layer with the form of the Hall bar on top of the heterostructure.

The second step focuses on the elimination of the Pt layer through Ar-ion milling. This process used Ar and an etching angle of 10°. Beam parameters include a voltage of 201 V and a current of 2.7 mA, with a sample voltage of 60 V and radiofrequency power of 73 W (3 W reflected). The sample is continuously rotating during the process. The total etching time is around 300 seconds until the atomic signal of Fe -

V is obtained by the SIMS spectrometer. Following this, the resin is removed with a “1165 Remover” (*Kayaku Advanced Materials*) for 1 hour at 80°C without ultrasonics (lift-off process), followed by a thorough cleaning of the surface. This step’s outcome has the form of a Hall bar shape on the heterostructure.

Finally, metallic top electrodes (10 nm Ti/150 nm Au) are evaporated to safeguard the Pt layer during the wire bonding process. A bilayer of resin “LOR3A” (*Kayaku Advanced Materials*) is applied to the surface, in order to improve the stick of the resin. The first spin coating is conducted at 7,000 rpm during 40 s and with an acceleration of 4,000 rpm s⁻¹, while the second is carried out at 10,000 rpm and also during 40 s and with an acceleration of 4,000 rpm s⁻¹. Between each spin coating and after the second coating, an annealing process is conducted with a hotplate at 140°C for 120 seconds. UV lithography is then performed and the “1813 resist” is applied again at 10,000 rpm and, during 40 s and with an acceleration of 4,000 rpm s⁻¹, followed by a baking process at 115°C for 60 s.

The exposure on MJB4 is done for 20 seconds at 150 mJ cm⁻² in a contact vacuum. The development step is carried out with MF319 for 60 seconds at 20°C without ultrasonics, followed by rinsing with DI water for 15 seconds at 20°C with ultrasonics. Thermal evaporation of 10 nm Ti and 150 nm Au is performed using chemical vapour deposition, followed by lift-off with “remover 1165” (*Kayaku Advanced Materials*) and a final cleaning.

2.3. Heterostructure characterisation

As shown by **Figure IV.4.**, the surface of the STO substrate before deposition (a), an FVO(40 nm)//STO thin film (b) and an unetched Pt(3 nm)/FVO(40 nm)//STO heterostructure (c) have been imaged by AFM.

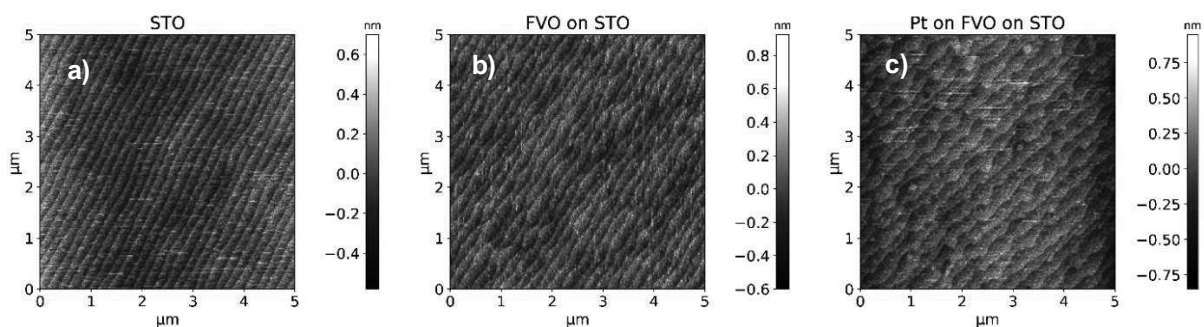


Figure IV.4. AFM images of the STO substrate after the HF treatment and subsequent annealing – (a), as well as that of the sample post FVO – (b), and post Pt – (c) depositions.

The image of the STO substrate was taken after the treatment with HF and high-temperature annealing (900°C, 2h), which lead to a surface roughness of ca. 0.16 nm showing a step-terrace surface (**Figure IV.4a**). The deposition of an FVO layer resulted in a roughness of ca. 0.19 nm (**Figure IV.4b**), whereas

the deposition of the Pt/FVO layers (**Figure IV.4c**) gave a roughness value of ca. 0.21 nm. The step-terrace structure is kept after both depositions. Roughness values have been obtained through surface region analyses of the shown surface areas.

The thickness of the platinum upper layer was determined via XRR measurements, as previously described on page 37. As shown in **Figure IV.5**, the oscillations of the Pt layer overshadowed those coming from FVO, and the determination of the FMI's thickness was determined by XRR analyses conducted on FVO//STO thin films.

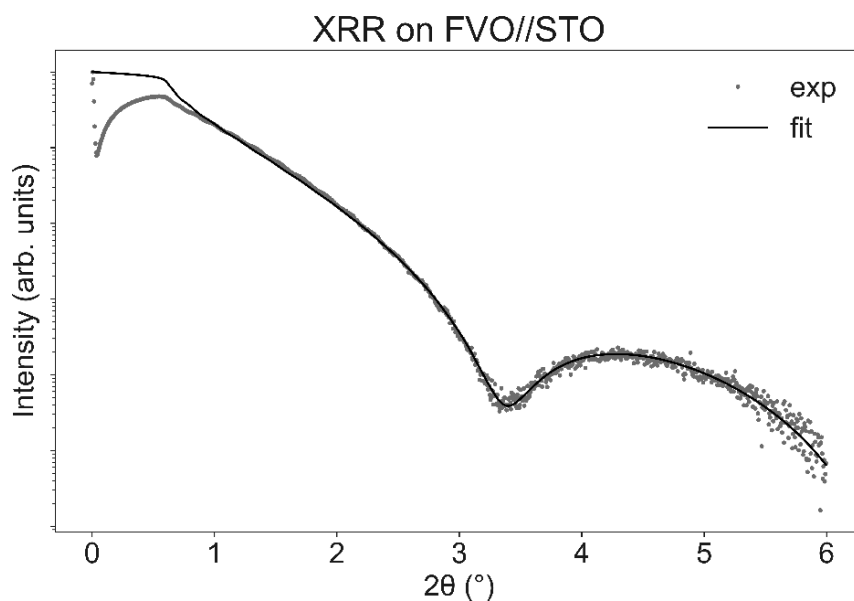


Figure IV.5. XRR – experimental data and best fit for a Pt/FVO//STO heterostructure. Fitted thickness for the Pt layer: 3.12(2) nm.

Finally, XRD measurements were conducted to confirm the correct crystal phase of the spinel structure at the FMI. 2D-RSM were conducted, leading to the same results as FVO//STO thin films (not shown here). θ - 2θ measurements also lead to diffractograms equivalent to the thin films', with the Pt layer manifesting in the form of a small bump next to a substrate's peak, as shown in **Figure IV.6**. Such a broad peak shape does not enable a determination of lattice parameter of Pt.

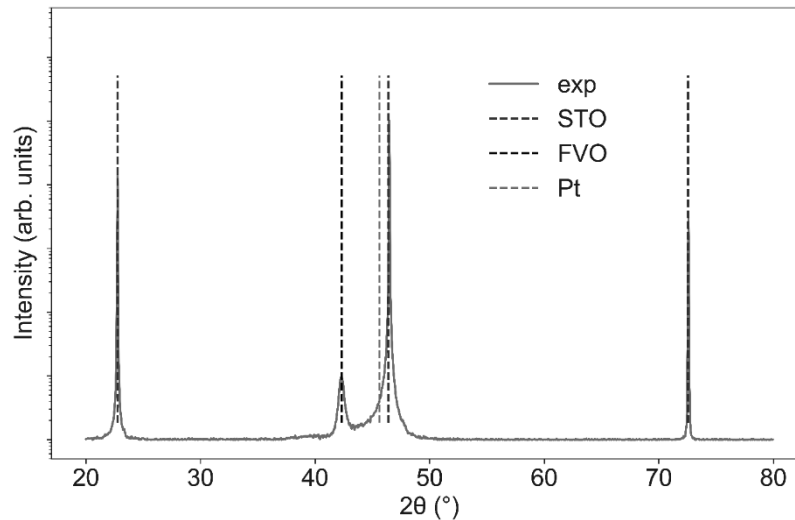


Figure IV.6. Theta-2theta diffractogram of the Pt/FVO//STO heterostructures, with the $\{00l\}$ reflections.

2.4. Magnetometry measurements on the heterostructures

Field-cooled (0.5 T) magnetisation vs. temperature measurements have been conducted in order to determine the magnetic behavior as a function of temperature of the Pt/FVO//STO heterostructures. The measurement has been conducted with superconducting quantum interference device vibrating sample magnetometer (SQUID VSM MPMS 3, *Quantum Design*).

As shown in **Figure IV.7**, the magnetisation profile indicates a ferrimagnetic-to-paramagnetic transition at around 140 K, coinciding with previous results in the literature[71], [273], the expected transition for bulk FVO[19], [53] and the results previously presented for FVO//STO thin films (c.f. **Figure II.36**).

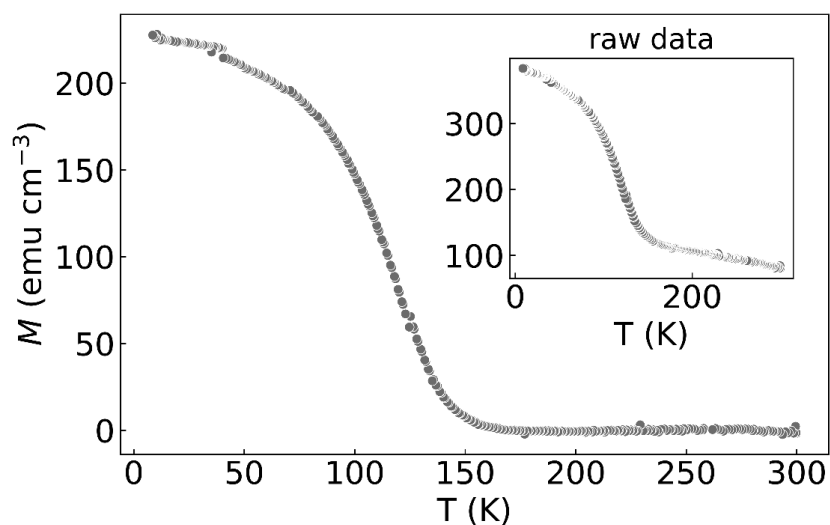


Figure IV.7. Magnetisation vs. temperature for the Pt/FVO//STO heterostructure. Main plot: data with paramagnetic correction. Inner plot: raw data (as measured).

As anticipated, the addition of the upper Pt layer does not affect the temperature for the magnetic transition. However, as shown in the raw data, the magnetisation does not fall down to zero and a ferro(i)magnetic component might survive beyond the transition temperature with no coercivity. The origin of this component is yet to be clarified.

Figure IV.8a shows the magnetic hysteresis loop (M vs. H) of our heterostructures, measured with a magnetic field applied in both in-plane IP and OOP directions at 10 K. The measured OOP M vs. H loop is rectangular in shape, and thus, representative of a system showing a strong PMA. Moreover, our OOP loop is characterised by two main features in line with already existing literature [70]: a step-like jump observed in the low field region and a large coercive (H_c) field.

As previously described, the magnetisation at saturation (M_s) reaches $2 \mu_B$ per formula unit (f.u.) at 10 K and is much larger in the OOP configuration than IP, in agreement with previous reports [70], [71]. In a spin-only scenario with quenched orbital angular momentum, an antiparallel alignment of Fe^{II} ($4 \mu_B$) and V^{III} ($2 \mu_B$) would result in a net zero M_s . The non-zero value found is explained via a nonnegligible SOC in V^{III}, which reduces the cation's magnetic contribution to *ca.* $0.85 \mu_B$ – measured in bulk FVO [19]. In our heterostructures, assuming a spin-only scenario for Fe^{II} results in a net moment of around $1 \mu_B$ per V^{III} site.

Figure IV.8b shows the temperature dependence of H_c , as measured in OOP configuration, for FVO//STO films. This figure is identical to **Figure II.40**, but has been reproduced in this chapter due to its significance to the discussions. H_c values rapidly drop upon increasing temperature and become zero for about 120 K.

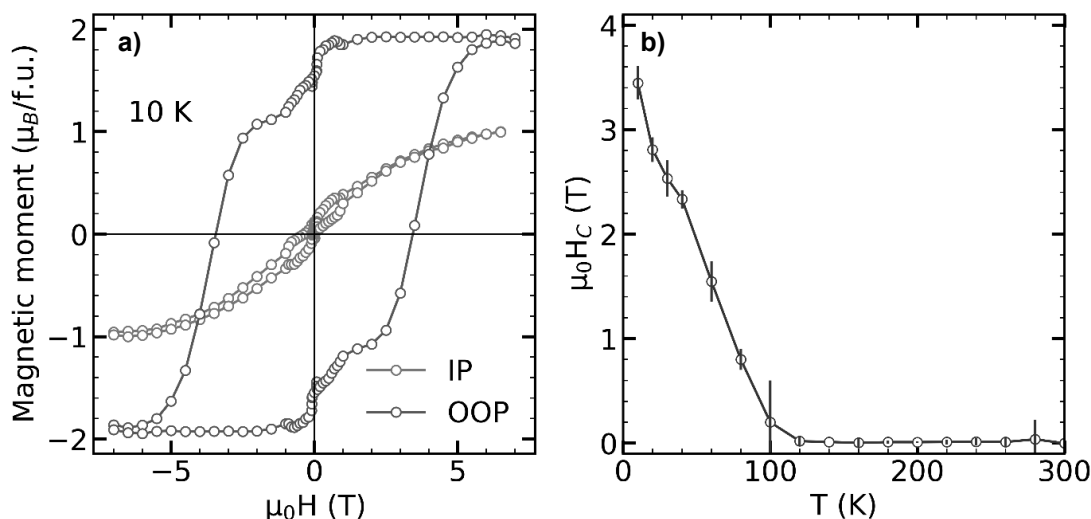


Figure IV.8. (a) M vs. H curves of the Pt(3 nm)/FVO(40 nm)//STO heterostructure in IP and OOP configurations at 10 K, showing strong PMA, (b) Temperature evolution of the OOP coercive field, as extracted from OOP M vs. H curves.

The small step-like jumps, observed in the OOP geometry, have been attributed to the presence of two magnetic phases with different coercivities coexisting within the same crystal structure, which seem to be strongly coupled in the IP direction but decoupled along the OOP. The large H_c is attributed to defects pinning the magnetic domains hindering their re-orientation [58], [70].

3. Magnetotransport studies of Pt/FVO/STO heterostructures

3.1. Longitudinal studies

3.1.1. Longitudinal resistivity vs. out-of-plane magnetic field

The longitudinal resistivity of Pt under no applied magnetic field (ρ_0) has been measured as a function of temperature, as shown in **Figure IV.9a**. As expected for a metal, platinum's resistivity linearly increases with temperature, as scattering events become more frequent. The resistivity presents no upturn at low temperature (down to 2 K), with a ρ_0 of ca. $3 \times 10^{-7} \Omega \text{ m}$, while the ρ_0 at 300K was found to be around five times the Pt bulk value (ρ_b), which is of the same order as measured for high-crystalline Pt films of the same thickness, and grown by magnetron sputtering ($\approx 3\rho_b$) [296]. Such a low resistivity is a good indicator of the layer's good crystallinity, since defects and impurities in the layer would increase the nominal value of the resistivity. This low value is a proof of the growth optimisation of the Pt layer onto FVO by PLD.

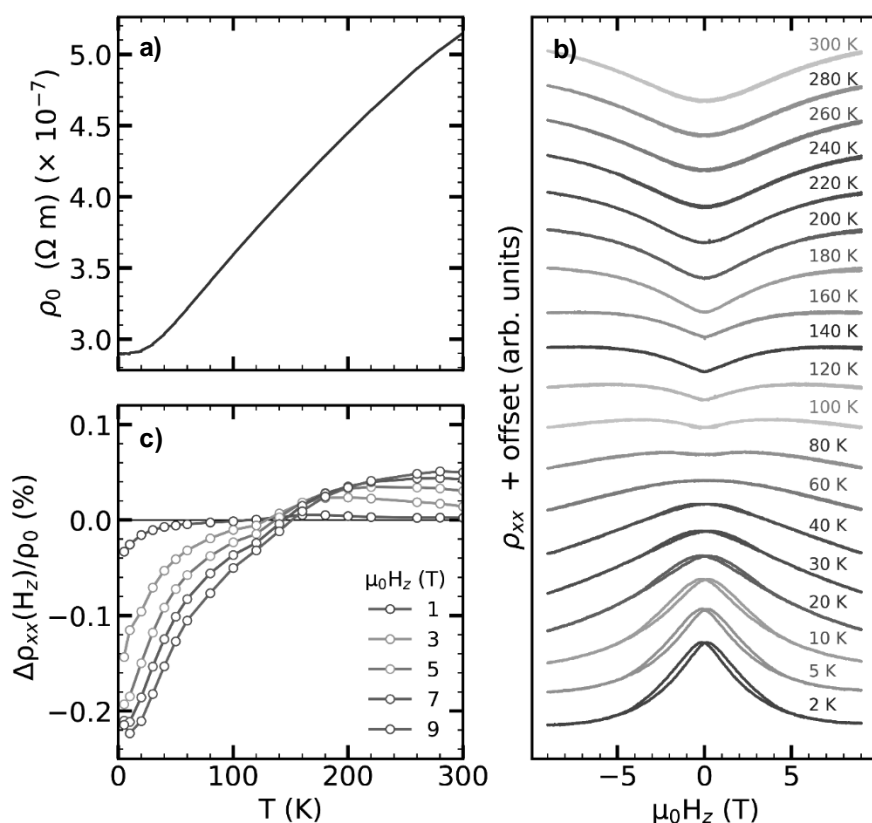


Figure IV.9. (a) ρ_0 vs. T. (b) ρ_{xx} as a function of H_z , for temperatures in the 2 - 300 K range. (c) Calculated temperature dependence of the longitudinal magnetoresistance for different H_z . One can notice a sign change around 120 K.

The room-temperature resistivity of FVO//STO is $5.4(2) \times 10^{-3} \Omega \text{ m}$, which is ca. 2×10^4 times larger than the room-temperature resistivity of Pt/FVO//STO. This ratio increases with decreasing temperature, as Pt resistivity decreases while FVO's exponentially increases – (c.f. **Figure II.41**). Therefore, the contributions of the insulating ferrimagnet on the MR effects can be neglected.

Figure IV.9b displays the variation of the longitudinal resistance (ρ_{xx}) vs. magnetic fields applied in the OOP direction (H_z) at different temperatures. Measurements have been conducted in temperatures ranging from 2 to 300 K, with fields from - 9 T to 9 T. In the 2 - 40 K temperature range, we observe a spin-valve-like effect that manifests itself as openings in the MR curves. The spin-valve effect is a phenomenon observed in magnetic multilayer structures, where the electrical resistance of the structure changes depending on the relative alignment of the magnetisation in adjacent magnetic layers [297], [298]. As shown in **Figure IV.8** and as previously confirmed by Zhou et al. for Fe_{1+x}V_{2-x}O₄//STO films [70], the magnetic structure of FVO is composed by two distinct magnetic phases. These regions, each possessing different magnetic anisotropies (and coercivities) might behave similarly to the ferromagnetic layers in a spin-valve structure, only saturating at high H_z values.

The MR at low temperatures is negative, becoming positive at around 120 K. This change in the MR sign can be better observed in **Figure IV.9c**, which shows the relative variation of the magnetoresistance: $\Delta\rho_{xx}(H_z)/\rho_0 = (\rho_{xx}(H_z) - \rho_0)/\rho_0$ as a function of temperature. This change of sign can be understood when considering a competition between the different MR phenomena. For that purpose, the different MR components must be isolated by appropriate angular scans, as detailed in the next section of this chapter.

3.1.2. Angle-dependent longitudinal studies

As previously described in page 135, a γ -scan can be used to quantify the AMR effect: $\rho_{xx} = \rho_0 + \Delta\rho_{\text{AMR}} \cos^2 \gamma$ whereas a β -scan can be employed to isolate the SMR component: $\rho_{xx} = \rho_0 + \Delta\rho_{\text{SMR}\parallel} \cos^2 \beta$. α -, β - and γ - scans have been carried out in temperatures between 2 and 300 K and using magnetic fields ranging from 1 T to 9 T. The angle-dependent measurements at 2 K and 9 T are displayed in **Figure IV.10a, b** and **c**.

The linear MR ($\Delta\rho_{xx}/\rho_0 = (\rho_{xx} - \rho_0)/\rho_0$) in each of the angular configurations has been fitted using a $A \cos^2(\theta + b)$ function, where A represents the magnetoresistance's amplitude and b the angle offset due to sample mounting. The amplitude of the oscillations as a function of temperature for the three different angular scans is presented in **Figure IV.10d, e** and **f**.

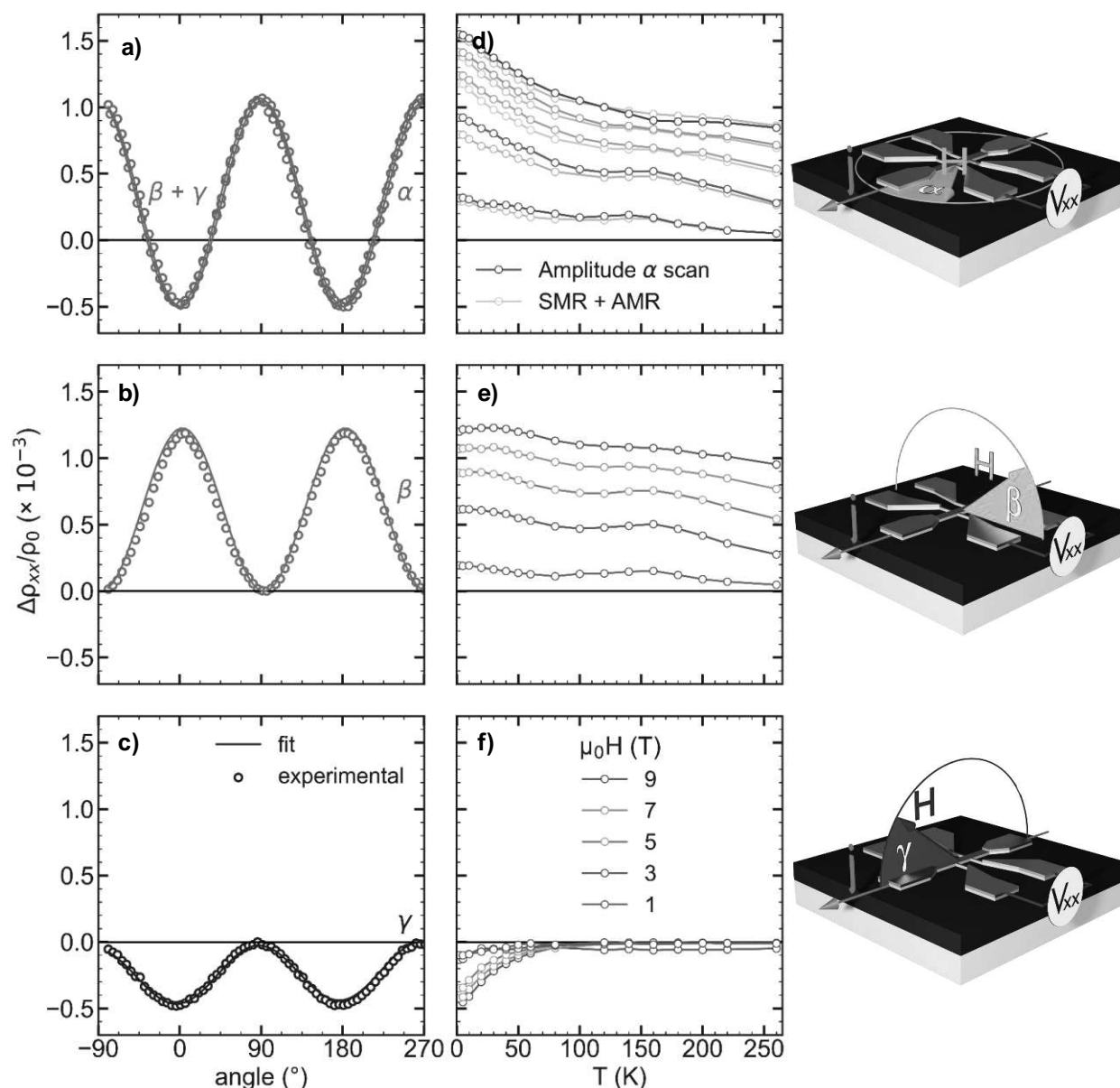


Figure IV.10. (a), (b) and (c) angle-dependent measurements (α , β and γ) at 9 T and 2 K, solid lines are fit to the experimental data. (d), (e) and (f) Amplitudes of the angle-dependent measurements as a function of temperature, for different magnetic field values.

The SMR amplitude (obtained by β -scans) is particularly large at low temperatures, with values reaching 0.12 % at 2 K. This MR effect matches the maximum values obtained for properly optimised Pt/YIG samples [262], and is of one degree of magnitude larger than the SMR found in other functional oxides like Pt/Ga_{0.6}Fe_{1.4}O₃ [283]. SMR values are larger than AMR values (obtained by γ -scans) at all temperatures, demonstrating that the spin Hall component of the magnetoresistance dominates over the MPE-driven phenomena. Furthermore, SMR amplitudes have a significant magnitude at all temperatures, even beyond the magnetic transition temperature.

On the contrary, the AMR amplitude sharply decreases when temperature increases, until zeroing out at the paramagnetic-to-ferrimagnetic transition (at around 120 K). The temperature at which this amplitude nullifies is not exactly the same as the FMI's T_c , since the transport measurements do not probe the FMI directly but the magnetisation induced by the FMI on the HM.

Comparing the resistivity values to ρ_0 , the SMR and AMR signals have opposite signs, and this result was anticipated by previous reports [279]. Since the overall longitudinal resistivity is a sum of both contributions (c.f. **Equation (IV.7)**), the overall MR behaviour presented in **Figure IV.9** can be explained via a competition of the two phenomena. The MPE behind the AMR effect is known to be stronger at low temperatures, due to a strong exchange coupling between the cations' 3d and the Pt 5d orbitals [37], but decays with increasing temperatures. As a result, at a certain threshold temperature, both SMR and AMR contributions cancel each other, and beyond that point the former dominates the MR.

The α -scan captures MR variations above and below ρ_0 , and the oscillations have also been described in the form of $A\cos^2(\alpha + b)$. As the three angles have been described (c.f. **Figure IV.3**), the $\alpha = 0^\circ$ scenario equals the $\gamma = 0$, while the $\alpha = 90^\circ$ configuration is the same as $\beta = 0^\circ$. Therefore, the amplitude of this azimuthal scan can be described as: $\Delta\rho_{xx}/\rho_0 = \Delta\rho_{AMR} \cos^2 \alpha + \Delta\rho_{SMR||} \sin^2 \alpha$. The amplitude of the total oscillation would be $\Delta\rho_{SMR||} - \Delta\rho_{AMR}$. **Figure IV.10a** shows the total equivalence of the α -scan with the sum (in absolute values) of the SMR and AMR components at 2 K and 9 T, and **Figure IV.10d** shows that these two values are equivalent at all temperatures and field values.

Finally, the equivalence of the γ -scan (at 2 K, 9T) and a magnetic field-dependent measurement for $\gamma = 0$ (at 2 K) is displayed in **Figure IV.11**, furtherly confirming the results shown for the longitudinal MR.

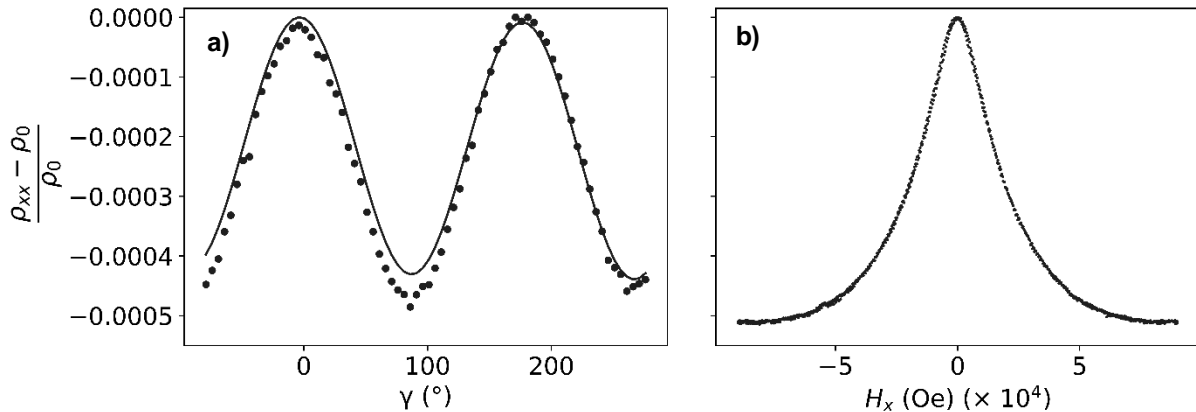


Figure IV.11. (a) γ -scan at 2 K and 9 T. (b) H_x -scan at 2 K in the [-9 T, 9T] field range. The maximum amplitude coincides between the two measurements, which confirms the consistency of the analyses. In Figure (a) there is a 90° degree offset compared to **Figure IV.10c**.

3.1.3. Thickness-dependent longitudinal study

Heterostructures with five different Pt thicknesses ranging from 1 to 10 nm were elaborated. The thickness of the FVO sublayer was kept constant (40 nm) for all the heterostructures. The objective of this thickness-dependent analysis is to determine the spin transport parameters which participate in the SMR effect.

As described by **Equation (IV.15)**, the SMR amplitude ($A_{SMR} = \Delta\rho_{SMR||}/\rho_0$) depends on σ (easily known, since $\sigma = 1/\rho_0$), on the thickness (t) and on the spin transport parameters: θ_{SH} , G_r and λ_{sd} . θ_{SH} is the spin Hall angle, a quantification of the SHE. It describes the efficiency of the transformation of a charge current into a spin current. G_r , the real part of the spin mixing conductance, accounts for the interface properties between different layers in a heterostructure. It quantifies how efficiently spins are transmitted at the interface. Finally, λ_{sd} is the spin diffusion length, a measure of how far spins can travel in a material before their orientation is randomised due to scattering events. It describes the mean distance over which the spin polarisation of the electron system persists. Therefore, the A_{SMR} vs. t curve can be used to find values for these three parameters [262].

$$\frac{\Delta\rho_{SMR||}}{\rho_0} = \theta_{SH}^2 \frac{\frac{\lambda_{sd}}{t} \tanh^2 \frac{t}{2\lambda_{sd}}}{\frac{\sigma}{2\lambda_{sd}G_r} + \coth \frac{t}{\lambda_{sd}}} \quad (\text{IV.15})$$

Longitudinal β -scans have been conducted in all the heterostructures in temperatures from 2 to 300 K with an applied field of 9 T. The MR curves have been fitted with a $A_{SMR} \cos^2 \beta$ function, leading to A_{SMR} values for all the given thicknesses at different temperatures. The results of the fit $A_{SMR}(t)$ are shown in **Figure IV.14a** at 10 K. The curve fit led to a spin diffusion length of $\lambda_{sd} = 1.48(8) \times 10^{-9}$ m, a spin mixing conductance of $G_r = 5.1(2) \times 10^{13} \text{ m}^{-2}$ and a spin Hall angle of $\theta_{SH} = 5.48(5) \times 10^{-2}$ at 10 K. These results are coherent (same order of magnitude) with the widely studied Pt/YIG system [275].

This procedure has been carried out at curves obtained for different temperatures. The variation of the θ_{SH} , G_r and λ_{sd} parameters with temperature has been represented in **Figure IV.14b, c** and **d**, respectively.

The θ_{SH} parameter does not vary significantly with the temperature (15 % difference from the lowest to the largest value), but a general decreasing trend is observed. This trend in temperature is also shared by the SMR amplitude (c.f. **Figure IV.10e**) and is comparable analogous studies in Pt/YIG [262], [299]. The broad maximum as a function of temperature, followed by a soft decrease, has been attributed to a diffusive scenario predicted for the spin motion in a system with a strong interfacial Rashba Spin-Orbit coupling [300], [301]. That means that the spin-orbit mechanism has an intrinsic origin (connected to the device's material properties), and that any extrinsic contribution would be much weaker to the overall spin transport in the heterostructure. Opposingly, in a ballistic scenario in which the extrinsic

contributions (mostly from impurities) were predominant, an increasing behaviour with temperature would be expected.

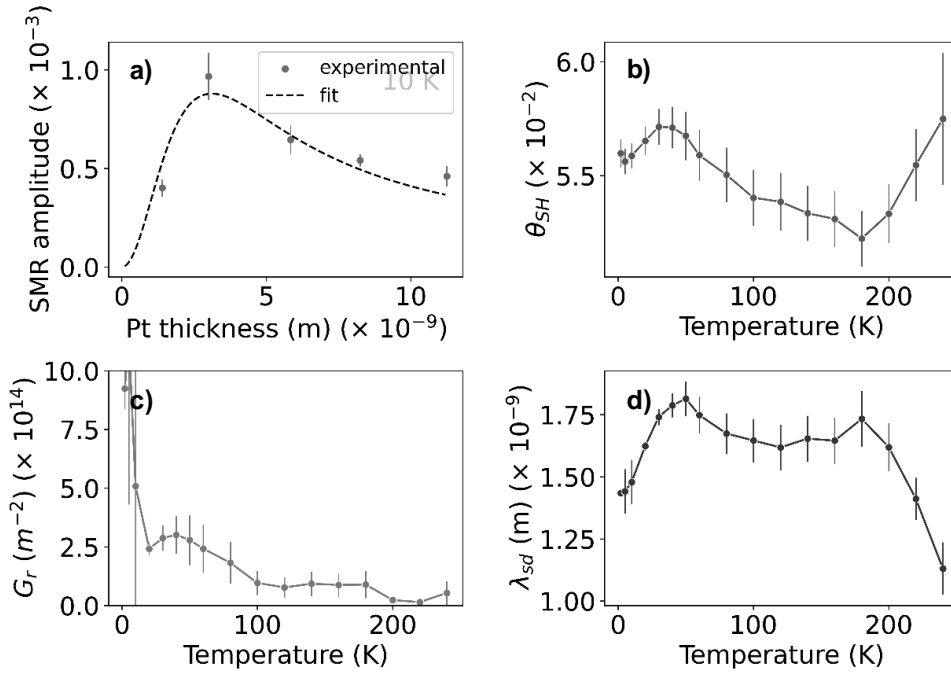


Figure IV.12. (a) SMR amplitude as a function of thickness, experimental data (red) and fit (black). (b) Spin Hall angle as a function of the temperature. (c) Real part of the spin mixing conductance as a function of the temperature. (d) Spin diffusion length as a function of the temperature.

In terms of the spin diffusion length, a decreasing trend with temperature ($\lambda_{sd} \sim 1/T$) would be expected if our system followed a conventional spin relaxation mechanism (Elliot-Yafet spin-orbit scattering model) as for Pt/YIG [302]. However, at lower temperatures the diffusion length seems to increase with temperature, then reaches a plateau, and starts to decrease around 180 K. This indicates that the spin relaxation mechanism is more complex than simple phonon scattering, and a more dominant effect for spin momentum relaxation is present in our heterostructures. A maximum in the spin diffusion length has already been reported in other systems, also diverging from the Elliot-Yafet phonon-based spin scattering model. Villamor et al. [303] have proposed a temperature dependence by the contribution of the defects in the spin transport mechanism, but the temperature dependence of θ_{SH} showed just the opposite. Another hypothesis would be a surface contribution, arising from the fact that the surface scattering time is inversely proportional to the bulk's value and surface contribution to spin scattering should predominate at low temperatures [304]. This would align with the ultra-low thickness of the platinum layer. However, this phenomenon would bring about a signature in the material's resistivity with temperature, whereas a conventional metallic behaviour has been observed.

The spin mixing conductance depends on the reflection of spins from the Pt/FVO interface. In archetypical Pt/YIG, this parameter is supposed not to vary significantly with temperature, since most

measurements take place far from the magnetic compensation temperature (550 K) [302] However, in our heterostructures, it has a clear decreasing behaviour, with several noticeable trend changes. The unusual variations in G_r and λ_{sd} may come from structural changes in our ferrimagnet. Differently to ubiquitous YIG, FVO undergoes several structural transitions with temperature, which could affect the spin transport mechanism in the Pt/FVO heterostructures. The variation with temperature for the different spin transport parameters suffers trend changes for the same temperature values, such as the decrease after 30 K for all the parameters. At this temperature and in the bulk form, a non-magnetic structural transition (tetragonal to orthorhombic) is observed [54], and a similar phenomenon could have taken place in our thin-film heterostructures. A change in the atomic distribution could affect the way spin currents are absorbed/reflected and might be the reason behind such anomalous trends.

Notwithstanding the observed trends with the temperature, the author acknowledges the limitations of the presented conclusions. The determination of three different parameters in curves containing only five experimental points has a non-negligible error, which is hinted by the large uncertainties shown in **Figure IV.14b, c** and **d**. The finding of the best parameters have been carried out using the “*curve_fit*” function by the in-built Python package “*scipy*”. This module uses the Levenberg-Marquardt algorithm for the minimisation of the square errors, until finding the set of parameters which matches the best the given function. The algorithm, however, might lead to different local minima depending upon the initial parameter values, the measurement noise, and algorithmic parameters [305]. In the case of this study, the model’s complexity (c.f. **Equation (IV.15)**) causes the existence of numerous (θ_{SH} , G_r and λ_{sd}) sets of parameters leading to reasonably good fits for the A_{SMR} vs. t curves. As a result, further thicknesses should be concluded to elucidate the variation of the spin transport parameters.

3.2. Transverse studies

3.2.1. Transverse resistivity vs. out-of-plane field

Similar to its longitudinal counterpart, the transverse MR has been firstly studied in means of its H_z -dependence. Such a study, $V_{xy}(H_z)$ with $\beta = \gamma = 90^\circ$ – commonly known as Hall cycle study; has been conducted from $H_z = [-9 \text{ T}, 9 \text{ T}]$ at temperatures from 2 to 300 K. The measured OOP component, as defined in **Equation (IV.8)**, corresponds to $\rho_2 = \Delta\rho_{AHE} + \Delta\rho_{SMR\perp} + \Delta\rho_{OHE}$. Linear fits have been carried out in the high-field domains ($|\mu_0 H_z| > 7 \text{ T}$) in order to extract the ordinary component (OHE). The OHE contribution has been corrected from the ρ_2 term: $\rho_2' = \rho_2 - \Delta\rho_{OHE}$, and the results are displayed in **Figure IV.13a**.

ρ_2' values are odd with respect to H_z . At low temperatures, the transverse MR is again negative, becoming positive above around 140 K. The change in sign can be observed in **Figure IV.13b**, where $\rho_2'(\mu_0 H_z = 9 \text{ T})$ and $\rho_2'(\mu_0 H_z = -9 \text{ T})$ are represented as a function of temperature. The trends match the evolution of the longitudinal resistivity (c.f. **Figure IV.9a**), and its explanations can be shared.

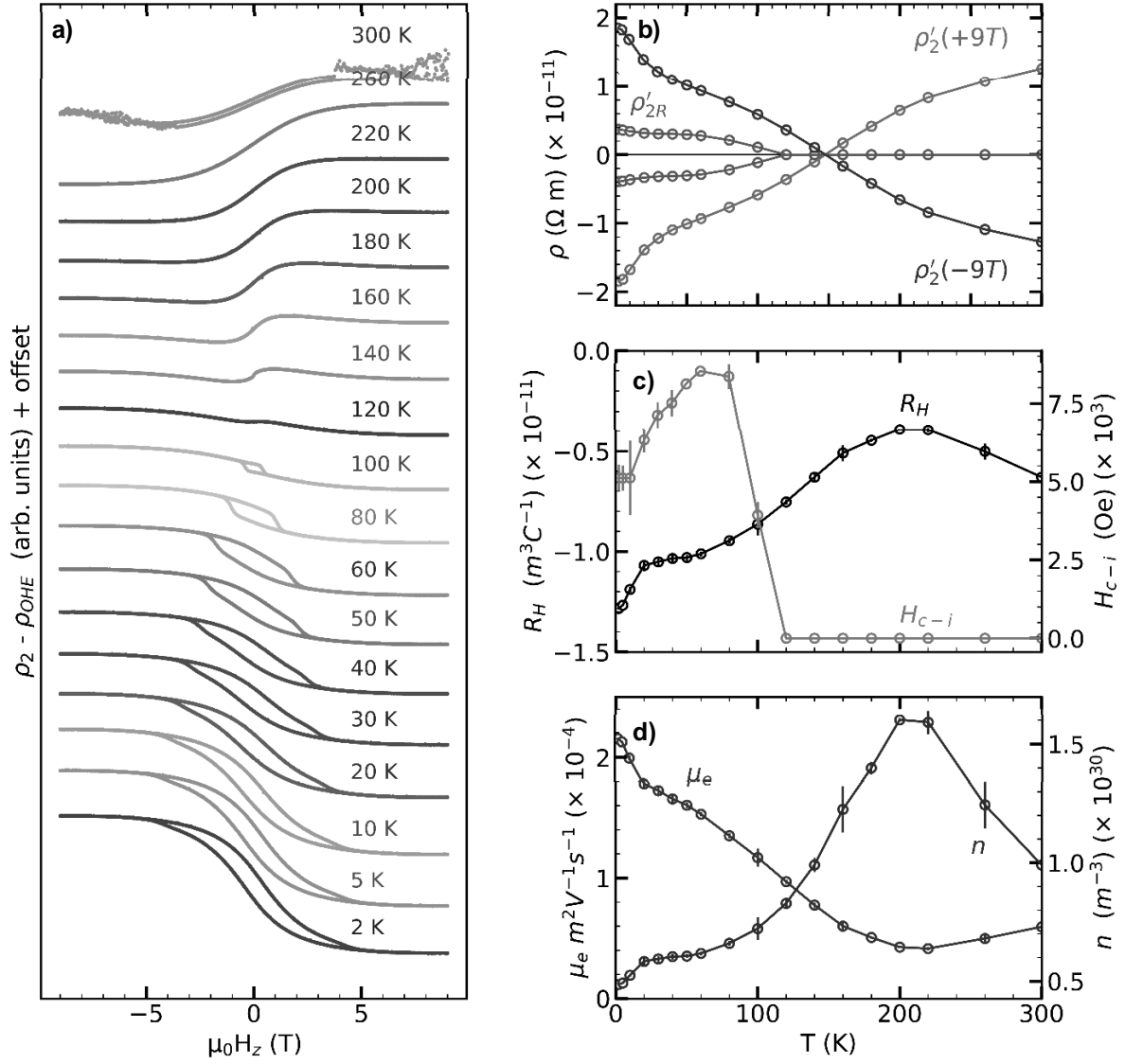


Figure IV.13. (a) $\rho_2' = \rho_2 - \Delta\rho_{OHE}$ hysteresis loops at various temperatures with an artificial offset for better visualisation. (b) ρ_2' at -9 and 9 T vs. of T , with ρ_{2R}' , the remnant resistivity at zero field. (c) Hall constant value vs. T , and coercive field for ρ_2' curves. (d) Electron mobility and charge carrier density vs. T .

$$\frac{\rho_2'}{\rho_0} \approx \frac{2\lambda_{sd}^2 \theta_{SH}^2}{t} \frac{\sigma G_i \tanh^2 \frac{t}{2\lambda_{sd}}}{\left(\sigma + 2\lambda_{sd} G_r + \coth \frac{t}{\lambda_{sd}}\right)^2} \quad (\text{IV.16})$$

However, the two bumps of the hysteresis loop are not observed in the magnetotransport measurements. The physical phenomena leading to a MR response take place predominantly in the Pt/FVO interface. This suggests that the two magnetic sublattices have a thickness-dependent distribution, and only the one closer to the interface is probed when performing magnetotransport

measurements. This would also explain the considerably lower coercivity of the magnetotransport response compared to the hysteresis loops. In this case, the hard magnetic phase (at low FVO thicknesses) would be untouched by the effects exerted by the platinum layer, and the more bulk-like phase (at higher thicknesses) would manifest in the MR measurements. These explanations align with those given in the thickness-dependent magnetometry study conducted in the section “Magnetic properties of FeV₂O₄ thin films” of **Chapter II** – page 80.

The sign-reversal for ρ_2' vs. T has already been reported in the case of Pt/YIG[274]. On a phenomenological basis, this change has been attributed to a change in the imaginary part of the spin mixing conductance (G_i) [274], as described by **Equation (IV.16)** [266], where G_r is the real part of the spin mixing conductance (indicator on the spin scattering and transmission at the Pt/FVO interface), while t , σ and θ_{SH} represent the Pt thickness, conductivity and spin Hall angle, respectively.

Differently from our system, in Pt/YIG the change in ρ_2' sign occurs from positive at low temperature to negative at higher temperatures, with an inversion at around 100 K [273], [274]. A similar trend has been reported in our group for previously investigated Pt/Ga_{0.6}Fe_{1.4}O₃ heterostructures [283].

Similar to the longitudinal MR, the OOP component of the transverse MR encompasses an MPE and a spin-Hall-caused components: $\rho_2' = \Delta\rho_{AHE} + \Delta\rho_{SMR\perp}$. Therefore, the variations in ρ_2' can also be explained by a competition between the two phenomena. As previously mentioned, MPE is known to be stronger at low temperatures but weakens at higher temperatures. At a certain threshold temperature (around 120 K), both $\Delta\rho_{SMR\perp}$ and $\Delta\rho_{AHE}$ contributions cancel each other, and beyond that point the former dominates in the transverse resistivity. Another explanation for that sign inversion, proposed by Zhou et al. [306] could originate in the paramagnetic state of the Pt layer for which both the curvature of the Fermi surface and the density of states drastically change with temperature.

The remanent resistivity at zero field ($\rho_{2R'}$) decreases with temperature, cancelling out as the ferrimagnet's magnetic order fades away. As illustrated in **Figure IV.13c**, the coercive field for the resistivity reversal (H_{c-i}) defined as the magnetic field at which $\rho_2' = 0$, increases with the temperature as the ρ_2' hysteresis close up, and drops sharply to zero once ferrimagnetism disappears. In the same figure, the evolution of the Hall constant (R_H) as a function of temperature has been represented. R_H has been extracted from the OHE correction carried out in the ρ_2' determination. As expected for a metal material with electronic charge carriers, R_H is negative at all temperatures.

The profile of R_H with temperature suffers several erratic upturns, which are not expected for a simple Pt layer. The same information can be stated about the charge mobility (μ_e) and the carrier density (n), both calculated from R_H using the following expressions: $n = 1/eR_H$ and $\mu_e = -R_H/\rho$; and whose evolution is represented in **Figure IV.13d**.

The drop in the charge carrier density and the Hall constant (in absolute value) at higher temperatures could be explained via a hole-contribution by the FVO sublayer, when it starts becoming more conducting. However, no signature in the resistivity vs. temperature curve was observed to support this

hypothesis. Furthermore, FVO's contribution onto the transport in the Pt layer can be neglected, since the latter's room-temperature resistivity is four orders of magnitude lower than the former's.

The observed bumps could ultimately be associated with transitions in the FVO's layer, as the upturn at 60 K to the bulk's phase transition (c.f. **Figure II.20**), which might affect the Pt layer due to proximity effects. A structural resolution in temperature for the heterostructures would be needed to elucidate the temperature dependence of the heterostructures' magnetotransport properties but, up to now, no conclusive explanations have been found for the evolution of the R_H , μ_e and n parameters as a function of temperature.

3.2.2. Angle-dependent transverse studies

Angle-dependent studies have been conducted for the characterisation of the IP transverse $\rho_1 = \Delta\rho_{PHE} - \Delta\rho_{SMR||}$ component, as defined in **Equation (IV.8)**. Azimuthal (α) scans were conducted with an applied field of 7 T. The measured resistivity can be described with the expression $\rho_{xy} = \rho_1 \cos^2 \alpha$, as shown in **Figure IV.14a**. The samples contain a longitudinal component which has been subtracted ($-\rho_{offset}$).

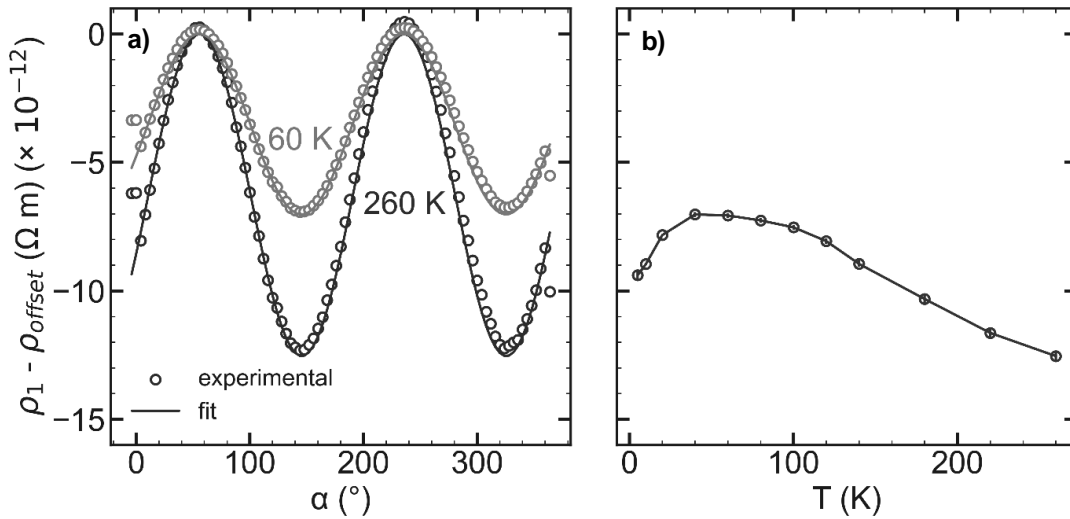


Figure IV.14. (a) IP angle-dependent magnetoresistance for an applied magnetic field of 7 T at two different temperatures: 60 and 260 K. (b) Amplitude of the oscillation vs. T.

Figure IV.14b shows the amplitude of the oscillations as a function of temperature, which quantifies the extent of the IP transverse MR ρ_1 . ρ_1 decreases in absolute value up to 60 K, and then continuously increases. As it was the case for ρ_2 , the observed variation can be explained through a competition of the ρ_{PHE} and the $\rho_{SMR||}$ components.

3.2.3. Two harmonics dynamic study

The first and second harmonic response for the transverse resistivity has been measured from 10 K to 140 K, applying currents from 2 to 10 mA and magnetic fields from 0.5 T to 7 T.

The first harmonic data was fitted using the relationship in **Equation (IV.13)** to quantify the anisotropy field (H_k), as displayed in **Figure IV.15a** for the measurement at 100 K with an applied current of 2.0 mA and a magnetic field of 7 T. To ensure that the magnetisation follows the applied magnetic field, only measurements with fields over 4 T have been considered. This procedure has been repeated for all the different applied fields, currents and temperatures, leading to the results shown in **Figure IV.15b**.

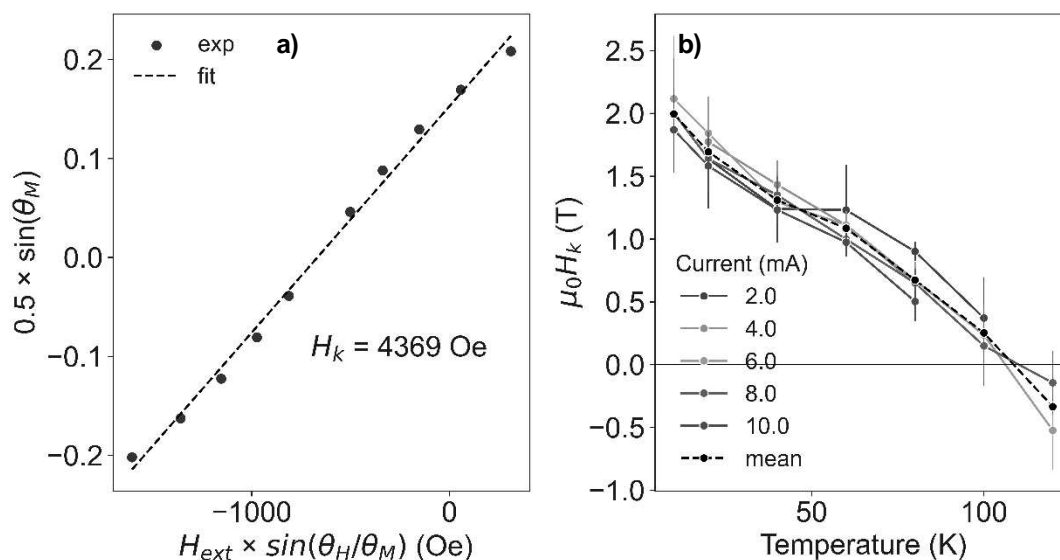


Figure IV.15. (a) Fit leading to H_k at 100 K and for an applied current of 2.0 mA. (b) H_k values as a function of temperature for five different applied currents (coloured) and mean value (dotted black).

The H_k values found for the different applied currents, as seen in **Figure IV.15b**, are all coherent to one another and with the mean value at each temperature – as expected, since H_k depends solely on FVO's anisotropy. The thermal effects on the magnetic properties can be therefore neglected. The passage to a negative H_k (or null, when considering the uncertainties) at 120 K coincides with the loss of the induced magnetism in the HM, which precedes the ferrimagnetic-to-paramagnetic transition in the FVO sublayer, as shown in **Figure IV.7**.

H_k values decrease with the temperature, since the magnetic anisotropy is strongly dependent on the thermal agitation of the atomic magnetic moments. The temperature behaviour is consistent with the temperature evolution of the coercivity (c.f. **Figure IV.8b**). As temperature increases, the thermal energy provided to the system enhances the random motion of these atomic moments. This makes it harder for the material to maintain its preferred magnetic orientation. Furthermore, as temperature rises, the overall

magnetisation of the material tends to decrease due to the increased thermal fluctuations, leading to an even more weakened magnetic anisotropy.

The temperature-dependent values of the anisotropy field have been then used for the obtention of H_{DL} values. Both the data treatment and the presentation of results are conducted using voltages (as experimentally acquired), instead of resistivities, but the aforementioned relationships are formulas are still valid. The results shown hereby correspond to measurements at 60 K and an applied current of 10 mA.

The first harmonic response (**Figure IV.16a**) follows a \cos –like profile, as anticipated by **Equation (IV.9)**, whose fitting enables the determination of the anomalous component (V_{AHE}) after subtraction of the OHE field-dependent component. After taking into account the relationship between the angle of the applied field (θ_H , or also γ in this case), the voltage values of the second harmonic response (**Figure IV.16b**) have been linearly fitted in respect to θ_M , as shown in (**Figure IV.16c**). The linear fit leads to an individual value of $V_{2\omega} / \sin \theta_M$. The figures correspond to measurements with an applied magnetic field of 7 T.

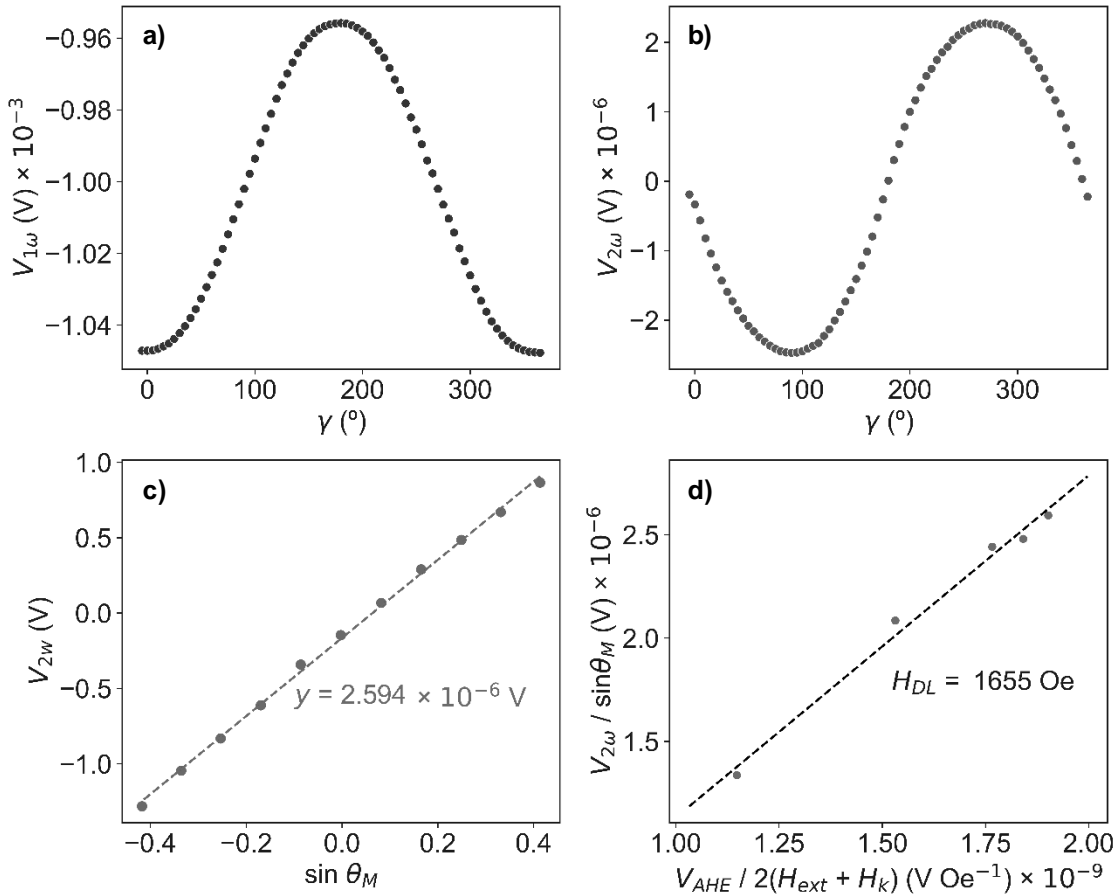


Figure IV.16. Treatment of the data for the two-harmonic study, at 60 K and with 10 mA of injected current. **(a)** First harmonic response. **(b)** Second harmonic response. **(c)** Fit of the second harmonic response for the determination of $V_{2\omega} / \sin \theta_M$. **(d)** $V_{2\omega} / \sin \theta_M$ vs. $V_{AHE} / 2(H_{ext} + H_k)$ for the determination of H_{DL} . Note: for **a**, **b** and **c** $\mu_0 H_{ext} = 7$ T, whereas H_{ext} varies in **d**.

This procedure is repeated for different magnetic fields. The obtained $V_{2\omega}/\sin\theta_M$ values are represented as a function of $V_{AHE}/2(H_{ext} + H_k)$ which, as shown in **Figure IV.16d**, has H_{DL} as the linear relationship's slope (c.f. **Equation (IV.11)**).

At each given temperature, higher charge currents generate higher spin currents, and this is manifested in stronger SOT and higher H_{DL} values. This phenomenon is displayed in **Figure IV.17a**, where H_{DL} values are shown to linearly grow with the applied current at all temperatures. Linear fits of H_{DL}/j have been conducted at each temperature, and the torque efficiency (ξ_{DL}) has been calculated using the relationship indicated in **Equation (IV.14)** – with M_s extracted from **Figure IV.7**. As shown in **Figure IV.17b**, and anticipated by the H_{DL}/j linear relationships – all possessing a similar slope, ξ_{DL} values are kept relatively constant (between 15 and 20) with temperature in the 10 to 100 K range.

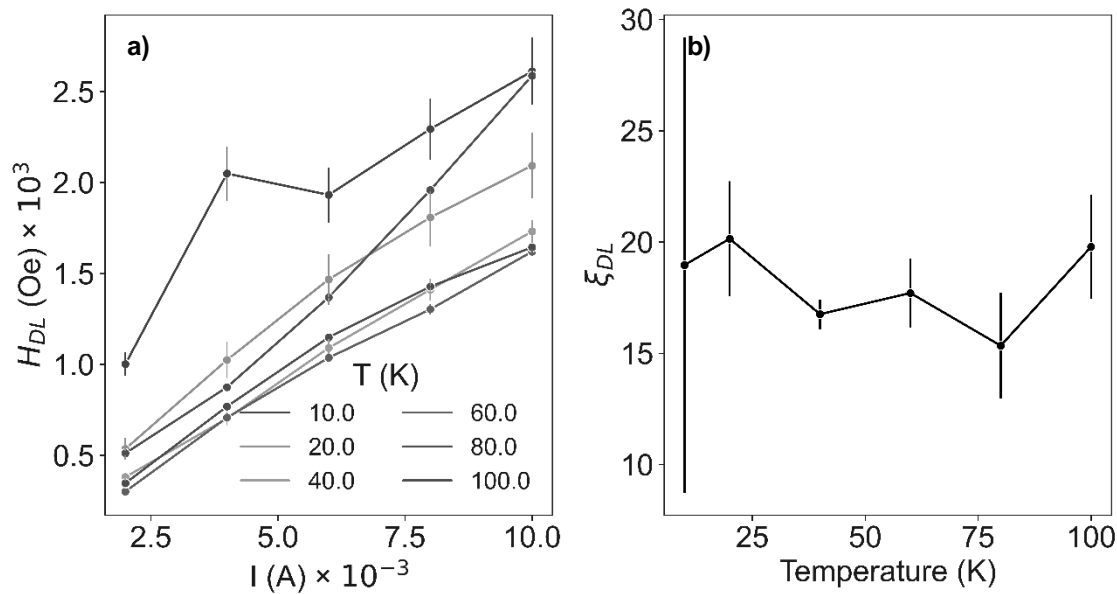


Figure IV.17. (a) H_{DL} as a function of the applied current for temperatures from 10 to 100 K. (b) ξ_{DL} as a function of temperature.

The determination of ξ_{DL} and H_{DL} values has been extensively debated for the reasons outlined below. We have rigorously examined the numerical analysis, and our partners at the Jean-Lamour Institute independently performed the analysis and found the same results. Therefore, errors performed in the data processing or the calculation happen to be unlikely.

The values found for the H_{DL} are anomalously high when compared to the H_{DL} found in the literature for other systems, e.g. ≈ 5 Oe on FeTb layers [291] or ≈ 70 Oe for CuPt/CoPt [307]. The model's fitness has been attested by the linearity of the relationship leading to H_{DL} values (c.f. **Figure IV.16d**) and, more importantly, these H_{DL} have been shown to linearly increase with the applied current (**Figure IV.17a**). As a result, these H_{DL} values possess some physical significance, but their doubtful magnitude has made the authors treat the analysis' results with precaution. Nonetheless, even if these H_{DL} field values were

to be valid, they would be still substantially lower than the material's coercivity (c.f. **Figure IV.8**), hindering any successful reversal of the magnetisation.

In terms of torque effectiveness, the found results (ξ_{DL} between 15 and 20) also diverge from the reports in the literature. The great majority of torque effectiveness are smaller than the unit, as it has been shown for GdFeCo alloys [308] or for TaS₂ Monolayers [309], among others. Zhu et. al [292] present a representative sample of ξ_{DL} values for different systems, most of which falling under the unit.

However, there exist literature reports with current-induced fields of over 1,000 Oe and torque effectiveness of ca. 18, as the one by DC et al. on Bi_xSe_(1-x) [310], who found such values via both angle-dependent and Spin Torque Ferromagnetic Resonance (ST-FMR) techniques. The ST-FMR study of the FVO heterostructures would help in confronting the previously described results, but presents other challenges due to the hard magnetic properties of the samples.

4. Summary and future perspectives

The presented results constitute the first study of spin transport properties in Pt/FeV₂O₄//SrTiO₃ heterostructures. The system's large PMA is ideal for spin-orbitronic applications. Angle-dependent magnetotransport longitudinal measurements were performed to determine the AMR and SMR contributions to magnetoresistance, showing that the spin-based component dominates in all scenarios and reaches a value of 0.12% at 2 K, comparable to that obtained for largely optimised Pt/YIG heterostructures. This suggests efficient spin injection at the Pt/FVO interface, indicating the potential of FVO-based structures for SOT-induced magnetisation switching.

A thickness-dependent study has enabled the determination of the spin transport parameters in temperature. More thickness values should be considered to reduce the values' uncertainties and have a more precise determination of these parameters.

Transverse measurements have been conducted to quantify the anomalous component of the heterostructure. Its evolution with temperature can be associated with changes in FVO's magnetic behaviour, proving the influence of the ferrimagnet's magnetisation onto the non-magnetic heavy metal above.

Two-harmonic analyses have been employed to quantify the SOT response. The torque effectiveness is anomalously high (between 15 and 20), as well as the damping-like field associated to the magnetisation reversals. Further analyses need to be conducted to verify these values. Nevertheless, these values are substantially lower than the material's coercivity. Future studies should address this issue, by means of reducing the FMI's thickness, via chemical doping or through strain engineering (different substrate choice).

Another important issue is the temperature domain of applicability for the heterostructures, with the magnetic functionalities only exploitable under 120 K. The next chapter will address this problem by increasing the iron content in FVO, and other spinel systems will be tested in the near future in our group.

In conclusion, this work provides a first comprehensive study of the spin-dependent magnetotransport properties of Pt/FVO heterostructures, underscoring the promise of iron vanadate in upcoming multifunctional spintronic applications.

Chapter V. Spinel thin films beyond iron vanadate

Spinel oxides demonstrate significant technological promise due to the vast array of interrelated physical properties that their unique structure supports. Specifically, the $\text{Fe}_{1+x}\text{V}_{2-x}\text{O}_4$ spinel system garners extensive interest due to the presence of orbitally ordered states and multiferroism.

As we have described in the chapters up to now, iron vanadate (FeV_2O_4) outstands in the spinel oxide family due to its several interconnected degrees of freedom. Nevertheless, its technological applicability is limited by the fact that its magnetic, ferroelectric and orbital orderings only appear at low temperatures. Fortunately, iron addition in the $\text{Fe}_{1+x}\text{V}_{2-x}\text{O}_4$ spinel system has been long proven as an approach for the increase of the ferroic transition temperatures [311]. This chapter's objective is the successful deposition of vanadium ferrite Fe_2VO_4 ($x = 1$) thin films with the final aim of bringing the multifunctional properties of FeV_2O_4 into the room-temperature realm.

The content of this chapter has been partially shared in the form of a scientific article [312]. The chapter starts with the elaboration of high-quality vanadium ferrite thin films on MgO substrates via pulsed laser deposition. Structural analyses confirm the epitaxial growth of the films, their high crystallinity and fully strained nature. The cationic distribution and stoichiometry are investigated using Resonant Elastic X-ray Scattering experiments, in conjunction with comprehensive characterisation of the films' physical and electrical properties.

The films exhibit room-temperature magnetism, with a magnetisation consistent with the $(\text{Fe}^{3+})_{\text{Td}}[\text{Fe}^{2+}\text{V}^{3+}_2]_{\text{Oh}}\text{VO}_4$ inverse spinel structure unveiled by anomalous diffraction. Unlike FeV_2O_4 thin films, Fe_2VO_4 films present an in-plane magnetic anisotropy and the richness in phase transitions appears to be lost with the iron replacement. This reduces the technological potential of vanadium ferrite when compared to its vanadate counterpart but opens new research paths yet to be explored.

In conclusion, this chapter represents the inaugural successful deposition of Fe_2VO_4 thin films, thereby expanding the family of spinel vanadium oxide thin films with a new member that demonstrates room-temperature magnetic properties.

1. Introduction: the Fe-V-O system

The $\text{Fe}_{1+x}\text{V}_{2-x}\text{O}_4$ system crystallises in a spinel crystal structure. However, it has the particularity of adopting either a direct spinel – $(\text{A}^{\text{II}})_{\text{Td}}[\text{B}^{\text{III}}\text{C}^{\text{III}}]_{\text{Oh}}$ – or inverse spinel – $(\text{B}^{\text{III}})_{\text{Td}}[\text{A}^{\text{II}}\text{C}^{\text{III}}]_{\text{Oh}}$ – structure contingent on the proportion of Fe^{3+} , V^{3+} and Fe^{2+} . O_h and T_d represent octahedral and tetrahedral sites, respectively, and will be simplified as squared – $[\]$ – and rounded – $()$ – brackets hereafter. A^{II} refers to a divalent cation, whereas B^{III} and C^{III} represent trivalent cationic species.

For low iron concentrations ($0 \leq x \leq 0.35$), and just like the FeV_2O_4 (FVO) iron vanadate, the system adopts a direct spinel structure: $(\text{Fe}^{2+})[\text{Fe}^{3+}_x\text{V}^{3+}_{2-x}]_{\text{Oh}}\text{O}_4$. For higher iron contents ($0.35 \leq x \leq 1$), the structure slowly transforms into a 3-2-3 inverse spinel structure: $(\text{Fe}^{3+})[\text{Fe}^{2+}_x\text{V}^{3+}_{2-x}]_{\text{Oh}}\text{O}_4$, and such is the case of the Fe_2VO_4 (VFO) vanadium ferrite. The inverse spinel structure is retained for higher iron concentrations ($1 \leq x \leq 2$): $(\text{Fe}^{3+})[\text{Fe}^{2+}\text{Fe}^{3+}_{x-1}\text{V}^{3+}_{2-x}]_{\text{Oh}}\text{O}_4$, with trivalent iron gradually supplanting trivalent vanadium, until the composition parallels that of magnetite (Fe_3O_4) [311], [313], [314].

As previously mentioned in “**Chapter I.** FeV_2O_4 in the spinel vanadate family”, the three cations in $\text{Fe}_{1+x}\text{V}_{2-x}\text{O}_4$ present a magnetic behaviour, with the following spin values: $S\text{-Fe}^{3+} = 2.5$, $S\text{-Fe}^{2+} = 2$ and $S\text{-V}^{3+} = 1$. Their relative orientation, primarily governed by antiferromagnetic super-exchange interactions between O_h - and T_d -sites, dictates the material's magnetism, which can adopt complex noncollinear magnetic textures [311]. Furthermore, two of the cations are Jahn-Teller (JT) active: V^{3+} in an octahedral site exhibits a t_{2g}^2 electronic configuration and Fe^{2+} either a $t_{2g}^4e_g^2$ or a $e^3t_2^3$ depending on whether it occupies an octahedral or a tetrahedral site, respectively. V^{3+} also presents a non-negligible orbital moment [19] which results into spin-orbit coupling (SOC) effects, increasing the complexity of interactions in the $\text{Fe}_{1+x}\text{V}_{2-x}\text{O}_4$ system.

As fully detailed in the first chapter of this thesis, the interplay between JT and SOC phenomena explains why FVO adopts diverse orbitally-ordered states and undergoes up to four structural transformations with temperature [53], [54]. Along with these structural changes, FVO's magnetic structure changes from paramagnetic to collinear ferrimagnetic, and then to non-collinear ferrimagnetic [19]. FVO has also proved to show a ferroelectric behaviour [29], making this spinel vanadate compound a multiferroic oxide with interconnected orbital, spin and charge degrees of freedom. Despite these diverse functionalities, the restriction of ferroic orderings in FVO to low temperatures (below 110 K) poses an obstacle to its incorporation into room-temperature functional devices.

One approach to move FVO's properties up in temperature is through the addition of a strain degree of freedom, for instance, depositing the material as thin films [71]. On top of that, thin films present promising avenues to utilize the coupling of ferroic order parameters in practical devices for logic, memory, and sensor technologies [70]. The deposition in thin films has however only increased the magnetic transition temperature up to 150 K [77]. The increase in iron content is another strategy for the transition temperature increase, with the Curie temperature (T_c) arising from 110 K for FVO, to 454 K for VFO and to 851 K for Fe_3O_4 [311].

On the one hand, Fe_3O_4 ($x = 2$) exhibits a magnetic ordering at room temperature, accompanied by a cubic-to-monoclinic Verwey transition [315]. In the thin-film form it displays a giant magnetoresistance behaviour whose temperature dependence is itself affected by the Verwey transition, and the material's properties as a thin film have been largely documented in the literature [316]–[318].

On the other hand, the understanding of VFO's ($x = 1$) is comparatively limited. In the bulk form, the structure and magnetic properties of the $\text{Fe}_{1+x}\text{V}_{2-x}\text{O}_4$ spinel system have been documented by Wakihara et al. [311]. In the bulk form, VFO crystallises in a cubic spinel structure with $a = 8.418(2)$ Å, presents room-temperature ferrimagnetism and a saturation magnetisation (M_s) of around $0.73 \mu_B$ per formula unit ($\mu_B/\text{f.u.}$) at 77 K. Mössbauer spectroscopy studies have confirmed the cationic arrangement corresponding to an inverse spinel structure [313], [319]. Consistent results regarding the M_s and the cationic distribution have been reported in micron-sized VFO coatings [320]. The exploration of VFO in thin films however remains until now absent from the literature.

This fifth and final chapter aims at the production of high-quality epitaxial VFO thin films on MgO substrates, as illustrated in **Figure V.1**, with the main objective of bringing the unique properties of VFO up in temperature.

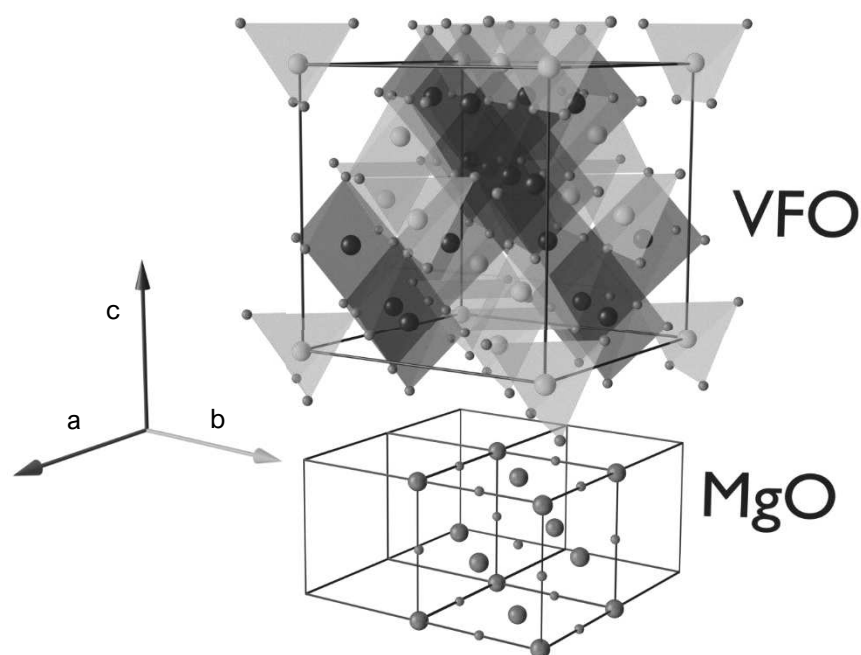


Figure V.1. Schematic representation of epitaxial VFO (top) and MgO (bottom). On VFO: blue – cations at O_h site, orange – cations at T_d site. MgO: green – Mg cations. In both: red – O.

2. Bulk VFO: synthesis and characterisation

The initial step towards acquiring VFO thin films involved the solid-state synthesis of a high-quality target possessing the desired VFO phase. The ceramic method for the VFO synthesis has been the same as the one for FVO, as detailed in the “Bulk target elaboration” part of the second chapter of this thesis – page 26. However, differently to FVO, VFO contains iron cations in both trivalent and divalent oxidation states. Consequently, the partial reduction of Fe(III) into Fe(II) necessitates a mildly reducing atmosphere to circumvent a total reduction into Fe(II) or even the production of metallic Fe.

Similarly to FVO, the transformation of V(V) into V(III) requires more severe reducing conditions and it is extremely important to have V(V) reduced into V(III) before heating to temperatures higher than 690°C, because V_2O_5 melts at this temperature [79]. A two-step heating treatment in a mildly reducing atmosphere of (99.5% Ar/0.5% H_2) – which is less reducing than in FVO's synthesis – facilitated the achievement of the desired synthesis without any remaining precursors or over-reduced products. The overall chemical process has been indicated in **Equation (V.1)**, with water added as a subproduct in order to valence the oxygen transformation.



The precursor mixture was calcinated in a tubular furnace under a mildly reducing atmosphere of 99.5% Ar/0.5% H_2 at a flow of 110 sscm. It was first taken up to 600°C at a heating rate of 100°C/h and left at this temperature for ten hours. After this calcination state, the Fe_2VO_4 powder was manually ground with an agate stone mortar and milled by ball attrition with ethanol as dispersant. As shown in **Figure V.2**, submicron median size was found after 1 hour of ball attrition process, time beyond which the particle size and the size distribution stay relatively constant.

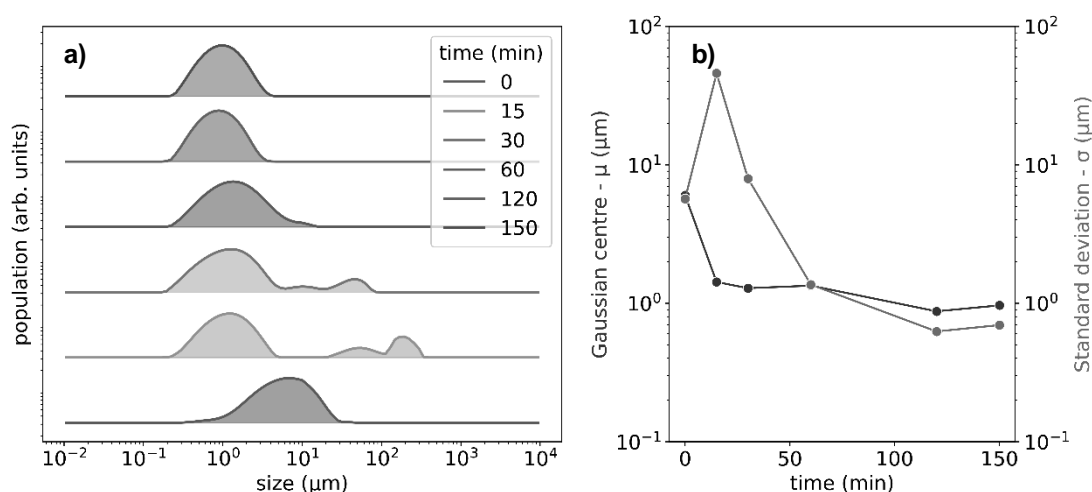


Figure V.2. (a) Population distributions as a function of size for attrition times ranging from 0 to 180 minutes. (b) Centre of gaussian peaks for the population distribution (blue) and standard deviations of the distributions (red) as a function of time. This figure is equivalent to **Figure II.14** for FVO.

The fine dry Fe_2VO_4 powder was then mixed with a minor quantity of polyvinyl alcohol and subjected to uniaxial pressure under a 60-bar load to form a pellet with a thickness of 4 mm and a diameter of 15 mm. Finally, the pellet was finally sintered at 1300°C, a temperature attained at a rate of 100°C/h, during 20h at a reducing atmosphere (99.5% Ar/0.5% H_2) and cooled down to room temperature at 200°C. The sintering yield (c.f. **Equation (II.2)**) of the obtained pellet was $\tau_s = 0.84$, showing a correct solid densification.

The powder X-ray diffractogram of the VFO ceramic target is shown in **Figure V.3**. A profile matching analysis using the FULLPROF program [321] confirmed the cubic spinel structure with $a = 8.429(2)$ Å. No spurious phases have been observed, attesting both the correct crystal phase and the absence of impurities. This value is close to the one reported in the literature for VFO: $a = 8.418(2)$ Å [311]. EDS analyses indicated an Fe-to-V ratio of 1.98(3) a value closely aligned with the expected 2.0.

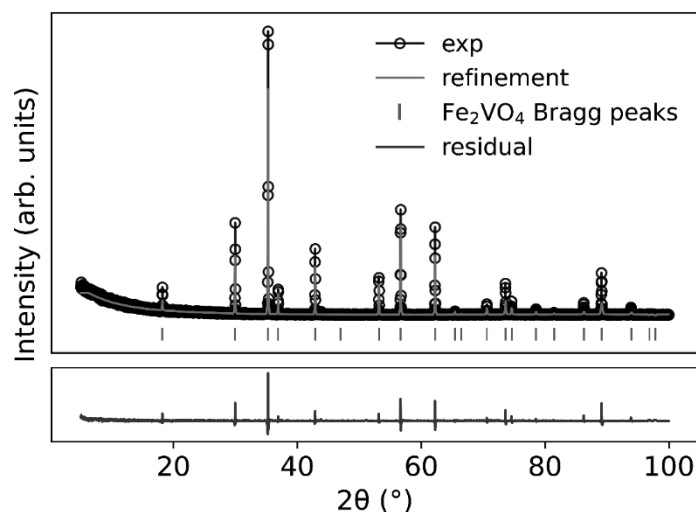


Figure V.3. X-ray characterisation of the VFO target, showing the experimental diffractogram (black), the FULLPROF refinement (red), the position of the Bragg peaks predicted for a $Fd\bar{3}m$ structure (green) and the residual between the experimental and refined data (blue).

3. VFO thin films

3.1. Thin film obtention and characterisation

40 nm thick Fe_2VO_4 thin films were grown by PLD using a KrF excimer laser ($\lambda = 248$ nm). The sintered pellet was used as PLD target, and commercial $\text{MgO}(001)$ substrates ($a = 4.211$ Å, CODEX) [75] were chosen due to their small lattice mismatch (-0.2%). The target-to-substrate distance was kept at 50 mm. Argon was chosen as gas because any O_2 pressure suggested the oxidation of V(III) into V(V) and the formation of a V_2O_5 sublayer [77].

The deposition conditions were optimised from those of FVO thin films, using different deposition temperatures (between 400°C and 600°C), various Ar partial pressures (0.001 to 0.1 mbar), laser fluences (from 1.3 to 4 J cm^{-2}) and laser deposition rates (2 to 10 Hz) – see “Optimisation of FeV_2O_4 thin-film deposition” on page 62. Similarly to FVO, the optimised conditions for VFO were 400°C, 0.01 mbar, 4 J cm^{-2} and 5 Hz, with the temperature and the Ar pressure being the most influential parameters for the resulting film’s quality.

The AFM image of a $5 \times 5 \mu\text{m}^2$ surface area is shown in **Figure V.4b** together with the image of a MgO substrate prior to deposition (**Figure V.4a**), for comparison. The AFM images show a relatively smooth surface for both the substrate and the thin film. Root mean square roughness (R_q) values were obtained from region analysis studies on the shown areas and are of ≈ 0.5 nm for MgO and ≈ 0.6 nm for VFO//MgO.

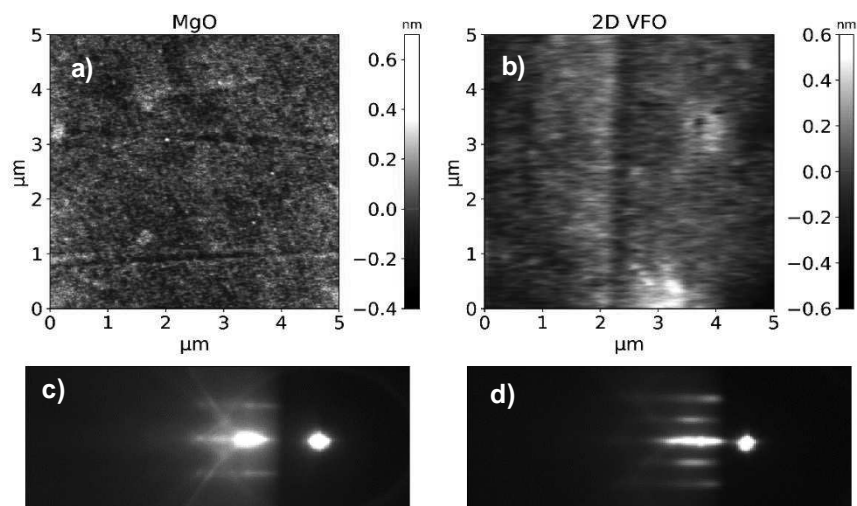


Figure V.4. AFM images of (a) MgO prior to deposition and (b) VFO//MgO films, both acquired in non-contact mode. RHEED patterns before (c) and after (d) deposition.

The RHEED pattern observed before deposition (**Figure V.4c**) consists of a series of streaks, as anticipated for single-crystalline MgO substrates. The images show Kikuchi lines, indicator of a high quality of the crystal surface [159], [160], [162]. The RHEED pattern of VFO//MgO after deposition (**Figure V.4d**) consists of rod-shaped spots which is associated to a 2D smooth and flat surface, and still shows Kikuchi lines, indicating both a good surface state and crystallinity inside the material [128].

XRR measurements allowed determining that the sample's thickness is 40.8(2) nm, as shown in **Figure V.5**.

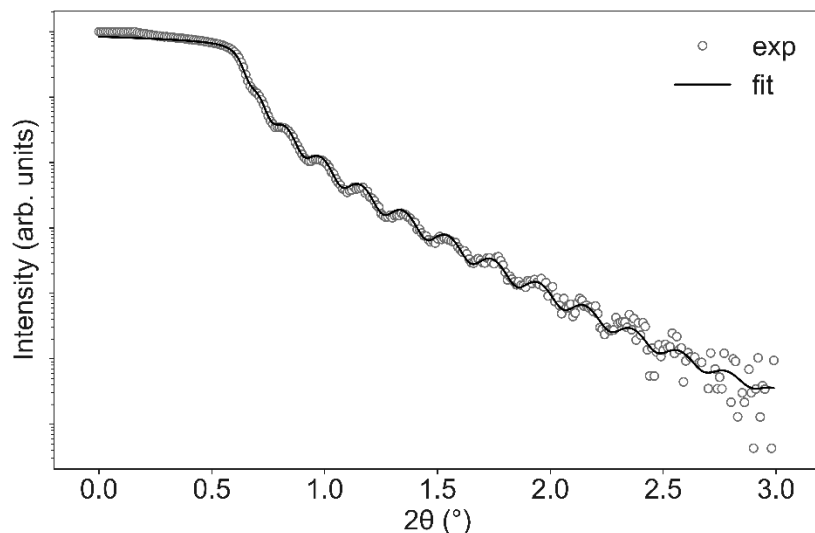


Figure V.5. XRR – measurement (red) and refinement (black) for a VFO//MgO thin film.

The film was finely characterised in its out-of-plane direction thanks to a precise θ - 2θ diffractogram on the 004 reflection (**Figure V.6a**) with a wavelength of 1.74331 Å, acquired at the D2AM beamline of ESRF Synchrotron facility. A diffractogram covering a broader θ - 2θ range is shown in the annexes of the thesis – **Figure A.9**. Compared to the bulk sample, only the 00 l reflections are observed, confirming the film epitaxy and the absence of parasitic phases. The diffractograms show a fringe-like profile centred around the peak's maximum. The presence of these oscillations, known as Laue oscillations, is frequently used as evidence of high sample quality, indicating that grown films are highly crystalline, homogenous, have a low density of defects and possess a smooth substrate/film interface [118], [119].

The 004 peak was fitted using the layer builder of the *xrayutilities* package [149]. The position of the peaks indicates an out-of-plane lattice parameter of 8.408(2) Å for VFO and 4.2113(1) Å for MgO, in perfect agreement with the 4.211 Å theoretical value [75]. The oscillation frequency was used to determine the sample's thickness: 38.7(1) nm, close to the value determined via XRR: 40.9(2) nm.

Azimuthal Φ scans were carried out at constant $2\theta - \omega$ angles, or the VFO {026} and secondly for the MgO {024} reflections, as shown in **Figure V.6b**. $\Phi = 0$ represents a parallel alignment with the substrate's edge. Both scans show four distinct equidistant peaks in the 0 – 360° range. The presence

of film and substrate peaks at the same angles is evidence of the crystallographic alignment between their structures, and therefore, of the epitaxial nature of the growth of the thin film system.

Finally, the 2D-RSM images probed the substrate and the film simultaneously for the MgO 024 reflection and the VFO 048 reflections located in close vicinity (**Figure V.6c**), and only the film for its 026 reflection of FVO (**Figure V.6d**). The sole presence of clearly defined peaks for the films is another proof of a well-crystallised single-phased film.

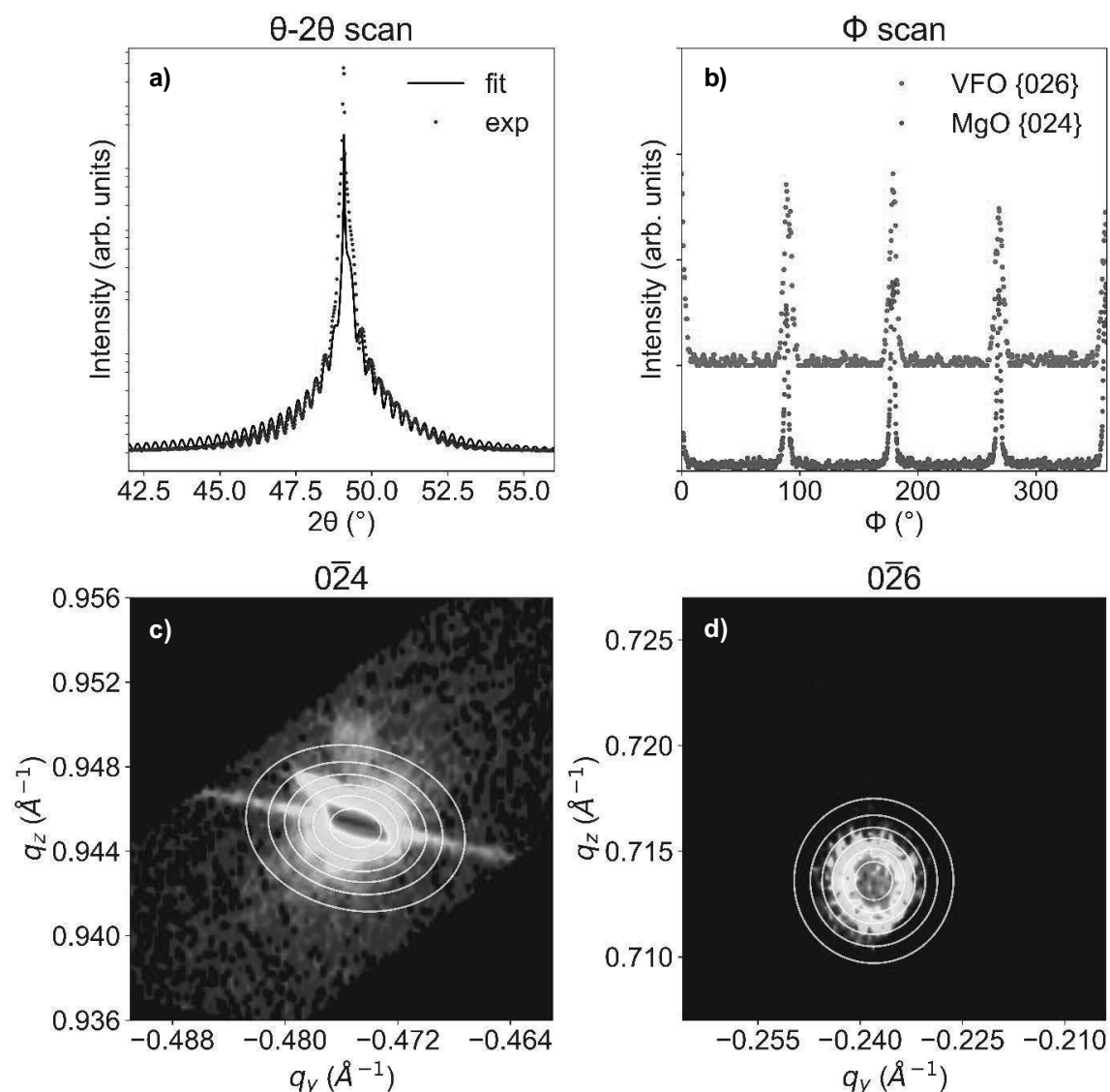


Figure V.6. (a) θ - 2θ diffractogram of the VFO//MgO thin films, acquired with an X-ray wavelength of 1.74331 \AA – experimental data (black) and *xrayutilities* fit (blue). (b) Φ scan on a 026 reflection of VFO and 024 reflection for MgO. (c) reciprocal space mappings acquired for the $0\bar{2}4$ reflection of MgO (eclipsing the $0\bar{4}8$ reflection of VFO) and the $0\bar{2}6$ reflection of VFO

The substrate's signal eclipses the film's one in the MgO 024 – VFO 048 map, since they appear at very close q_z and q_x values. A lattice parameter of $a = 4.213(2)$ was found for MgO, in concordance with the theoretical value of 4.211 \AA [75]. The film's 026 reflection, not accompanied with any substrate reflection, enabled a determination of the lattice parameters: $a = b = 8.415(6) \text{ \AA}$ and $c = 8.407(3) \text{ \AA}$. The in-plane lattice parameter is very close to twice that of MgO: $4.211 \times 2 = 8.422 \text{ \AA}$. Consequently, the VFO lattice is compressed in a fully strained mode to adjust its lattice parameter to MgO, as expected for the epitaxial nature of the deposition and enabled by the small lattice mismatch ($\approx -0.1\%$). The out-of-plane lattice parameter is consistent with the value found via θ - 2θ measurements. The lattice parameters of the substrate and the film have been determined by the mapping of their four equivalent $\{048\}$ and $\{026\}$ reflections, respectively.

Compared to their bulk counterparts, VFO thin films suffer a lattice shrinking of $\approx -0.7\%$ and a strain-based structural tetragonalisation. We observe that an in-plane lattice compression does not translate into an out-of-plane lattice elongation, as it would be expected. The simultaneous shrinking of both lattice parameters corresponds to a mechanical response known as “auxetic behaviour”, as previously described in page 77. This phenomenon has already been reported in other spinel thin films [168], [169] and, as shown in **Table II.1** (page 76), it was also present in $\text{FeV}_2\text{O}_4//\text{MgO}$. Auxetism can be also quantified through the negative value of the effective Poisson's ratio [166] $\nu^* \approx -0.8$, as defined in **Equation (II.9)**.

Finally, EDS measurements on the thin films led to an Fe/V ratio of $2.2(3)$, slightly exceeding the expected value of 2.0. In the soft X-ray region, the vanadium signal suffers significant interference from oxygen [322] due to the close proximity of O K-edge (530 eV) [225] with the V L-edges ($520 - 530 \text{ eV}$) [323], resulting in an underestimation of the vanadium content and an overestimation of the Fe/V ratio. For higher X-ray energies, the beam's penetration length is larger than the thin film thickness, and the elements which compose the substrate crystal (Mg, O) are unavoidably included in the quantification and their presence in the film is also overestimated. The substrate also presents a non-negligible amount of Fe which furtherly increases the Fe/V ratio.

3.2. Cationic distribution in the thin film

REXS experiments were executed to determine the cationic distribution of the Fe and V species in the O_h and T_d sites. We have characterised the positions of both Fe and V cations by studying XANES (x-ray absorption near the edge structure) spectra acquired at the Fe K-edge – around 7130 eV [223]. REXS simultaneously allows an element and orbital-sensitive analysis of the crystal [193], and the XANES region of the spectrum can give fruitful insights on the cation's state. DANES has already been proved successful in characterising the cation's state (occupation and valence state) in thin films [220], [221]. Furthermore, we have previously used EXAFS experiments to successfully locate oxygen cations in oxide thin films [188], c.f. section “EDAFS on FVO films: oxygen positions” of **Chapter III** – page 108.

By using the *insexs* software, as well as the methodology that we have developed along the code [187], we have chosen the reflections 333 and 115 as the most adequate for the characterisation of the cations. REXS spectra (-20 eV, +25 eV) have been acquired around the Fe K-edge (- 20 eV, + 25 eV) for both reflections. This edge choice, compared to the V K-edge, is dictated by the smaller wavelength of the incident X-rays which results in fewer self-absorption issues and a better signal-to-noise ratio [188].

Theoretical spectra with the formula $(\text{Fe}_{1-x}\text{V}_x)_{\text{Td}}(\text{V}_{2(1-y)}\text{Fe}_{2y})_{\text{Oh}}\text{O}_4$ have been simulated with x and y values varying between 0 and 1 with increments of 0.005. The simulations have been conducted using the *ab initio* FDMNES software [210]. The difference between the experimental (ES) and the theoretical (TS) spectra ($\chi^2 = \int TS(E) - ES(E)dE$) has been calculated for all (x, y) combinations, as illustrated in **Figure V.7a**. The χ^2 minimum (best fit) unequivocally takes place at $x = 0.021(8)$ and $y = 0.54(2)$.

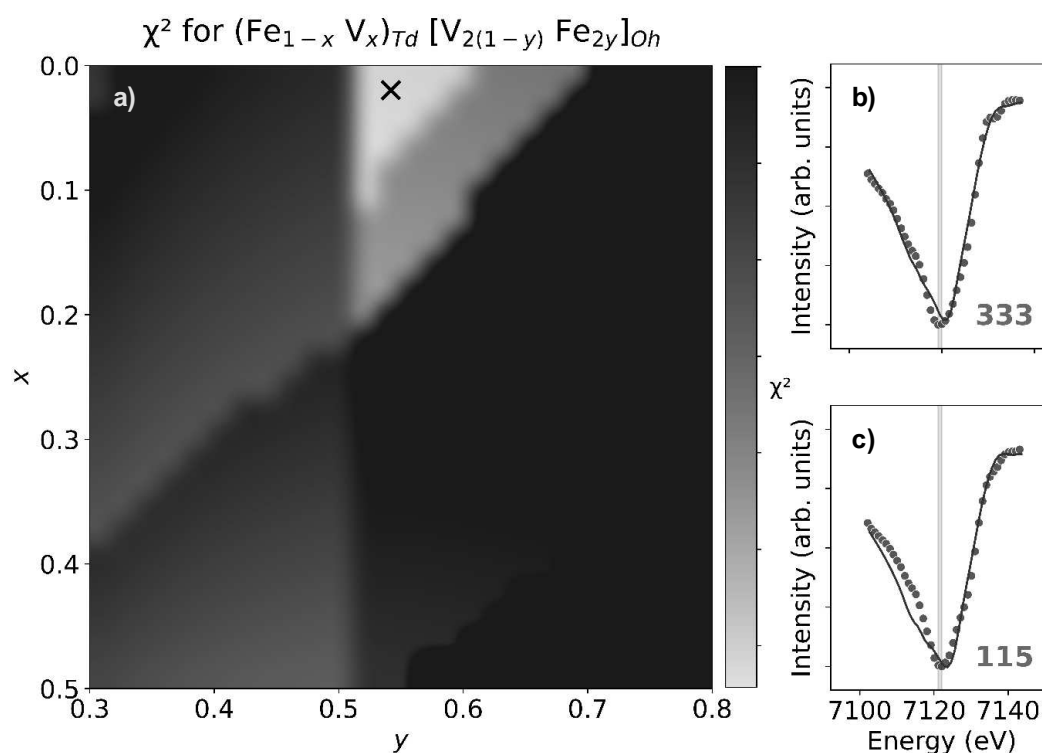


Figure V.7. (a) Difference calculated between the experimental spectra and the theoretical spectra simulated for all (x, y) combinations. (b) and (c) experimental spectra for the 333 (b) and 115 (c) reflections (green points) and fit with the spectrum simulated for the best (x, y) (blue line)

When using the neural networks for the XANES spectra, the average value found for the best optimal models for each 333/115 reflections is $x = 0.01(4)$ and $y = 0.54(3)$. These results further confirm the efficiency of ANN models to fit DANES spectra. Furthermore, the spectra simulated at these conditions perfectly fit the experimental data acquired at the 333 and 115 reflections, as indicated in **Figure V.7b** and **Figure V.7c**, respectively.

This (x, y) minimum leads to a cationic occupation of $(\text{Fe}_{0.979(8)}\text{V}_{0.021(8)})_{\text{Td}}[\text{V}_{0.92(4)}\text{Fe}_{1.08(4)}]_{\text{Oh}}\text{O}_4$, that is, an experimental formula unit of $\text{V}_{0.94(5)}\text{Fe}_{2.05(5)}\text{O}_4$ for VFO films and an Fe/V ratio of 2.1(1), consistent with the ratio observed in the bulk of 1.98(3). These values are in adequacy with the EDS results and are a confirmation of the stoichiometric transfer of matter from the target to the film during deposition. The cationic occupation is very close to the expected scenario $(\text{Fe})[\text{VFe}]\text{O}_4$ in which all the V ions occupy O_h sites, whereas the Fe ones occupy both the T_d and O_h sites.

3.3. Magnetic and transport properties of VFO films

The magnetic response of the thin films was characterised via magnetisation (M) vs. applied field (H) measurements at 300 K in in-plane (IP) and out-of-plane (OOP) configurations, as shown in **Figure V.8a**. The sample shows a non-negligible saturation magnetisation (M_s) of around $0.8 \mu_B/\text{f.u.}$ with an easy magnetisation axis in the in-plane direction and an IP coercive field of 205(5) Oe ($1.98(4) \times 10^4 \text{ A m}^{-1}$). The M_s value is consistent with the one already reported for the bulk [311]. The sample therefore presents a magnetic ordering at room temperature.

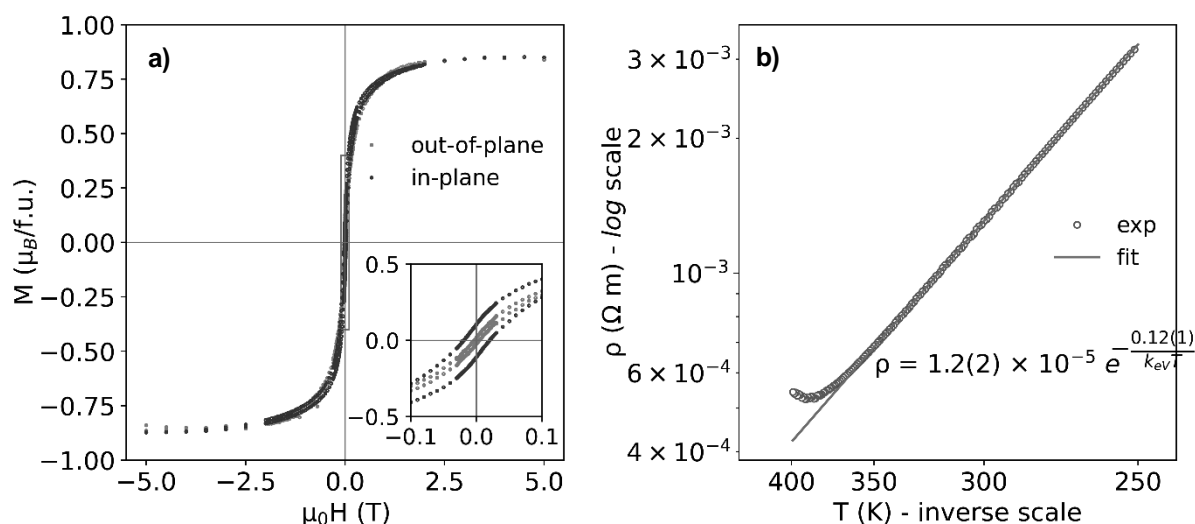


Figure V.8. (a) Magnetisation hysteresis loops measured at 300 K, for the in-plane (blue) and out-of-plane (red) configurations. (b) Longitudinal resistivity (\log scale) vs. temperature ($^{-1}$ scale) – experimental data in green circles, fit using the thermal activation model in solid red line.

The transport properties of the films have been characterised via sheet resistivity vs. temperature measurements in the range 250 – 400 K, as illustrated in **Figure V.8b**. Voltage values exceeded the limit value of our PPMS below 250 K. The temperature evolution of the material's resistivity can be modelled by a thermal activation (TA) model, as previously defined in **Equation (II.10)**. The resistivity thus follows an Arrhenius-like activation process of charge carriers whose presence in the conduction band

becomes more notorious with increasing temperature [179]. A discontinuity in the model trend starts to appear at around 400 K, also suggesting the vicinity of a phase transition.

The model enabling an optimal fit of the spin transport vs. temperature differs with FVO//MgO thin films. As described in the section “Transport properties of thin films” of the second chapter of this thesis – page 84, the variable-range hopping (VRH) model provides a more suitable approach for FVO//MgO, but the TA model will be employed to compare both thin film systems. The TA fit on the FVO//MgO thin films had the form $\rho_{FVO//MgO} = 1.48(4) \times 10^{-4} e^{-0.136(1)/k_{ev}T}$, while the resistivity relationship becomes $\rho_{VFO//MgO} = 1.2(2) \times 10^{-5} e^{-0.12(1)/k_{ev}T}$ for VFO films. The pre-exponential factor for FVO//MgO is an order of magnitude higher than that for VFO//MgO, and the thermal bandgap is ca. 13% larger, suggesting that FVO//MgO has inherently higher resistivity compared to VFO//MgO under similar conditions. This can be explained due to smaller interatomic distances and the presence of both Fe³⁺ and Fe²⁺ in VFO's lattice.

Using the elementary distribution determined by the DANES analysis, and introducing the valence of the cations, the cation distribution can vary between a (Fe²⁺)[Fe³⁺V³⁺]O₄ direct spinel configuration and a (Fe³⁺)[Fe²⁺V³⁺]O₄ inverse spinel one. In both direct and inverse spinel configurations, an antiparallel alignment of the magnetic moments between cations at O_h and T_d sites is expected [324], [325], and the observed moment of $\mu_{VFO} = 0.8 \mu_B/f.u.$ can therefore be written as $\mu_{VFO} = |\mu_{O_h} - \mu_{T_d}|$. Considering that the magnetic contribution of both Fe³⁺ and Fe²⁺ ions comes solely from the spin-only contribution ($\mu_{Fe^{2+}} \approx 4\mu_B$, $\mu_{Fe^{3+}} \approx 5\mu_B$), and that V³⁺ will align along the species in the O_h site, one can calculate the magnetic contribution of V³⁺. The net magnetic contribution of V³⁺ is expected to be smaller than a spin-only scenario ($\mu_{V^{3+}-SO} \approx 2\mu_B$) due to both canting phenomena, as reported in other spinel vanadates [326], and to the quenching of magnetic moments due to the spin-orbit coupling [19].

Two possible scenarios for the magnetic moment of V³⁺ arise depending on whether VFO adopts a direct ($\mu_{V^{3+}} = \mu_{Fe^{2+}} - \mu_{Fe^{3+}} \mp \mu_{VFO}$) or an inverse ($\mu_{V^{3+}} = \mu_{Fe^{3+}} - \mu_{Fe^{2+}} \mp \mu_{VFO}$) spinel structure. For the direct spinel structure, the $\approx 0.8 \mu_B$ per unit cell cannot be reached with a parallel alignment between the V³⁺ and Fe³⁺ cations in O_h sites. The only possible combination is found for the inverse spinel configuration, with V³⁺ contributions of either $\approx 0.2 \mu_B$ or $\approx 1.8 \mu_B$ that accompany Fe²⁺ in the O_h site. The latter value is the most probable since it is both closer to a spin-only scenario and to the experimental values of the orbitally quenched magnetic moment for V³⁺ in FVO [19]. As a result, VFO adopts an inverse spinel structure. These findings are consistent with the neutron diffraction studies carried out in bulk VFO [314] and can be explained by the more stable configuration of [Fe²⁺]_{O_h} when compared to its trivalent counterpart.

Finally, the magnetisation as a function of temperature has been measured in the [2 - 400 K] range under an applied magnetic field of 0.5 T, as shown in **Figure V.9**. The temperature boundaries correspond to the measurement limits of our PPMS. The raw data (**Figure V.9a**) shows a predominant paramagnetism, due to the presence of Fe impurities in the MgO substrate (confirmed by EDS). Similar

measurements on a virgin MgO have confirmed the paramagnetic behaviour of the substrate. After paramagnetic correction (**Figure V.9b**), by fitting with Curie's law and subtracting the paramagnetic component, no magnetic transition temperature has been detected in the aforementioned temperature range. Nevertheless, the decrease of the magnetic signal when approaching 400 K tends to indicate that the ordering temperature is close to that temperature, and matches the transition temperature reported for bulk VFO: 454 K [311].

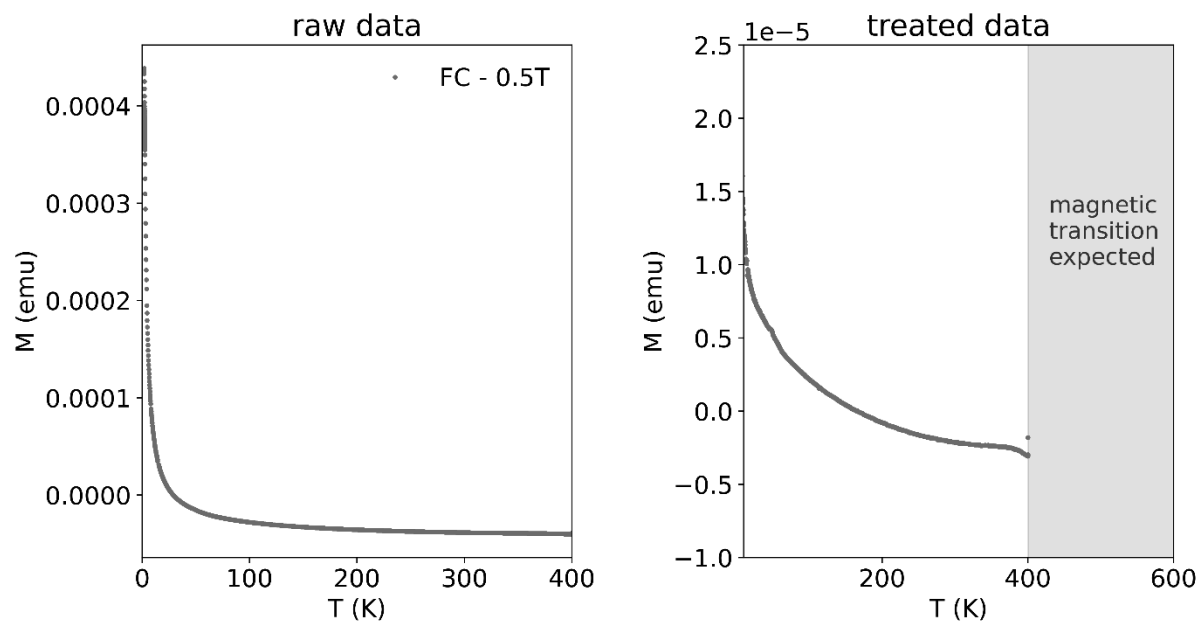


Figure V.9. Magnetisation as a function of temperature: (a) raw data, (b) after paramagnetic correction

The study hereby presented provides substantial insights into the synthesis, structural characterisation, and physical properties of VFO thin films, never reported yet. The thin films show a 2D growth, with a very low top roughness ($R_q \approx 0.6$ nm) and high crystalline quality. The nature of the VFO crystallographic phase was determined by XRD measurements to be a spinel one, growing epitaxially onto the MgO(001) substrate with the following lattice parameters: $a = b = 8.415(6)$ Å and $c = 8.407(3)$ Å. The spinel phase is tetragonally distorted because of the compressive strain effects, and the films exhibit an auxetic behaviour.

The stoichiometry of the VFO films have been confirmed by EDS and REXS measurements. The films are magnetically ordered at room temperature with a non negligible saturation magnetisation of around $0.8 \mu_B/f.u.$ The cationic distribution could be determined combining magnetic and REXS measurements. VFO adopts an inverse spinel structure close to $(Fe^{3+})[Fe^{2+}V^{3+}]O_4$. Both the magnetic and electric properties of the films suggest a possible phase transition around 400 K. The resistivity below this temperature can be modelled using a thermal activation model.

While VFO exhibits promising attributes such as room-temperature magnetic behavior and low coercivity, its in-plane magnetic anisotropy presents a significant obstacle for direct applications in Spin-Orbit Torque (SOT)-based magnetic memories. To overcome this limitation, future research endeavours will concentrate on inducing perpendicular magnetic anisotropy (PMA) in VFO. Various strategies, including chemical doping and strain engineering through substrate selection or thickness variation, will be explored. The ultimate objective is to develop VFO heterostructures that not only operate at room temperature but also possess PMA, thereby making them more suitable for memory application purposes.

General conclusions and future perspectives

The main objective of this PhD work consisted in a deep exploration of FeV_2O_4 (FVO) thin films, encompassing their synthesis, structural characterization, and physical properties. The comprehensive investigation presented across five substantive chapters has considerably enriched our understanding of FVO thin films, from their basic science to their technological applicability.

Chapter I served as an indispensable foundation, framing the complex physical phenomena influencing the unique properties of FVO within the broader vanadate family and the spinel vanadates subgroup.

Chapter II offers a detailed methodological guide for synthesising and depositing FVO thin films, ensuring accurate crystal phase identification and setting the stage for subsequent analyses. The deposition of FVO films onto two different substrates (MgO and SrTiO_3) is thoroughly described, accompanied by various characterisations, ranging from crystal structure to magnetic and transport properties. Future analyses will supplement the current work with additional techniques such as transmission electron microscopy (TEM) and magnetic force microscopy (MFM).

Further research will delve into the ferroelectric properties of the thin films, as the existing equipment at our institute is limited to room-temperature measurements. Additionally, we will explore various substrate combinations to investigate the strain effects on the FVO structure. An ancillary project – not presented in this PhD work – focused on chemically doping FVO thin films with different cationic species (Li, Ni, and Co). Of these, only the FVO:Li structures achieved proper crystallisation. This Li-doping study will be completed in due course to highlight its scientific value, and further efforts will be dedicated to optimising the synthesis of the other doping variants.

The crystal structure of FVO thin films has been exhaustively examined in Chapter III through the innovative application of resonant diffraction methods like resonant elastic x-ray scattering (REXS). REXS has been successfully employed to determine the cationic distribution in the thin films and, for the first time, the technique was used to locate oxygen atoms in oxide thin films. Work is currently underway to assess the structural changes in FVO thin films with temperature variations, and the findings will be used to refine the temperature-dependent analysis of oxygen positions, ultimately leading to the orbital ordering of FVO films as a function of temperature.

The third chapter also introduces *insexs*, a newly developed computer program designed for resonant diffraction analyses. Conceived as a framework for REXS applications, future updates will extend the

software's current capabilities. These enhancements aim to contribute to the broader goal of popularizing resonant diffraction techniques for the characterization of oxide thin films.

Chapter III also begins the discussion on the use of artificial neural networks for refining REXS spectra. The results for the cationic distribution align well with other standard techniques, which require significantly more computational time. However, the analysis of oxygen positions could benefit from further refinement. This study is currently being completed with the structural resolution of the FVO structure with temperature variation as well as the application of convolutional neural networks.

Chapter IV extended the discourse to technological horizons, investigating the applicability of FVO thin films in spintronics through the fabrication and study of Pt/FeV₂O₄//STO heterostructures, motivated by the considerable perpendicular magnetic anisotropy (PMA) of the FVO//STO system. The spin transport of FVO-based heterostructures have been studied for the very first time, and the spin-driven contribution of the magnetoresistance has been shown to dominate over the magnetic-driven part.

To overcome the limitations in our thickness-dependent study, additional data points for Pt thicknesses will be collected to refine the spin transport parameters. The conflicting results in the harmonic study necessitate further investigations to clarify the observed values. Besides, future work will involve thickness-dependent studies of the ferrimagnetic layer, aiming to reduce the material's coercivity to levels manageable by spin-orbit torques (SOT).

For the heterostructure characterisation of the thin-film heterostructures, ferromagnetic resonance (FMR) will be employed, pending the access to the necessary equipment. Additionally, sputtering equipment will be soon added to our current deposition setup, enhancing the quality of the Pt layer deposition. This will enable the use of alternative heavy-metal top electrodes like Pd, or other transition metals like Cu for orbital-driven effects studies. Proposals have been made to perform X-ray circular dichroism (XMCD) measurements on the heterostructures with applied currents on the Pt top layer. However, these were not approved. Resolving this would provide valuable insights into the impact of spin current on the ferrimagnetic layer via SOT phenomena. Finally, it is still unclear the interplay between the spin transport and the different degrees of freedom of FVO. Future research endeavours will focus on the junction between the heterostructures' spin transport properties and the multifunctionalities that FVO offers.

Finally, Chapter V aimed at overcoming the main applicability issue that FVO presents: its low-temperature functional domain. The chapter moved beyond FVO to explore the intriguing properties of vanadium ferrite Fe₂VO₄ (VFO) thin films, offering new pathways for future research by demonstrating their room-temperature magnetism. By means of REXS experiments and in junction with magnetometry analysis, VFO films have been showed to crystallise in an indirect spinel structure.

In terms of the future perspectives, high-temperature magnetometry measurements are essential for determining the films' transition temperature. Despite its room-temperature magnetism, VFO does not exhibit PMA on MgO substrates, nor on SrTiO₃ substrates as our preliminary tests indicate (not

presented here). Inducing PMA is a challenge that needs to be addressed. Future research should also explore how the addition of iron impacts the desired multifunctional properties of FVO.

In summary, my PhD work has advanced our understanding of FVO thin films, filling a research gap that existed at the outset of my doctoral studies. The study of FVO thin films has led to methodological contributions, particularly in the realm of resonant diffraction, that can be applied to other oxide thin film systems. For the first time, the spin transport properties of spinel vanadate structures have been explored. This research serves as a foundation for investigating other spinel vanadate thin films, as is currently the case with CoV_2O_4 in our team's ongoing work. Beyond FVO-based heterostructures for spintronics, my PhD research has also opened new avenues for future studies, including the exploration of novel Fe_2VO_4 thin films. In conclusion, I humbly hope that my contributions will prove valuable to my colleagues and the broader scientific community.

– This page intentionally left blank –

2. Derivation of the two anomalous terms for the atomic scattering factor

This part aims at obtaining the expressions of anomalous terms of the atomic scattering factor: f' and f'' , as described in **Equations (III.7) and (III.8)**. As defined in **Equation (III.5)** – also shown below, the atomic scattering factor (f) depends on the frequency (ω), the resonance frequency (ω_s) and the damping factor (k).

$$f = \frac{\omega^2}{\omega^2 - ik\omega - \omega_s^2} \quad (\text{III.5})$$

This expression can be simplified by taking away the Thomson scattering factor (f_0) which, in the case of a single electron, is equal to one; leading to the expression in **Equation (A.1)**.

$$f = f_0 + f' - if'' = 1 + \frac{\omega_s^2 + ik\omega}{\omega^2 - ik\omega - \omega_s^2} \quad (\text{A.1})$$

The latter part of this expression represents $f' - if''$. Multiplying both numerator and denominator times the complex conjugate of the denominator, the latter becomes a real number. Then, we group the terms in the numerator and obtain the values of f' and f'' , as shown in **Equation (A.2)**.

$$\begin{aligned} f' - if'' &= \frac{\omega_s^2 - ik\omega}{\omega^2 - ik\omega - \omega_s^2} = \frac{(\omega_s^2 + ik\omega)(\omega^2 + ik\omega - \omega_s^2)}{(\omega^2 - \omega_s^2)^2 + k^2\omega^2} = \\ &= \frac{\omega_s^2(\omega^2 - \omega_s^2) - k^2\omega^2}{(\omega^2 - \omega_s^2)^2 + k^2\omega^2} + i \frac{k^2\omega^2}{(\omega^2 - \omega_s^2)^2 + k^2\omega^2} \end{aligned} \quad (\text{A.2})$$

The expressions found for f' and f'' correspond to the ones shown in **Equation (III.7) and (III.8)**:

$$f' = \frac{\omega_s^2(\omega^2 - \omega_s^2) - k^2\omega^2}{(\omega^2 - \omega_s^2)^2 + k^2\omega^2} \quad (\text{III.7})$$

$$f'' = \frac{k\omega^3}{(\omega^2 - \omega_s^2)^2 + k^2\omega^2} \quad (\text{III.8})$$

3. Additional information on artificial neural networks

3.1. CV prediction deviations. XANES 115

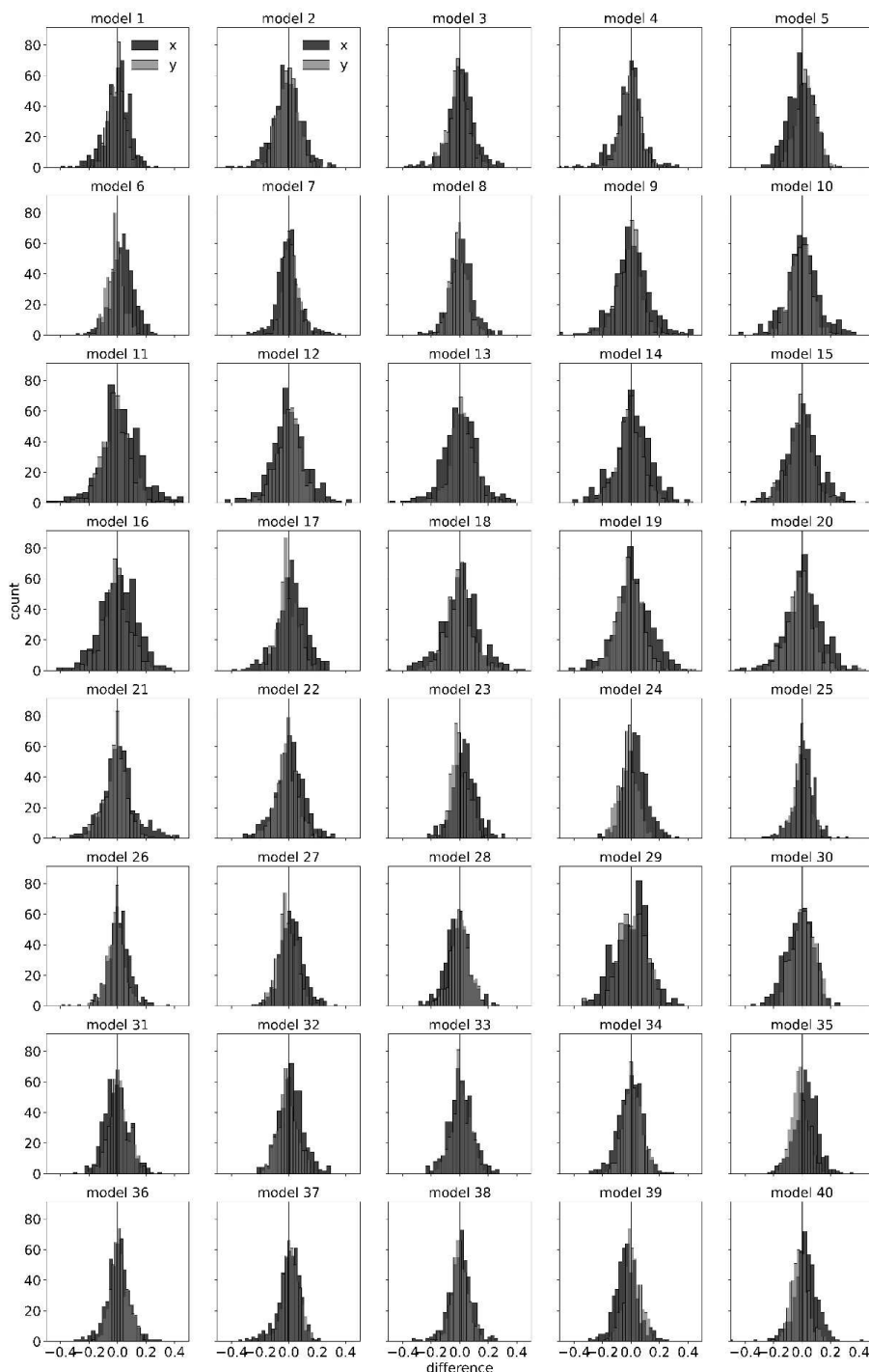


Figure A.3. Difference between the predicted and actual values for x (dark) and y (light) for the CV dataset, for the 115 reflection (XANES). Both parameters describe the cationic occupation. Blue graphs correspond to “ReLU” models, whereas red correspond to “sigmoid”.

3.2. Artificial neural network architectures

Table A.1. Information on the ANN models used in the refinement of REXS spectra: number of the model, activation function used (blue if 'ReLU'), number of layers (not considering the input layer), total number of neurons and model architecture (with output).

model	activation	layers	neurons	architecture				
1	ReLU	3	82	64	16	2		
2	sigmoid	3	82	64	16	2		
3	ReLU	4	162	32	64	64	2	
4	sigmoid	4	162	32	64	64	2	
5	ReLU	3	50	16	32	2		
6	sigmoid	3	50	16	32	2		
7	ReLU	3	66	32	32	2		
8	sigmoid	3	66	32	32	2		
9	ReLU	5	258	32	64	128	32	2
10	sigmoid	5	258	32	64	128	32	2
11	ReLU	5	354	32	64	128	128	2
12	sigmoid	5	354	32	64	128	128	2
13	ReLU	5	482	256	128	64	32	2
14	ReLU	6	994	512	256	128	64	32 2
15	ReLU	6	1474	512	512	256	128	64 2
16	ReLU	6	1502	128	256	526	526	64 2
17	ReLU	5	962	512	256	128	64	2
18	sigmoid	5	482	256	128	64	32	2
19	sigmoid	6	994	512	256	128	64	32 2
20	sigmoid	6	1474	512	512	256	128	64 2
21	sigmoid	6	1502	128	256	526	526	64 2
22	sigmoid	5	962	512	256	128	64	2
23	ReLU	3	34	16	16	2		
24	sigmoid	3	34	16	16	2		
25	ReLU	4	42	16	16	8	2	
26	sigmoid	4	42	16	16	8	2	
27	ReLU	4	30	16	8	4	2	
28	sigmoid	4	30	16	8	4	2	
29	ReLU	3	14	8	4	2		
30	sigmoid	3	14	8	4	2		
31	ReLU	3	26	8	16	2		
32	sigmoid	3	26	8	16	2		
33	ReLU	3	26	16	8	2		
34	sigmoid	3	26	16	8	2		
35	ReLU	3	50	32	16	2		
36	sigmoid	3	50	32	16	2		
37	ReLU	5	62	32	16	8	4	2
38	sigmoid	5	62	32	16	8	4	2
39	ReLU	4	58	32	16	8	2	
40	sigmoid	4	58	32	16	8	2	

3.3. MSE model comparison – 333 XANES

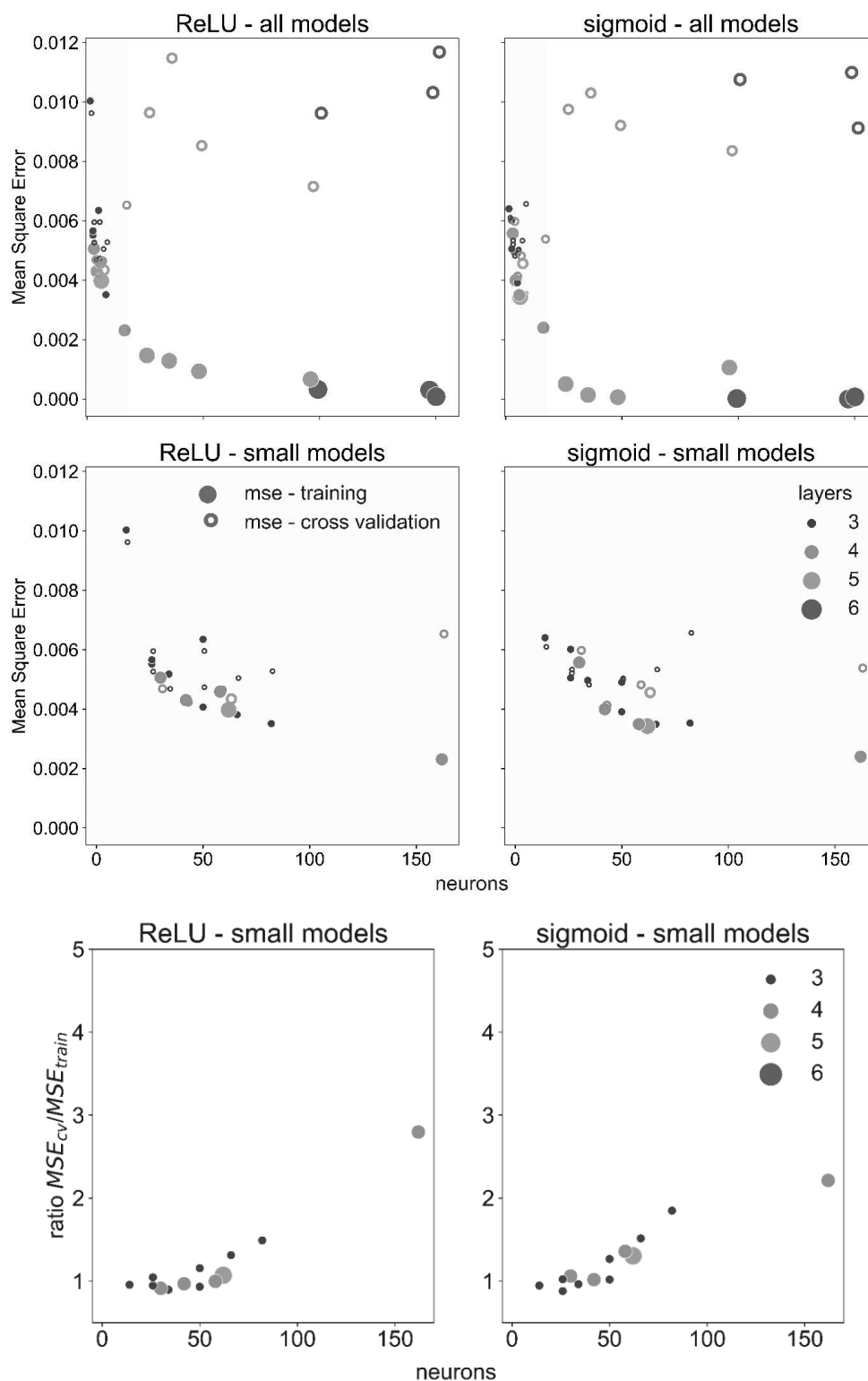


Figure A3. MSE model comparison for the 333 reflection (XANES – cation distribution). Left: “ReLU” models. Right: “sigmoid” models. Top: MSE comparison for all models. Centre: MSE comparison for small models (under 200 neurons). Bottom: MSE ratio between CV and train datasets.

3.4. CV-train prediction deviations. XANES 333

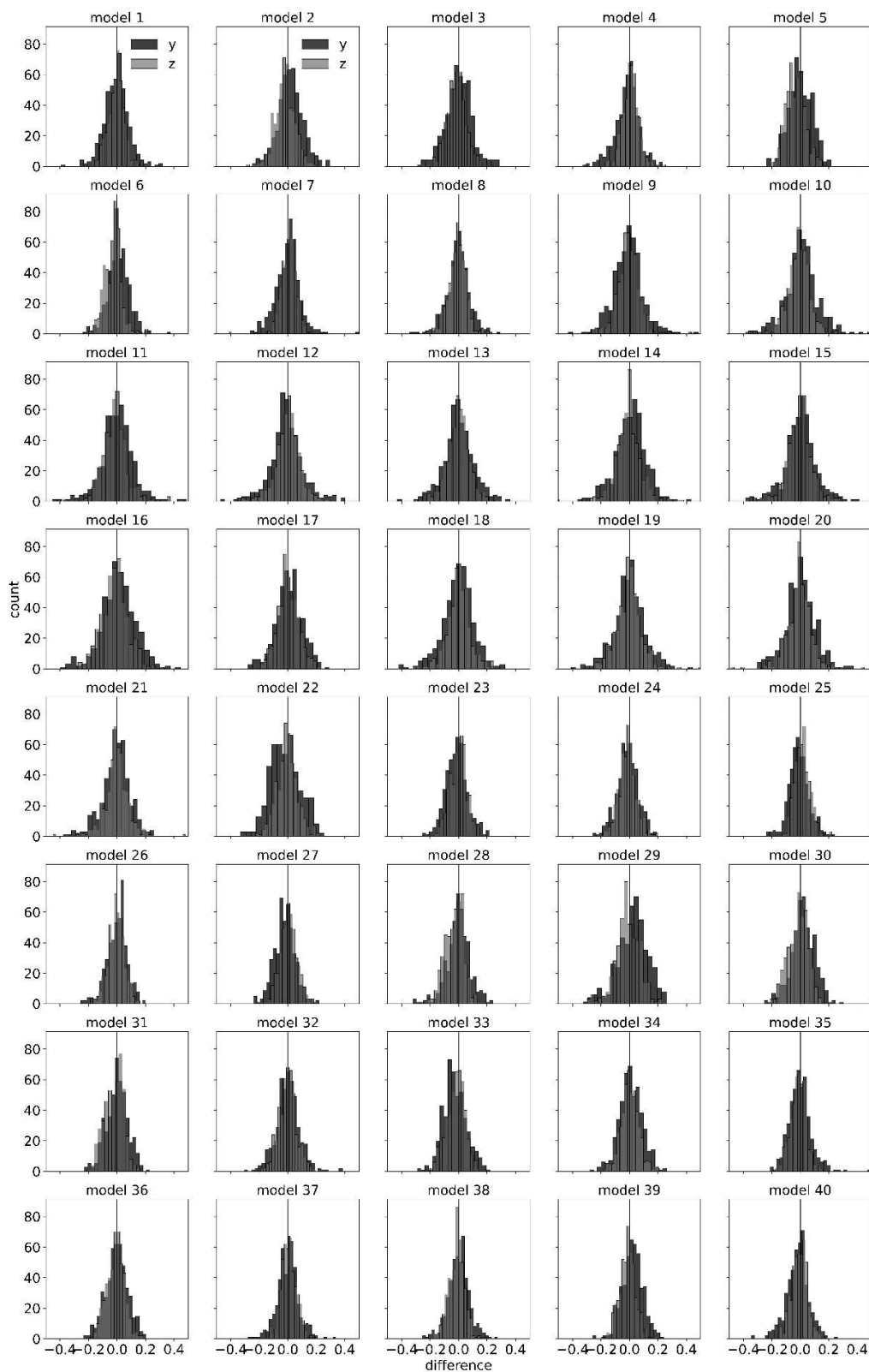


Figure A.4. Difference between the predicted and actual values for x (dark) and y (light) for the CV dataset, for the 333 reflection (XANES). Both parameters describe the cationic occupation. Blue graphs correspond to “ReLU” models, whereas red correspond to “sigmoid”.

3.5. CV prediction deviations. EXAFS 115

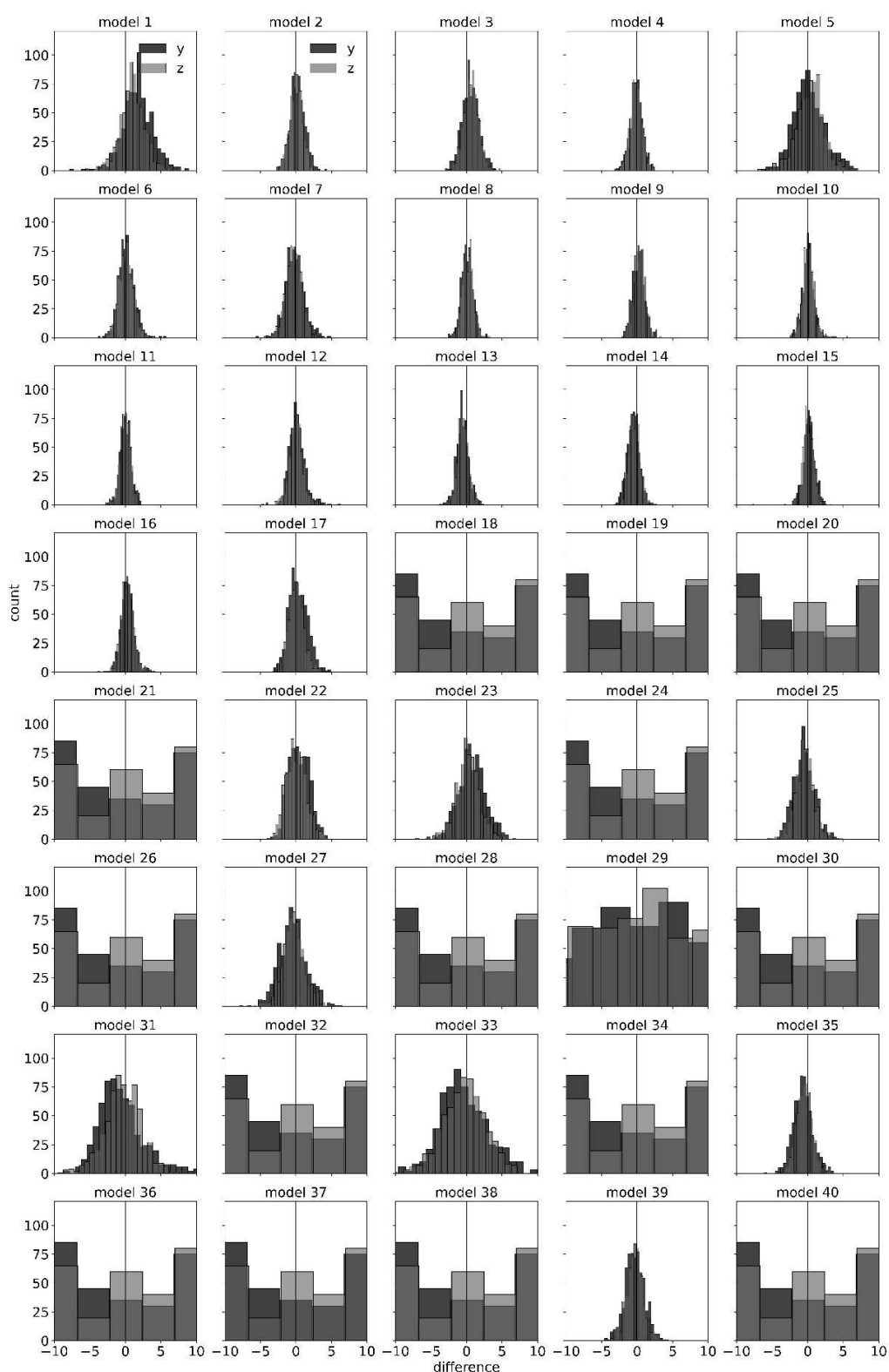


Figure A.5. Difference between the predicted and actual values for y (dark) and z (light) for the CV dataset, for the 115 reflection (EXAFS). The parameters indicate the oxygen positions. Blue graphs correspond to “ReLU” models, whereas red correspond to “sigmoid”.

3.6. CV prediction deviations. EXAFS 115

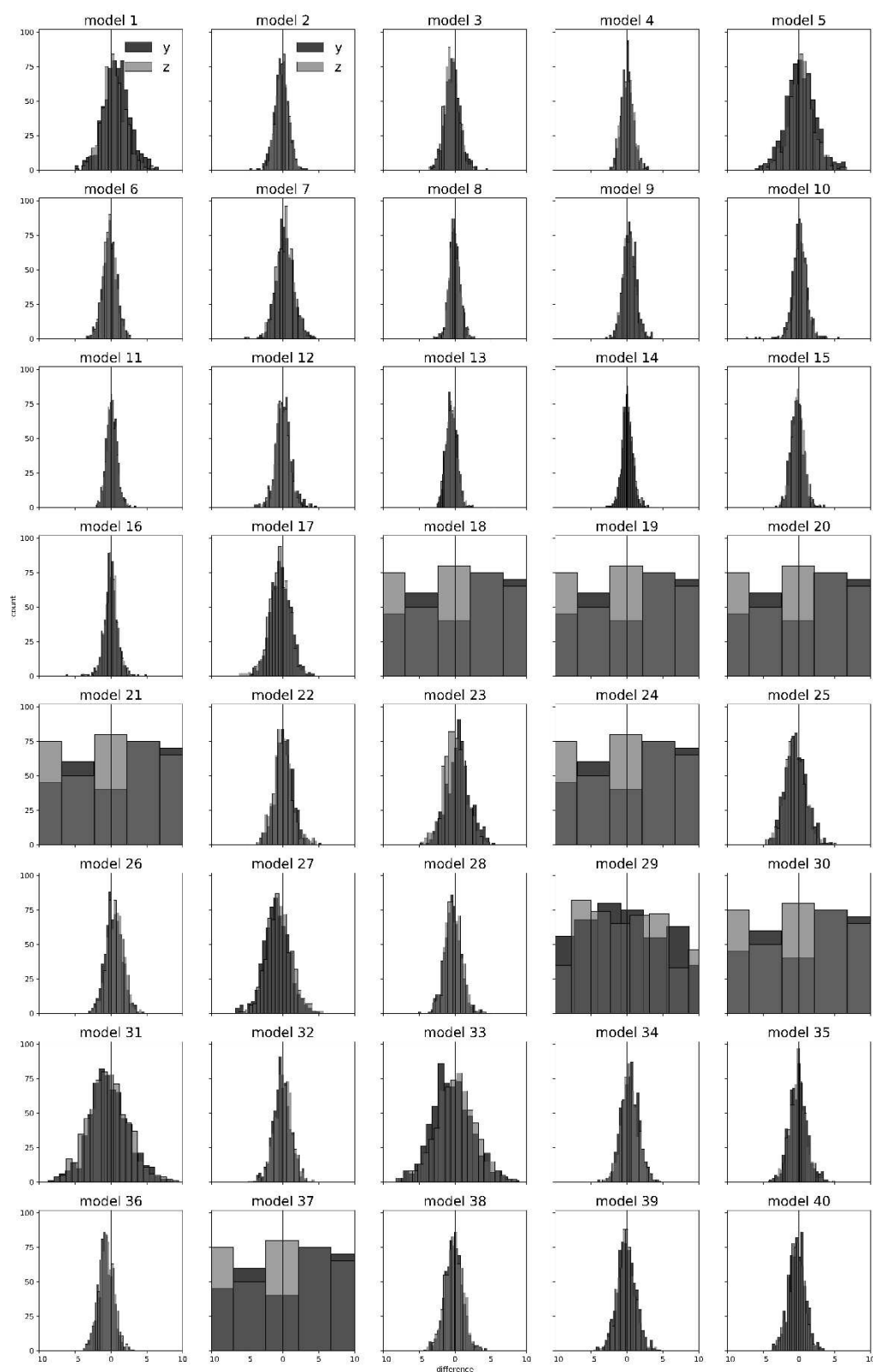


Figure A.6. Difference between the predicted and actual values for y (dark) and z (light) for the CV dataset, for the 333 reflection (EXAFS). The parameters indicate the oxygen positions. Blue graphs correspond to “ReLU” models, whereas red correspond to “sigmoid

3.7. MSE evaluation for model comparison – EXAFS 115

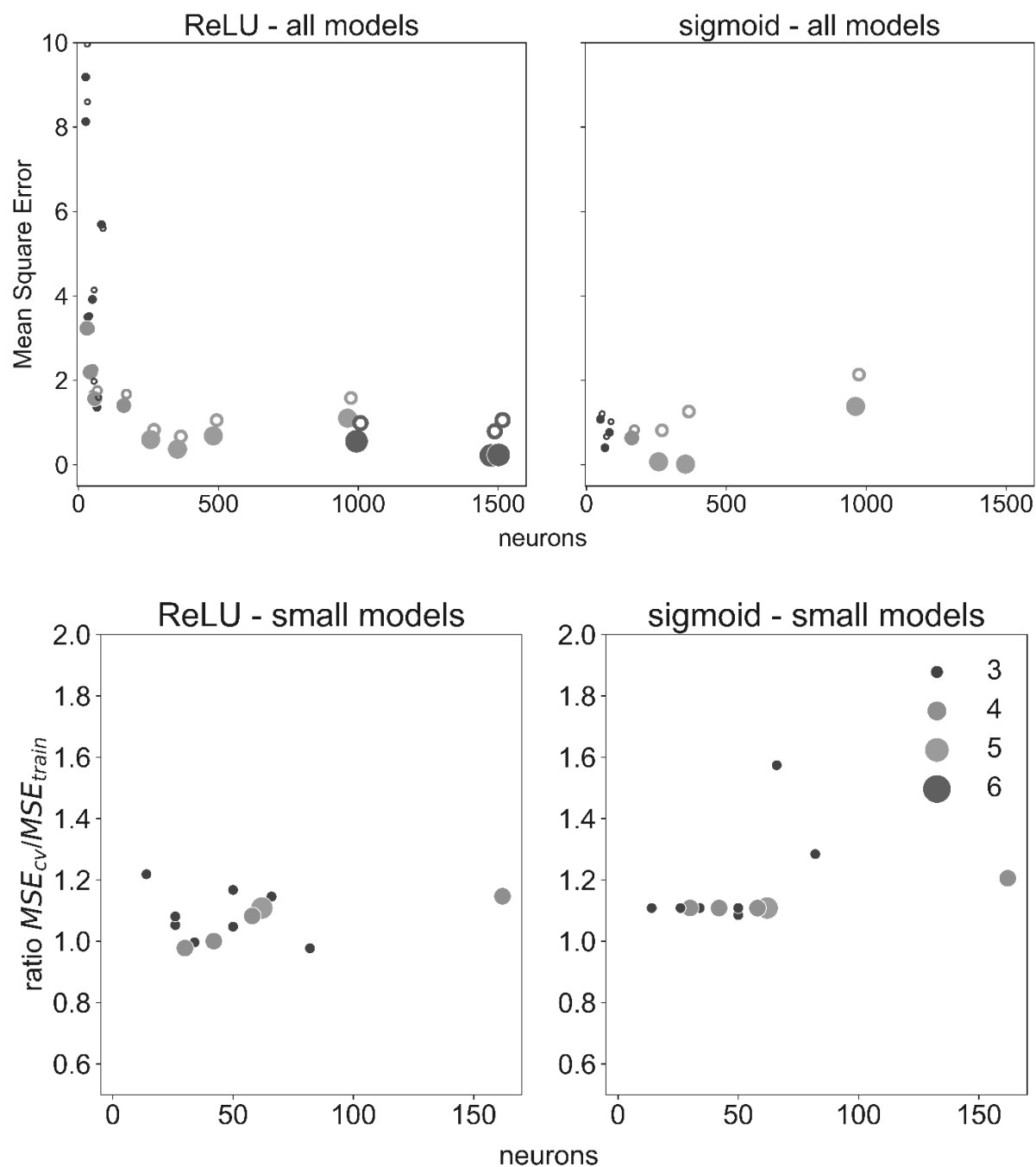


Figure A.7. MSE model comparison for the 115 reflection (EXAFS – oxygen position). Left: “ReLU” models. Right: “sigmoid” models. Top: MSE comparison for all models.: MSE ratio between CV and train datasets.

3.8. MSE evaluation for model comparison – EXAFS 333

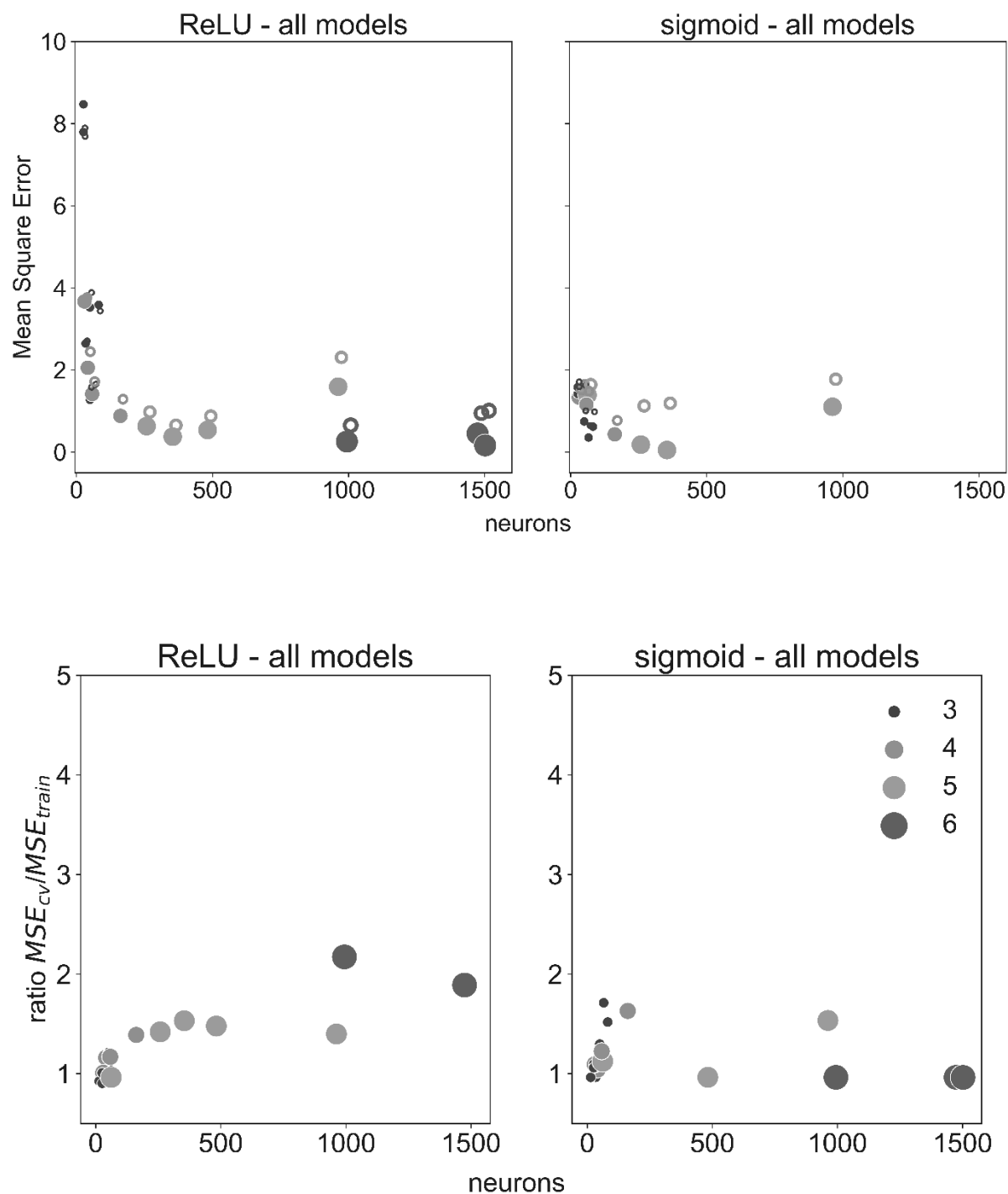


Figure A.8. MSE model comparison for the 333 reflection (EXAFS – oxygen position). Left: “ReLU” models. Right: “sigmoid” models. Top: MSE comparison for all models.: MSE ratio between CV and train datasets.

4. Whole-range diffractogram of $\text{Fe}_2\text{VO}_4//\text{MgO}$ thin films

The diffractogram has been acquired at the institute's *Rigaku SmartLab* diffractometer with a copper anode ($K_{\alpha 1} = 1.54056 \text{ \AA}$).

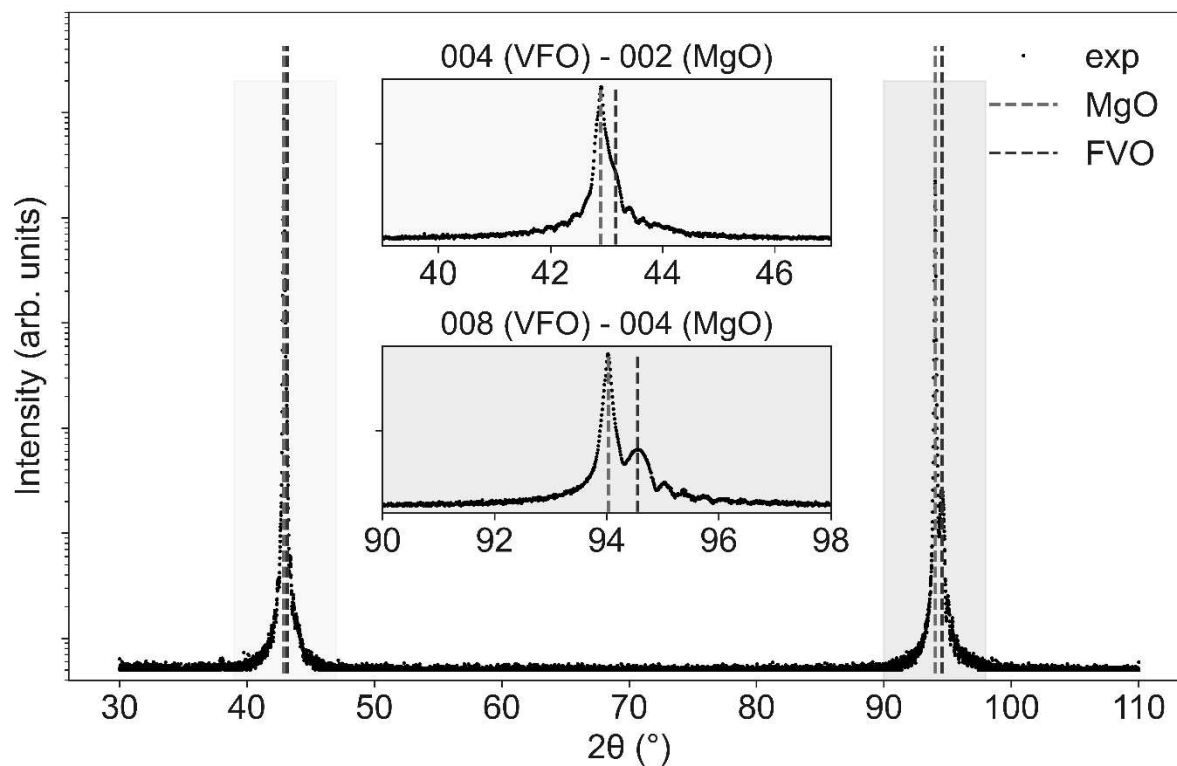


Figure A.9. θ - 2θ diffractogram for the study of the $00l$ reflections of MgO (red dashed lines) and VFO (blue).

– This page intentionally left blank –

Résumé de thèse en français

1. Introduction

Les matériaux multifonctionnels se situent à l'avant-garde de la recherche moderne en sciences des matériaux. La multifonctionnalité se manifeste par la capacité à présenter des propriétés spécifiques dans divers domaines, e.g. électroniques, magnétiques et optiques [1]. En exploitant ces attributs combinés, les matériaux multifonctionnels ouvrent la voie à des percées technologiques autrefois considérées comme inaccessibles, offrant de nouveaux paradigmes tant dans la conception que dans les applications.

En explorant davantage le domaine des matériaux multifonctionnels, les multiferroïques apparaissent comme un sous-ensemble particulièrement intrigant. Ces matériaux possèdent plusieurs ordres ferroïques primaires. Cette coexistence d'ordres permet une interaction riche entre leurs propriétés distinctes, conduisant à de nouvelles fonctionnalités. Un exemple de multiferroïsme se présente sous la forme de matériaux magnétoélectriques, possédant simultanément des ordres magnétiques et électriques [2]. La propriété unique de ces matériaux est leur capacité à induire une réponse magnétique lorsqu'ils sont soumis à un champ électrique, et vice versa. Ce couplage magnétoélectrique peut être exploité pour des applications de dispositifs innovants, tels que les capteurs [3], les actionneurs [4] et les transducteurs [5].

Dans le contexte des matériaux multiferroïques, les matériaux en couches minces ont suscité une attention considérable pour la conception de dispositifs, permettant l'exploitation des différents ordres ferroïques sous forme de dispositifs à l'échelle nanométrique. Les avancées dans les techniques de croissance de films minces ont fourni un moyen contrôlé de synthétiser des films minces monophasés de haute qualité, et ont permis d'adapter les propriétés des matériaux existants par l'ingénierie des contraintes [6]. De plus, la géométrie en film mince induit parfois des propriétés absentes dans le matériau massif [7], [8].

L'objet de ce travail de doctorat a été l'étude d'un matériau multifonctionnel et multiferroïque : le vanadate de fer de structure spinelle FeV_2O_4 (FVO), sous forme de couche mince. Le vanadate de fer se distingue par ses degrés de liberté interconnectés : magnétiques, ferroélectriques et orbitaux ; ainsi que par la manifestation d'une pléthore de transitions structurales et magnétiques avec la température. Au début de ce doctorat, de nombreuses études sur FVO massif étaient recensées mais la littérature du matériau sous la forme de couche mince était succincte. Par conséquent, l'objectif principal de cette thèse était de combler le déficit de connaissances concernant les films minces de vanadate de fer.

Comme on peut l'observer dans ce diagramme, le commencement de cette recherche avait une forte composante de chimie solide, qui a progressivement évolué vers les sciences des matériaux et, en fin de compte, vers les domaines de la spintronique et de la cristallographie.

La thèse commence avec le « **Chapitre I** : FeV_2O_4 dans la famille des vanadates spinelles ». Ce premier chapitre offre une introduction complète au vanadate de fer. Pour ce faire, un bref parcours à travers la famille élargie des vanadates a été entrepris, soulignant son importance croissante dans les recherches récentes. L'exploration s'est ensuite focalisée sur le sous-groupe des vanadates spinelles (AV_2O_4). Ces composés sont caractérisés par leur structure cristalline cubique, qui consiste en un arrangement de type spinelle ($Fd\bar{3}m$, 227 : 2) d'atomes d'oxygène situés aux positions 32e (x, x, x).

Cet empilement d'oxygènes détermine deux sites cationiques différents dans la structure spinelle. Tout d'abord, les sites octaédriques (O_h), placés en position spéciale 16d ($\frac{1}{2}, \frac{1}{2}, \frac{1}{2}$) et occupés par des atomes de V dans les vanadates spinelles. Deuxièmement, les sites tétraédriques (T_d), situés en position 8a ($\frac{1}{8}, \frac{1}{8}, \frac{1}{8}$) et remplis d'un autre cation métallique (A). Les atomes de V forment un sous-réseau de type pyrochlore où les tétraèdres de V partagent leurs sommets. Un tel arrangement spécial des atomes de V provoque un fort chevauchement d'orbitales 3d et des interactions d'échange significatives entre les différents atomes de la sous-maille [17]. La structure spinelle et le sous-réseau pyrochlore sont schématisées dans la **Figure F.2**.

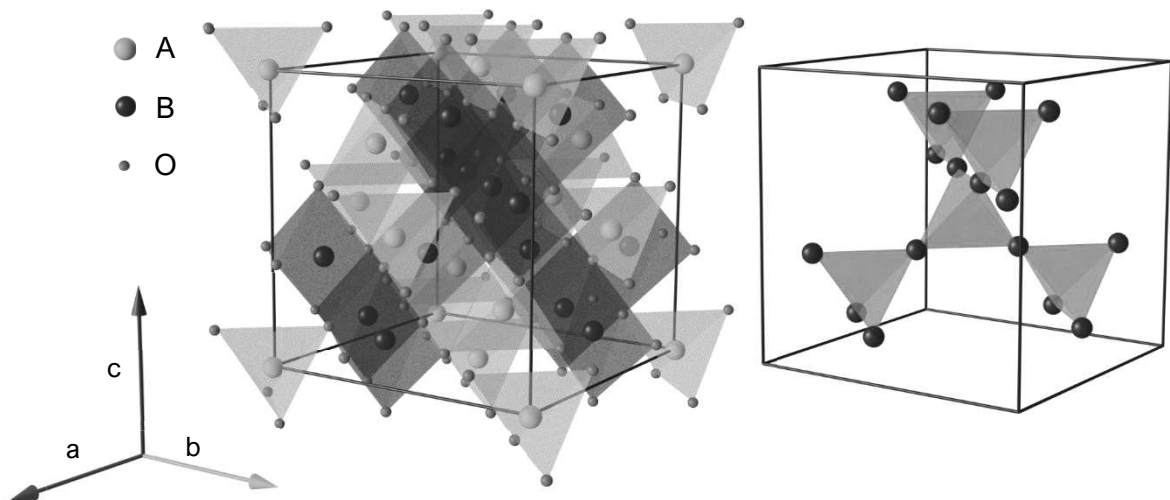


Figure F.2. À gauche : structure spinelle (AB_2O_4) avec A (T_d) en orange et B (O_h) en bleu. Origine numéro 1 : A à 0, 0, 0. Tous les octaèdres et tétraèdres incluant des atomes dans la maille sont représentés. Une maille élémentaire contient quatre unités de formule de AB_2O_4 . À droite : réseau de pyrochlore V-V composé de tétraèdres partageant leurs sommets entre les atomes situés dans les sites O_h .

La nature du cation métallique (A) différencie fortement les différents membres de cette sous-famille de matériaux, et leurs particularités sont présentées en détail dans le premier chapitre. De plus, les propriétés de transport des vanadates spinelles peuvent être modifiées en changeant la distance V-V.

Il a été montré comment le vanadate de fer se distingue parmi les vanadates spinelles, principalement en raison des effets Jahn-Teller et du couplage spin-orbite, schématisés dans la **Figure F.3** pour le cation V^{3+} . Ces effets permettent au FVO de présenter une multitude de transitions structurales qui, à la fois, présentent des ordres magnétiques, orbitaux et ferroélectriques.

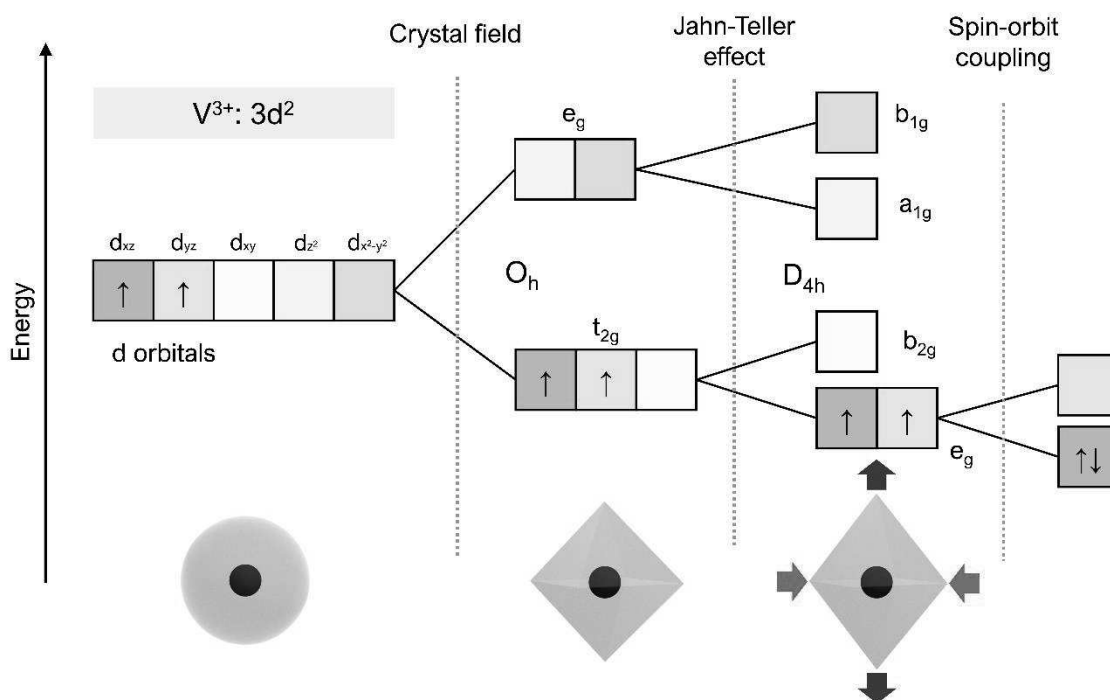


Figure F.3. Représentation schématique de la stabilisation énergétique de V^{3+} dans une densité électronique octaédrique, avec les différentes déformations susceptibles de rompre la dégénérescence 3d : i) effet du champ cristallin, ii) effet Jahn-Teller et iii) couplage spin-orbite. Les figures en bas correspondent aux environnements électroniques ressentis par le cation.

Le vanadate sous forme de couche mince est également présenté. L'attrait inhérent au dépôt de ce matériau multifonctionnel sous cette forme a été discuté, et l'état actuel de la recherche sur les films minces de FVO a été présenté de manière élaborée.

En somme, ce chapitre a servi de socle fondamental pour les sections suivantes de la thèse. En établissant les fondements théoriques des composés spinelles et plus particulièrement du vanadate de fer, il a préparé le terrain pour une exploration plus approfondie et plus nuancée dans les chapitres suivants.

2. FeV_2O_4 : du massif aux couches minces

Le deuxième chapitre de cette thèse, intitulé « **Chapitre II** : FeV_2O_4 : du massif au film mince », détaille le processus d'élaboration de films minces de vanadate de fer à partir des cibles céramiques.

L'élaboration des cibles a utilisé la méthode céramique, une technique courante en chimie du solide pour l'obtention des poudres [78]. Elle implique le mélange de précurseurs sous forme de poudres fines pour une réaction à l'état solide dans un four à haute température. Pour la synthèse de FVO sous forme de poudre, les précurseurs étaient Fe_2O_3 et V_2O_5 . Ces cations doivent être réduits pour correspondre à l'état d'oxydation dans la forme spinelle : Fe doit passer de +3 à +2 et V de +5 à +3. Une fois obtenue la bonne phase cristalline, des cibles denses ont été élaborées par un processus de frittage à haute température et sous atmosphère réductrice.

La structure cristallographique de la cible a été vérifiée par des expériences de diffraction des rayons X (DRX) en poudre. L'analyse des diffractogrammes a confirmé le groupe d'espace cubique $Fd\bar{3}m$ à température ambiante, avec un paramètre de maille de $a = 8,4575(1)$ Å, comme montré dans la **Figure F.4**. L'affinement Rietveld a en outre confirmé la bonne stœchiométrie et que les atomes sont positionnés en $x = 0,262(2)$. Ces résultats correspondent aux valeurs rapportées dans la littérature pour le FVO à température ambiante [53] et confirment l'obtention de la phase spinelle correcte.

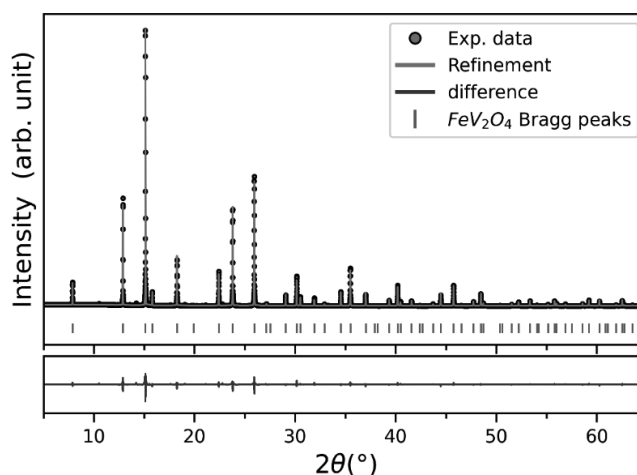


Figure F.4. Données expérimentales de diffraction des rayons X en poudre (en gris) et meilleur diffractogramme affiné (en rouge) en utilisant les stratégies de concordance de profil et de raffinement de Rietveld. La différence entre le diffractogramme expérimental et simulé est indiquée en bleu, tandis que les positions des pics de Bragg sont montrées en lignes vertes.

Différentes caractérisations ont été effectuées sur FVO massif. La microscopie électronique à balayage en parallèle avec l'EDS a confirmé le bon rapport V/Fe. Les mesures magnétiques et de diffraction des rayons X en fonction de la température sont cohérentes avec la littérature existante [53]. Les mesures de susceptibilité alternative ont été effectuées afin de caractériser l'éventuel état de verre de spin dans

le matériau, rapporté par Nishihara et al. [61] dans la littérature. Malheureusement cet état n'a pas été trouvé.

Le dépôt de couches minces a eu lieu par ablation laser pulsée (PLD) sur des substrats monocristallins de MgO et SrTiO₃ (STO), à partir des cibles élaborées précédemment. Toutes les dépositions de films minces de FVO rapportées dans la littérature avant le début de cette thèse utilisaient une atmosphère d'oxygène [69]–[71], [76], conduisant à un excès de fer dans les films et à la formation d'une couche parasite de V₂O₅ [77]. Une étude de l'optimisation a été effectuée pour obtenir la phase spinelle FVO la plus cristalline. Des analyses θ - 2θ ont confirmé la qualité du dépôt, comme illustré dans la **Figure F.5** montre pour les dépôts sur MgO.

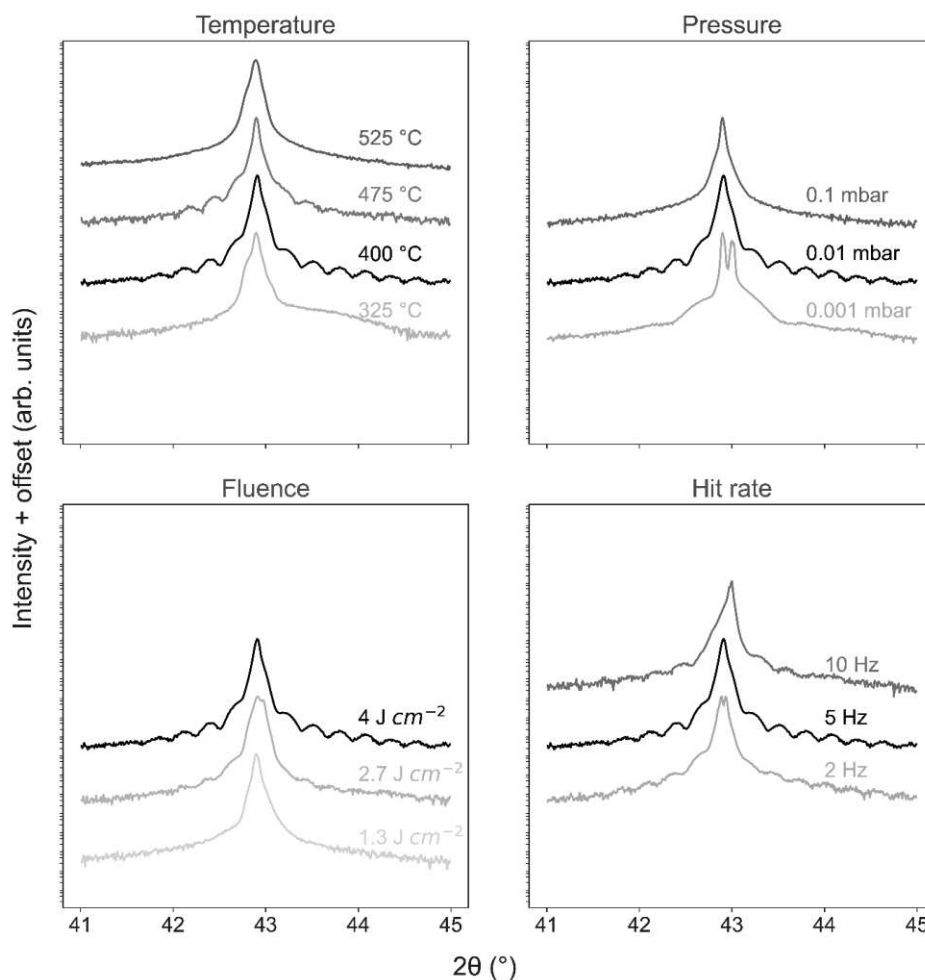


Figure F.5. θ - 2θ sur le pic 004 pour les films FVO/MgO dans différentes conditions. Chaque graphique correspond à des films différents dans lesquels tous les paramètres sont maintenus identiques sauf le paramètre qui titre le graphique. À droite de chaque graphique, la valeur du paramètre variable. Le film qui présente la meilleure cristallinité a été placé au milieu du graphique en couleur noire.

Les meilleures conditions ont été trouvées à 400°C, avec une pression partielle d'argon de 0,01 mbar, une fluence laser de 4 J cm⁻² et une fréquence de 5 Hz. La température et la pression ont eu une grande influence sur la qualité du film, avec des fenêtres optimales étroites pour ces paramètres. La fluence du laser a également été ajustée afin d'améliorer la qualité du film. En revanche, la fréquence du laser n'a pas semblé avoir un grand impact sur la qualité du film.

L'épaisseur des films a été caractérisée à l'aide de mesures de réflectivité aux rayons X. Par ailleurs, les mesures EDS ont permis de vérifier la stœchiométrie des films minces, assurant ainsi un bon transfert stœchiométrique entre la cible et les films. Les mesures RHEED (diffraction d'électrons à haute énergie rétrodiffusés) ont révélé un état de dépôt 2D lisse du film, confirmant la qualité supérieure de la couche déposée. En complément, des mesures AFM (microscopie à force atomique) ont également été réalisées, attestant de l'excellent état de surface des films. Ces méthodes de caractérisation variées et complémentaires confirment la haute qualité des films produits, tant au niveau de la stœchiométrie que de la morphologie de surface.

La bonne phase cristalline a été vérifiée par DRX, comme le montrent les analyses θ -2 θ dans la **Figure F.6** pour FVO//MgO et **Figure F.7** pour FVO//STO. Ceci permet également d'obtenir les paramètres cristallins hors plan.

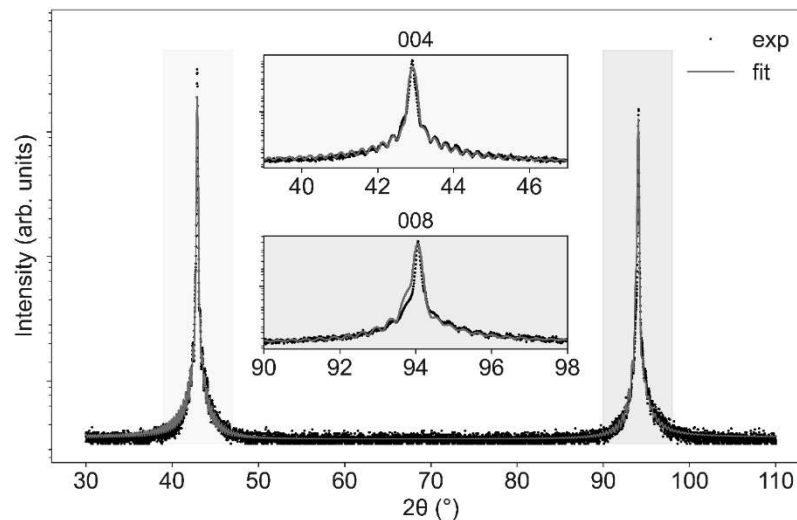


Figure F.6. Diffractogrammes $\theta/2\theta$ pour les films minces de FVO//MgO dans une plage de 2θ allant de 30 à 100° avec les données expérimentales (en noir) et le meilleur ajustement de xrayutilities (en rouge). Des zooms ont été effectués dans les plages [39°, 47°] et [90°, 96°] pour une meilleure observation des réflexions 004 et 008 sur FVO, respectivement.

Les films FVO//MgO ont montré des pics très proches des réflexions 004 de MgO, avec des franges de Laue oscillantes indiquant une bonne cristallinité du matériau. Par ailleurs, l'ajustement du profil d'intensité a confirmé une épaisseur de film et un paramètre de maille hors plan très proches des valeurs

attendues. En revanche, les films FVO//STO ont montré une nette séparation des pics entre le substrat et le film, ainsi qu'une absence de franges de Laue, ce qui pourrait être attribué à un désaccord significatif entre les paramètres de FVO et du STO. Cette différence dans la correspondance des mailles affecte l'intégrité structurale des films FVO, entraînant une plus grande mosaïcité cristalline lorsqu'ils sont déposés sur du STO.

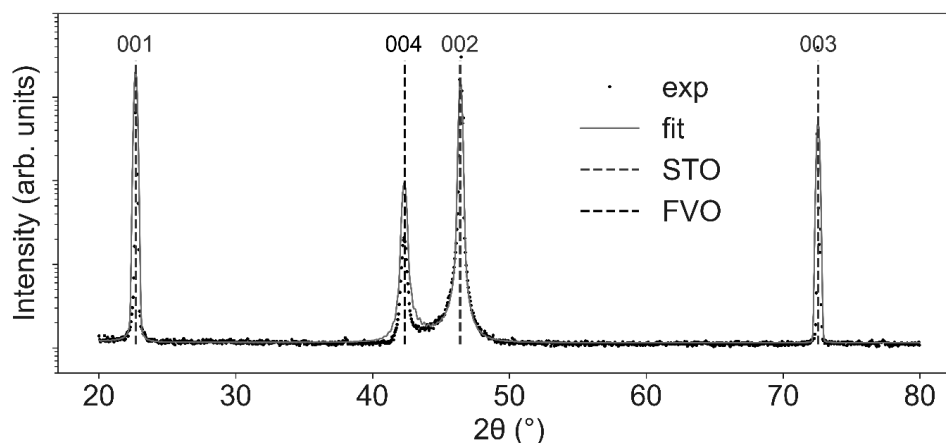


Figure F.7. Diffractogrammes $\theta/2\theta$ pour les films minces de FVO//STO dans une plage de 2θ allant de 20 à 80° avec les données expérimentales (en noir) et le meilleur ajustement de *xrayutilities*. Les positions ajustées pour les réflexions de FVO ont été indiquées en pointillés noirs, et pour les réflexions de STO en bleu.

Des mesures complémentaires ont été effectuées pour confirmer la bonne phase cristalline des couches minces. Les Phi-scans ont validé la bonne épitaxie cristalline entre les substrats et les films minces. De plus, des mesures de cartographie de l'espace réciproque (RSM) ont été effectuées pour étudier les paramètres de réseau dans le plan, comme montré dans la **Figure F.8** pour FVO//MgO. Ces différentes analyses confirment la qualité et la structure des films produits.

Les informations structurales pour les deux systèmes de films minces FVO//MgO et FVO//STO sont résumées dans le **Tableau F.1**. L'étude révèle des différences significatives dans les propriétés structurales des films minces de FVO déposés sur des substrats STO et MgO. Sur le substrat STO, le film subit une distorsion tétragonale et une contrainte compressive plus prononcées que sur MgO. Cependant, le substrat STO n'est pas en mesure d'accommoder complètement la structure contrainte. L'étude met également en lumière le comportement "auxétique" intrigant de FVO//MgO, où les paramètres de maille à la fois dans le plan et hors du plan se contractent, un phénomène rare dans les oxydes mais déjà observé dans d'autres systèmes spinelles. Ce comportement structural a un impact sur les propriétés magnétiques et de transport du film et offre des perspectives sur les effets de la contrainte induite par le substrat.

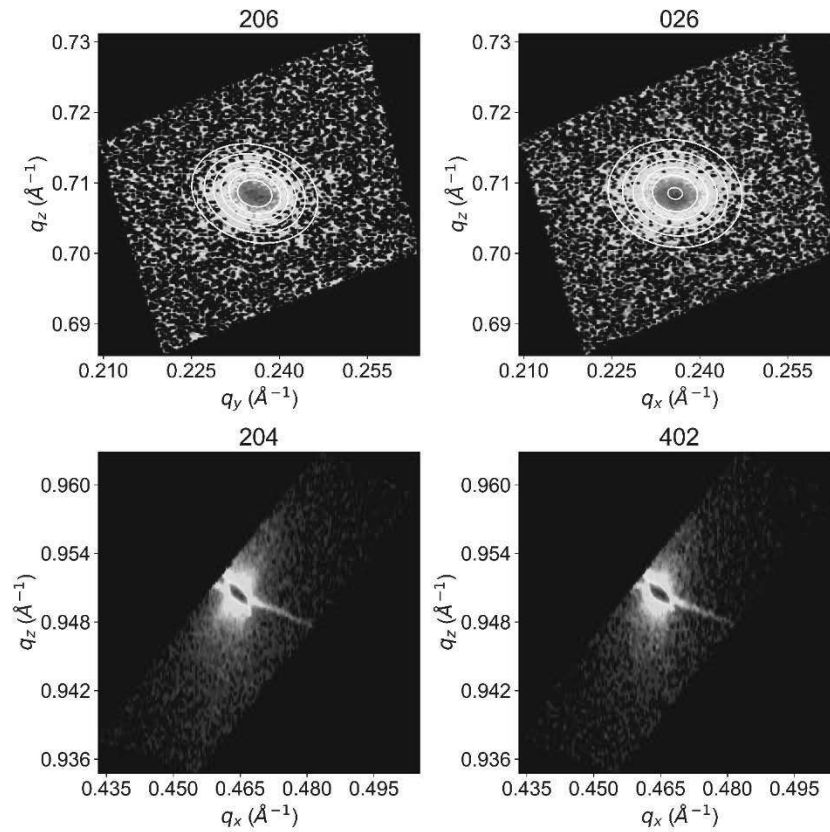


Figure F.8. Résultats de RSM pour les films FVO//MgO. En haut : RSM 2D effectuée sur deux réflexions {206} pour FVO. En bas : RSM 2D au niveau des réflexions {204} de MgO, montrant les contributions à la fois de l'échantillon et du matériau du film.

Tableau F.1. Compendium structural pour les systèmes FVO//MgO et FVO//STO par rapport à la poudre. Les paramètres de maille théoriques ont été utilisés pour les valeurs de désaccord de maille, et les expérimentaux pour le reste.

Couche mince	FVO//MgO	FVO//STO	Massif
$a = b$ (Å)	8.426(4)	8.356(7)	8.4575(1)
c (Å)	8.4525(2)	8.505(1)	
V (Å ³)	597.2(1)	592.3(1)	603.22(2)
τ (%)	- 0.4	- 8.2	-
f_{tetra} (%)	0.31(2)	1.79(1)	0
ν^*	- 0.27(7)	1.7(1)	0

L'étude du magnétisme en fonction de la température a été menée sur des films de FVO d'une épaisseur de 40 nm déposés sur des substrats de STO et MgO, comme montre la **Figure F.9**. Les films montrent un comportement paramagnétique significatif, plus marqué pour les films FVO//MgO. Des ajustements

linéaires ont été réalisés pour obtenir les températures de transition magnétique (T_c), qui diffèrent considérablement entre les échantillons en poudre et les films. Les propriétés magnétiques des films dépendent aussi de l'épaisseur du film.

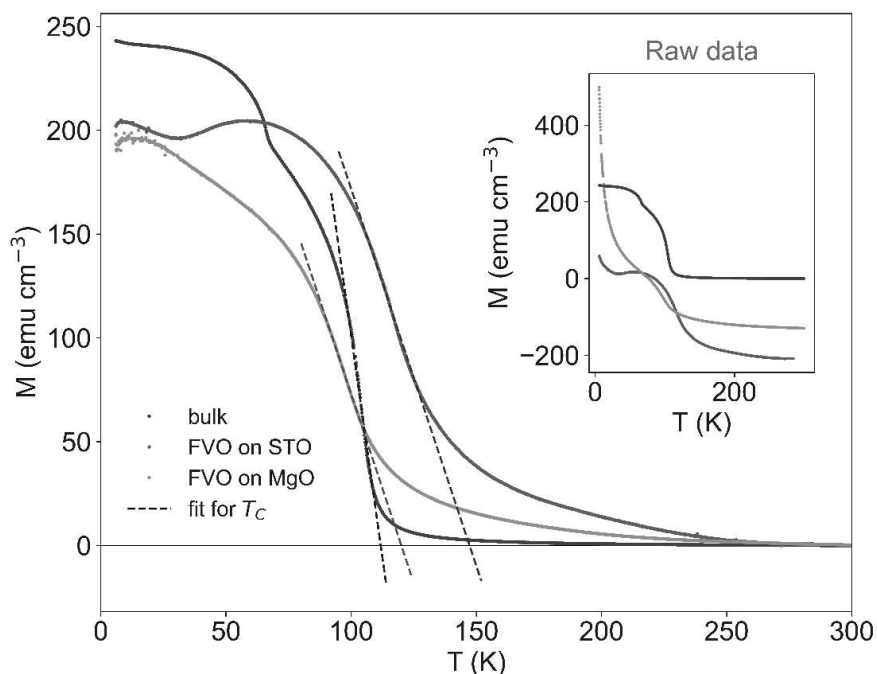


Figure F.9. M vs. T dans la plage de température de 2 à 300 K en mode FC, sous $H = 5000$ Oe. À droite, les données brutes ont été tracées, tandis que le graphique principal correspond aux données avec une correction paramagnétique. Les ajustements linéaires pour la température de transition sont indiqués par des lignes pointillées, tandis que les points en pointillés représentent les valeurs expérimentales : bleu pour FVO massif, rouge pour FVO//STO et orange pour FVO//MgO.

L'étude a également examiné l'hystérèse magnétique des films de FVO en utilisant des mesures d'aimantation en fonction du champ appliqué. Les films plus épais montrent une anisotropie magnétique perpendiculaire (PMA) et un comportement à "deux sauts", ce qui pourrait indiquer l'existence de deux phases magnétiques de coercitivités différentes. Pour FVO//STO, l'effet PMA est plus prononcé, ce qui est attribué à une contrainte compressive plus importante dans ces films. Plusieurs autres facteurs, tels que les défauts structuraux et la polycristallinité, peuvent également influencer les propriétés magnétiques.

Les propriétés de transport des films minces de FVO ont été étudiées en fonction de la température, en utilisant deux modèles différents pour ajuster les courbes de résistivité : le modèle d'activation thermique (TA) et le modèle de saut à portée variable (VRH). Les films de FVO sur STO (FVO//STO) se sont révélés plus conducteurs que ceux sur MgO (FVO//MgO), avec des différences notables dans les

valeurs de résistivité et dans l'énergie d'activation. Le modèle VRH, qui décrit mieux les isolants de Mott comme le FVO, a donné des ajustements plus précis pour les courbes de résistivité par rapport au modèle TA. Ces résultats montrent que les films FVO//MgO sont plus résistifs en raison de leur plus grande énergie d'activation et de la température de Mott plus élevée, ce qui implique que des énergies plus importantes sont nécessaires pour le saut électronique entre les états localisés.

En somme, le deuxième chapitre de cette thèse a méticuleusement exploré la synthèse et la caractérisation de films minces de vanadate de fer (FVO) en passant par plusieurs étapes cruciales : la synthèse de cibles via la méthode céramique, leur caractérisation structurale, et enfin le dépôt sur deux substrats différents par ablation laser pulsée. Les différentes techniques d'analyse utilisées, notamment la diffraction des rayons X, la microscopie électronique à balayage, et les mesures EDS, ont confirmé la haute qualité et la stoechiométrie correcte des films produits. De plus, la thèse révèle des nuances significatives dans les propriétés structurales, magnétiques et de transport en fonction du choix du substrat, ajoutant un nouveau levier de pour moduler les propriétés.

3. Étude structurale avancée par diffraction résonante

Dans le « **Chapitre III** : étude structurale avancée des couches de FeV_2O_4 par diffraction résonante », nous avons mis l'accent à été mis sur l'importance cruciale de comprendre la structure cristallographique des matériaux, en particulier des oxydes fonctionnels comme le FVO. Connaître la position précise des atomes dans ces matériaux est souvent une étape capitale avant leur intégration dans des dispositifs technologiques. Le chapitre a abordé différentes méthodes pour localiser les atomes dans ces matériaux, notamment sous la forme de couche minces.

La diffraction résonante (ou anormale) a été introduite comme une méthode prometteuse, en particulier la diffusion élastique de rayons X résonants (REXS), illustrée dans la **Figure F.10**. Un logiciel spécifique, « *inserexs* », a été développé pour faciliter les expériences REXS et a été validé par des simulations théoriques et des résultats expérimentaux.

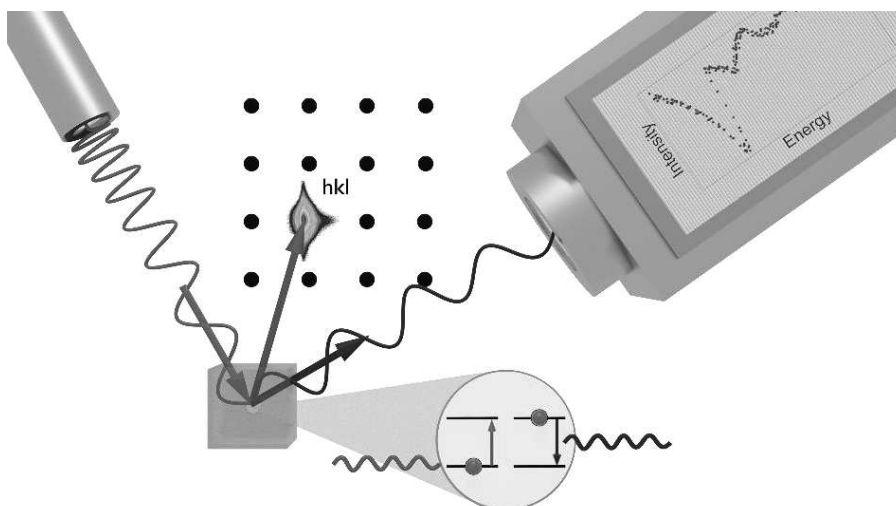


Figure F.10. Représentation schématique d'une configuration et d'une expérience REXS. En vert, le faisceau incident ; en bleu, le faisceau diffracté. La source de rayons X, le matériau cible et le détecteur de rayons X sont orientés de manière à ce que la condition de diffraction soit respectée pour la réflexion souhaitée (hkl).

inserexs a été conçu pour aider les utilisateurs de REXS à sélectionner les meilleures réflexions pour explorer des paramètres spécifiques d'un matériau. Écrit en Python et doté d'une interface utilisateur graphique intuitive, le logiciel est de libre accès et protégé sous une licence BSD. Il est compatible avec les systèmes d'exploitation Windows 10 et Ubuntu 20.04 LTS. Le code source est ouvert et disponible sur GitHub. Le programme calcule les facteurs de structure et les intensités des réflexions pour aider les chercheurs à choisir les meilleures réflexions avant de procéder à des expériences réelles.

Le logiciel est composé de trois modules principaux qui interagissent entre eux et avec le programme externe FDMNES. Les utilisateurs peuvent charger des données cristallographiques à partir de fichiers .cif et ajuster divers paramètres directement depuis l'interface utilisateur. Les valeurs d'intensité et de sensibilité sont calculées en fonction des données fournies, et le logiciel peut être configuré pour prendre en compte des réflexions normalement interdites dans les expériences conventionnelles de diffraction des rayons X.

Trois exemples d'applications du logiciel sont fournis, chacun se concentrant sur des matériaux aux propriétés distinctes. Dans chaque cas, *inserexs* a réussi à identifier les réflexions les plus sensibles et intenses pour les paramètres d'intérêt, tels que la position des cations ou l'occupation des sites d'oxygène.

Nous avons utilisé *inserexs* pour choisir les meilleures conditions pour l'étude de la répartition cationique dans les couches de FVO. Pour ce faire, des mesures REXS dans le domaine XANES (aux alentours du seuil d'absorption) ont été utilisées. La distribution cationique dans le système Fe-V-O est modélisée par une grille $(\text{Fe}_{1-x}\text{V}_x)_{\text{Td}}[\text{V}_{2(1-y)}\text{Fe}_{2y}]_{\text{Oh}}\text{O}_4$, où les paramètres x et y représentent la quantité de vanadium et de fer dans les sites cristallins T_d et O_h respectivement. Ces techniques spectroscopiques ont permis de simuler et de comparer les profils XANES pour différents cations, et il a été conclu que les bords d'énergie pour le fer et le vanadium sont tous deux adaptés pour cette analyse.

Les résultats obtenus montrent que la structure la plus probable pour le système Fe-V-O est celle du spinelle direct, représenté par la formule $(\text{Fe}^{\text{II}})_{\text{Td}}[\text{V}^{\text{III}}_2]_{\text{Oh}}\text{O}_4$. Ceci conduit à une bonne correspondance avec les spectres expérimentaux, comme montré dans **Figure F.11**.

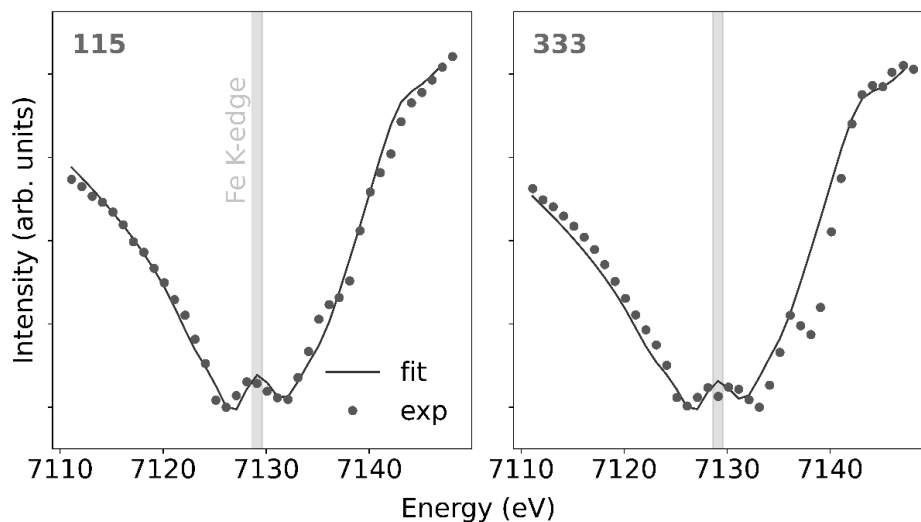


Figure F.11. Spectres DANES autour du seuil K de Fe (-20, +25 eV) pour les réflexions 115 (à gauche) et (333) : expérimentaux (en vert pointillé) et simulés avec $(x = 0, y = 0)$ (en lignes bleues).

L'approche DANES a montré son efficacité pour caractériser les cations métalliques, mais elle est impraticable pour sonder directement les atomes d'oxygène en raison des faibles énergies et des longueurs d'onde impliquées.

Pour résoudre ce problème, nous avons proposé d'utiliser le domaine EDAFS (Extended X-ray Absorption Fine Structure) en complément du DANES. Après une validation théorique démontrant que les spectres EXAFS sont sensibles aux positions des atomes d'oxygène, nous avons procédé à des expériences sur des échantillons massifs. Les résultats étaient en accord avec les données obtenues par des méthodes classiques comme la diffraction des rayons X (S-XRD) couplées aux affinements de Rietveld, confirmant ainsi l'efficacité de notre méthode. Cela a constitué une preuve de concept pour l'utilisation de la diffraction résonante pour la localisation des atomes d'oxygènes dans ce système.

Après avoir validé notre méthode sur des échantillons massif, nous avons étendu notre approche aux films minces d'oxydes. En raison de la contrainte du substrat, la structure du FVO est distordue, et les positions des atomes d'oxygène dépendent de deux paramètres $(0, y, z)$. La position des atomes dans le film mince a été déterminée et concorde bien avec les spectres théoriques, comme illustré dans la **Figure F.12**.

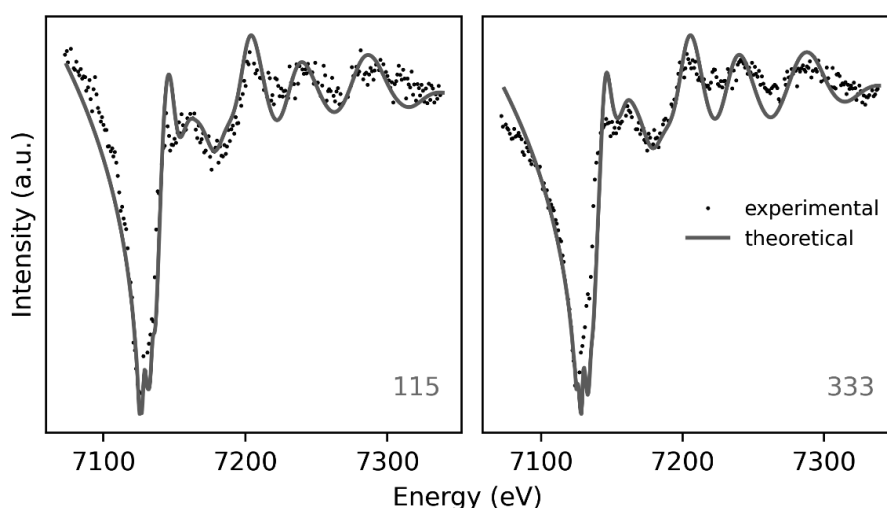


Figure F.12. Spectres REXS pour les réflexions expérimentales 511 et 333 comparés aux données théoriques, pour le film mince FVO//MgO.

L'approche est donc validée non seulement pour les échantillons massifs mais aussi pour les couches minces. La technique permet une sonde indirecte des ligands entourant les cations et pourrait être généralisée à d'autres systèmes. En somme, cette étude a démontré l'efficacité d'une approche basée sur REXS pour déterminer la position des atomes d'oxygène de manière non destructive, à la fois dans les échantillons massifs et les films minces, ce qui est prometteur pour la caractérisation et le développement de futurs dispositifs à base de systèmes nanométriques.

Des spectres REXS dans le domaine EXAFS ont été acquis à différentes températures pour étudier ces positions, mais la variabilité de la température n'a pas montré de changements significatifs dans les spectres. Cependant, un problème majeur de cette analyse est que les paramètres de la maille cristalline utilisés pour générer les spectres théoriques sont basés sur des mesures à température ambiante, ce qui pourrait être inexact à d'autres températures.

Malgré le succès des techniques présentés pour l'exploitation des spectres REXS, le coût en temps de calcul reste un obstacle majeur. Pour pallier ce problème, nous avons fait appel à des réseaux de neurones artificiels (RNA). Ces modèles ont été spécifiquement formés pour extraire des informations structurales des spectres REXS, en particulier dans le système Fe-V-O. Différentes architectures de modèles et fonctions d'activation, telles que ReLU et sigmoid, ont été testées.

Les modèles RNA se sont avérés efficaces pour apprendre les nuances des spectres REXS, notamment pour l'étude de la distribution cationique. Ils ont donné des résultats comparables à ceux obtenus par des méthodes plus coûteuses en temps de calcul. Cependant, la nécessité d'un réglage plus précis est apparue, surtout lorsqu'il s'agit d'analyser les positions des atomes d'oxygène dans les films minces FVO. Des pistes pour améliorer les résultats incluent l'exploration d'autres algorithmes d'apprentissage machine, comme les réseaux neuronaux convolutionnels, et l'adaptation des modèles pour tenir compte des variations de paramètres en fonction de la température.

4. Hétérostructures de Pt/FeV₂O₄ pour la spintronique

Le quatrième chapitre, « **Chapitre IV** : les hétérostructures de Pt/FeV₂O₄ pour la spintronique », a visé à explorer l'applicabilité technologique des films minces à base de vanadate de fer, sous forme de hétérostructures Pt/FeV₂O₄//STO, pour des applications en spintronique. Le chapitre commence par une large introduction à la spintronique et, plus spécifiquement, au contrôle des états magnétiques par le spin. Ensuite, il présente les effets des phénomènes causés par le spin sur les propriétés de magnétotransport des matériaux et décrit la quantification des couples de spin-orbite pour l'inversion de l'aimantation.

Nous avons étudié les propriétés de transport de spins des hétérostructures à travers des mesures de magnétotransport, conçues avec une géométrie de barre de Hall – comme décrit dans **Figure F.13**. Nous avons donc étudié la variation des propriétés de transports (longitudinales et transversales) sous les applications des champs magnétiques et de courants électriques. Lors de ces études, le vanadate de fer est introduit pour la première fois comme isolant ferrimagnétique dans le domaine de la spintronique. La forte PMA sur STO rend FVO un candidat prometteur pour des dispositifs basés sur le couple spin-orbite (SOT).

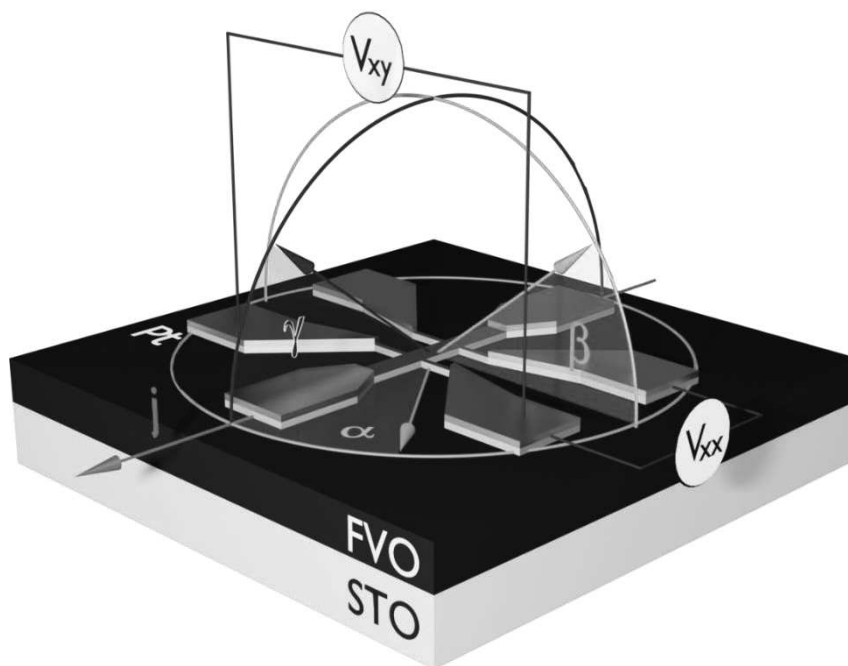


Figure F.13. Représentation du dispositif en barre de Hall, indiquant les trois différentes configurations de balayage angulaire (α , β et γ) et les deux différentes tensions mesurées (V_{xx} et V_{xy}).

La résistivité longitudinale du platine (Pt) sans champ magnétique appliqué (ρ_0) augmente linéairement avec la température, une caractéristique typique des métaux. Une faible valeur de ρ_0 est un bon indicateur de la bonne cristallinité de la couche de Pt, preuve de l'optimisation de sa croissance sur FVO par PLD. Des mesures ont été effectuées à différentes températures (de 2 à 300 K) et différents champs magnétiques, révélant un effet de "spin-valve" dans la plage de température de 2 à 40 K. Cet effet est attribué à la présence de deux phases magnétiques distinctes dans FVO. Par ailleurs, on observe un changement de signe dans la MR autour de 120 K, qui peut s'expliquer par une compétition entre différents phénomènes de MR : un venant de la magnétorésistance hall de Spin (SMR) et l'autre ayant l'anisotropie magnétique (AMR) comme origine.

Des analyses de résistivité basées sur trois configurations angulaires différentes (α , β et γ) ont été réalisées sur des échantillons à des températures allant de 2 à 300 K et dans des champs magnétiques variant de 1 T à 9 T, comme illustré dans **Figure F.14**.

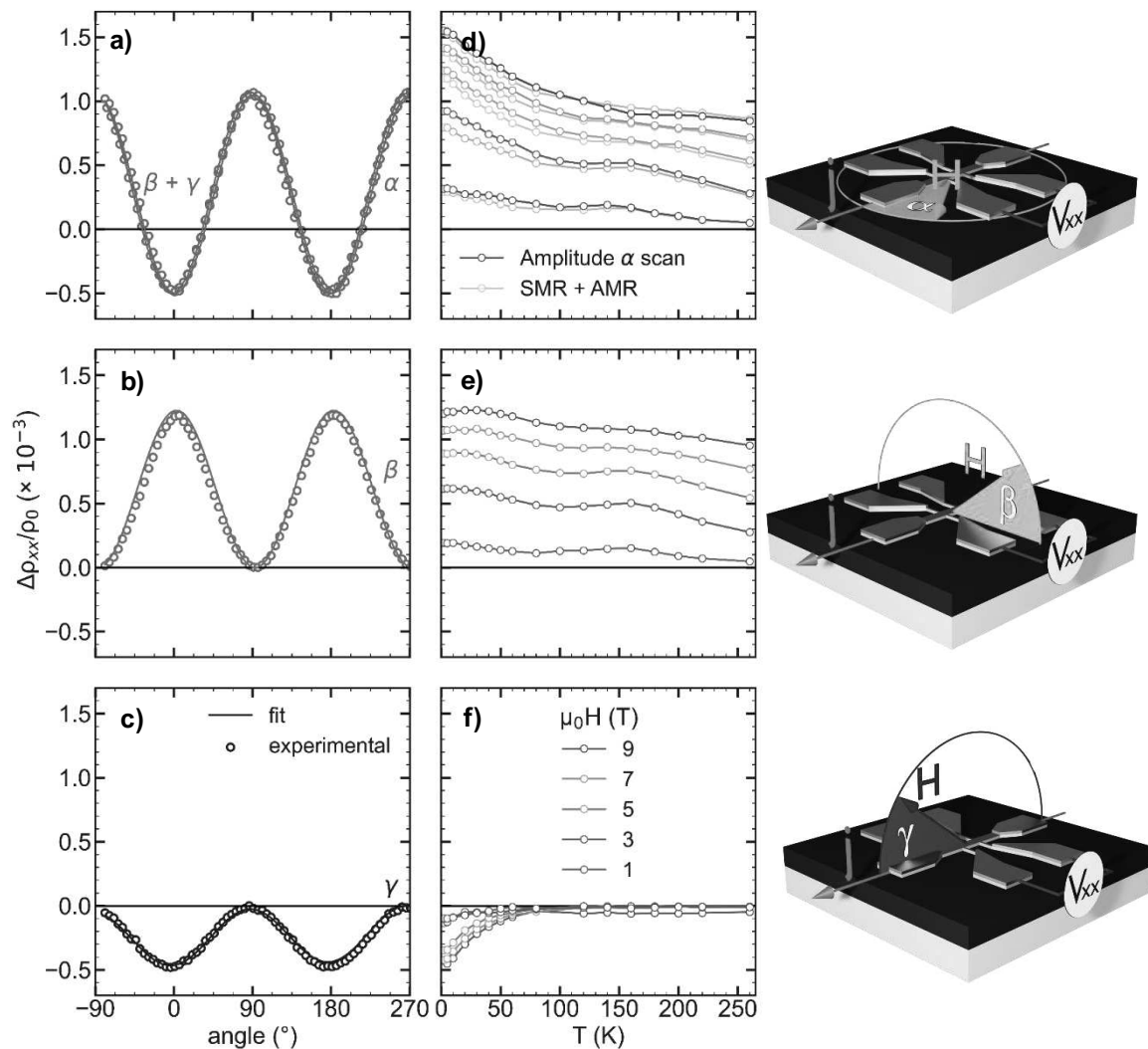


Figure F.14. (a), (b) et (c) mesures dépendant de l'angle (α , β et γ) à 9 T et 2 K, les lignes pleines correspondent aux ajustements des données expérimentales. (d), (e) et (f) amplitudes des mesures dépendant de l'angle en fonction de la température, pour différentes valeurs de champ magnétique.

Ces mesures ont permis de quantifier et d'isoler les composants de la magnétorésistance – AMR et SMR. Les amplitudes de ces effets ont été comparées en fonction de la température et du champ magnétique. Il a été trouvé que l'amplitude de la SMR est particulièrement grande à basse température, atteignant 0,12 % à 2 K, comparable aux meilleures valeurs obtenues pour le transport de spin dans des autres oxydes. [258]

L'amplitude de la SMR est supérieure à celle de l'AMR à toutes les températures, suggérant que la composante de Hall de spin domine sur les phénomènes pilotés par les effets magnétiques de proximité (MPE). Par ailleurs, l'amplitude de l'AMR diminue brusquement avec l'augmentation de la température, s'annulant autour de 120 K. Ce comportement peut être expliqué par une compétition entre les effets de SMR et d'AMR. Le balayage α a également montré que ces deux composants sont équivalents en valeur absolue à toutes les températures et valeurs de champ, corroborant l'idée que les deux phénomènes sont en compétition et peuvent se neutraliser à une certaine température seuil.

Puis, des hétérostructures avec cinq épaisseurs différentes de Pt allant de 1 à 10 nm ont été élaborées, avec une épaisseur constante de la sous-couche FVO de 40 nm. L'étude dépendante de l'épaisseur vise à déterminer les paramètres de transport de spin dans l'effet SMR. Des β -scans longitudinaux ont été effectués à différentes températures et un champ de 9 T. L'ajustement des courbes a permis de trouver des valeurs pour les trois paramètres de transport de spin : θ_{SH} , G_r et λ_{sd} , qui sont cohérentes avec le système Pt/YIG largement étudié. Des tendances variables avec la température pour ces paramètres ont été observées, suggérant des mécanismes de relaxation de spin complexes. Des anomalies dans les tendances pourraient être dues aux transitions structurales de FVO. Malgré ces résultats, l'étude admet des limitations liées au nombre de points expérimentaux et à la complexité du modèle.

Nous avons ensuite analysé les comportements de la magnétorésistance transversale en relation avec les champs magnétiques hors plan. Nous avons mené une étude de cycle de Hall, $V_{xy}(H_z)$, sur une gamme de températures et d'intensités de champ magnétique. Les phénomènes observés englobent divers composants avec l'AMR et la SMR comme origine. Plusieurs mécanismes, notamment la conductance de mélange de spin et la compétition entre différents effets résistifs, contribuent aux changements de signe observés dans la MR, en particulier par rapport à la température.

De plus, nous nous sommes intéressés à la dépendance angulaire de la résistivité transversale dans le plan (IP). Les comportements de la résistivité pour divers angles azimutaux sont explorés, montrant de nouveau une compétition entre les effets magnétiques et ceux venant du spin. Des variations intrigantes dans des paramètres de Hall en fonction de la température sont également soulignées.

Nous avons étudié la réponse en première et deuxième harmonique de la résistivité transversale dans une gamme de température de 10 K à 140 K, avec des courants allant de 2 à 10 mA et des champs magnétiques de 0,5 T à 7 T. Nous avons l'objectif de quantifier le champ magnétique engendré par l'accumulation de spin dans l'interface.

Les résultats ont montré que le champ d'anisotropie est principalement affecté par l'anisotropie du matériau et peu influencé par les effets thermiques. En outre, les valeurs obtenues pour le champ de précession (H_{DL}) et l'efficacité du couple ont été trouvées anormalement élevées par rapport à la littérature, bien que cohérentes dans le contexte de notre étude, ouvrant ainsi la voie à des discussions plus approfondies sur leur validité et leurs implications.

En conclusion, ce travail offre une première étude complète des propriétés de magnéto-transport dépendantes du spin dans les hétérostructures Pt/FVO, soulignant le potentiel du vanadate de fer dans les futures applications spintroniques.

5. Les couches minces de spinelles oxides au-delà de FeV_2O_4

Ce cinquième chapitre, « **Chapitre V** : les couches minces de spinelles au-delà de FeV_2O_4 » a eu comme objectif de, pour la première fois, produire de films minces épitaxiaux de haute qualité de ferrite de vanadium Fe_2VO_4 (VFO) sur des substrats de MgO, dans le but d'augmenter la plage de température où les propriétés uniques de FVO sont observables. Le chapitre explore en profondeur le système de spinelle $\text{Fe}_{1+x}\text{V}_{2-x}\text{O}_4$, qui présente des structures cristallines et des propriétés magnétiques complexes en fonction de la concentration de fer.

En utilisant la voie céramique, nous avons obtenu des cibles de VFO avec la bonne stœchiométrie et une excellente cristallinité, confirmés par des mesures EDS et DRX, respectivement. Des films minces de VFO de 40 nm d'épaisseur ont été fabriqués par PLD. Des conditions de dépôt ont été optimisées pour assurer la qualité des films. **Figure F.15** montre les détails de la caractérisation.

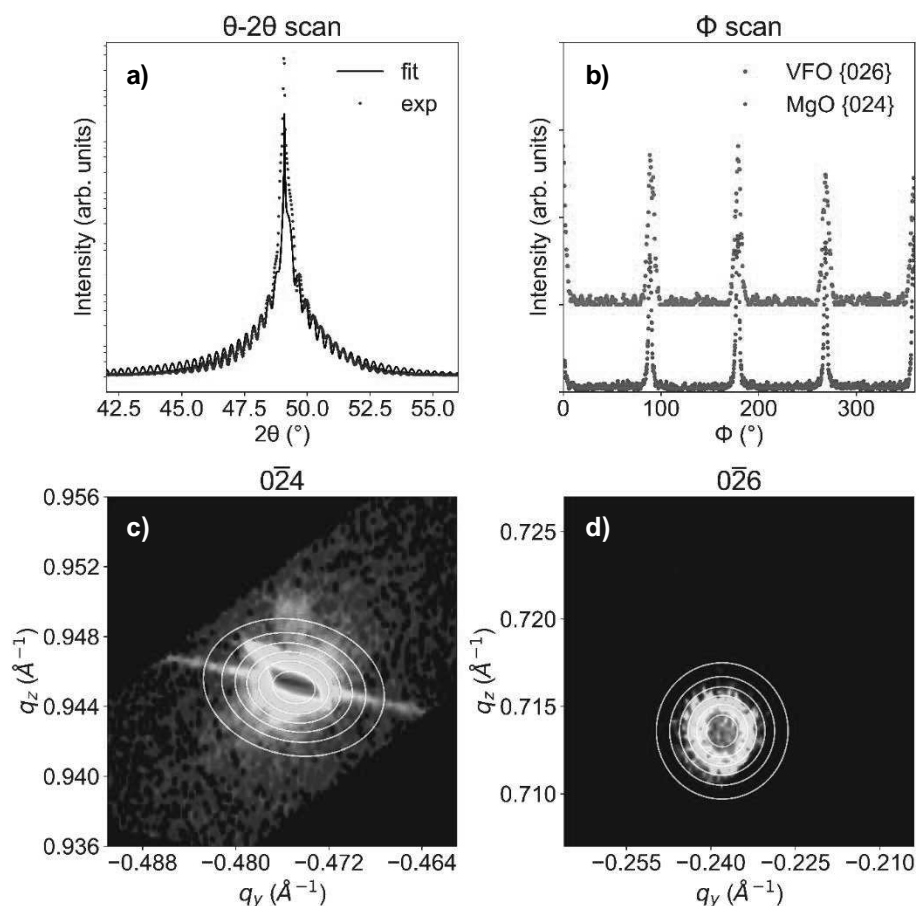


Figure F.15. (a) Diffractogramme θ - 2θ des films minces de VFO//MgO, acquis avec une longueur d'onde des rayons X de 1,74331 \AA - données expérimentales (en noir) et ajustement avec xrayutilities (en bleu). (b) Balayage Φ sur une réflexion 026 de VFO et une réflexion 024 pour MgO. (c) RSM pour MgO 024 (d) RSM pour FVO 026

Des techniques d'analyse comme l'AFM et le RHEED ont montré que le film et le substrat en MgO présentent des surfaces relativement lisses et des cristallinités élevées. De plus, des mesures de XRR et de diffractogrammes θ - 2θ ont confirmé l'épaisseur et la qualité cristalline des films. Les RSM ont permis d'obtenir les paramètres de maille dans le plan, dévoilant une structure tétragonale avec $a = b = 8,415(6)$ Å et $c = 8,407(3)$ Å.

Des expériences DANES ont été menées pour déterminer la distribution cationique des espèces Fe et V dans les sites O_h et T_d , comme illustré dans la **Figure F.16**. Le logiciel inserexs et une méthodologie spécifique ont été utilisés pour choisir les réflexions 333 et 115 comme les plus appropriées pour cette caractérisation. Les résultats indiquent une occupation cationique de $(Fe_{0.979(8)}V_{0.021(8)})_{Td}[V_{0.92(4)}Fe_{1.08(4)}]_{Oh}O_4$, pour les films VFO, cohérente avec le ratio Fe/V observé dans le matériau massif. L'approche classique ainsi que l'utilisation de RNA donnent des résultats équivalents, montrant l'efficacité de ces derniers pour l'affinement des spectres de diffraction anormale.

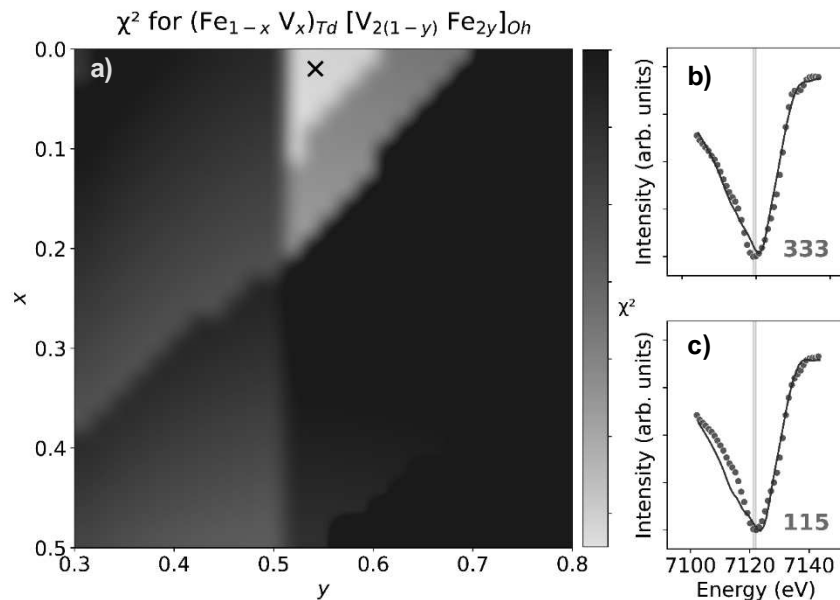


Figure F.16. (a) Différence calculée entre les spectres expérimentaux et les spectres théoriques simulés pour toutes les combinaisons (x, y) . (b) et (c) spectres expérimentaux pour les réflexions 333 (b) et 115 (c) (points verts) et ajustement avec le spectre simulé pour la meilleure combinaison (x, y) (ligne bleue).

Les films minces de VFO ont été caractérisés pour leurs propriétés magnétiques et de transport. Ils présentent une aimantation à saturation d'environ $0,8 \mu_B/f.u.$ à température ambiante, avec un axe d'aimantation facile dans le plan. Cette valeur nous permet de confirmer la structure spinelle inverse : $(Fe^{3+})[Fe^{2+}V^{3+}]O_4$. Les propriétés de transport indiquent une résistivité qui suit un modèle d'activation thermique, suggérant une possible transition de phase autour de 400 K. Malgré les propriétés magnétiques à température ambiante, des recherches supplémentaires sont nécessaires pour surmonter le problème de l'anisotropie magnétique dans le plan.

– This page intentionally left blank –

References

- [1] K. Salonitis, J. Pandremenos, J. Paralikas, and G. Chryssolouris, 'Multifunctional materials: engineering applications and processing challenges', *Int J Adv Manuf Technol*, vol. 49, no. 5–8, pp. 803–826, Jul. 2010, doi: 10.1007/s00170-009-2428-6.
- [2] N. A. Spaldin and R. Ramesh, 'Advances in magnetoelectric multiferroics', *Nature Mater*, vol. 18, no. 3, pp. 203–212, Mar. 2019, doi: 10.1038/s41563-018-0275-2.
- [3] J. Gao, Z. Jiang, S. Zhang, Z. Mao, Y. Shen, and Z. Chu, 'Review of Magnetoelectric Sensors', *Actuators*, vol. 10, no. 6, p. 109, May 2021, doi: 10.3390/act10060109.
- [4] S. Dong, 'REVIEW ON PIEZOELECTRIC, ULTRASONIC, AND MAGNETOELECTRIC ACTUATORS', *J. Adv. Dielect.*, vol. 02, no. 01, p. 1230001, Jan. 2012, doi: 10.1142/S2010135X12300010.
- [5] L. Bian, Y. Wen, P. Li, Q. Gao, and M. Zheng, 'Magnetoelectric transducer with high quality factor for wireless power receiving', *Sensors and Actuators A: Physical*, vol. 150, no. 2, pp. 207–211, Mar. 2009, doi: 10.1016/j.sna.2009.01.003.
- [6] N. Ortega, A. Kumar, J. F. Scott, and R. S. Katiyar, 'Multifunctional magnetoelectric materials for device applications', *J. Phys.: Condens. Matter*, vol. 27, no. 50, p. 504002, Dec. 2015, doi: 10.1088/0953-8984/27/50/504002.
- [7] C. Becher *et al.*, 'Strain-induced coupling of electrical polarization and structural defects in SrMnO₃ films', *Nature Nanotech*, vol. 10, no. 8, pp. 661–665, Aug. 2015, doi: 10.1038/nnano.2015.108.
- [8] H.-J. Freund, 'The Surface Science of Catalysis and More, Using Ultrathin Oxide Films as Templates: A Perspective', *J. Am. Chem. Soc.*, vol. 138, no. 29, pp. 8985–8996, Jul. 2016, doi: 10.1021/jacs.6b05565.
- [9] J.-H. Huang, F. Huang, L. Evans, and S. Glasauer, 'Vanadium: Global (bio)geochemistry', *Chemical Geology*, vol. 417, pp. 68–89, Dec. 2015, doi: 10.1016/j.chemgeo.2015.09.019.
- [10] J. M. Dyke, B. W. J. Gravenor, M. P. Hastings, and A. Morris, 'High-temperature photoelectron spectroscopy: the vanadium monoxide molecule', *J. Phys. Chem.*, vol. 89, no. 21, pp. 4613–4617, Oct. 1985, doi: 10.1021/j100267a040.
- [11] V. Mounasamy, G. K. Mani, D. Ponnusamy, K. Tsuchiya, A. K. Prasad, and S. Madanagurusamy, 'Template-free synthesis of vanadium sesquioxide (V₂O₃) nanosheets and their room-temperature sensing performance', *J. Mater. Chem. A*, vol. 6, no. 15, pp. 6402–6413, 2018, doi: 10.1039/C7TA10159G.
- [12] T. D. Manning and I. P. Parkin, 'Vanadium(IV) oxide thin films on glass and silicon from the atmospheric pressure chemical vapour deposition reaction of VOCl₃ and water', *Polyhedron*, vol. 23, no. 18, pp. 3087–3095, Dec. 2004, doi: 10.1016/j.poly.2004.09.020.
- [13] A. B. Goldfine, D. C. Simonson, F. Folli, M. E. Patti, and C. R. Kahn, 'Metabolic effects of sodium metavanadate in humans with insulin-dependent and noninsulin-dependent diabetes mellitus in vivo and in vitro studies.', *The Journal of Clinical Endocrinology & Metabolism*, vol. 80, no. 11, pp. 3311–3320, Nov. 1995, doi: 10.1210/jcem.80.11.7593444.
- [14] J. L. Domingo, M. Gómez, J. M. Llobet, J. Corbella, and C. L. Keen, 'Improvement of Glucose Homeostasis by Oral Vanadyl or Vanadate Treatment in Diabetic Rats is Accompanied by Negative Side Effects', *Pharmacology & Toxicology*, vol. 68, no. 4, pp. 249–253, Apr. 1991, doi: 10.1111/j.1600-0773.1991.tb01233.x.
- [15] Y. Tian *et al.*, 'Micron-Sized Nanoporous Vanadium Pentoxide Arrays for High-Performance Gel Zinc-Ion Batteries and Potassium Batteries', *Chem. Mater.*, vol. 32, no. 9, pp. 4054–4064, May 2020, doi: 10.1021/acs.chemmater.0c00787.
- [16] F. F. Abdi, L. Han, A. H. M. Smets, M. Zeman, B. Dam, and R. van de Krol, 'Efficient solar water splitting by enhanced charge separation in a bismuth vanadate-silicon tandem photoelectrode', *Nat Commun*, vol. 4, no. 1, p. 2195, Jul. 2013, doi: 10.1038/ncomms3195.
- [17] Y. Shimizu, H. Takeda, M. Tanaka, M. Itoh, S. Niitaka, and H. Takagi, 'An orbital-selective spin liquid in a frustrated heavy fermion spinel LiV₂O₄', *Nat Commun*, vol. 3, no. 1, p. 981, Jul. 2012, doi: 10.1038/ncomms1979.

References

- [18] B. Canals and C. Lacroix, 'Quantum spin liquid: The Heisenberg antiferromagnet on the three-dimensional pyrochlore lattice', *Phys. Rev. B*, vol. 61, no. 2, pp. 1149–1159, Jan. 2000, doi: 10.1103/PhysRevB.61.1149.
- [19] G. J. MacDougall, V. O. Garlea, A. A. Aczel, H. D. Zhou, and S. E. Nagler, 'Magnetic order and ice rules in the multiferroic spinel FeV_2O_4 ', *Phys. Rev. B*, vol. 86, no. 6, p. 060414, Aug. 2012, doi: 10.1103/PhysRevB.86.060414.
- [20] K. Takubo *et al.*, 'Electronic structure of AV_2O_4 ($A = \text{Li}, \text{Zn}, \text{and Cd}$) studied by x-ray photoemission spectroscopy', *Phys. Rev. B*, vol. 74, no. 15, p. 155103, Oct. 2006, doi: 10.1103/PhysRevB.74.155103.
- [21] Y. Zhong Zhang, P. Fulde, P. Thalmeier, and A. Yaresko, 'Charge Ordering in the Spinel AlV_2O_4 and LiV_2O_4 ', *J. Phys. Soc. Jpn.*, vol. 74, no. 8, pp. 2153–2156, Aug. 2005, doi: 10.1143/JPSJ.74.2153.
- [22] M. Onoda, 'Mixed-Valence Ion Model for Incoherent Metallic State in Heavy-Fermion Spinel LiV_2O_4 ', *J. Phys. Soc. Jpn.*, vol. 90, no. 3, p. 034701, Mar. 2021, doi: 10.7566/JPSJ.90.034701.
- [23] S. Niitaka *et al.*, 'High-field magnetization study of the heavy fermion oxide', *Journal of Magnetism and Magnetic Materials*, vol. 310, no. 2, pp. e258–e260, Mar. 2007, doi: 10.1016/j.jmmm.2006.10.149.
- [24] S. Kondo *et al.*, ' LiV_2O_4 : A Heavy Fermion Transition Metal Oxide', *Phys. Rev. Lett.*, vol. 78, no. 19, pp. 3729–3732, May 1997, doi: 10.1103/PhysRevLett.78.3729.
- [25] A. J. Browne, C. Lithgow, S. A. J. Kimber, and J. P. Attfield, 'Orbital Molecules in the New Spinel GaV_2O_4 ', *Inorg. Chem.*, vol. 57, no. 5, pp. 2815–2822, Mar. 2018, doi: 10.1021/acs.inorgchem.7b03221.
- [26] J. H. Lee *et al.*, 'Magnetic Frustration Driven by Itinerancy in Spinel CoV_2O_4 ', *Sci Rep*, vol. 7, no. 1, p. 17129, Dec. 2017, doi: 10.1038/s41598-017-17160-0.
- [27] E. Pavarini, E. Koch, J. van den Brink, G. Sawatzky, Institute for Advanced Simulation, and German Research School for Simulation Sciences, Eds., *Quantum materials: experiments and theory: lecture notes of the Autumn School on Correlated Electrons 2016: at Forschungszentrum Jülich, 12-16 September 2016*. in Schriften des Forschungszentrums Jülich. Reihe Modeling and Simulation, no. Band 6. Jülich: Forschungszentrum, Zentralbibliothek, 2016.
- [28] H. Ishibashi *et al.*, 'Small crystal distortion and long-range antiferro-orbital ordering in the spinel oxide CoV_2O_4 ', *Phys. Rev. B*, vol. 96, no. 14, p. 144424, Oct. 2017, doi: 10.1103/PhysRevB.96.144424.
- [29] Q. Zhang *et al.*, 'Ordering process and ferroelectricity in a spinel derived from FeV_2O_4 ', *Phys. Rev. B*, vol. 85, no. 5, p. 054405, Feb. 2012, doi: 10.1103/PhysRevB.85.054405.
- [30] H. Mamiya, M. Onoda, T. Furubayashi, J. Tang, and I. Nakatani, 'Structural and magnetic studies on vanadium spinel MgV_2O_4 ', *Journal of Applied Physics*, vol. 81, no. 8, pp. 5289–5291, Apr. 1997, doi: 10.1063/1.364518.
- [31] M. Reehuis, A. Krimmel, N. Böttgen, A. Loidl, and A. Prokofiev, 'Crystallographic and magnetic structure of ZnV_2O_4 ', *The European Physical Journal B - Condensed Matter*, vol. 35, no. 3, pp. 311–316, Oct. 2003, doi: 10.1140/epjb/e2003-00282-4.
- [32] L. Wang *et al.*, 'Phase transition and critical behaviors of spin-orbital coupling spinel compound CdV_2O_4 ', *Journal of Applied Physics*, vol. 119, no. 9, p. 093908, Mar. 2016, doi: 10.1063/1.4941845.
- [33] H. Tsunetsugu and Y. Motome, 'Magnetic transition and orbital degrees of freedom in vanadium spinels', *Phys. Rev. B*, vol. 68, no. 6, p. 060405, Aug. 2003, doi: 10.1103/PhysRevB.68.060405.
- [34] O. Tchernyshyov, 'Structural, Orbital, and Magnetic Order in Vanadium Spinel', *Phys. Rev. Lett.*, vol. 93, no. 15, p. 157206, Oct. 2004, doi: 10.1103/PhysRevLett.93.157206.
- [35] S. Di Matteo, G. Jackeli, and N. B. Perkins, 'Orbital order in vanadium spinels', *Phys. Rev. B*, vol. 72, no. 2, p. 020408, Jul. 2005, doi: 10.1103/PhysRevB.72.020408.
- [36] K. Adachi, T. Suzuki, K. Kato, K. Osaka, M. Takata, and T. Katsufuji, 'Magnetic-Field Switching of Crystal Structure in an Orbital-Spin-Coupled System: MnV_2O_4 ', *Phys. Rev. Lett.*, vol. 95, no. 19, p. 197202, Nov. 2005, doi: 10.1103/PhysRevLett.95.197202.
- [37] T. Suzuki, M. Katsumura, K. Taniguchi, T. Arima, and T. Katsufuji, 'Orbital Ordering and Magnetic Field Effect in MnV_2O_4 ', *Phys. Rev. Lett.*, vol. 98, no. 12, p. 127203, Mar. 2007, doi: 10.1103/PhysRevLett.98.127203.
- [38] S. Shimono *et al.*, 'Phase transitions and off-stoichiometric effects of vanadium spinel oxide CoV_2O_4 ', *Mater. Res. Express*, vol. 3, no. 6, p. 066101, Jun. 2016, doi: 10.1088/2053-1591/3/6/066101.

- [39] Y. Huang, Z. Yang, and Y. Zhang, 'Magnetic, structural, and thermal properties of CoV_2O_4 ', *J. Phys.: Condens. Matter*, vol. 24, no. 5, p. 056003, Feb. 2012, doi: 10.1088/0953-8984/24/5/056003.
- [40] M. Imada, A. Fujimori, and Y. Tokura, 'Metal-insulator transitions', *Rev. Mod. Phys.*, vol. 70, no. 4, pp. 1039–1263, Oct. 1998, doi: 10.1103/RevModPhys.70.1039.
- [41] P. Shahi *et al.*, 'Chemical Pressure effect at the boundary of Mott insulator and itinerant electron limit of Spinel Vanadates', *sci adv mater*, vol. 7, no. 6, pp. 1187–1196, Jun. 2015, doi: 10.1166/sam.2015.2247.
- [42] S. Blanco-Canosa *et al.*, 'Enhanced Pressure Dependence of Magnetic Exchange in $\text{A}^{2+}[\text{V}^{2+}]_2\text{O}_4$ Spinel Approaching the Itinerant Electron Limit', *Phys. Rev. Lett.*, vol. 99, no. 18, p. 187201, Nov. 2007, doi: 10.1103/PhysRevLett.99.187201.
- [43] W. A. Harrison, *Electronic structure and the properties of solids: the physics of the chemical bond*, Dover ed. New York: Dover Publications, 1989.
- [44] J. B. Goodenough, *Magnetism and the chemical bond*. Huntington, N.Y: R. E. Krieger Pub. Co, 1976.
- [45] M. V. Talanov, V. B. Shirokov, L. A. Avakyan, V. M. Talanov, and K. Sh. Borlakov, 'Vanadium clusters formation in geometrically frustrated spinel oxide AlV_2O_4 ', *Acta Crystallogr B Struct Sci Cryst Eng Mater*, vol. 74, no. 4, pp. 337–353, Aug. 2018, doi: 10.1107/S2052520618007242.
- [46] J. B. Goodenough, G. Dutta, and A. Manthiram, 'Lattice instabilities near the critical V-V separation for localized versus itinerant electrons in $\text{LiV}_{1-y}\text{M}_y\text{O}_2$ ($\text{M}=\text{Cr}$ or Ti) $\text{Li}_{1-x}\text{VO}_2$ ', *Phys. Rev. B*, vol. 43, no. 13, pp. 10170–10178, May 1991, doi: 10.1103/PhysRevB.43.10170.
- [47] J. B. Goodenough, 'Direct Cation-Cation Interactions in Several Oxides', *Phys. Rev.*, vol. 117, no. 6, pp. 1442–1451, Mar. 1960, doi: 10.1103/PhysRev.117.1442.
- [48] D. B. Rogers, R. J. Arnett, A. Wold, and J. B. Goodenough, 'The preparation and properties of some vanadium spinels', *Journal of Physics and Chemistry of Solids*, vol. 24, no. 3, pp. 347–360, Mar. 1963, doi: 10.1016/0022-3697(63)90193-8.
- [49] A. Kiswandhi, J. Ma, J. S. Brooks, and H. D. Zhou, 'Effects of inter-vanadium distance and A-site magnetism in AV_2O_4 ($\text{A} = \text{Cd}, \text{Mg}, \text{Zn}$) spinels near the itinerant electron limit', *Phys. Rev. B*, vol. 90, no. 15, p. 155132, Oct. 2014, doi: 10.1103/PhysRevB.90.155132.
- [50] S. Kondo, *Shinichiro Kondo. Iowa State University. Retrospective Theses and Dissertations. 11866*. 1998.
- [51] G.-W. Chern, N. Perkins, and Z. Hao, 'Quantum 120° model on pyrochlore lattice: Orbital ordering in MnV_2O_4 ', *Phys. Rev. B*, vol. 81, no. 12, p. 125127, Mar. 2010, doi: 10.1103/PhysRevB.81.125127.
- [52] Y. Nii *et al.*, 'Orbital structures in spinel vanadates AV_2O_4 ($\text{A} = \text{Fe}, \text{Mn}$)', *Phys. Rev. B*, vol. 86, no. 12, p. 125142, Sep. 2012, doi: 10.1103/PhysRevB.86.125142.
- [53] S. Kawaguchi *et al.*, 'Orthorhombic distortion and orbital order in the vanadium spinel FeV_2O_4 ', *Phys. Rev. B*, vol. 93, no. 2, p. 024108, Jan. 2016, doi: 10.1103/PhysRevB.93.024108.
- [54] T. Katsufuji *et al.*, 'Structural and Magnetic Properties of Spinel FeV_2O_4 with Two Ions Having Orbital Degrees of Freedom', *J. Phys. Soc. Jpn.*, vol. 77, no. 5, p. 053708, May 2008, doi: 10.1143/JPSJ.77.053708.
- [55] J. Okabayashi, S. Miyasaka, M. Takahashi, and S. Tajima, 'Local electronic and magnetic properties of ferro-orbital-ordered FeV_2O_4 ', *Jpn. J. Appl. Phys.*, vol. 57, no. 9, p. 0902BD, Sep. 2018, doi: 10.7567/JJAP.57.0902BD.
- [56] W. Xie, X. Xing, and Z. Cao, 'Successive orbital ordering transitions in FeV_2O_4 from first-principles calculation', *Journal of Applied Physics*, vol. 126, no. 24, p. 244904, Dec. 2019, doi: 10.1063/1.5126877.
- [57] K. Matsuura, H. Sagayama, Y. Nii, N. D. Khanh, N. Abe, and T. Arima, 'X-ray magnetic circular dichroism study of an orbital ordered state in the spinel-type vanadium oxide AV_2O_4 ($\text{A} = \text{Mn}, \text{Fe}$)', *Phys. Rev. B*, vol. 92, no. 3, p. 035133, Jul. 2015, doi: 10.1103/PhysRevB.92.035133.
- [58] B. R. Myoung, S. J. Kim, J. T. Lim, T. Kouh, and C. S. Kim, 'Microscopic evidence of magnetic and structure phase transition in multiferroic spinel FeV_2O_4 ', *AIP Advances*, vol. 7, no. 5, p. 055828, May 2017, doi: 10.1063/1.4977549.
- [59] J. Krishna *et al.*, 'Complete description of the magnetic ground state in spinel vanadates', *Phys. Rev. B*, vol. 100, no. 8, p. 081102, Aug. 2019, doi: 10.1103/PhysRevB.100.081102.
- [60] S. T. Bramwell and M. J. P. Gingras, 'Spin Ice State in Frustrated Magnetic Pyrochlore Materials', *Science*, vol. 294, no. 5546, pp. 1495–1501, Nov. 2001, doi: 10.1126/science.1064761.

References

- [61] S. Nishihara, W. Doi, H. Ishibashi, Y. Hosokoshi, X.-M. Ren, and S. Mori, 'Appearance of magnetization jumps in magnetic hysteresis curves in spinel oxide FeV₂O₄', *Journal of Applied Physics*, vol. 107, no. 9, p. 09A504, May 2010, doi: 10.1063/1.3337683.
- [62] N. Liu, K. H. Zhao, X. L. Shi, and L. W. Zhang, 'Fe³⁺ doping effects on the structure and multiferroicity of Fe_{1-x}V_{2-x}O₄ (0 ≤ x ≤ 0.4) spinels', *Journal of Applied Physics*, vol. 111, no. 12, p. 124112, Jun. 2012, doi: 10.1063/1.4730767.
- [63] G. Giovannetti *et al.*, 'Dielectric properties and magnetostriction of the collinear multiferroic spinel CdV₂O₄', *Phys. Rev. B*, vol. 83, no. 6, p. 060402, Feb. 2011, doi: 10.1103/PhysRevB.83.060402.
- [64] Y. Yamasaki, S. Miyasaka, Y. Kaneko, J.-P. He, T. Arima, and Y. Tokura, 'Magnetic Reversal of the Ferroelectric Polarization in a Multiferroic Spinel Oxide', *Phys. Rev. Lett.*, vol. 96, no. 20, p. 207204, May 2006, doi: 10.1103/PhysRevLett.96.207204.
- [65] H. Katsura, N. Nagaosa, and A. V. Balatsky, 'Spin Current and Magnetoelectric Effect in Noncollinear Magnets', *Phys. Rev. Lett.*, vol. 95, no. 5, p. 057205, Jul. 2005, doi: 10.1103/PhysRevLett.95.057205.
- [66] T. A. Kaplan and S. D. Mahanti, 'Canted-spin-caused electric dipoles: A local symmetry theory', *Phys. Rev. B*, vol. 83, no. 17, p. 174432, May 2011, doi: 10.1103/PhysRevB.83.174432.
- [67] K.-H. Zhao, Y.-H. Wang, X.-L. Shi, N. Liu, and L.-W. Zhang, 'Ferroelectricity in the Ferrimagnetic Phase of Fe_{1-x}Mn_xV₂O₄', *Chinese Phys. Lett.*, vol. 32, no. 8, p. 087503, Aug. 2015, doi: 10.1088/0256-307X/32/8/087503.
- [68] A. Kismarahardja, J. S. Brooks, H. D. Zhou, E. S. Choi, K. Matsubayashi, and Y. Uwatoko, 'Dielectric properties of single crystal spinels in the series FeV₂O₄, MnV₂O₄, and CoV₂O₄ in high magnetic fields', *Phys. Rev. B*, vol. 87, no. 5, p. 054432, Feb. 2013, doi: 10.1103/PhysRevB.87.054432.
- [69] X. Shi, Y. Wang, K. Zhao, N. Liu, G. Sun, and L. Zhang, 'Structural and magnetic anisotropy in the epitaxial FeV₂O₄ (110) spinel thin films', *AIP Advances*, vol. 5, no. 11, p. 117146, Nov. 2015, doi: 10.1063/1.4936634.
- [70] D. Zhou *et al.*, 'Magnetic and Magnetodielectric Properties of Epitaxial Iron Vanadate Thin Films', *Adv. Electron. Mater.*, vol. 3, no. 1, p. 1600295, Jan. 2017, doi: 10.1002/aelm.201600295.
- [71] X. Shi, Y. Wang, K. Zhao, X. Lai, and L. Zhang, 'Strain effects in epitaxial FeV₂O₄ thin films fabricated by pulsed laser deposition', *Journal of Crystal Growth*, vol. 419, pp. 102–107, Jun. 2015, doi: 10.1016/j.jcrysgro.2015.03.014.
- [72] M. Arya *et al.*, 'Combining experimental and modelling approaches to understand the expansion of lattice parameter of epitaxial SrTi_{1-x}TaxO₃ (x = 0–0.1) films', *Computational Materials Science*, vol. 217, p. 111917, Jan. 2023, doi: 10.1016/j.commatsci.2022.111917.
- [73] A. Zahoor, M. Isa, and T. Mahmood, 'Computational study of Be doped LaAlO₃ perovskite', *Physica B: Condensed Matter*, vol. 652, p. 414631, Mar. 2023, doi: 10.1016/j.physb.2022.414631.
- [74] C. Pratapkumar, S. C. Prashantha, H. Nagabhushana, and D. M. Jnaneshwara, 'Photoluminescence and photometric studies of low temperature prepared red emitting MgAl₂O₄:Cr³⁺ nanophosphors for solid state displays', *Journal of Science: Advanced Materials and Devices*, vol. 3, no. 4, pp. 464–470, Dec. 2018, doi: 10.1016/j.jsamd.2018.09.002.
- [75] D.-N. Zhang, L. Zhao, J.-F. Wang, and Y.-L. Li, 'ELECTRONIC STRUCTURES AND THE STABILITY OF MgO SURFACE: DENSITY FUNCTIONAL STUDY', *Surf. Rev. Lett.*, vol. 22, no. 03, p. 1550037, Jun. 2015, doi: 10.1142/S0218625X15500377.
- [76] D. Kim, D. Zhou, S. Hu, D. H. T. Nguyen, N. Valanoor, and J. Seidel, 'Temperature-Dependent Magnetic Domain Evolution in Noncollinear Ferrimagnetic FeV₂O₄ Thin Films', *ACS Appl. Electron. Mater.*, vol. 1, no. 6, pp. 817–822, Jun. 2019, doi: 10.1021/acsaelm.9b00153.
- [77] F. Roulland *et al.*, 'Promoting the magnetic exchanges in PLD deposited strained films of FeV₂O₄ thin films', *Materials Chemistry and Physics*, vol. 276, p. 125360, Jan. 2022, doi: 10.1016/j.matchemphys.2021.125360.
- [78] 'Ceramic Methods', in *Essentials of Inorganic Materials Synthesis*, Hoboken, NJ: John Wiley & Sons, Inc, 2015, pp. 17–21. doi: 10.1002/9781118892671.ch3.
- [79] R. J. Sullivan, T. T. Srinivasan, and R. E. Newnham, 'Synthesis of V₂O₃ Powder by Evaporative Decomposition of Solutions and H₂ Reduction', *J American Ceramic Society*, vol. 73, no. 12, pp. 3715–3717, Dec. 1990, doi: 10.1111/j.1151-2916.1990.tb04285.x.
- [80] R. M. German, *Powder metallurgy science*, 2nd ed. Princeton, N.J: Metal Powder Industries Federation, 1994.

- [81] Y. Sun, W. Su, H. Yang, and J. Ruan, 'Effects of WC particle size on sintering behavior and mechanical properties of coarse grained WC–8Co cemented carbides fabricated by unmilled composite powders', *Ceramics International*, vol. 41, no. 10, pp. 14482–14491, Dec. 2015, doi: 10.1016/j.ceramint.2015.07.086.
- [82] L. Y. Sadler, D. A. Stanley, and D. R. Brooks, 'Attrition mill operating characteristics', *Powder Technology*, vol. 12, no. 1, pp. 19–28, Jul. 1975, doi: 10.1016/0032-5910(75)85004-2.
- [83] K. Shinohara, B. Golman, T. Uchiyama, and M. Otani, 'Fine-grinding characteristics of hard materials by attrition mill', *Powder Technology*, vol. 103, no. 3, pp. 292–296, Jul. 1999, doi: 10.1016/S0032-5910(99)00042-X.
- [84] M. Wood *et al.*, 'Exploring the relationship between solvent-assisted ball milling, particle size, and sintering temperature in garnet-type solid electrolytes', *Journal of Power Sources*, vol. 484, p. 229252, Feb. 2021, doi: 10.1016/j.jpowsour.2020.229252.
- [85] Z. H. Loh, A. K. Samanta, and P. W. Sia Heng, 'Overview of milling techniques for improving the solubility of poorly water-soluble drugs', *Asian Journal of Pharmaceutical Sciences*, vol. 10, no. 4, pp. 255–274, Jul. 2015, doi: 10.1016/j.ajps.2014.12.006.
- [86] A. K. S. Varghese, and T. Kurian, 'Effect of ball size on milling efficiency of zinc oxide dispersions', *Particulate Science and Technology*, vol. 36, no. 3, pp. 308–311, Apr. 2018, doi: 10.1080/02726351.2016.1248258.
- [87] N. A. Shepelin, Z. P. Tehrani, N. Ohannessian, C. W. Schneider, D. Pergolesi, and T. Lippert, 'A practical guide to pulsed laser deposition', *Chem. Soc. Rev.*, p. 10.1039/D2CS00938B, 2023, doi: 10.1039/D2CS00938B.
- [88] M. N. R. Ashfold, F. Claeysens, G. M. Fuge, and S. J. Henley, 'Pulsed laser ablation and deposition of thin films', *Chem. Soc. Rev.*, vol. 33, no. 1, p. 23, 2004, doi: 10.1039/b207644f.
- [89] Myerlas, Robert, 'KEY PARAMETERS OF PULSED LASER DEPOSITION FOR SOLID ELECTROLYTE THIN FILM GROWTH', Feb. 2017, doi: 10.5281/ZENODO.3951361.
- [90] X. Zhang *et al.*, 'Influence of substrate temperature on structures and dielectric properties of pyrochlore Bi_{1.5}Zn_{1.0}Nb_{1.5}O₇ thin films prepared by pulsed laser deposition', *Applied Surface Science*, vol. 256, no. 22, pp. 6607–6611, Sep. 2010, doi: 10.1016/j.apsusc.2010.04.056.
- [91] K. Kordek-Khalil, A. de Rosset, and P. Rutkowski, 'Influence of pulsed laser ablation temperature on structure, morphology and electrocatalytic properties of cobalt-based films deposited on carbon cloth', *Applied Surface Science*, vol. 509, p. 145263, Apr. 2020, doi: 10.1016/j.apsusc.2020.145263.
- [92] P. C. Korir, F. B. Dejene, M. L. Chenene, and L. K. Munguti, 'Influence of deposition atmosphere on the structural and photoluminescence properties of pulsed laser deposited (Y–Gd)₃Al₅O₁₂:Ce³⁺ thin films', *Materials Chemistry and Physics*, vol. 243, p. 122626, Mar. 2020, doi: 10.1016/j.matchemphys.2020.122626.
- [93] Y. Zhou *et al.*, 'Critical Effect of Oxygen Pressure in Pulsed Laser Deposition for Room Temperature and High Performance Amorphous In–Ga–Zn–O Thin Film Transistors', *Nanomaterials*, vol. 12, no. 24, p. 4358, Dec. 2022, doi: 10.3390/nano12244358.
- [94] A. H. Youssef, G. Kolhatkar, A. Merlen, R. Thomas, and A. Ruediger, 'Surface preparation and the evolution of atomically flat step terrace morphology of MgO single crystals', *AIP Advances*, vol. 8, no. 9, p. 095025, Sep. 2018, doi: 10.1063/1.5047029.
- [95] M. Kawasaki *et al.*, 'Atomic Control of the SrTiO₃ Crystal Surface', *Science*, vol. 266, no. 5190, pp. 1540–1542, Dec. 1994, doi: 10.1126/science.266.5190.1540.
- [96] J. J. Peng, C. S. Hao, H. Y. Liu, and Y. Yan, 'Two-step treatment to obtain single-terminated SrTiO₃ substrate and the related difference in both LaAlO₃ film growth and electronic property', *AIP Advances*, vol. 11, no. 8, p. 085303, Aug. 2021, doi: 10.1063/5.0053323.
- [97] J. J. Prentice, J. A. Grant-Jacob, S. V. Kurilchik, J. I. Mackenzie, and R. W. Eason, 'Particulate reduction in PLD-grown crystalline films via bi-directional target irradiation', *Appl. Phys. A*, vol. 125, no. 2, p. 152, Feb. 2019, doi: 10.1007/s00339-019-2456-5.
- [98] H. M. Christen and G. Eres, 'Recent advances in pulsed-laser deposition of complex oxides', *J. Phys.: Condens. Matter*, vol. 20, no. 26, p. 264005, Jul. 2008, doi: 10.1088/0953-8984/20/26/264005.
- [99] J. I. Goldstein, D. E. Newbury, J. R. Michael, N. W. M. Ritchie, J. H. J. Scott, and D. C. Joy, *Scanning Electron Microscopy and X-Ray Microanalysis*. New York, NY: Springer New York, 2018. doi: 10.1007/978-1-4939-6676-9.

- [100] L. Reimer, *Scanning Electron Microscopy: Physics of Image Formation and Microanalysis*, vol. 45. in Springer Series in Optical Sciences, vol. 45. Berlin, Heidelberg: Springer Berlin Heidelberg, 1998. doi: 10.1007/978-3-540-38967-5.
- [101] Giorgio Capuccio and L. Terranov, 'THIN FILM CHARACTERISATION BY ADVANCED X-RAY DIFFRACTION TECHNIQUES. V School on X-ray Diffraction from Polycrystalline Materials (Frascati)'. 1996.
- [102] A. Pandey, S. Dalal, S. Dutta, and A. Dixit, 'Structural characterization of polycrystalline thin films by X-ray diffraction techniques', *J Mater Sci: Mater Electron*, vol. 32, no. 2, pp. 1341–1368, Jan. 2021, doi: 10.1007/s10854-020-04998-w.
- [103] T. C. Huang, R. Gilles, and G. Will, 'Thin-film thickness and density determination from x-ray reflectivity data using a conventional power diffractometer', *Thin Solid Films*, vol. 230, no. 2, pp. 99–101, Aug. 1993, doi: 10.1016/0040-6090(93)90499-F.
- [104] Z. Zhang, F. Zhou, and E. J. Lavernia, 'On the analysis of grain size in bulk nanocrystalline materials via x-ray diffraction', *Metall and Mat Trans A*, vol. 34, no. 6, pp. 1349–1355, Jun. 2003, doi: 10.1007/s11661-003-0246-2.
- [105] A. Segmüller and M. Murakami, 'X-Ray Diffraction Analysis of Strains and Stresses in Thin Films', in *Treatise on Materials Science & Technology*, vol. 27, Elsevier, 1988, pp. 143–200. doi: 10.1016/B978-0-12-341827-2.50010-8.
- [106] C. Suryanarayana and M. G. Norton, *X-Ray diffraction: a practical approach*. New York: Plenum Press, 1998.
- [107] B. B. He, 'Introduction to two-dimensional X-ray diffraction', *Powder Diffraction*, vol. 18, no. 2, pp. 71–85, Jun. 2003, doi: 10.1154/1.1577355.
- [108] D. Kriegner, Z. Matěj, R. Kužel, and V. Holý, 'Powder diffraction in Bragg–Brentano geometry with straight linear detectors', *J Appl Crystallogr*, vol. 48, no. 2, pp. 613–618, Apr. 2015, doi: 10.1107/S1600576715003465.
- [109] J. Als-Nielsen and D. McMorrow, *Elements of modern X-ray physics*, 2nd ed. Hoboken: Wiley, 2011.
- [110] M. Yasaka, 'X-Ray Thin-Film Measurement Techniques V. X-Ray Reflectivity Measurement', *The Rigaku Journal*, vol. 26, no. 2, pp. 1–9, 2010.
- [111] H. Kiessig, 'Interferenz von Röntgenstrahlen an dünnen Schichten', *Ann. Phys.*, vol. 402, no. 7, pp. 769–788, 1931, doi: 10.1002/andp.19314020702.
- [112] C. H. Lee and S. Y. Tseng, 'In Situ Fixed-Angle X-ray Reflectivity Measurement of Thin-Film Roughness and Thickness during Deposition', *J Appl Crystallogr*, vol. 31, no. 2, pp. 181–184, Apr. 1998, doi: 10.1107/S002188989700928X.
- [113] K. Usami, N. K. Norio Kobayashi, and A. M. Akihiro Miyauchi, 'Study of X-Ray Reflectivity from Si Film/Interface Layer/Si Substrate and Application to Low-Temperature Epitaxially Grown Si/Si Substrate', *Jpn. J. Appl. Phys.*, vol. 32, no. 7R, p. 3312, Jul. 1993, doi: 10.1143/JJAP.32.3312.
- [114] K. S. Iida, 'Fourier Analysis of Interference Structure in X-Ray Specular Reflection from Thin Films', *Jpn. J. Appl. Phys.*, vol. 31, no. 2A, p. L113, Feb. 1992, doi: 10.1143/JJAP.31.L113.
- [115] K. Moffat, 'Laue diffraction and time-resolved crystallography: a personal history', *Phil. Trans. R. Soc. A.*, vol. 377, no. 2147, p. 20180243, Jun. 2019, doi: 10.1098/rsta.2018.0243.
- [116] Ch. Schetelich, S. Brenner, and V. Geist, 'Laue and Kossel Diffraction on Quasicrystals by Means of Synchrotron Radiation', *J Synchrotron Rad*, vol. 5, no. 2, pp. 102–106, Mar. 1998, doi: 10.1107/S0909049597017901.
- [117] A. M. Miller, M. Lemon, M. A. Choffel, S. R. Rich, F. Harvel, and D. C. Johnson, 'Extracting information from X-ray diffraction patterns containing Laue oscillations', *Zeitschrift für Naturforschung B*, vol. 77, no. 4–5, pp. 313–322, May 2022, doi: 10.1515/znb-2022-0020.
- [118] M. Althammer *et al.*, 'Role of interface quality for the spin Hall magnetoresistance in nickel ferrite thin films with bulk-like magnetic properties', *Appl. Phys. Lett.*, vol. 115, no. 9, p. 092403, Aug. 2019, doi: 10.1063/1.5097600.
- [119] J. Xu *et al.*, 'Growth of uniform CaGe₂ films by alternating layer molecular beam epitaxy', *Journal of Crystal Growth*, vol. 460, pp. 134–138, Feb. 2017, doi: 10.1016/j.jcrysgro.2016.12.102.
- [120] J. A. Switzer, J. C. Hill, N. K. Mahenderkar, and Y.-C. Liu, 'Nanometer-Thick Gold on Silicon as a Proxy for Single-Crystal Gold for the Electrodeposition of Epitaxial Cuprous Oxide Thin Films', *ACS Appl. Mater. Interfaces*, vol. 8, no. 24, pp. 15828–15837, Jun. 2016, doi: 10.1021/acsami.6b04552.

- [121] L. B. Freund and S. Suresh, *Thin Film Materials: Stress, Defect Formation and Surface Evolution*, 1st ed. Cambridge University Press, 2004. doi: 10.1017/CBO9780511754715.
- [122] 'S. Cecchi. Lecture notes on "Use of X-ray diffraction for the study of epitaxial thin films and heterostructures". Part 2. Paul-Drude-Institut für Festkörperelektronik.'
- [123] P. F. Fewster, 'Reciprocal Space Mapping', in *X-Ray and Neutron Dynamical Diffraction*, vol. 357, A. Authier, S. Lagomarsino, and B. K. Tanner, Eds., in NATO ASI Series, vol. 357. , Boston, MA: Springer US, 1996, pp. 269–288. doi: 10.1007/978-1-4615-5879-8_19.
- [124] P. H. Fuoss and I. K. Robinson, 'Apparatus for X-ray diffraction in ultrahigh vacuum', *Nuclear Instruments and Methods in Physics Research*, vol. 222, no. 1–2, pp. 171–176, May 1984, doi: 10.1016/0167-5087(84)90523-4.
- [125] A. Ichimiya and P. I. Cohen, *Reflection high-energy electron diffraction*. Cambridge, U.K. ; New York: Cambridge University Press, 2004.
- [126] Y. J. Shin *et al.*, 'Oxygen Partial Pressure during Pulsed Laser Deposition: Deterministic Role on Thermodynamic Stability of Atomic Termination Sequence at SrRuO₃/BaTiO₃ Interface', *ACS Appl. Mater. Interfaces*, vol. 9, no. 32, pp. 27305–27312, Aug. 2017, doi: 10.1021/acsami.7b07813.
- [127] J. M. Van Hove, 'The dependence of RHEED oscillations on MBE growth parameters', *J. Vac. Sci. Technol. B*, vol. 3, no. 2, p. 563, Mar. 1985, doi: 10.1116/1.583180.
- [128] Y. Xiang, F.-W. Guo, T.-M. Lu, and G.-C. Wang, 'Reflection high-energy electron diffraction measurements of reciprocal space structure of 2D materials', *Nanotechnology*, vol. 27, no. 48, p. 485703, Dec. 2016, doi: 10.1088/0957-4484/27/48/485703.
- [129] S. Hasegawa, 'Reflection High-Energy Electron Diffraction', in *Characterization of Materials*, E. N. Kaufmann, Ed., Hoboken, NJ, USA: John Wiley & Sons, Inc., 2012, p. com139. doi: 10.1002/0471266965.com139.
- [130] V. Gervilla, G. A. Almyras, F. Thunström, J. E. Greene, and K. Sarakinos, 'Dynamics of 3D-island growth on weakly-interacting substrates', *Applied Surface Science*, vol. 488, pp. 383–390, Sep. 2019, doi: 10.1016/j.apsusc.2019.05.208.
- [131] I.-C. Robin, R. André, and J.-M. Gérard, 'Relation between growth procedure and confinement properties of Cd Se/Zn Se quantum dots', *Phys. Rev. B*, vol. 74, no. 15, p. 155318, Oct. 2006, doi: 10.1103/PhysRevB.74.155318.
- [132] G. Krieger, 'Structural and orbital engineering in nickelate thin films: on the road of superconductivity', University of Strasbourg, 2022.
- [133] F. Gellé, 'Hétérostructures épitaxiées avec des propriétés dépendantes de spin et de charges pour des applications en spintronique', University of Strasbourg, 2019.
- [134] N. Jalili and K. Laxminarayana, 'A review of atomic force microscopy imaging systems: application to molecular metrology and biological sciences', *Mechatronics*, vol. 14, no. 8, pp. 907–945, Oct. 2004, doi: 10.1016/j.mechatronics.2004.04.005.
- [135] M. Ohtsu, Ed., *Optical and Electronic Process of Nano-Matters*. Dordrecht: Springer Netherlands, 2001. doi: 10.1007/978-94-017-2482-1.
- [136] A. Sanner, W. G. Nöhring, L. A. Thimons, T. D. B. Jacobs, and L. Pastewka, 'Scale-dependent roughness parameters for topography analysis', *Applied Surface Science Advances*, vol. 7, p. 100190, Feb. 2022, doi: 10.1016/j.apsadv.2021.100190.
- [137] D. Sinkhonde, 'Quantitative study on surface porosity and roughness parameters of mineral and organic admixtures based on multi-scale characterisation techniques', *Cleaner Materials*, vol. 7, p. 100166, Mar. 2023, doi: 10.1016/j.clema.2022.100166.
- [138] M. Buchner, K. Höfler, B. Henne, V. Ney, and A. Ney, 'Tutorial: Basic principles, limits of detection, and pitfalls of highly sensitive SQUID magnetometry for nanomagnetism and spintronics', *Journal of Applied Physics*, vol. 124, no. 16, p. 161101, Oct. 2018, doi: 10.1063/1.5045299.
- [139] K. Gramm, L. Lundgren, and O. Beckman, 'SQUID Magnetometer for Magnetization Measurements', *Phys. Scr.*, vol. 13, no. 2, pp. 93–95, Feb. 1976, doi: 10.1088/0031-8949/13/2/004.
- [140] M. Sawicki, W. Stefanowicz, and A. Ney, 'Sensitive SQUID magnetometry for studying nanomagnetism', *Semicond. Sci. Technol.*, vol. 26, no. 6, p. 064006, Jun. 2011, doi: 10.1088/0268-1242/26/6/064006.
- [141] M. Naftaly *et al.*, 'Sheet Resistance Measurements of Conductive Thin Films: A Comparison of Techniques', *Electronics*, vol. 10, no. 8, p. 960, Apr. 2021, doi: 10.3390/electronics10080960.
- [142] M. Yamashita, T. Nishii, and H. Mizutani, 'Resistivity Measurement by Dual-Configuration Four-Probe Method', *Jpn. J. Appl. Phys.*, vol. 42, no. Part 1, No. 2A, pp. 695–699, Feb. 2003, doi: 10.1143/JJAP.42.695.

References

- [143] L. J. Van Der Pauw, 'A METHOD OF MEASURING SPECIFIC RESISTIVITY AND HALL EFFECT OF DISCS OF ARBITRARY SHAPE', in *Semiconductor Devices: Pioneering Papers*, WORLD SCIENTIFIC, 1991, pp. 174–182. doi: 10.1142/9789814503464_0017.
- [144] F. S. Oliveira, R. B. Cipriano, F. T. Da Silva, E. C. Romão, and C. A. M. Dos Santos, 'Simple analytical method for determining electrical resistivity and sheet resistance using the van der Pauw procedure', *Sci Rep*, vol. 10, no. 1, p. 16379, Oct. 2020, doi: 10.1038/s41598-020-72097-1.
- [145] D. K. De Vries and A. D. Wieck, 'Potential distribution in the van der Pauw technique', *American Journal of Physics*, vol. 63, no. 12, pp. 1074–1078, Dec. 1995, doi: 10.1119/1.18013.
- [146] W. K. Chan, 'On the calculation of the geometric factor in a van der Pauw sheet resistance measurement', *Rev. Sci. Instrum.*, vol. 71, no. 10, p. 3964, 2000, doi: 10.1063/1.1290496.
- [147] A. A. Ramadan, R. D. Gould, and A. Ashour, 'On the Van der Pauw method of resistivity measurements', *Thin Solid Films*, vol. 239, no. 2, pp. 272–275, Mar. 1994, doi: 10.1016/0040-6090(94)90863-X.
- [148] R. Chwang, B. J. Smith, and C. R. Crowell, 'Contact size effects on the van der Pauw method for resistivity and Hall coefficient measurement', *Solid-State Electronics*, vol. 17, no. 12, pp. 1217–1227, Dec. 1974, doi: 10.1016/0038-1101(74)90001-X.
- [149] D. Kriegner, E. Wintersberger, and J. Stangl, '*xrayutilities*: a versatile tool for reciprocal space conversion of scattering data recorded with linear and area detectors', *J Appl Crystallogr*, vol. 46, no. 4, pp. 1162–1170, Aug. 2013, doi: 10.1107/S0021889813017214.
- [150] S. F. Edwards and P. W. Anderson, 'Theory of spin glasses', *J. Phys. F: Met. Phys.*, vol. 5, no. 5, pp. 965–974, May 1975, doi: 10.1088/0305-4608/5/5/017.
- [151] A. J. Bray and M. A. Moore, 'Chaotic Nature of the Spin-Glass Phase', *Phys. Rev. Lett.*, vol. 58, no. 1, pp. 57–60, Jan. 1987, doi: 10.1103/PhysRevLett.58.57.
- [152] K. Binder and A. P. Young, 'Spin glasses: Experimental facts, theoretical concepts, and open questions', *Rev. Mod. Phys.*, vol. 58, no. 4, pp. 801–976, Oct. 1986, doi: 10.1103/RevModPhys.58.801.
- [153] A. T. Ogielski and I. Morgenstern, 'Critical behavior of three-dimensional Ising spin-glass model', *Phys. Rev. Lett.*, vol. 54, no. 9, pp. 928–931, Mar. 1985, doi: 10.1103/PhysRevLett.54.928.
- [154] Y. Li, P. G. LaBarre, D. M. Pajerowski, A. P. Ramirez, S. Rosenkranz, and D. Phelan, 'Neutron Scattering Study of Fluctuating and Static Spin Correlations in the Anisotropic Spin Glass Fe₂TiO₅', 2022, doi: 10.48550/ARXIV.2207.07085.
- [155] J. A. Moyer, R. Gao, P. Schiffer, and L. W. Martin, 'Epitaxial growth of highly-crystalline spinel ferrite thin films on perovskite substrates for all-oxide devices', *Sci Rep*, vol. 5, no. 1, p. 10363, Jun. 2015, doi: 10.1038/srep10363.
- [156] Y. Muraoka, K. Ueda, H. Tabata, and T. Kawai, 'Preparation and thickness dependence of magnetic properties of (111)-oriented Mg_{1.5}FeTi_{0.5}O₄ spinel films on sapphire by pulsed laser deposition technique', *Vacuum*, vol. 59, no. 2–3, pp. 622–627, Nov. 2000, doi: 10.1016/S0042-207X(00)00325-0.
- [157] N. Farid, S. S. Harilal, H. Ding, and A. Hassanein, 'Emission features and expansion dynamics of nanosecond laser ablation plumes at different ambient pressures', *Journal of Applied Physics*, vol. 115, no. 3, p. 033107, Jan. 2014, doi: 10.1063/1.4862167.
- [158] A. Rebhi *et al.*, 'Effect of the Helium Background Gas Pressure on the Structural and Optoelectronic Properties of Pulsed-Laser-Deposited PbS Thin Films', *Nanomaterials*, vol. 11, no. 5, p. 1254, May 2021, doi: 10.3390/nano11051254.
- [159] J. Pawlak, M. Przybylski, and Z. Mitura, 'An Analysis of Kikuchi Lines Observed with a RHEED Apparatus for a TiO₂-Terminated SrTiO₃ (001) Crystal', *Materials*, vol. 14, no. 22, p. 7077, Nov. 2021, doi: 10.3390/ma14227077.
- [160] Y. Kainuma, 'The Theory of Kikuchi patterns', *Acta Cryst*, vol. 8, no. 5, pp. 247–257, May 1955, doi: 10.1107/S0365110X55000832.
- [161] C. J. Ball, 'Accurate determination of crystallographic orientation from Kikuchi patterns', *Philosophical Magazine A*, vol. 44, no. 6, pp. 1307–1317, Dec. 1981, doi: 10.1080/01418618108235811.
- [162] R. K. Karakhanyan and K. R. Karakhanyan, 'Influence of limited defects in crystals on the Kikuchi lines', *J. Contemp. Phys.*, vol. 42, no. 2, pp. 82–83, Feb. 2007, doi: 10.3103/S1068337207020087.
- [163] H.-C. Su, M.-Z. Lin, T.-W. Huang, and C.-H. Lee, 'Comparison between the atomic force microscopy and x-ray reflectivity on the characterization of the roughness of a surface', presented

- at the NDE for Health Monitoring and Diagnostics, N. Meyendorf, G. Y. Baaklini, and B. Michel, Eds., San Diego, CA, Jul. 2004, p. 123. doi: 10.1117/12.539761.
- [164] A. L. Ravensburg, G. K. Pálsson, M. Pohlit, B. Hjörvarsson, and V. Kapaklis, 'Influence of misfit strain on the physical properties of Fe thin films', *Thin Solid Films*, vol. 761, p. 139494, Nov. 2022, doi: 10.1016/j.tsf.2022.139494.
- [165] C.-E. Cheng *et al.*, 'Revealing the flexoelectricity in the mixed-phase regions of epitaxial BiFeO₃ thin films', *Sci Rep*, vol. 5, no. 1, p. 8091, Jan. 2015, doi: 10.1038/srep08091.
- [166] E. Ferreiro-Vila *et al.*, 'Apparent auxetic to non-auxetic crossover driven by Co²⁺ redistribution in CoFe₂O₄ thin films', *APL Materials*, vol. 7, no. 3, p. 031109, Mar. 2019, doi: 10.1063/1.5087559.
- [167] G. N. Greaves, A. L. Greer, R. S. Lakes, and T. Rouxel, 'Poisson's ratio and modern materials', *Nature Mater*, vol. 10, no. 11, pp. 823–837, Nov. 2011, doi: 10.1038/nmat3134.
- [168] E. Martin *et al.*, 'Non-auxetic/auxetic transitions inducing modifications of the magnetic anisotropy in CoFe₂O₄ thin films', *Journal of Alloys and Compounds*, vol. 836, p. 155425, Sep. 2020, doi: 10.1016/j.jallcom.2020.155425.
- [169] M. Hoppe, S. Döring, M. Gorgoi, S. Cramm, and M. Müller, 'Enhanced ferrimagnetism in auxetic NiFe₂O₄ in the crossover to the ultrathin-film limit', *Phys. Rev. B*, vol. 91, no. 5, p. 054418, Feb. 2015, doi: 10.1103/PhysRevB.91.054418.
- [170] A. Kiswandhi, J. S. Brooks, J. Lu, J. Whalen, T. Siegrist, and H. D. Zhou, 'Chemical pressure effects on structural, magnetic, and transport properties of Mn_{1-x}Co_xV₂O₄', *Phys. Rev. B*, vol. 84, no. 20, p. 205138, Nov. 2011, doi: 10.1103/PhysRevB.84.205138.
- [171] M. Spangenberg *et al.*, 'Observation of a low Curie temperature ferromagnetic phase of ultrathin epitaxial Fe films on GaAs(001)', *Journal of Magnetism and Magnetic Materials*, vol. 292, pp. 241–247, Apr. 2005, doi: 10.1016/j.jmmm.2004.10.117.
- [172] G. Garreau, M. Farle, E. Beaupre, and K. Baberschke, 'Curie temperature and morphology in ultrathin Co/W(110) films', *Phys. Rev. B*, vol. 55, no. 1, pp. 330–335, Jan. 1997, doi: 10.1103/PhysRevB.55.330.
- [173] A. A. Burema, J. J. L. Van Rijn, and T. Banerjee, 'Temperature-dependent out-of-plane anisotropy in compressively strained La_{0.67}Sr_{0.33}MnO₃ thin films', *Journal of Magnetism and Magnetic Materials*, vol. 549, p. 168910, May 2022, doi: 10.1016/j.jmmm.2021.168910.
- [174] F. Han *et al.*, 'Perpendicular magnetic anisotropy induced by La_{2/3}Sr_{1/3}MnO₃-YBaCo₂O_{5+δ} interlayer coupling', *J. Phys. D: Appl. Phys.*, vol. 54, no. 18, p. 185302, May 2021, doi: 10.1088/1361-6463/abdeff.
- [175] P. Bruno, 'Tight-binding approach to the orbital magnetic moment and magnetocrystalline anisotropy of transition-metal monolayers', *Phys. Rev. B*, vol. 39, no. 1, pp. 865–868, Jan. 1989, doi: 10.1103/PhysRevB.39.865.
- [176] S. Alraddadi, W. Hines, G. Gu, and B. Sinkovic, 'The finite size effect on the transport and magnetic properties of epitaxial Fe₃O₄ thin films', *mat express*, vol. 8, no. 5, pp. 443–449, Oct. 2018, doi: 10.1166/mex.2018.1452.
- [177] W. Eerenstein, T. T. M. Palstra, T. Hibma, and S. Celotto, 'Origin of the increased resistivity in epitaxial Fe₃O₄ films', *Phys. Rev. B*, vol. 66, no. 20, p. 201101, Nov. 2002, doi: 10.1103/PhysRevB.66.201101.
- [178] S. Jain, A. O. Adeyeye, and C. B. Boothroyd, 'Electronic properties of half metallic Fe₃O₄ films', *Journal of Applied Physics*, vol. 97, no. 9, p. 093713, May 2005, doi: 10.1063/1.1889247.
- [179] T. T. Lin *et al.*, 'Variable-Range Hopping and Thermal Activation Conduction of Y-Doped ZnO Nanocrystalline Films', *IEEE Trans. Nanotechnology*, vol. 13, no. 3, pp. 425–430, May 2014, doi: 10.1109/TNANO.2013.2280648.
- [180] N. F. Mott, 'Conduction in non-crystalline materials: III. Localized states in a pseudogap and near extremities of conduction and valence bands', *Philosophical Magazine*, vol. 19, no. 160, pp. 835–852, Apr. 1969, doi: 10.1080/14786436908216338.
- [181] Y. Zhou *et al.*, 'The effects of oxygen vacancies on ferroelectric phase transition of HfO₂-based thin film from first-principle', *Computational Materials Science*, vol. 167, pp. 143–150, Sep. 2019, doi: 10.1016/j.commatsci.2019.05.041.
- [182] M. Woińska, S. Grabowsky, P. M. Dominiak, K. Woźniak, and D. Jayatilaka, 'Hydrogen atoms can be located accurately and precisely by x-ray crystallography', *Sci. Adv.*, vol. 2, no. 5, p. e1600192, May 2016, doi: 10.1126/sciadv.1600192.

References

- [183] K. Shahzad, M. N. Khan, G. Shabbir, and J. Bashir, 'Neutron and X-Ray Diffraction Crystal Structure Rietveld Analysis of PbTiO₃ Ceramics', *Ferroelectrics*, vol. 414, no. 1, pp. 155–161, Jan. 2011, doi: 10.1080/00150193.2011.577332.
- [184] M.-M. Blum *et al.*, 'Rapid determination of hydrogen positions and protonation states of diisopropyl fluorophosphatase by joint neutron and X-ray diffraction refinement', *PNAS*, vol. 106, no. 3, pp. 713–718, Jan. 2009, doi: 10.1073/pnas.0807842106.
- [185] G. Steciuk *et al.*, 'Precession electron diffraction tomography on twinned crystals: application to CaTiO₃ thin films', *J Appl Crystallogr*, vol. 52, no. 3, pp. 626–636, Jun. 2019, doi: 10.1107/S1600576719005569.
- [186] H. Rotella *et al.*, 'Structural analysis of strained LaVO₃ thin films', *J. Phys.: Condens. Matter*, vol. 27, no. 17, p. 175001, May 2015, doi: 10.1088/0953-8984/27/17/175001.
- [187] A. Peña Corredor, N. Viart, and C. Lefevre, '*insex*: reflection choice software for resonant elastic X-ray scattering', *J Appl Crystallogr*, vol. 56, no. 3, Jun. 2023, doi: 10.1107/S1600576723002212.
- [188] A. Peña Corredor *et al.*, 'Oxygen crystallographic positions in thin films by non-destructive resonant elastic X-ray scattering', *J Appl Crystallogr*, vol. 55, no. 3, pp. 526–532, Jun. 2022, doi: 10.1107/S1600576722003673.
- [189] Coster, 'The atomic scattering factor for X-rays in the region of anomalous dispersion', *Proc. R. Soc. Lond. A*, vol. 139, no. 838, pp. 459–466, Feb. 1933, doi: 10.1098/rspa.1933.0030.
- [190] I. J. Pickering, M. Sansone, J. Marsch, and G. N. George, 'Diffraction anomalous fine structure: a new technique for probing local atomic environment', *J. Am. Chem. Soc.*, vol. 115, no. 14, pp. 6302–6311, Jul. 1993, doi: 10.1021/ja00067a052.
- [191] V. E. Dmitrienko, 'Forbidden reflections due to anisotropic X-ray susceptibility of crystals', *Acta Crystallogr A Found Crystallogr*, vol. 39, no. 1, pp. 29–35, Jan. 1983, doi: 10.1107/S0108767383000057.
- [192] S. Grenier and Y. Joly, 'Basics of Resonant Elastic X-ray Scattering theory', *J. Phys.: Conf. Ser.*, vol. 519, p. 012001, May 2014, doi: 10.1088/1742-6596/519/1/012001.
- [193] C. Vettier, 'Resonant elastic X-ray scattering: Where from? where to?', *Eur. Phys. J. Spec. Top.*, vol. 208, no. 1, pp. 3–14, Jun. 2012, doi: 10.1140/epjst/e2012-01602-7.
- [194] J.-L. Hodeau, V. Favre-Nicolin, S. Bos, H. Renevier, E. Lorenzo, and J.-F. Berar, 'Resonant Diffraction', *Chem. Rev.*, vol. 101, no. 6, pp. 1843–1868, Jun. 2001, doi: 10.1021/cr0000269.
- [195] P. M. Platzman and E. D. Isaacs, 'Resonant inelastic x-ray scattering', *Phys. Rev. B*, vol. 57, no. 18, pp. 11107–11114, May 1998, doi: 10.1103/PhysRevB.57.11107.
- [196] A. Kotani and S. Shin, 'Resonant inelastic x-ray scattering spectra for electrons in solids', *Rev. Mod. Phys.*, vol. 73, no. 1, pp. 203–246, Feb. 2001, doi: 10.1103/RevModPhys.73.203.
- [197] L. J. P. Ament, M. Van Veenendaal, T. P. Devereaux, J. P. Hill, and J. Van Den Brink, 'Resonant inelastic x-ray scattering studies of elementary excitations', *Rev. Mod. Phys.*, vol. 83, no. 2, pp. 705–767, Jun. 2011, doi: 10.1103/RevModPhys.83.705.
- [198] J. P. Hu *et al.*, 'On-site interband excitations in resonant inelastic x-ray scattering from Cu 2 O', *Phys. Rev. B*, vol. 77, no. 15, p. 155115, Apr. 2008, doi: 10.1103/PhysRevB.77.155115.
- [199] M. W. Haverkort, 'Theory of Resonant Inelastic X-Ray Scattering by Collective Magnetic Excitations', *Phys. Rev. Lett.*, vol. 105, no. 16, p. 167404, Oct. 2010, doi: 10.1103/PhysRevLett.105.167404.
- [200] D. Betto *et al.*, 'Three-dimensional dispersion of spin waves measured in NiO by resonant inelastic x-ray scattering', *Phys. Rev. B*, vol. 96, no. 2, p. 020409, Jul. 2017, doi: 10.1103/PhysRevB.96.020409.
- [201] H. Y. Huang *et al.*, 'Jahn-Teller distortion driven magnetic polarons in magnetite', *Nat Commun*, vol. 8, no. 1, p. 15929, Jun. 2017, doi: 10.1038/ncomms15929.
- [202] J. Li *et al.*, 'Unraveling the Orbital Physics in a Canonical Orbital System KCuF₃', *Phys. Rev. Lett.*, vol. 126, no. 10, p. 106401, Mar. 2021, doi: 10.1103/PhysRevLett.126.106401.
- [203] J. Fink, E. Schierle, E. Weschke, and J. Geck, 'Resonant elastic soft x-ray scattering', *Rep. Prog. Phys.*, vol. 76, no. 5, p. 056502, May 2013, doi: 10.1088/0034-4885/76/5/056502.
- [204] M. Wilke, F. Farges, P.-E. Petit, G. E. Brown, and F. Martin, 'Oxidation state and coordination of Fe in minerals: An Fe K- XANES spectroscopic study', *American Mineralogist*, vol. 86, no. 5–6, pp. 714–730, May 2001, doi: 10.2138/am-2001-5-612.
- [205] H. Yoshida, S. Nonoyama, and Y. Y. T. Hattori, 'Quantitative Determination of Platinum Oxidation State by XANES Analysis', *Physica Scripta*, p. 813, 2005, doi: 10.1238/Physica.Topical.115a00813.

- [206] S. M. A. M. Bouwens, J. A. R. Van Veen, D. C. Koningsberger, V. H. J. De Beer, and R. Prins, 'EXAFS determination of the structure of cobalt in carbon-supported cobalt and cobalt-molybdenum sulfide hydrodesulfurization catalysts', *J. Phys. Chem.*, vol. 95, no. 1, pp. 123–134, Jan. 1991, doi: 10.1021/j100154a028.
- [207] C. R. A. Catlow, A. V. Chadwick, G. N. Greaves, and L. M. Moroney, 'EXAFS Study of Yttria-Stabilized Zirconia', *J American Ceramic Society*, vol. 69, no. 3, pp. 272–277, Mar. 1986, doi: 10.1111/j.1151-2916.1986.tb07425.x.
- [208] F. Babonneau, S. Doeuff, A. Leautic, C. Sanchez, C. Cartier, and M. Verdaguer, 'XANES and EXAFS study of titanium alkoxides', *Inorg. Chem.*, vol. 27, no. 18, pp. 3166–3172, Sep. 1988, doi: 10.1021/ic00291a024.
- [209] A. Juhin, G. Calas, D. Cabaret, L. Galoisy, and J.-L. Hazemann, 'Structural relaxation around substitutional Cr³⁺ in pyrope garnet', *American Mineralogist*, vol. 93, no. 5–6, pp. 800–805, May 2008, doi: 10.2138/am.2008.2823.
- [210] O. Bunău and Y. Joly, 'Self-consistent aspects of x-ray absorption calculations', *J. Phys.: Condens. Matter*, vol. 21, no. 34, p. 345501, Aug. 2009, doi: 10.1088/0953-8984/21/34/345501.
- [211] S. Sasaki, 'Numerical tables of anomalous scattering factors', *National Lab. for High Energy Physics*, vol. 20 KEK--88--14, no. 24 20081580, p. 137, 1989.
- [212] H. J. Bernstein *et al.*, 'Specification of the Crystallographic Information File format, version 2.0', *J Appl Crystallogr*, vol. 49, no. 1, pp. 277–284, Feb. 2016, doi: 10.1107/S1600576715021871.
- [213] P. J. Brown, A. G. Fox, E. N. Maslen, M. A. O'Keefe, and B. T. M. Willis, 'Intensity of diffracted intensities', in *International Tables for Crystallography*, 1st ed., vol. C, E. Prince, Ed., in International Tables for Crystallography, vol. C., Chester, England: International Union of Crystallography, 2006, pp. 554–595. doi: 10.1107/97809553602060000600.
- [214] N. Barrett *et al.*, 'Influence of the ferroelectric polarization on the electronic structure of BaTiO₃ thin films: Influence of the ferroelectric polarization on BaTiO₃ thin films', *Surf. Interface Anal.*, vol. 42, no. 12–13, pp. 1690–1694, Dec. 2010, doi: 10.1002/sia.3369.
- [215] G. H. Kwei, A. C. Lawson, S. J. L. Billinge, and S. W. Cheong, 'Structures of the ferroelectric phases of barium titanate', *J. Phys. Chem.*, vol. 97, no. 10, pp. 2368–2377, Mar. 1993, doi: 10.1021/j100112a043.
- [216] K. Maaz, A. Mumtaz, S. K. Hasanain, and A. Ceylan, 'Synthesis and magnetic properties of cobalt ferrite (CoFe₂O₄) nanoparticles prepared by wet chemical route', *Journal of Magnetism and Magnetic Materials*, vol. 308, no. 2, pp. 289–295, Jan. 2007, doi: 10.1016/j.jmmm.2006.06.003.
- [217] Z. Cao and C. Zuo, 'Direct Synthesis of Magnetic CoFe₂O₄ Nanoparticles as Recyclable Photo-Fenton Catalysts for Removing Organic Dyes', *ACS Omega*, vol. 5, no. 35, pp. 22614–22620, Sep. 2020, doi: 10.1021/acsomega.0c03404.
- [218] Y. Noguchi, H. Matsuo, Y. Kitanaka, and M. Miyayama, 'Ferroelectrics with a controlled oxygen-vacancy distribution by design', *Sci Rep*, vol. 9, no. 1, p. 4225, Dec. 2019, doi: 10.1038/s41598-019-40717-0.
- [219] I. Sosnowska *et al.*, 'Crystal and Magnetic Structure in Co-Substituted BiFeO₃', *Inorg. Chem.*, vol. 52, no. 22, pp. 13269–13277, Nov. 2013, doi: 10.1021/ic402427q.
- [220] C Lefevre *et al.*, 'Potentialities offered by the Resonant X-ray Scattering to the crystallographic study of oxide thin films', 2017, doi: 10.13140/RG.2.2.36071.55207.
- [221] A. Thomasson *et al.*, 'Effects of iron concentration and cationic site disorder on the optical properties of magnetoelectric gallium ferrite thin films', *RSC Adv.*, vol. 3, no. 9, p. 3124, 2013, doi: 10.1039/c2ra22681b.
- [222] P. Frank, K. O. Hodgson, K. Kustin, and W. E. Robinson, 'Vanadium K-edge X-ray Absorption Spectroscopy Reveals Species Differences within the Same Ascidian Genera', *Journal of Biological Chemistry*, vol. 273, no. 38, pp. 24498–24503, Sep. 1998, doi: 10.1074/jbc.273.38.24498.
- [223] H. Husain, B. Hariyanto, M. Sulthonul, P. Thamatkeng, and S. Pratapa, 'Local structure examination of mineral-derived Fe₂O₃ powder by Fe K-edge EXAFS and XANES', *IOP Conf. Ser.: Mater. Sci. Eng.*, vol. 367, p. 012027, May 2018, doi: 10.1088/1757-899X/367/1/012027.
- [224] O. L. G. Alderman *et al.*, 'Iron K-edge X-ray absorption near-edge structure spectroscopy of aerodynamically levitated silicate melts and glasses', *Chemical Geology*, vol. 453, pp. 169–185, Mar. 2017, doi: 10.1016/j.chemgeo.2017.01.020.
- [225] F. Frati, M. O. J. Y. Hunault, and F. M. F. de Groot, 'Oxygen K-edge X-ray Absorption Spectra', *Chem. Rev.*, vol. 120, no. 9, pp. 4056–4110, May 2020, doi: 10.1021/acs.chemrev.9b00439.

- [226] L. Tröger, D. Arvanitis, K. Baberschke, H. Michaelis, U. Grimm, and E. Zschech, 'Full correction of the self-absorption in soft-fluorescence extended x-ray-absorption fine structure', *Phys. Rev. B*, vol. 46, no. 6, pp. 3283–3289, Aug. 1992, doi: 10.1103/PhysRevB.46.3283.
- [227] H. Stragier, J. O. Cross, J. J. Rehr, L. B. Sorensen, C. E. Bouldin, and J. C. Woicik, 'Diffraction anomalous fine structure: A new x-ray structural technique', *Phys. Rev. Lett.*, vol. 69, no. 21, pp. 3064–3067, Nov. 1992, doi: 10.1103/PhysRevLett.69.3064.
- [228] N. A. Katcho *et al.*, 'Structural properties of Ge/Si(001) nano-islands and AlGaN nanowires by Diffraction Anomalous Fine Structure and Multiwavelength Anomalous Diffraction', *J. Phys.: Conf. Ser.*, vol. 190, p. 012129, Nov. 2009, doi: 10.1088/1742-6596/190/1/012129.
- [229] H. M. Rietveld, 'A profile refinement method for nuclear and magnetic structures', *J Appl Crystallogr*, vol. 2, no. 2, pp. 65–71, Jun. 1969, doi: 10.1107/S0021889869006558.
- [230] T. Roisnel and J. Rodríguez-Carvajal, 'WinPLOTR: A Windows Tool for Powder Diffraction Pattern Analysis', *MSF*, vol. 378–381, pp. 118–123, Oct. 2001, doi: 10.4028/www.scientific.net/MSF.378-381.118.
- [231] J. S. Meyer, C. G. Ingersoll, L. L. McDonald, and M. S. Boyce, 'Estimating Uncertainty in Population Growth Rates: Jackknife vs. Bootstrap Techniques', *Ecology*, vol. 67, no. 5, pp. 1156–1166, Oct. 1986, doi: 10.2307/1938671.
- [232] A. K. Jain, R. C. Dubes, and C.-C. Chen, 'Bootstrap Techniques for Error Estimation', *IEEE Trans. Pattern Anal. Mach. Intell.*, vol. PAMI-9, no. 5, pp. 628–633, Sep. 1987, doi: 10.1109/TPAMI.1987.4767957.
- [233] S.-C. Wang, 'Artificial Neural Network', in *Interdisciplinary Computing in Java Programming*, Boston, MA: Springer US, 2003, pp. 81–100. doi: 10.1007/978-1-4615-0377-4_5.
- [234] J. Schmidhuber, 'Deep learning in neural networks: An overview', *Neural Networks*, vol. 61, pp. 85–117, Jan. 2015, doi: 10.1016/j.neunet.2014.09.003.
- [235] I. Goodfellow, Y. Bengio, and A. Courville, *Deep learning*. in Adaptive computation and machine learning. Cambridge, Massachusetts: The MIT Press, 2016.
- [236] P. L. Fernández-Cabán, F. J. Masters, and B. M. Phillips, 'Predicting Roof Pressures on a Low-Rise Structure From Freestream Turbulence Using Artificial Neural Networks', *Front. Built Environ.*, vol. 4, p. 68, Nov. 2018, doi: 10.3389/fbuil.2018.00068.
- [237] A. Martini *et al.*, 'Revisiting the Extended X-ray Absorption Fine Structure Fitting Procedure through a Machine Learning-Based Approach', *J. Phys. Chem. A*, vol. 125, no. 32, pp. 7080–7091, Aug. 2021, doi: 10.1021/acs.jpca.1c03746.
- [238] M. M. M. Madkhali, C. D. Rankine, and T. J. Penfold, 'Enhancing the analysis of disorder in X-ray absorption spectra: application of deep neural networks to T-jump-X-ray probe experiments', *Phys. Chem. Chem. Phys.*, vol. 23, no. 15, pp. 9259–9269, 2021, doi: 10.1039/D0CP06244H.
- [239] S. Xiang *et al.*, 'Solving the structure of "single-atom" catalysts using machine learning – assisted XANES analysis', *Phys. Chem. Chem. Phys.*, vol. 24, no. 8, pp. 5116–5124, 2022, doi: 10.1039/D1CP05513E.
- [240] M. R. Baker and R. B. Patil, '[No title found]', *Reliable Computing*, vol. 4, no. 3, pp. 235–239, 1998, doi: 10.1023/A:1009951412412.
- [241] T. Dietterich, 'Overfitting and undercomputing in machine learning', *ACM Comput. Surv.*, vol. 27, no. 3, pp. 326–327, Sep. 1995, doi: 10.1145/212094.212114.
- [242] C. Nwankpa, W. Ijomah, A. Gachagan, and S. Marshall, 'Activation Functions: Comparison of trends in Practice and Research for Deep Learning', 2018, doi: 10.48550/ARXIV.1811.03378.
- [243] E. Oostwal, M. Straat, and M. Biehl, 'Hidden unit specialization in layered neural networks: ReLU vs. sigmoidal activation', *Physica A: Statistical Mechanics and its Applications*, vol. 564, p. 125517, Feb. 2021, doi: 10.1016/j.physa.2020.125517.
- [244] T. Szandata, 'Review and Comparison of Commonly Used Activation Functions for Deep Neural Networks', in *Bio-inspired Neurocomputing*, vol. 903, A. K. Bhoi, P. K. Mallick, C.-M. Liu, and V. E. Balas, Eds., in Studies in Computational Intelligence, vol. 903. , Singapore: Springer Singapore, 2021, pp. 203–224. doi: 10.1007/978-981-15-5495-7_11.
- [245] D. P. Kingma and J. Ba, 'Adam: A Method for Stochastic Optimization', 2014, doi: 10.48550/ARXIV.1412.6980.
- [246] U. Anders and O. Korn, 'Model selection in neural networks', *Neural Networks*, vol. 12, no. 2, pp. 309–323, Mar. 1999, doi: 10.1016/S0893-6080(98)00117-8.
- [247] C. Schaffer, 'Selecting a classification method by cross-validation', *Mach Learn*, vol. 13, no. 1, pp. 135–143, Oct. 1993, doi: 10.1007/BF00993106.

- [248] J. Gu *et al.*, 'Recent advances in convolutional neural networks', *Pattern Recognition*, vol. 77, pp. 354–377, May 2018, doi: 10.1016/j.patcog.2017.10.013.
- [249] Y. Wang, M. Li, R. Ji, M. Wang, Y. Zhang, and L. Zheng, 'Mark-Spectra: A convolutional neural network for quantitative spectral analysis overcoming spatial relationships', *Computers and Electronics in Agriculture*, vol. 192, p. 106624, Jan. 2022, doi: 10.1016/j.compag.2021.106624.
- [250] A. Peña Corredor *et al.*, 'Spin transport properties of spinel vanadate-based heterostructures', *Applied Physics Letters*, vol. 123, no. 7, p. 072407, Aug. 2023, doi: 10.1063/5.0165642.
- [251] S. Bhatti, R. Sbiaa, A. Hirohata, H. Ohno, S. Fukami, and S. N. Piramanayagam, 'Spintronics based random access memory: a review', *Materials Today*, vol. 20, no. 9, pp. 530–548, Nov. 2017, doi: 10.1016/j.mattod.2017.07.007.
- [252] S. A. Wolf *et al.*, 'Spintronics: A Spin-Based Electronics Vision for the Future', *Science*, vol. 294, no. 5546, pp. 1488–1495, Nov. 2001, doi: 10.1126/science.1065389.
- [253] D. C. Vaz, A. Barthélémy, and M. Bibes, 'Oxide spin-orbitronics: New routes towards low-power electrical control of magnetization in oxide heterostructures', *Jpn. J. Appl. Phys.*, vol. 57, no. 9, p. 0902A4, Sep. 2018, doi: 10.7567/JJAP.57.0902A4.
- [254] J. C. Slonczewski, 'Current-driven excitation of magnetic multilayers', *Journal of Magnetism and Magnetic Materials*, vol. 159, no. 1–2, pp. L1–L7, Jun. 1996, doi: 10.1016/0304-8853(96)00062-5.
- [255] P. Grünberg, R. Schreiber, Y. Pang, M. B. Brodsky, and H. Sowers, 'Layered Magnetic Structures: Evidence for Antiferromagnetic Coupling of Fe Layers across Cr Interlayers', *Phys. Rev. Lett.*, vol. 57, no. 19, pp. 2442–2445, Nov. 1986, doi: 10.1103/PhysRevLett.57.2442.
- [256] M. N. Baibich *et al.*, 'Giant Magnetoresistance of (001)Fe/(001)Cr Magnetic Superlattices', *Phys. Rev. Lett.*, vol. 61, no. 21, pp. 2472–2475, Nov. 1988, doi: 10.1103/PhysRevLett.61.2472.
- [257] M. D. Stiles and A. Zangwill, 'Anatomy of spin-transfer torque', *Phys. Rev. B*, vol. 66, no. 1, p. 014407, Jun. 2002, doi: 10.1103/PhysRevB.66.014407.
- [258] T. Kato, S. Iwata, and D. Oshima, 'Progress on efficient current-induced magnetization switching', *Electr Eng Jpn*, vol. 212, no. 1–4, pp. 3–10, Sep. 2020, doi: 10.1002/eej.23278.
- [259] P. Gambardella and I. M. Miron, 'Current-induced spin-orbit torques', *Phil. Trans. R. Soc. A.*, vol. 369, no. 1948, pp. 3175–3197, Aug. 2011, doi: 10.1098/rsta.2010.0336.
- [260] Q. Shao *et al.*, 'Roadmap of Spin-Orbit Torques', *IEEE Trans. Magn.*, vol. 57, no. 7, pp. 1–39, Jul. 2021, doi: 10.1109/TMAG.2021.3078583.
- [261] M. Trassin, 'Low energy consumption spintronics using multiferroic heterostructures', *J. Phys.: Condens. Matter*, vol. 28, no. 3, p. 033001, Jan. 2016, doi: 10.1088/0953-8984/28/3/033001.
- [262] M. Althammer *et al.*, 'Quantitative study of the spin Hall magnetoresistance in ferromagnetic insulator/normal metal hybrids', *Phys. Rev. B*, vol. 87, no. 22, p. 224401, Jun. 2013, doi: 10.1103/PhysRevB.87.224401.
- [263] M. Creff, J.-E. Wegrowe, and E. Olive, 'Screening effect in spin Hall devices', *Phys. Rev. B*, vol. 105, no. 17, p. 174419, May 2022, doi: 10.1103/PhysRevB.105.174419.
- [264] Y.-T. Chen *et al.*, 'Theory of spin Hall magnetoresistance (SMR) and related phenomena', *J. Phys.: Condens. Matter*, vol. 28, no. 10, p. 103004, Mar. 2016, doi: 10.1088/0953-8984/28/10/103004.
- [265] H. Nakayama *et al.*, 'Spin Hall Magnetoresistance Induced by a Nonequilibrium Proximity Effect', *Phys. Rev. Lett.*, vol. 110, no. 20, p. 206601, May 2013, doi: 10.1103/PhysRevLett.110.206601.
- [266] Y.-T. Chen *et al.*, 'Theory of spin Hall magnetoresistance', *Phys. Rev. B*, vol. 87, no. 14, p. 144411, Apr. 2013, doi: 10.1103/PhysRevB.87.144411.
- [267] N. Jiang, B. Yang, Y. Bai, Y. Jiang, and S. Zhao, 'The sign reversal of anomalous Hall effect derived from the transformation of scattering effect in cluster-assembled Ni_{0.8}Fe_{0.2} nanostructural films', *Nanoscale*, vol. 13, no. 27, pp. 11817–11826, 2021, doi: 10.1039/D1NR02313F.
- [268] K. Tang, Z. Wen, Y.-C. Lau, H. Sukegawa, T. Seki, and S. Mitani, 'Magnetization switching induced by spin-orbit torque from Co₂MnGa magnetic Weyl semimetal thin films', *Appl. Phys. Lett.*, vol. 118, no. 6, p. 062402, Feb. 2021, doi: 10.1063/5.0037178.
- [269] J. Sinova, S. O. Valenzuela, J. Wunderlich, C. H. Back, and T. Jungwirth, 'Spin Hall effects', *Rev. Mod. Phys.*, vol. 87, no. 4, pp. 1213–1260, Oct. 2015, doi: 10.1103/RevModPhys.87.1213.
- [270] J. J. Hauser, 'Magnetic Proximity Effect', *Phys. Rev.*, vol. 187, no. 2, pp. 580–583, Nov. 1969, doi: 10.1103/PhysRev.187.580.
- [271] T. McGuire and R. Potter, 'Anisotropic magnetoresistance in ferromagnetic 3d alloys', *IEEE Trans. Magn.*, vol. 11, no. 4, pp. 1018–1038, Jul. 1975, doi: 10.1109/TMAG.1975.1058782.

References

- [272] J. X. Li, M. W. Jia, Z. Ding, J. H. Liang, Y. M. Luo, and Y. Z. Wu, 'Pt -enhanced anisotropic magnetoresistance in Pt / Fe bilayers', *Phys. Rev. B*, vol. 90, no. 21, p. 214415, Dec. 2014, doi: 10.1103/PhysRevB.90.214415.
- [273] X. Zhou *et al.*, 'Magnetotransport in metal/insulating-ferromagnet heterostructures: Spin Hall magnetoresistance or magnetic proximity effect', *Phys. Rev. B*, vol. 92, no. 6, p. 060402, Aug. 2015, doi: 10.1103/PhysRevB.92.060402.
- [274] S. Meyer *et al.*, 'Anomalous Hall effect in YIG|Pt bilayers', *Appl. Phys. Lett.*, vol. 106, no. 13, p. 132402, Mar. 2015, doi: 10.1063/1.4916342.
- [275] T. Kosub *et al.*, 'Anomalous Hall-like transverse magnetoresistance in Au thin films on Y₃Fe₅O₁₂', *Appl. Phys. Lett.*, vol. 113, no. 22, p. 222409, Nov. 2018, doi: 10.1063/1.5053902.
- [276] Ł. Karwacki *et al.*, 'Optimization of spin Hall magnetoresistance in heavy-metal/ferromagnetic-metal bilayers', *Sci Rep*, vol. 10, no. 1, p. 10767, Jul. 2020, doi: 10.1038/s41598-020-67450-3.
- [277] J. M. Gomez-Perez *et al.*, 'Strong Interfacial Exchange Field in a Heavy Metal/Ferromagnetic Insulator System Determined by Spin Hall Magnetoresistance', *Nano Lett.*, vol. 20, no. 9, pp. 6815–6823, Sep. 2020, doi: 10.1021/acs.nanolett.0c02834.
- [278] A. Ghosh, K. Garello, C. O. Avci, M. Gabureac, and P. Gambardella, 'Interface-Enhanced Spin-Orbit Torques and Current-Induced Magnetization Switching of Pd / Co / AlO_x Layers', *Phys. Rev. Applied*, vol. 7, no. 1, p. 014004, Jan. 2017, doi: 10.1103/PhysRevApplied.7.014004.
- [279] S. Ding *et al.*, 'Anomalous Hall effect in magnetic insulator heterostructures: Contributions from spin-Hall and magnetic-proximity effects', *Phys. Rev. B*, vol. 104, no. 22, p. 224410, Dec. 2021, doi: 10.1103/PhysRevB.104.224410.
- [280] M. Isasa *et al.*, 'Spin Hall magnetoresistance at Pt/CoFe₂O₄ interfaces and texture effects', *Appl. Phys. Lett.*, vol. 105, no. 14, p. 142402, Oct. 2014, doi: 10.1063/1.4897544.
- [281] A. Anadón *et al.*, 'Characteristic length scale of the magnon accumulation in Fe₃O₄ /Pt bilayer structures by incoherent thermal excitation', *Appl. Phys. Lett.*, vol. 109, no. 1, p. 012404, Jul. 2016, doi: 10.1063/1.4955031.
- [282] R. Gao *et al.*, 'Electric Control of the Hall effect in Pt/Bi_{0.9}La_{0.1}FeO₃ bilayers', *Sci Rep*, vol. 6, no. 1, p. 20330, Apr. 2016, doi: 10.1038/srep20330.
- [283] S. Homkar *et al.*, 'Spin Current Transport in Hybrid Pt/Multifunctional Magnetoelectric Ga_{0.6}Fe_{1.4}O₃ Bilayers', *ACS Appl. Electron. Mater.*, vol. 3, no. 10, pp. 4433–4440, Oct. 2021, doi: 10.1021/acsaelm.1c00586.
- [284] A. Anadón *et al.*, 'Thermal Spin-Current Generation in the Multifunctional Ferrimagnet Ga_{0.6}Fe_{1.4}O₃', *Phys. Rev. Applied*, vol. 18, no. 5, p. 054087, Nov. 2022, doi: 10.1103/PhysRevApplied.18.054087.
- [285] G. J. MacDougall *et al.*, 'Magnons and a two-component spin gap in FeV₂O₄', *Phys. Rev. B*, vol. 89, no. 22, p. 224404, Jun. 2014, doi: 10.1103/PhysRevB.89.224404.
- [286] K.-H. Zhao, Y.-H. Wang, X.-L. Shi, N. Liu, and L.-W. Zhang, 'Ferroelectricity in the Ferrimagnetic Phase of Fe_{1-x}Mn_xV₂O₄', *Chinese Phys. Lett.*, vol. 32, no. 8, p. 087503, Aug. 2015, doi: 10.1088/0256-307X/32/8/087503.
- [287] M. V. Eremin, 'Coupling of spins with an electric field in FeV₂O₄', *Phys. Rev. B*, vol. 100, no. 14, p. 140404, Oct. 2019, doi: 10.1103/PhysRevB.100.140404.
- [288] C. Song *et al.*, 'Emergent perpendicular magnetic anisotropy at the interface of an oxide heterostructure', *Phys. Rev. B*, vol. 104, no. 11, p. 115162, Sep. 2021, doi: 10.1103/PhysRevB.104.115162.
- [289] Z. Wang *et al.*, 'Modulation of field-like spin orbit torque in heavy metal/ferromagnet heterostructures', *Nanoscale*, vol. 12, no. 28, pp. 15246–15251, 2020, doi: 10.1039/D0NR02762F.
- [290] T. Taniguchi, S. Mitani, and M. Hayashi, 'Critical current destabilizing perpendicular magnetization by the spin Hall effect', *Phys. Rev. B*, vol. 92, no. 2, p. 024428, Jul. 2015, doi: 10.1103/PhysRevB.92.024428.
- [291] Q. Liu, L. Zhu, X. S. Zhang, D. A. Muller, and D. C. Ralph, 'Giant bulk spin-orbit torque and efficient electrical switching in single ferrimagnetic FeTb layers with strong perpendicular magnetic anisotropy', *Applied Physics Reviews*, vol. 9, no. 2, p. 021402, Jun. 2022, doi: 10.1063/5.0087260.
- [292] L. Zhu, K. Sobotkiewicz, X. Ma, X. Li, D. C. Ralph, and R. A. Buhrman, 'Strong Damping-Like Spin-Orbit Torque and Tunable Dzyaloshinskii–Moriya Interaction Generated by Low-Resistivity Pd_{1-x}Pt_x Alloys', *Adv. Funct. Mater.*, vol. 29, no. 16, p. 1805822, Apr. 2019, doi: 10.1002/adfm.201805822.

- [293] H. Yang, H. Chen, M. Tang, S. Hu, and X. Qiu, 'Characterization of spin-orbit torque and thermoelectric effects via coherent magnetization rotation', *Phys. Rev. B*, vol. 102, no. 2, p. 024427, Jul. 2020, doi: 10.1103/PhysRevB.102.024427.
- [294] P. He, X. Qiu, V. L. Zhang, Y. Wu, M. H. Kuok, and H. Yang, 'Continuous Tuning of the Magnitude and Direction of Spin-Orbit Torque Using Bilayer Heavy Metals', *Adv. Electron. Mater.*, vol. 2, no. 9, p. 1600210, Sep. 2016, doi: 10.1002/aelm.201600210.
- [295] P. He *et al.*, 'Quadratic Scaling of Intrinsic Gilbert Damping with Spin-Orbital Coupling in L 1 0 FePdPt Films: Experiments and *Ab Initio* Calculations', *Phys. Rev. Lett.*, vol. 110, no. 7, p. 077203, Feb. 2013, doi: 10.1103/PhysRevLett.110.077203.
- [296] J. S. Agustsson *et al.*, 'Electrical resistivity and morphology of ultra thin Pt films grown by dc magnetron sputtering on SiO₂', *J. Phys.: Conf. Ser.*, vol. 100, no. 8, p. 082006, Mar. 2008, doi: 10.1088/1742-6596/100/8/082006.
- [297] B. Dieny *et al.*, 'Magnetotransport properties of magnetically soft spin-valve structures (invited)', *Journal of Applied Physics*, vol. 69, no. 8, pp. 4774–4779, Apr. 1991, doi: 10.1063/1.348252.
- [298] B. Dieny, 'Classical theory of giant magnetoresistance in spin-valve multilayers: influence of thicknesses, number of periods, bulk and interfacial spin-dependent scattering', *J. Phys.: Condens. Matter*, vol. 4, no. 40, pp. 8009–8020, Oct. 1992, doi: 10.1088/0953-8984/4/40/013.
- [299] C. Hahn, G. de Loubens, O. Klein, M. Viret, V. V. Naletov, and J. Ben Youssef, 'Comparative measurements of inverse spin Hall effects and magnetoresistance in YIG/Pt and YIG/Ta', *Phys. Rev. B*, vol. 87, no. 17, p. 174417, May 2013, doi: 10.1103/PhysRevB.87.174417.
- [300] C. Gorini, U. Eckern, and R. Raimondi, 'Spin Hall Effects Due to Phonon Skew Scattering', *Phys. Rev. Lett.*, vol. 115, no. 7, p. 076602, Aug. 2015, doi: 10.1103/PhysRevLett.115.076602.
- [301] L. Ma *et al.*, 'Spin diffusion length and spin Hall angle in Pd_{1-x}Pt_x/YIG heterostructures: Examination of spin relaxation mechanism', *Phys. Rev. B*, vol. 98, no. 22, p. 224424, Dec. 2018, doi: 10.1103/PhysRevB.98.224424.
- [302] S. R. Marmion, M. Ali, M. McLaren, D. A. Williams, and B. J. Hickey, 'Temperature dependence of spin Hall magnetoresistance in thin YIG/Pt films', *Phys. Rev. B*, vol. 89, no. 22, p. 220404, Jun. 2014, doi: 10.1103/PhysRevB.89.220404.
- [303] E. Villamor, M. Isasa, L. E. Hueso, and F. Casanova, 'Contribution of defects to the spin relaxation in copper nanowires', *Phys. Rev. B*, vol. 87, no. 9, p. 094417, Mar. 2013, doi: 10.1103/PhysRevB.87.094417.
- [304] G. Mihajlović, J. E. Pearson, S. D. Bader, and A. Hoffmann, 'Surface Spin Flip Probability of Mesoscopic Ag Wires', *Phys. Rev. Lett.*, vol. 104, no. 23, p. 237202, Jun. 2010, doi: 10.1103/PhysRevLett.104.237202.
- [305] H. P. Gavin, 'The Levenberg-Marquardt algorithm for nonlinear least squares curve-fitting problems', 2022.
- [306] X. Zhou *et al.*, 'Tuning magnetotransport in PdPt/Y₃Fe₅O₁₂: Effects of magnetic proximity and spin-orbit coupling', *Appl. Phys. Lett.*, vol. 105, no. 1, p. 012408, Jul. 2014, doi: 10.1063/1.4890239.
- [307] L. Liu *et al.*, 'Symmetry-dependent field-free switching of perpendicular magnetization', *Nat. Nanotechnol.*, vol. 16, no. 3, pp. 277–282, Mar. 2021, doi: 10.1038/s41565-020-00826-8.
- [308] S. Husain *et al.*, 'Large Damping-Like Spin–Orbit Torque in a 2D Conductive 1T-TaS₂ Monolayer', *Nano Lett.*, vol. 20, no. 9, pp. 6372–6380, Sep. 2020, doi: 10.1021/acs.nanolett.0c01955.
- [309] H. Damas *et al.*, 'Ferrimagnet GdFeCo Characterization for Spin-Orbitronics: Large Field-Like and Damping-Like Torques', *Physica Rapid Research Ltrs*, vol. 16, no. 6, p. 220035, Jun. 2022, doi: 10.1002/pssr.202200035.
- [310] M. Dc *et al.*, 'Room-temperature high spin–orbit torque due to quantum confinement in sputtered BixSe(1–x) films', *Nature Mater*, vol. 17, no. 9, pp. 800–807, Sep. 2018, doi: 10.1038/s41563-018-0136-z.
- [311] M. Wakihara, Y. Shimizu, and T. Katsura, 'Preparation and magnetic properties of the FeV₂O₄–Fe₃O₄ system', *Journal of Solid State Chemistry*, vol. 3, no. 4, pp. 478–483, Nov. 1971, doi: 10.1016/0022-4596(71)90089-2.
- [312] A. P. Peña Corredor *et al.*, 'Room-temperature magnetism and controlled cation distribution in vanadium ferrite thin films', 2023, doi: 10.48550/ARXIV.2307.09598.
- [313] M. Abe, M. Kawachi, and S. Nomura, 'Mössbauer study of the FeV₂O₄–Fe₃O₄ system', *Journal of Solid State Chemistry*, vol. 10, no. 4, pp. 351–356, Aug. 1974, doi: 10.1016/0022-4596(74)90044-9.

References

- [314] M. Nohair, P. Perriat, B. Domenichini, and B. Gillot, 'Cationic distribution and mechanism of the oxidation of V³⁺ ions in vanadium-substituted magnetites', *Thermochimica Acta*, vol. 244, pp. 223–234, Oct. 1994, doi: 10.1016/0040-6031(94)80221-1.
- [315] H. M. Do *et al.*, 'Oxidation-controlled magnetism and Verwey transition in Fe/Fe₃O₄ lamellae', *Journal of Science: Advanced Materials and Devices*, vol. 5, no. 2, pp. 263–269, Jun. 2020, doi: 10.1016/j.jsamd.2020.04.001.
- [316] G. Q. Gong, A. Gupta, G. Xiao, W. Qian, and V. P. Dravid, 'Magnetoresistance and magnetic properties of epitaxial magnetite thin films', *Phys. Rev. B*, vol. 56, no. 9, pp. 5096–5099, Sep. 1997, doi: 10.1103/PhysRevB.56.5096.
- [317] G. Zhang *et al.*, 'Magnetic and transport properties of magnetite thin films', *Journal of Magnetism and Magnetic Materials*, vol. 293, no. 2, pp. 737–745, May 2005, doi: 10.1016/j.jmmm.2004.11.529.
- [318] J. G. Zheng, G. E. Sterbinsky, J. Cheng, and B. W. Wessels, 'Epitaxial Fe₃O₄ on SrTiO₃ characterized by transmission electron microscopy', *J. Vac. Sci. Technol. B*, vol. 25, no. 4, p. 1520, 2007, doi: 10.1116/1.2748412.
- [319] M. J. Rossiter, 'The Mössbauer spectra of some spinel oxides containing iron', *Journal of Physics and Chemistry of Solids*, vol. 26, no. 4, pp. 775–779, Apr. 1965, doi: 10.1016/0022-3697(65)90032-6.
- [320] K. J. Kim, S. Choi, Y. Ran Park, J. Han Lee, J. Yun Park, and S. Jin Kim, 'Magnetic and electronic properties of vanadium-substituted magnetite V_xFe_{3-x}O₄ thin films', *Journal of Magnetism and Magnetic Materials*, vol. 310, no. 2, pp. e876–e877, Mar. 2007, doi: 10.1016/j.jmmm.2006.10.868.
- [321] J. Rodríguez-Carvajal, 'Recent advances in magnetic structure determination by neutron powder diffraction', *Physica B: Condensed Matter*, vol. 192, no. 1–2, pp. 55–69, Oct. 1993, doi: 10.1016/0921-4526(93)90108-I.
- [322] D. E. Newbury, 'Mistakes Encountered during Automatic Peak Identification in Low Beam Energy X-ray Microanalysis', *Scanning*, vol. 29, no. 4, pp. 137–151, Jul. 2007, doi: 10.1002/sca.20009.
- [323] G. A. Horrocks *et al.*, 'Vanadium K-Edge X-ray Absorption Spectroscopy as a Probe of the Heterogeneous Lithiation of V₂O₅: First-Principles Modeling and Principal Component Analysis', *J. Phys. Chem. C*, vol. 120, no. 42, pp. 23922–23932, Oct. 2016, doi: 10.1021/acs.jpcc.6b06499.
- [324] X. Zeng *et al.*, 'Direct observation of cation distributions of ideal inverse spinel CoFe₂O₄ nanofibres and correlated magnetic properties', *Nanoscale*, vol. 9, no. 22, pp. 7493–7500, 2017, doi: 10.1039/C7NR02013A.
- [325] R. Nisticò, 'A synthetic guide toward the tailored production of magnetic iron oxide nanoparticles', *Boletín de la Sociedad Española de Cerámica y Vidrio*, vol. 60, no. 1, pp. 29–40, Jan. 2021, doi: 10.1016/j.bsecv.2020.01.011.
- [326] C. J. Thompson *et al.*, 'Spin canting and orbital order in spinel vanadate thin films', *Phys. Rev. Materials*, vol. 2, no. 10, p. 104411, Oct. 2018, doi: 10.1103/PhysRevMaterials.2.104411.

Acknowledgements

I deeply thank all the people who have helped me in either a professional or personal level during these three last years. My gratitude towards you goes much beyond this acknowledgement section.

First of all, I would like to begin by extending my gratitude to the members of the jury for their willingness to assess my PhD research: Fèlix Casanova, Silviu Colis, Maryline Guilloux-Viry, Yves Joly, Florencio Sánchez Barrera and Nathalie Viart. I look forward to engaging in constructive discussions following my thesis defence. Special thanks are due to the examiners who will delve into the finer details of this dissertation.

Then, I truly thank my PhD supervisor, Christophe Lefevre, for his scientific guidance and mentorship. You have trusted me, treated as an equal and given me all the freedom that I could have wished for. Your attitude towards adversities and your kindness have made these three years a much less of a sinuous path. I have really appreciated this PhD journey that we have travelled together, and I will always admire you both in a scientific level and as a person.

I would also like to express my honest gratitude towards Nathalie Viart, who made me love Crystallography long ago and also introduced me to the IPCMS. I have always looked up to your serenity, integrity and passion towards science. Thank you doesn't quite cover it, but please know that your guidance has been invaluable to me over these years.

A special thanks goes to Daniele Preziosi. Your scientific mentorship has been nothing short of essential. I can't thank you enough for your time, effort, and genuine investment in my journey. I will forever carry with me the love for science and the sense of professional integrity that you've instilled in me. Thanks also for the coffee machine.

I would also like to thank the rest of colleagues in the "thin-film oxides" group at IPCMS. Firstly, to the ensemble of PhD students who have accompanied me during these three years: to Guillaume Krieger and his admirable composure, to Laurianne Wendling for her indispensable help and to Suvidyakumar Homkar, who mentored me and introduced me to the fascinating world of oxide thin films. Thanks also to Laurent Schlur and Gilles Versini, whose technical support has been vital for the work of this thesis. I am also very grateful to François Roulland, for his technical help and personal mentorship; and to Silviu Colis for our fruitful discussions during these years. Special thanks also go to Lamiae El Khabchi, with whom I have had my first mentorship experience and whose willpower and determination I truly admire; and to Matthieu Gamarde, for his positiveness and great work quality.

I also acknowledge the technical and personal support of many other people of the institute. I thank Jérôme Robert for his help for the magnetism and transport part of the thesis, Marc Lenertz for his

Acknowledgements

essential help with the x-ray measurements, Cédric Leuvrey for his support for the SEM characterisations and to Guillaume Rogez for his assistance. Thanks also to my late office colleagues, Iryna Makarchuk and Hoshang Sahib and the rest of people at the DCMI department for their company and nice discussions during all this time, especially to Wissal Belayachi, Yihui Cai and Théo Lucante. Thanks a lot to the colleagues who have accompanied me in our HIIT sessions, which have been essential for the conservation of both my physical and mental health these years.

I honestly thank the colleagues who have become close friends during this PhD journey. I thank Mara Vázquez, whose acidic sense of humour towards adversity has really inspired me, and to whom I foresee a brilliant future. To Lisa Royer, for her valuable advice, essential moral support and for being a role model. And to Varun Kumar: good sport partner, even better dogkeeper and the nicest friend a person can possibly be.

I would also like to express my gratitude towards the people outside of the institute who have made a meaningful contribution on this PhD work. To Alberto Anadón, for introducing me to the realm of spintronics and for his professional and scientific guidance these last two years. To the rest of our collaborators at the Institut Jean Lamour in Nancy, specially to Sébastien Petit-Waterlot and Héloïse Damas, for their investment in the spin transport study. To Stéphane Grenier and Guillaume Beutier, for their support and guidance during our experiments in the European Synchrotron Radiation Facility in Grenoble. To Corinne Bouillet and David Troadec, for their investment in the rush TEM measurements. To Yves Joly, for our discussions regarding the *insex* software and whose work has settled the foundations of a great part of this PhD work. I also thank the rest of all the collaborators in all of my scientific articles and, in a broader manner, to the other many contributors who have helped me during these years.

I also thank my friends who, despite being out the lab, have supported me these three years: to Blanca Rodríguez, for bringing colour to my years in Strasbourg; to Miquel García and Paula Barber, my beloved Valencian friends whose visits and lifetime friendships have been a delice to me.

I cannot finish this part without thanking my family in Spain, for whom I allow myself to switch into Spanish. A pesar de nuestra separación física, vuestro apoyo y cariño han sido esenciales en este viaje. Agradezco especialmente a mi hermana Ana, por su infinito cariño y admiración. Has sido mi mejor compañera de vida, debo agradecerte todo lo que soy ahora y espero de verdad hacerte sentir orgullosa. Gracias a Daniel por alegrarnos la vida con tu nacimiento durante esta época de doctorado, estoy deseando explicarte en qué consiste este trabajo. También quiero dar las gracias a Curie, mi compañera perruna, a mi cuñado Paco y a mi padre. Por último, doy las gracias de verdad a mi madre, cuya voluntad de darme la mejor de las educaciones me ha traído hasta aquí. Su temprana ida no le permitió vivir el final de este viaje de doctorado, pero aún puedo sentir su guía y amor acompañándome donde quiera que vaya. Te echamos mucho de menos.

Finally, I would like to express my gratitude to my small family in Strasbourg. I unironically thank my four-pawed, one-eyed friend Willow, whose fluffy love has brought me the greatest joy. And last but not least, I thank my life partner Jérémy, who has made Strasbourg feel like home to me. Meeting you has been a blessing. I can't thank you enough for your generous love, support, and dedication, and I look forward to seeing what life awaits us. Thanks a lot, Jéjé, I love you.

– This page intentionally left blank –

– This page intentionally left blank –

Antonio PEÑA CORREDOR
Multifunctional iron vanadate
thin films for spintronics



Résumé

Le vanadate de fer (FeV_2O_4) est un oxyde multifonctionnel de structure spinelle, présentant des degrés de liberté magnétiques, ferroélectriques et orbitaux. Bien que sa forme massive ait été largement étudiée, les recherches sur sa variante en film mince sont rares. Des couches minces de FeV_2O_4 ont été élaborées par ablation laser pulsée sur deux substrats différents (MgO et SrTiO_3). La qualité et la bonne cristallinité des couches ont été caractérisées par diverses méthodes. Ces films présentent un comportement magnétique à des températures inférieures à 130 K et leurs propriétés physiques sont considérablement influencés par les effets de contrainte. Des analyses cristallographiques poussées sur les films ont été réalisées par diffraction résonante, révélant la distribution cationique des films ainsi que la position des atomes d'oxygène. Une telle étude a catalysé le développement de nombreuses techniques pour l'étude cristallographique de films minces d'oxyde, y compris le développement du logiciel *insex* et l'affinement des spectres de rayons X à l'aide de réseaux neuronaux artificiels. La forte anisotropie magnétique perpendiculaire de $\text{FeV}_2\text{O}_4//\text{SrTiO}_3$ a été exploitée pour étudier les propriétés de transport de spin sous forme d'hétérostructures à base de platine. Nos résultats montrent que la magnétorésistance de spin domine à toutes les températures, atteignant des niveaux comparables à des systèmes à base d'oxyde hautement optimisés. Enfin, nous avons élargi la famille des films minces d'oxydes spinelles avec le premier dépôt de ferrite de vanadium (Fe_2VO_4) sur MgO . Les films présentent un comportement magnétique à température ambiante et des expériences de diffraction anormale ont révélé une structure spinelle inverse dans le matériau.

Mots-clefs : vanadate de fer, spinelles en couche mince, REXS, spintronique, ferrite de vanadium

Résumé en anglais

Iron vanadate (FeV_2O_4) is a multifunctional spinel oxide material; displaying magnetic, ferroelectric and orbital degrees of freedom. While its bulk form has been extensively researched, studies on its thin-film variant are notably sparse. FeV_2O_4 thin films have been elaborated using pulsed laser deposition onto two different substrates (MgO and SrTiO_3), and their high-quality and crystal epitaxy have been attested by diverse characterisation methods. These films demonstrate magnetic behaviour at temperatures below 130 K and are substantially influenced by strain effects. An advanced crystallographic analysis on the films has been conducted resonant diffraction. This has unveiled the films' cationic distribution and the position of the oxygen atoms. Such a study has catalysed the development of loads of techniques for the crystallographic study of oxide thin films, including the development of the *insex* software and the refinement of X-ray spectra using artificial neural networks. The high perpendicular magnetic anisotropy of $\text{FeV}_2\text{O}_4//\text{SrTiO}_3$ has been exploited for the study of the spin transport properties in the form of Pt-based heterostructures. Our findings show that the spin magnetoresistance dominates at all temperatures, achieving levels comparable only to highly optimised oxide-based systems. Finally, we have expanded the spinel oxide thin-film family with the first deposition of vanadium ferrite (Fe_2VO_4) onto MgO . The films present room-temperature magnetic behaviour and anomalous diffraction experiments have unveiled an inverse spinel structure in the material.

Keywords: iron vanadate, spinel thin films, REXS, spintronics, vanadium ferrite